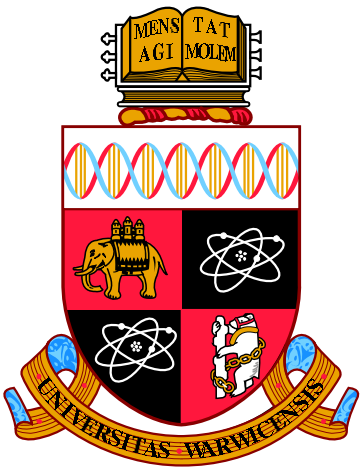

Resonant X-ray Scattering from Magnetic Multilayers and Patterned Arrays

by

Rachael Alice Procter

Thesis

Submitted to the University of Warwick

for the degree of

Doctor of Philosophy

Department of Physics

November 2017

Contents

List of Figures

Acknowledgements

I would like to take this opportunity to express my thanks and gratitude to the people who have in so many ways helped and supported me throughout my doctoral studies.

Firstly I would like to thank Dr Thomas Hase for his supervision. Our many conversations have shaped this work and I would like to thank him for all his help and support. I'm sure acknowledgements would not be complete without saying a further thanks for teaching me how to travel in style.

I would also like to thank the members of the materials physics group at the University of Uppsala. In particular Professor Björgvin Hjörvarsson, Dr Fridrik Magnus and Dr Vassilios Kapaklis, it was a privilege to work with you and your amazing group.

I would like to acknowledge the scientists at the various facilities used to collect data for this work and indeed it would not have been possible without their hard work and expertise. This includes Dr Laurence Bouchenoire at XMaS, Dr Daniel Haskel and Dr Yongseong Choi at 4-ID-D and Dr Cecilia Sánchez-Hanke at X13A.

Special thanks to all my friends in the physics department and our lunch time conversations which were quite dependably not about physics.

I must give huge thanks to my family for their continued support, hugs and lots of cups of tea. Finally, thanks to Gordon, it's been quite a journey for us and I couldn't have done it without you.

Declarations

This thesis is submitted to the University of Warwick in support of my application for the degree of Doctor of Philosophy. It has been composed by myself and has not been submitted in any previous application for any degree.

In Chapter 5, all samples, laboratory x-ray reflectivity/diffraction data and the SQUID and MOKE magnetometry were recorded by members of the Materials Physics group at the University of Uppsala and were provided to the author by Dr Vassilios Kapaklis. The x-ray resonant scattering measurements were collected at the XMaS beamline at the ESRF by the author and collaborators from the University of Uppsala under the supervision of Dr Vassilios Kapaklis, Dr Thomas Hase and Dr Laurence Bouchenoire.

In Chapter 6, the x-ray resonant scattering data was collected on beamline X13A at the NSLS by Dr Thomas Hase, Professor Björgvin Hjörvarsson and Dr Cecilia Sánchez-Hanke. The samples, laboratory x-ray reflectivity data, MOKE data and microscopy images were prepared by collaborators from the University of Uppsala and provided to the author by Dr Fridrik Magnus.

The x-ray resonant scattering measurements in Chapter 8 were recorded at beamline 4-ID-D at the APS by the author, Dr Thomas Hase, Dr Björgvin Hjörvarsson, Dr Daniel Haskel and Dr Yongseong Choi. The samples were prepared by members of the Materials Physics group at the University of Uppsala. The SEM images were provided to the author by Eric Östman at the University of Uppsala.

All data analysis and fitting in this thesis was performed by the author under the supervision of Dr Thomas Hase.

Publications

Magnetic leverage effects in amorphous SmCo/CoAlZr heterostructures.

R. A. Procter, F. Magnus, G. Andersson, C. Sánchez-Hanke, B. Hjörvarsson, and T. P. A. Hase

Applied physics letters, **107**, 062403 (2015)

Long-range magnetic interactions and proximity effects in an amorphous exchange-spring magnet

F. Magnus, M. E. Brooks-Bartlett, R. Moubah, **R. A. Procter**, G. Andersson, T. P. A. Hase, S. T. Banks and B. Hjörvarsson

Nature communications, **7**, ncomms11931 (2016)

Abstract

The structural and magnetic properties of thin films, multilayers and patterned arrays are studied using resonant x-ray scattering. This work shows how resonant scattering techniques can be highly effective when applied to the investigation of interactions across interfaces in a range of magnetic structures.

The effect of growth temperature on the roughness of interfaces in a Gd-Y superlattice is studied with specular reflectivity tuned to the Gd L_3 absorption edge. Superlattices containing thin layers of Ho within the Y are investigated where the Ho acts as a tagging layer to indirectly measure the Y magnetisation. High roughness meant the Ho could not be resolved in fits to the specular reflectivity.

A trilayer of amorphous SmCo and CoAlZr layers is characterised using element specific hysteresis loops recorded at the Co L_3 and Sm M_4 absorption edges. Evidence is found that the intra-layer interactions of the Co and Sm sub-networks within the SmCo layer are weaker than the inter-layer Co interactions due to the randomly distributed structure of the amorphous layers. There are Co rich regions which span the interface, confirmed by fits to specular reflectivity at the Co L_3 edge and modelling of the Co sub-network.

Lastly, element specific hysteresis loops recorded using resonant scattering at the Pd L_3 absorption edge are used to study magnetisation reversals of patterned arrays of FePd. Resonant specular reflectivity and rocking curves reveal that the circular islands are domed with the magnetisation evenly distributed throughout, and a non-magnetic oxide layer. Simulated rocking curves confirm that there is a non-magnetic oxide layer on the islands.

Chapter 1

Background

This chapter will outline previous work on magnetic thin films, multilayers and patterned arrays. An introduction to the properties of different types of magnetic materials is given. It will briefly introduce some of the phenomena observed when these materials are grown as thin films and how the reduction in geometry directly influences their magnetic properties. The chapter will then go on to show how thin films can be altered by combining them into multilayers or patterned arrays and will give some examples of the resulting magnetic properties of such structures.

1.1 Introduction

Magnetic materials were first discovered thousands of years ago with lodestone, a naturally occurring iron ore, being one of the first magnetic substances to be used [1]. Early uses of magnetic materials included compasses where the ability of a magnetic needle to point to true north was exploited for navigational purposes. Over the last two centuries the study of magnetism and magnetic materials has progressed rapidly with many applications in fields such as power generation, motors, construction and manufacturing [2]. Magnetic materials are not only important for technological applications but also in basic research where it has been shown that there is an inextricable relationship between magnetism and electricity. Indeed, many of our theories of electromagnetic waves, relativity and quantum mechanics have foundations in magnetism research [3].

Much of modern research is centred around magnetism at the nano-scale such as thin films, multilayers and patterned arrays. The study of magnetic nano-structures has principally been driven by capabilities in fabrication and surface-sensitive characterization techniques, most of which are only possible under vacuum.

As such, progress in vacuum technologies in the 1970s had a particularly significant impact on nano-scale magnetism research as new levels of control over growth conditions revolutionised the study of thin films. Improvements in the quality of samples produced, in turn led to an increase in the study of magnetic multilayers and superlattices [4]. Growth techniques like molecular beam epitaxy and sputtering became viable options to produce high quality thin films and multilayers with very low roughness between interfaces [5]. The development of materials in new configurations forms the foundation of many areas of basic and applied research. Magnetic nano-scale devices provide the underpinning science for a number of technologies including magnetic data storage [6–9], spintronics [10, 11], magnetic sensors [12] and even biological applications [13, 14].

Breakthroughs in vacuum science also made developments in lithography techniques possible and opened up new avenues of research into patterned arrays of magnetic nano-scale structures. Nanoimprint lithography allows growth of relatively large areas of patterned media with sub-100 nm resolution quickly and cost effectively [15]. Patterned arrays of magnetic nano-structures have become a popular research topic in recent years due to their uses in magnetic data storage devices.

Patterned arrays and multilayers therefore have an important role to play in modern technology but also provide a platform for basic research. The high levels of control over layer thickness and roughness, composition and crystallinity allow for the design of new structures where the properties can be tuned for a distinct purpose or to explore a particular physical mechanism. Novel magnetic devices can be designed which would otherwise not be found in nature allowing for tailored studies of fundamental magnetic properties of materials.

Fundamental to the development of the latest generation of magnetic materials is a detailed knowledge of both their structural and magnetic properties. To this end, a characterisation technique is needed which is suitable for studying such structures. One such technique is x-ray resonant magnetic scattering which offers a unique tool for the study of thin films, multilayers and patterned arrays which is surface-sensitive, element specific and non-destructive. Studying magnetic thin films and heterostructures using resonant x-ray reflectivity provides a highly sensitive characterisation technique which can be used to probe the magnetic structure as a function of depth.

This thesis aims to give an introduction to the theory required to understand resonant scattering processes and also details how scattering data can be fitted in order to extract structural information. The samples presented in this thesis are an epitaxial Gd-Y superlattice, an amorphous trilayer of CoAlZr/SmCo and an FePd

thin film which is patterned into an array of circular islands. The samples in this work will each clearly have different characteristics, but resonant scattering can be adapted to study their individual magnetic properties.

The following chapter will outline some of the many phenomena observed in magnetic multilayers and patterned arrays. It will give descriptions of the types of magnetic materials that are presented in this thesis, including the characteristics which result when layers of these materials are grown in contact with one another. It will also introduce the effect of reducing the dimensions of these materials, either as a thin film or by patterning a film into an array of small islands. The aim is to give an outline of the area of magnetic thin films to both emphasise the wide ranging impact that this field has and also to put the subsequent work in context.

1.2 Bulk Magnetic Materials

If the properties of multilayers and patterned arrays are to be fully understood and subsequently used to design novel magnetic structures, we must first have a thorough knowledge of the properties of bulk magnetic materials. Many of the fundamental principles in magnetism are centred around exchange interactions which are often used to describe the different kinds of magnetic ordering such as ferromagnetism or antiferromagnetism. Magnetic materials can be composed of pure elements such as Co or Fe but are often created by combining elements together to form alloys. Alloying has an effect on properties such as the magnetic ordering temperature and this can be highly dependent on composition allowing the material characteristics to be finely tuned. An understanding of the materials in bulk also includes whether they are magnetically hard or soft or if they have strong magnetocrystalline anisotropy. These concepts will be discussed in the first section of this chapter before going on to describe the effect of growing thin films and multilayers.

1.2.1 Exchange Interactions

In many models of magnetism, exchange interactions are key to explaining magnetic ordering. The exchange interaction between magnetic dipoles is a quantum mechanical effect described by both the Coulomb interaction and the Pauli exclusion principle. If we consider two electrons with position vectors $\mathbf{r_1}$ and $\mathbf{r_2}$, with wavefunctions $\psi_a(\mathbf{r_1})$ and $\psi_b(\mathbf{r_2})$. The electrons are indistinguishable from one another and therefore the wavefunction squared is invariant for the exchange of the electrons. As the electrons are fermions they must obey the Pauli exclusion principle, and thus the wave function must be antisymmetric. The derivation of the

spin-dependent Heisenberg Hamiltonian for a many-body system will not be shown here as it can be found in many standard texts [3, 16–18]. It is written as

$$\mathcal{H} = -\sum_{ij} J_{ij}\mathbf{S}_i.\mathbf{S}_j \tag{1.1}$$

where $\mathbf{S}$ are the spin operators and J_{ij} is the exchange constant (or exchange integral) which is positive for ferromagnetism or negative for antiferromagnetism.

When the electrons of nearest neighbours interact without the need for intermediary electrons, this is known as direct exchange. Very often, however, direct exchange cannot be the driving mechanism behind the observed magnetic properties as there is not enough direct overlap of neighbouring magnetic orbitals [3]. For example, in the rare earths, the $4f$ electrons are strongly localised and the direct exchange mechanism is unlikely to account for the observed magnetism in the rare earths. Even for the transition metals like Fe, Co and Ni where the $3d$ orbitals extend further from the nucleus, there is not enough overlap, to justify why these are strongly ferromagnetic materials.

The magnetism of the iron-series transition metal elements is better described by a model which includes delocalised, or *itinerant* electrons. The itinerant electrons lead to non-integer spin moments per atom, for example 2.2 μ_B for Fe, 1.7 μ_B for Co and 0.6 μ_B for Ni [19]. As each spin carries a moment of 1 μ_B, the non-integer values cannot be of ionic origin but are due to interatomic hopping of the moment-carrying electrons. Itinerant magnetism is often described using a band model of

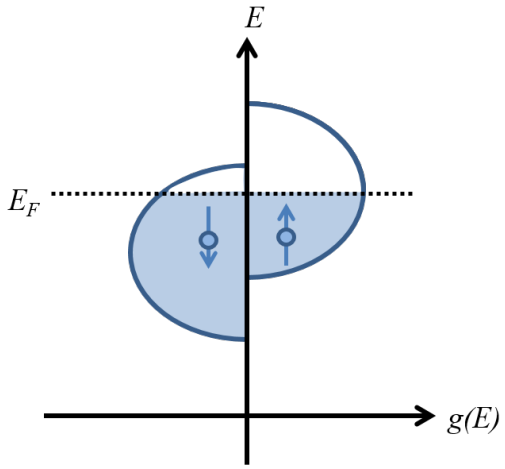

Figure 1.1: The Stoner model of ferromagnetic transition metals for the $3d$ shell. The shells are filled up to the Fermi energy E_F as marked by the shaded regions. Adapted from [16].

magnetism, the simplest of which is the Stoner model, which assumes that the interaction between $3d$ electrons causes a smearing of their energies into a band. For simplicity, the density of states $g(E)$ is approximated as a semicircle as shown in Figure 1.1 and the s and p states are not shown. The electrons occupy band states up to and including the Fermi energy. In this model, the conduction band is split into two bands, one for spin-up and one for spin-down electrons. As specified by Hund's rules, electrons at the Fermi energy preferentially occupy one sub-band over the other resulting in a spontaneous magnetisation [20].

RKKY Interactions

Ruderman and Kittel first suggested that a local moment (in their work they considered the nuclear rather than electronic spin) can induce a spin polarisation in the surrounding sea of conduction electrons [21]. Kasuya [22] and Yosida [23] used similar theories to treat the coupling of localised rare earth $4f$ moments with the conduction electrons. The combined work has led to the effect that is commonly called the RKKY exchange interaction in which a localised magnetic moment polarises the surrounding conduction electrons and because they are delocalised, they transfer the polarisation to a distant magnetic ion. This can be thought of as a free-electron gas of conduction electrons which are perturbed by the local magnetic moment. The perturbation is wave-like and yields an oscillating interaction where the interaction strength is given by [24]

$$J(R) = J_0 \frac{2k_F R\cos(2k_F R) - \sin(2k_F R)}{(2k_F R)^4} \tag{1.2}$$

where k_F is the Fermi wavevector and R the distance from the localised magnetic moment. This interaction strength is shown in Figure 1.2 and oscillates between positive and negative values as a function of R.

Rare-earth elements such as Sm, Gd or Dy exhibit behaviour which differs from the itinerant behaviour of the $3d$ transition metals and is best described using a model with both delocalised and localised electrons. The RKKY interaction was originally a model of dilute magnetic impurities in a metallic host and as such was not intended to describe rare-earth magnetism, but a similar oscillatory behaviour is observed with origins in the mixing of localised and delocalised electrons. The oscillatory behaviour of the interaction strength leads to a large variety of magnetic ordering in the rare earths and their alloys including antiferromagnetism, helical ordering and other more complex non-collinear arrangements depending on R and the sign of J.

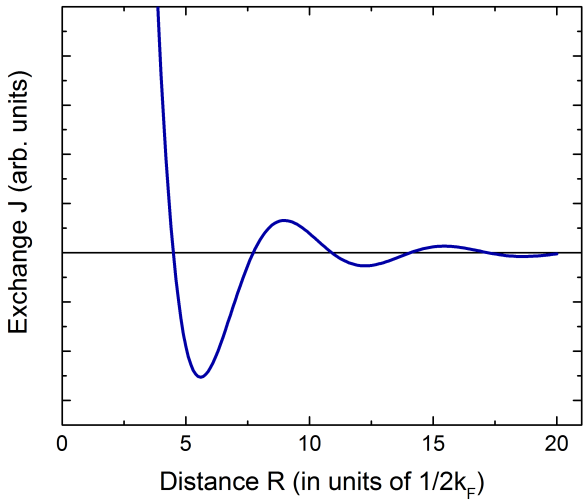

Figure 1.2: Oscillatory indirect exchange interaction typical of rare earth magnetism as a function of distance, R.

1.2.2 The Ordering Temperature

A ferromagnet has a spontaneous magnetisation even in the absence of an applied field. The Weiss mean-field model assumes individual atomic spins experience an exchange field created by neighbouring atoms and which is proportional to the average magnetisation, $\mathbf{M}$. The mean field is thus given as $\mathbf{B_{eff}} = \lambda\mathbf{M}$, where λ is a constant [25]. In principle, each spin experiences a field generated by all the other spins but this is normally simplified to consider only nearest neighbours.

The Curie temperature T_C is the temperature below which a spontaneous magnetisation exists, and it separates the disordered paramagnetic state at $T > T_\mathrm{C}$ from the ordered ferromagnetic phase when $T < T_\mathrm{C}$. The exchange constant not only determines the magnetic ordering but also the ordering temperature. Suppose that an atom has n nearest neighbours, each with an interaction strength with the central atom given by J, and only nearest neighbours are considered. The Curie temperature obtained from the mean-field Heisenberg model is then

$$T_\mathrm{C} = \frac{2S(S+1)}{3k_B} nJ \tag{1.3}$$

where k_B is the Boltzman constant. Equation 1.3 clearly shows that the ordering temperature is directly related to the exchange constant as $J \propto T_\mathrm{C}$.

The magnetisation, $\mathbf{M}$, can be found using the Curie-Weiss law and is of the form

$$\mathbf{M} = \alpha \left(1 - \frac{T}{T_\mathrm{C}}\right)^{\beta} \tag{1.4}$$

where T_C is the ordering temperature, α a scaling parameter and β the critical exponent [3]. In mean-field theory, the magnetisation behaves as $M \simeq \sqrt{T_C - T}$ corresponding to a mean-field critical exponent value of $\beta = 1/2$. In real systems, the behaviour of the magnetisation is as shown in Equation 1.4, but the critical exponent β is not necessarily equal to 1/2 and takes a value which is related to the spin dimensionality of the system.

1.2.3 Anisotropy

This chapter has shown that the magnetic alignment and ordering temperature are related to exchange interactions and so far it has been assumed that all nearest neighbours of a given atom have an equal exchange interaction strength, but this is not necessarily the case. In crystalline ferromagnetic materials there is often anisotropy which causes the magnetisation to preferentially align along certain crystallographic axes.

The crystallographic orientation can be important in some magnetic materials and the energy required to magnetise a material can be different depending on the angle between the magnetisation direction and the crystallographic axes [26]. Along certain crystallographic directions it is easier to magnetise a crystal, which leads to there existing a magnetic easy axis and hard axis. One very simplistic explanation of the origin of magnetocrystalline anisotropy is to consider the overlap of electron distributions between neighbouring atoms [25]. The spin-orbit interaction results in the charge distribution being spheroidal rather than spherical, as shown in Figure 1.3. The black arrows mark the spin directions, and a rotation of the spin directions relative to the crystal axes has a resulting effect on the exchange energy. In Figure 1.3, the energy of the configuration in (a) is different to that in (b).

It therefore follows that there are different forms of anisotropy energy de-

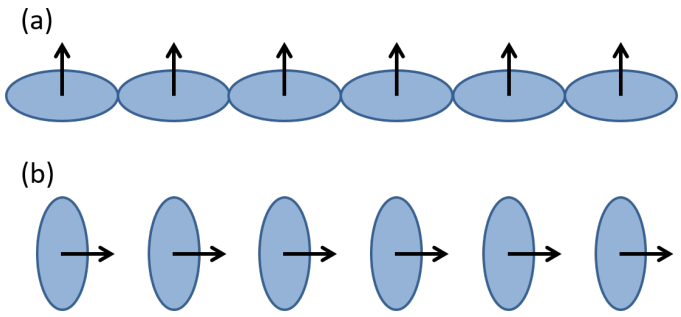

Figure 1.3: Illustration of overlapping electron distributions which provides a possible mechanism for magnetocrystalline anisotropy. Adapted from [25]

pending on the crystal structure of each material. For example, there is *uniaxial* anisotropy when there is only the one easy direction, for example in hexagonal Co which has a single easy direction along the hexagonal axis [27]. The anisotropy energy in this case would be directly related to the angle between the magnetisation and the hexagonal axis and would take the form

$$E_k = K_1 \sin^2(\theta) + K_2 \sin^4(\theta) + ... \tag{1.5}$$

where $K_1, K_2, ...$ are the anisotropy constants and θ is the angle between the magnetisation and the direction of the crystallographic axis [28]. A system with magnetocrystalline anisotropy requires an input of energy from an applied field to move the magnetisation away from the easy axis where the energy goes as $\sin^2\theta$. So it is possible to rotate the magnetisation from the easy axis at first with a small applied field but to rotate to 90° would require a much larger field.

In cubic crystals, any of the three cube edge directions are easy axes. The anisotropy energy can be represented in terms of $\alpha_1, \alpha_2, \alpha_3$ which are the direction cosines of the magnetisation direction with respect to the cubic axes of the crystal. The expression for the anisotropy energy must contain even powers of α_i, assuming that all three axes are magnetically equivalent. The lowest order combination of cosines is $\alpha_1 + \alpha_2 + \alpha_3$ but this is equal to unity and does not contribute to the anisotropy. The next order terms can be used to write the anisotropy energy in the form

$$E_k = K_0 + K_1(\alpha_1^2\alpha_2^2 + \alpha_1^2\alpha_3^2 + \alpha_2^2\alpha_3^2) + K_2(\alpha_1^2\alpha_2^2\alpha_3^2) + ... \tag{1.6}$$

where K_0, K_1 etc. are the anisotropy constants. This form of anisotropy energy has been observed in cubic crystals such as Fe and Ni and some of their alloys [29, 30].

1.2.4 Hard/Soft Magnetic Materials

The exchange constant, J_{ij}, can be used to describe the alignment and strength of the interaction between spins but does not reveal everything about how the bulk material will behave. In actual materials, the magnetic structure is composed of small regions called domains where the direction of the magnetisation in different domains is not necessarily parallel. When a sample is placed in an applied magnetic field, there are two main processes that occur to the magnetic domains which result in an increased overall magnetic moment. Firstly, domains which are oriented favourably with respect to the applied field increase in volume at the expense of those which are oriented unfavourably and secondly, the domain magnetisation rotates in the direction of the applied field.

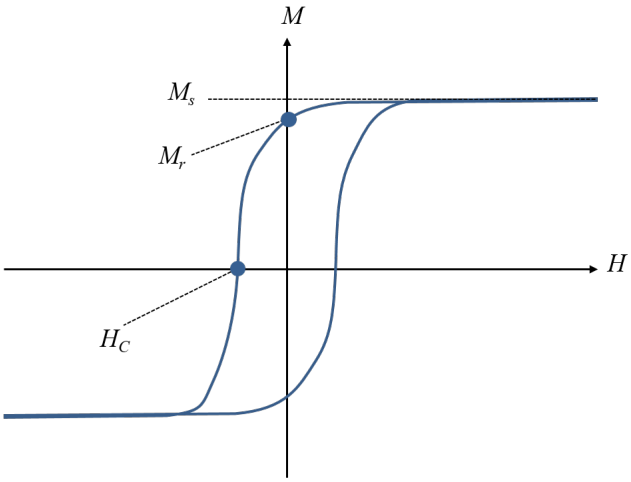

Figure 1.4: Magnetic hysteresis loop defining the saturation magnetisation M_s, the remanent magnetisation M_r and the coercive field H_C.

The properties of a magnetic material can be studied by measuring the effects of an applied field on the magnetisation and a curve is produced which often has some hysteresis like that illustrated in Figure 1.4. Additional to the effect that domains have, anisotropy will have a part to play in the way materials behave in a magnetic field and the magnetic domain structure and anisotropy can be studied by recording magnetic hysteresis loops. The hysteresis loops can be used to reveal information about the domain reversal processes which are effected by domain size and orientation plus the strength and direction of anisotropy.

There are certain parameters that can be extracted from hysteresis loops to give information about the magnetic properties, the most commonly used being the remanence M_r, saturation magnetisation M_s and coercivity H_C which are marked in Figure 1.4. The remanence is the value of the magnetisation of the material once a saturating applied field has been removed and the coercivity is the field required to demagnetise the material. Magnetic materials can be characterised as being magnetically hard or soft. A hard magnetic material must have a high remanent magnetisation and coercivity [28], and as such, a hard magnetic material can be characterised by having a hysteresis loop which encloses a larger area. The ability of hard magnetic materials to retain a large magnetisation once an applied field is removed is a requirement of most permanent magnets with examples such as SmCo and NdFeB. The large magnetic field required to reverse the magnetisation makes them highly stable and consequently makes hard magnetic materials useful for industrial applications and magnetic devices.

The area enclosed by a hysteresis loop represents an energy which is then

converted into heat [31]. Soft magnetic materials (such as NiFe alloys and FeSi) can be used which have small areas enclosed within their hysteresis loop; this minimises energy losses during magnetisation reversal processes. Magnetically soft materials allow changes in magnetisation to occur at much lower fields and have low coercive fields [32]. They are easy to magnetise and are often used in applications where the magnetisation needs to be reversed rapidly such as transformer coils, generators and motors [33]. Soft materials also have uses in magnetic devices and spintronics, and are often combined with hard materials for use in magnetic data storage [34].

1.2.5 Alloys

Combining elements together into alloys can open up the possibility of creating a large range of materials with varied and highly tunable properties. For example, rare earths and transition metals can be combined to create alloys which take properties typical of both groups resulting in materials which exhibit itinerant and localised features. In rare earth/transition metal intermetallics, the rare earth $4f$ shells remain well localised but couple to the itinerant $3d$ transition metal electrons [35]. The magnetisation in these alloys is found to mostly come from the transition metal, yet the anisotropy originates from the rare earth element.

Alloys containing heavy rare earths are often *ferrimagnetic*, where the two sublattices are anti-aligned [36]. The magnetisation of the two sublattices in a ferrimagnetic material are opposite but not equal such that there will be a net magnetisation. The two sublattices can have different ordering temperatures, resulting in an overall temperature dependence which reflects the behaviour of both. One sublattice can dominate at low temperature and the other at high temperature, the point at which they cancel out and reduce the net magnetisation to zero is called the compensation temperature.

Amorphous alloys are of particular interest due to the influence of the structural disorder on the basic magnetic properties compared to their crystalline counterparts. They give the opportunity to create new materials with a wide range of compositions and magnetic properties whilst reducing the need for lattice matching which is often a challenge when creating crystalline multilayers. With amorphous materials, they do not have a crystal structure with long range order and so should in principle have no intrinsic magnetic anisotropy. This is not actually the case in many materials as an anisotropy can be induced during growth. By carrying out the growth in an applied in-plane field during deposition, a large uniaxial anisotropy can be induced with the easy magnetization direction parallel to the direction of the applied field [37, 38].

1.3 Thin Films

So far the interactions within bulk magnetic materials have been considered, but by growing thin films it is possible to create materials with different properties due to the restrictions in geometry. The reduction in nearest neighbours at the interfaces results in an increase in the density of states at the Fermi energy which leads to the magnetic properties changing markedly in ultrathin films as compared with their bulk counterparts. For example, they have been found in some cases to have an enhanced magnetic moment at the interface [39]. Edge effects can also result in a shift of the ordering temperature T_C for ultrathin films which has been shown to be directly related to the number of atomic layers in the film, n [40]. $T_C(n)$ is suppressed when n is small and this has been experimentally observed in a range of ultrathin films [41–43]. The magnetic properties observed in structures composed of thin films are controlled by a balance between competing interactions. An introduction to some of these concepts will be given in the next sections, starting with the shape anisotropy in thin films.

Reducing the dimensions of a material such that it is a thin film also has an impact on the magnetic anisotropy and the easy direction of magnetisation. Similar to Equation 1.5, to lowest order the anisotropy energy of a ferromagnetic thin film can be written as [3]

$$E_{an} = K \sin^2 \theta \tag{1.7}$$

where θ is now the angle between the magnetisation and the surface normal. K is the anisotropy constant and has three terms

$$K = \frac{2K_s}{t} + K_v + \mu_0 M^2 \tag{1.8}$$

where K_s is the surface/interface anisotropy constant, K_v the volume anisotropy constant and t is the thickness of the layer. The factor of 2 is because generally a layer has 2 interfaces. K_s is affected by roughness at the interface and also by any lattice mismatch. The third term is the shape anisotropy of the film. In thicker films, the shape anisotropy term dominates and the magnetisation lies in the plane of the film. In very thin films, however, the $1/t$ term may become large enough that the spontaneous magnetisation can align perpendicular to the plane of the film. Perpendicular magnetic anisotropy has been observed in a wide range of magnetic thin films with some of the most studied being Co-Pd [44] and Co-Pt multilayered systems [45] and also single films of alloys like CoPt [46] and FePd [47].

Strain in a ferromagnet alters the magnetocrystalline anisotropy which can

result in changes in the magnetisation direction [48]. This effect is often called magnetoelastic anisotropy and is the reverse of magnetostriction which is when a change in magnetisation direction results in changes to the sample dimensions. The crystal will deform spontaneously if to do so acts to lower the magnetocrystalline anisotropy energy. The anisotropy energy associated with magnetostriction can be written for an elastically isotropic medium as

$$E_{me} = \frac{3}{2}\lambda_m E\varepsilon \cos^2\theta. \tag{1.9}$$

Here, λ_m is the magnetostriction constant, E is the elastic modulus and strain is denoted by ε. θ is the angle between the magnetisation and the direction of uniform strain.

1.4 Magnetic Multilayers

So far this chapter has shown that there are many materials available for use in magnetic thin films and nano-structures. They can be grown as crystalline or amorphous, they can be combined into different elemental combinations as alloys and a large range of magnetic properties can be achieved by the choice of material and growth conditions. Materials can be altered by growing them as single thin films where the restrictions in geometry have a direct influence on the magnetism. The next section will outline how the properties of magnetic structures can be further tuned by combining materials together into multilayers.

A good starting point is what happens when two ferromagnetic layers are grown in direct contact with one another. Multilayers of this type can be used to produce an exchange 'spring' magnet [49]. This occurs when one of the layers is magnetically hard and the other soft, with typical exchange springs constructed from a hard layer like SmCo in contact with a soft transition metal layer such as Fe or Co [50]. With the application of an external field, the spins in the soft layer exhibit a continuous rotation, similar to a Bloch wall, an illustration of which is given in Figure 1.5. The spins in the soft layer near the interface are strongly pinned at the interface while those away from the interface are free to rotate with the external field. The rotation of the spins is similar to that of a torsion spring, hence the name exchange 'spring'. The system has an exchange stiffness, similar to a spring constant and if the applied field is removed, the magnetisation returns to the previous direction due to pinning by the underlying hard magnet.

For systems where a soft layer is sandwiched between two hard layers, the

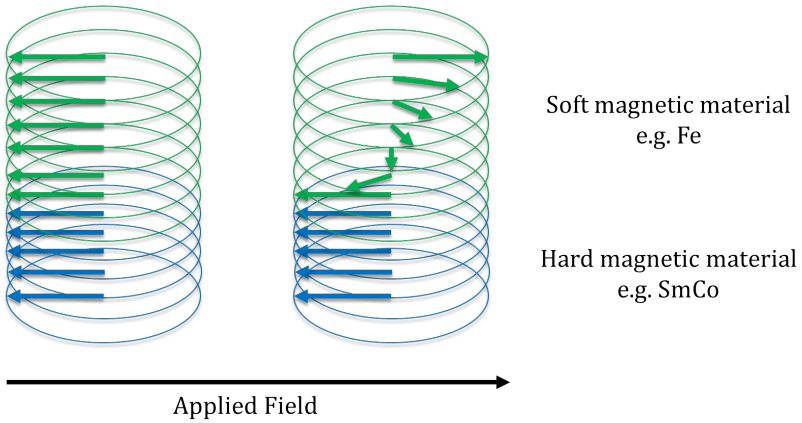

Figure 1.5: Illustration of an exchange spring state in a bilayer consisting of a hard magnetic and a soft magnetic layer.

magnetisation reversal mechanisms in exchange springs are dependent on the thickness of the soft layer. If the thickness is below a critical value, t_s, then the soft layer is rigidly coupled to the hard layer, resulting in the layers reversing at the same applied field value and subsequently a square hysteresis loop is recorded. The exchange spring structure can therefore only be formed when the soft layer thickness is greater than t_s, the value of which has been found to be approximately twice the domain wall width in the hard material. The domain wall width can be given by $\delta_h = \pi\sqrt{A_h/K_h}$ where A_h and K_h are the exchange and anisotropy constants respectively [51]. The energy required to rotate spins in the domain wall is therefore highly material dependent. When the soft layer thickness is above the critical value, the spins in the centre of the soft layer are free to rotate with the field whilst those near the interfaces with the hard layers rotate, and thus form an exchange spring.

One of the most widely studied and exploited phenomena of magnetic multilayers is coupling between magnetic layers across a non-magnetic or antiferromagnetic spacer layer. Giant magnetoresistance is observed in multilayers constructed from layers such as Co-Cu and Fe-Cr where there was found to be long range interactions between the ferromagnetic layers. The term magnetoresistance refers to the effect whereby the resistance of a material is dependent on whether the magnetic layers are aligned parallel or anti-parallel with respect to each other and the effect is used widely in magnetic data storage technologies [52]. The observed interaction in such multilayers is oscillatory depending on the thickness of the spacer layer. This is often described as being similar to an RKKY coupling but for inter-layer cou-

pling rather than between localised moments within the material because there is an oscillatory dependence on the spacer layer thickness similar to that shown in Figure 1.2. Multilayers involving rare-earths can also exhibit this oscillatory behaviour and this has been observed in Gd-Y multilayers where the layers switch between parallel and anti-parallel coupling depending on the Y spacer layer thickness [53]. Rare earth multilayers can also display more complex magnetic structures such as spiral configurations in Dy-Y [54].

The heavy transition metals such as Pd and Pt are often used in magnetic/non-magnetic multilayers [55] or alloys [56] with ferromagnetic elements because although they are paramagnetic at room temperature they possess an unusually high susceptibility due to a large Stoner enhancement factor [57]. This has the consequence that even dilute amounts of ferromagnetic material in Pd or Pt, or alternatively proximity to a ferromagnetic layer can produce a magnetic moment in an otherwise paramagnetic material.

Systems with layers of ferromagnetic material on an antiferromagnet have been seen to exhibit an increased coercivity when grown without an applied field. The increased coercivity is due to pinning by interfacial spins resulting in a higher applied field needed to reverse the magnetisation. There are two equally stable magnetisation directions which have the same energy and the same applied field is required to rotate the magnetisation by 180° which results in a hysteresis loop which is symmetrical about zero. If such a system is grown in an applied field, however, a phenomenon can occur whereby the centre of the hysteresis loop is shifted from zero by some amount, H_{ex}, and this effect is called exchange bias.

Exchange bias is not observed in bulk materials and so has been a topic of great interest as it must arise from interactions at the interface between the ferromagnet and antiferromagnet. The effect is thought to occur in part due to uncompensated spins at the interface where a small number of these spins are pinned during growth by the applied magnetic field. The pinned spins result in the sample being easier to magnetise in one direction than the other and as a consequence, the magnetic hysteresis loop is shifted. It has been shown, however, that the pinned spins do not account for the large exchange bias observed in many systems and it is thought to be more due to pinning from the domain walls in the antiferromagnet. The domains in the ferromagnet are directly determined by the domain structure of the antiferromagnet [58]. Additionally, the domain size is closely related to the size of the exchange bias with the relationship $H_{ex} \propto 1/d$ where d is the domain size [59]. It is clear that different combinations of layers with various magnetic structures can create new, interesting systems and that consideration must be given, not only

when layering materials with different magnetic structures, but also to the magnetic microstructure of the individual layers (i.e. properties such as the domain size).

1.5 Patterned Thin Films

It has been shown that the geometry of a magnetic material can be reduced by creating a thin film which restricts the magnetic moments in the xy-plane, but we can also pattern a film into an array of nano-scale islands. In a sufficiently small magnetic element, shape anisotropy becomes the dominant mechanism controlling the magnetic reversal and structure. When the sample size is reduced, surface energies (such as domain wall energies) compete with volume energies such that at a critical size, it becomes energetically unfavourable to form domain walls and as such a single domain state can occur [60].

The moments in islands preferentially align along the edge of the magnetic element so as to minimise stray fields. In a square island this can occur by forming a Landau pattern whereby domain walls are created as shown in Figure 1.6(left). The energy required to create domain walls is dependent on the size and thickness of the element and also the magnetic properties of the material. Sometimes, however, it is no longer energetically favourable for an element to form domain walls. In such cases, a magnetic vortex like that shown in Figure 1.6(right) can exist. For circular islands the most favourable single domain configuration is a magnetic vortex similar to that shown in Figure 1.6(right). The vortex structure has a net magnetisation of zero, with the central spin pointing in or out, which is characterised by the direction of the central spin and the chirality of the element.

For an elongated ellipsoidal or rectangular island, the magnetostatic energy is most often minimized when the moments align along the long axis which results

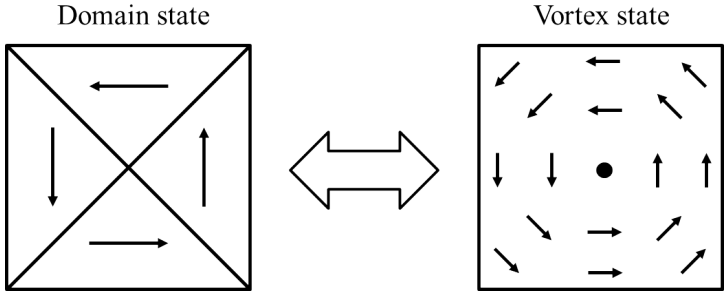

Figure 1.6: (left) Magnetic domains are formed in a square island which minimise stray fields. (right) When the energy cost of forming domain walls is too high, a vortex state can be induced.

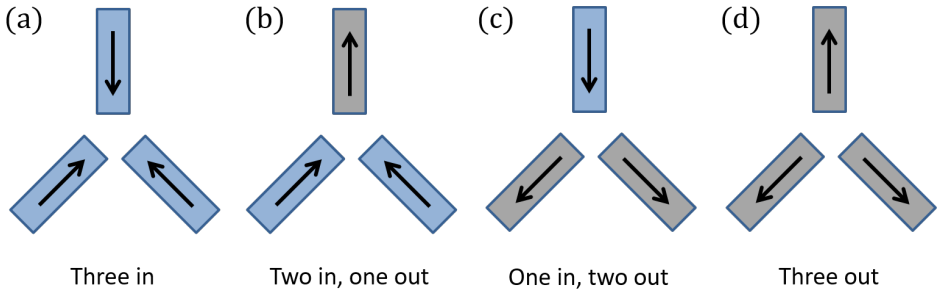

Figure 1.7: (a)-(d) Some possible moment configurations at a single vertex which would form part of a Kagome lattice. Adapted from [66]

in the islands behaving as macrospins. These macrospins can be parametrized by the Ising variable $S = \pm 1$, which encodes the direction the net magnetisation points along the long axis. The islands interact with each other via the dipole field and the coupling can be controlled through appropriate choices of their geometric properties with some of the most popular arrangements being square [61] and Kagome (honeycomb) [62]. Patterned arrays such as these can be used to produce artificial geometrically frustrated magnetic systems. Geometric frustration is observed in many physical systems, one of the most well-known being proton interactions in water ice. The analogy has lead to similar frustrated systems constructed of micromagnetic elements given the name 'artificial spin ice'. The artificial systems created from lithographically patterned thin films provide a two-dimensional analogue to the magnetic spin ice observed in bulk materials such as pyrochlores [63]. Artificial spin ice provides an ideal platform from which to study magnetic interactions and in particular frustrated magnetic systems. There has been much recent interest in studying thermally activated magnetic fluctuations [64] and the thermally driven dynamics in artificial spin ice can lead to currents of magnetic monopole excitations, which has opened up the possibility of magnetic charge-based circuitry [65].

Some example vertices from an array of micromagnets in a Kagome lattice with the magnetisation direction marked by the arrows is shown in Figure 1.7. This arrangement leads to a frustrated system as there is no possible way to achieve zero net magnetisation at a vertex. Figures 1.7(b) and (c) show the two allowed configurations which have two spins in and one out and vice versa. The configurations in Figure 1.7(a) and (d) where all spins point either in or out are not energetically favourable and hence are highly unlikely to occur.

The inter-island interactions can be controlled through choices of their geometry and arrangement on a lattice. They are not restricted to the square or

Kagome configurations already mentioned and a large range of shapes and orientations of nano-islands are available for study. It is also possible to pattern arrays from multilayered materials to take the design of magnetic devices further by combining both the properties of multilayered materials with the inter-island coupling found in patterned arrays [67].

Conclusion

This chapter has introduced bulk magnetism, showing how in some materials, direct exchange interactions drive magnetic ordering whereas others are better described by a band model of magnetism with itinerant electrons. The magnetic properties of a material are determined by the electronic structure, and they vary hugely from material to material. By combining different chemical elements into alloys, it is possible to create new materials with wide ranging magnetic properties which are dependent on the composition and growth conditions. New magnetic structures can be developed when interfaces are introduced into a magnetic material, either through restricting the geometry to produce a thin film or array of nano-scale elements, or by combining it with another material.

This introductory chapter has conveyed that this area of research is broad and active, and there are many ways in which we can tune the properties of heterostructures to produce new materials with wide ranging applications. Although the field of thin film magnetism and heterostructures is active and has seen rapid developments in the last decades, there is still much to learn about the full extent to which multilayers and patterned arrays can be exploited to further both device design and fundamental magnetism research.

Chapter 2

X-ray Scattering Theory

This chapter introduces the theoretical concepts relating to the scattering of x-rays by matter. The reasons for choosing x-ray reflectivity to study the particular samples presented in this work are given and x-ray scattering studies are compared to other popular techniques. The chapter then goes on to outline some of the theory behind interactions of polarised x-rays with matter. Finally, resonant scattering is discussed and how this is used to study the magnetic properties of a material.

2.1 Introduction

The magnetic properties of thin films and patterned arrays are not studied in isolation from the structural properties. As such, it is important to use a combination of characterisation techniques, each with their own advantages and disadvantages, to achieve a more complete understanding of the sample properties. There are many techniques that can be employed to investigate the properties of magnetic thin films and heterostructures including microscopy methods such as scanning electron microscopy (SEM) and atomic force microscopy (AFM). These can provide high resolution surface studies, revealing structure down to the nanometre scale [68, 69]. These two techniques provide slightly different information on surface structure due to the types of interactions which the techniques are sensitive to and they are highly dependent on the material being studied. SEM images are produced from electrons interacting with the sample whereas AFM images depend on the strength of the force between a cantilever and sample.

SEM and AFM are often used as complementary techniques and can provide a wealth of information about the surface structure of thin films and patterned arrays but they have limited penetration depth, and do not reveal structural information

about the bulk. Alternatively, transmission electron microscopy (TEM) can be used, where electrons are passed through a sample revealing structural and compositional features. This requires thin samples to allow sufficient transmission of electrons to produce an image or diffraction pattern and thus some sample preparation is required which can be a lengthy and also destructive process [70].

Microscopy can be used as a method to investigate the magnetic properties by employing AFM, using a cantilever tip with a magnetic moment. This technique is called magnetic force microscopy (MFM) and the magnetic force gradient is mapped whilst simultaneously obtaining topographical data to produce a magnetic image of the surface of the material [71]. TEM can also be used to achieve magnetic sensitivity in a technique called Lorentz microscopy [72]. This method makes use of the Lorentz force: as electrons pass through the sample, they are deflected by the magnetic field. The magnitude and direction of the deflection depends on the magnetisation of the domains and can be used to provide an image of the magnetic structure of the film.

These microscopy techniques can be used to give indications of sample quality, providing information on interface roughness, oxide thickness, and structure and uniformity of layers. They can also be useful for checking the size and shape of the elements in a patterned array [73]. They do not, however, provide a technique for recording the properties in the bulk, they often require destructive sample preparation and only provide information on selective areas.

To probe the magnetic properties of the bulk, one can turn to magnetometry techniques such as magneto-optical Kerr effect (MOKE) and superconducting quantum interference device (SQUID) measurements and these will be discussed in more detail in Chapter 3. For studies of layer-by-layer depth profiles of the structure, we turn to scattering experiments, in particular x-ray or neutron reflectivity. The basic scattering theory is similar for both x-rays and neutrons and they can be used as complementary techniques. Neutrons are neutral particles that are unaffected by the electronic charge. They interact with the nucleus of the atom via the strong force, which only acts over short distances and results in weak scattering. As such, neutrons can penetrate deeply into materials and can be used to study bulk properties or used at grazing incidence to probe the surface regions [74]. X-rays on the other hand, interact strongly with electrons and so have limited penetration depths making them particularly sensitive to surface regions (< 1 μm) [75].

The neutron scattering length, b, depends on the isotope nucleus and does not scale directly with the atomic number Z, whereas for x-rays the scattering is directly proportional to Z [76]. Importantly, neutrons have a magnetic moment which means that they can be used to perform scattering experiments which are

sensitive to the magnetisation of a sample, although this will not be discussed in detail here more details can be found in references such as [77]. X-rays, being a form of electromagnetic radiation, can also be used to probe the magnetic properties of a material, and this chapter will outline the interactions of x-rays with matter that make such studies possible.

The development of synchrotron radiation and very intense, tunable sources of x-rays, significantly changed how x-ray scattering techniques have been used. It was discovered that by tuning to an absorption edge, large enhancements in the magnetic signal could be achieved allowing studies of the magnetic structure with polarised x-rays [78]. The majority of the experimental results presented in this thesis were recorded using x-ray reflectivity to probe the structural and magnetic properties of thin films, multi-layers and patterned arrays and so this chapter will outline some of the theoretical concepts needed to analyse and interpret the experimental data.

2.2 Interactions of X-rays with Matter

These next few sections will outline some of the key scattering concepts, such as the scattering vector and differential cross-section. The atomic form factor will also be introduced and the link will be made between the form factor and the Fourier transform of the electron density.

2.2.1 Elastic Scattering

In the classical picture of x-ray scattering from an atom, the interaction of the electric field from an incident plane-wave x-ray causes the electrons to oscillate. An oscillating electron then becomes a source, re-radiating the x-ray. Elastic scattering from the electrons in this way is referred to as Thomson scattering. The scattering of an x-ray is characterised by the change in its momentum, $\Delta\mathbf{P}$, and energy, E. An incident particle with a wavevector $\mathbf{k}_i$ and angular frequency ω_i is scattered by the sample resulting in a final wavevector $\mathbf{k}_f$ and frequency ω_f. The momentum transfer during this process is

$$\Delta\mathbf{P} = \hbar\mathbf{k}_i - \hbar\mathbf{k}_f = \hbar\mathbf{q} \tag{2.1}$$

where h is the Planck constant with $\hbar = h/2\pi$ and $\mathbf{q} = \mathbf{k}_i - \mathbf{k}_f$ is known as the scattering vector [79]. The energy transfer in a scattering process is similarly given by $\Delta E = \hbar(\omega_i - \omega_f) = \hbar\omega$. This work will only concern elastic scattering where

there is no exchange of energy and as such $\Delta E = 0$.

2.2.2 Polarisation

X-rays are electromagnetic waves with electric **E** and magnetic **H** components as illustrated in Figure 2.1. For Thomson scattering it is appropriate to only consider the electronic charge scattering. The electric part of the electromagnetic field is given as

$$\mathbf{E}(\mathbf{r}, t) = \hat{\boldsymbol{\epsilon}} E_0 \exp^{-i(\omega t - \mathbf{k}.\mathbf{r})} \tag{2.2}$$

where $\hat{\boldsymbol{\epsilon}}$ is the polarisation unit vector and is chosen to be along the **E** vector direction.

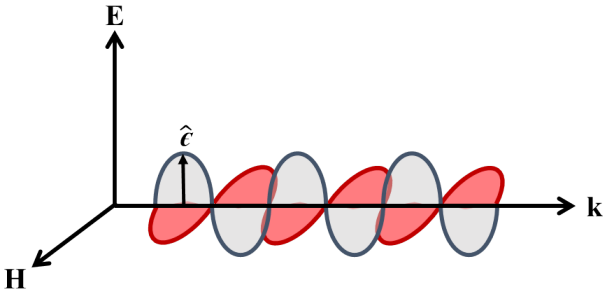

Figure 2.1: An x-ray is an electromagnetic wave where the electric field **E** and magnetic field **H** are perpendicular to each other and to the propagation vector **k**.

In a typical scattering experiment, polarised x-rays can be defined as having one component that is perpendicular to the scattering plane, $\boldsymbol{\sigma}$, and one parallel, $\boldsymbol{\pi}$. The orientation of $\boldsymbol{\sigma}$ and $\boldsymbol{\pi}$ relative to the scattering plane are indicated in Figure 2.2. The electric polarisation unit vectors are $\hat{\boldsymbol{\epsilon}}_{\boldsymbol{\sigma}}$ and $\hat{\boldsymbol{\epsilon}}_{\boldsymbol{\pi}}$ are along the direction of $\boldsymbol{\sigma}$ and $\boldsymbol{\pi}$ respectively. Light in the form of a plane wave which has only $\boldsymbol{\sigma}$ components (or alternatively $\boldsymbol{\pi}$ components) is said to have linear polarisation. If the electric field is represented as a matrix then linear polarisation can be expressed as

$$\mathbf{E}_{\boldsymbol{\sigma}} = \begin{pmatrix} 1 \\ 0 \end{pmatrix}, \quad \mathbf{E}_{\boldsymbol{\pi}} = \begin{pmatrix} 0 \\ 1 \end{pmatrix} \tag{2.3}$$

where $\mathbf{E}_{\boldsymbol{\sigma}}$ and $\mathbf{E}_{\boldsymbol{\pi}}$ denote waves polarized in $\boldsymbol{\sigma}$ and $\boldsymbol{\pi}$ direction, respectively [80]. This representation uses a normalisation condition where $\mathbf{E}^* \cdot \mathbf{E} = 1$. If the wave, however, has equal $\boldsymbol{\sigma}$ and $\boldsymbol{\pi}$ components, then the light is circularly polarised and

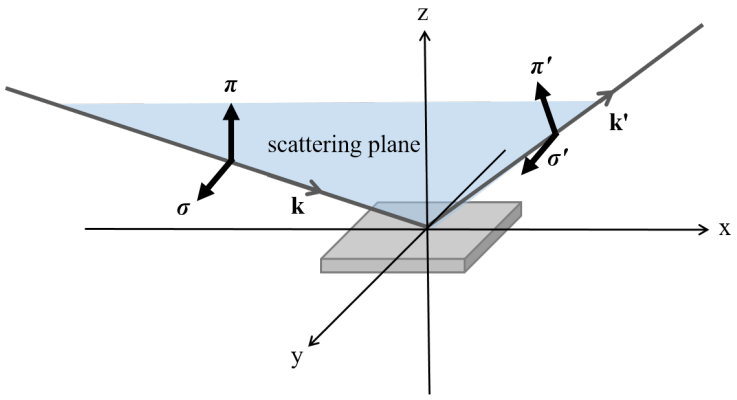

Figure 2.2: Geometry of scattering experiment with polarised light showing the directions of the $\boldsymbol{\sigma}$ and $\boldsymbol{\pi}$ vectors with respect to the scattering plane.

its polarisation can be expressed as

$$\mathbf{E}_L = \frac{1}{\sqrt{2}}\begin{pmatrix}1\\ i\end{pmatrix}, \quad \mathbf{E}_R = \frac{1}{\sqrt{2}}\begin{pmatrix}1\\ -i\end{pmatrix} \tag{2.4}$$

for left and right handed polarisation respectively. Non-equal $\boldsymbol{\sigma}$ and $\boldsymbol{\pi}$ components give elliptically polarised light. It will later be shown (in Section 2.5) that the use of polarised light is fundamental to resonant scattering studies of magnetic materials. The interactions of x-rays with matter described in the next sections therefore assume the incident photon is polarised.

2.2.3 Scattering from a Single Electron

We first consider the case of scattering of an x-ray by the most elementary scattering object, a single, free electron. In the classical description of the scattering event, the electric field of the incident x-ray is given as in Equation 2.2. Interactions are described using the differential cross-section, which is a measure of how efficient an object is at scattering, and is defined as

$$\frac{d\sigma}{d\Omega} = \frac{R}{N\Phi\Delta\Omega} \tag{2.5}$$

where N is the number of scattered photons per second recorded by the detector which is a distance R from the scattering object and subtends a solid angle $\Delta\Omega$ [81]. The flux of the incident beam, which is the number of photons passing through a unit area per second, is denoted by Φ.

Following a scattering event, the ratio of the scattered wave's electric field

to that of the incident wave is

$$\frac{E_{rad}(R,t)}{E_{in}} = -r_0 \frac{\exp^{ikR}}{R} |\hat{\boldsymbol{\epsilon}} \cdot \hat{\boldsymbol{\epsilon}}'| \tag{2.6}$$

with r_0, the Thomson scattering length given as $r_0 = \frac{e^2}{4\pi\epsilon_0 mc^2} = 2.82 \times 10^{-5}$ Å and $\boldsymbol{\epsilon}$ and $\boldsymbol{\epsilon}'$ are the polarisation vectors of the incident and reflected wave respectively. Using equations Equation 2.5 and Equation 2.6, the differential cross-section can be written as

$$\left(\frac{d\sigma}{d\Omega}\right) = r_0^2 |\hat{\boldsymbol{\epsilon}} \cdot \hat{\boldsymbol{\epsilon}}'|^2 \tag{2.7}$$

which is the Thomson differential scattering cross-section of an electromagnetic wave by a free electron and $|\hat{\boldsymbol{\epsilon}} \cdot \hat{\boldsymbol{\epsilon}}'|^2$, the polarisation factor. For non-resonant scattering, the polarisation factor, shows that $\boldsymbol{\sigma}$ to $\boldsymbol{\pi}$ transitions and vice versa are forbidden [82]. For other cases it gives

$$|\hat{\boldsymbol{\epsilon}} \cdot \hat{\boldsymbol{\epsilon}}'|^2 = \begin{cases} 1, & (\boldsymbol{\sigma} \rightarrow \boldsymbol{\sigma}') \\ \cos^2(2\theta), & (\boldsymbol{\pi} \rightarrow \boldsymbol{\pi}') \end{cases} \tag{2.8}$$

where 2θ is the angle between $\mathbf{k}_i$ and $\mathbf{k}_f$ which are the incident and reflected wave vectors respectively. Note that, Equation 2.8 is only valid for charge scattering with no dependence on the magnetic moment. For now, only charge scattering will be considered but Section 2.5.1 will show how this is not the complete picture.

2.2.4 Scattering from an Atom

Now, let us consider scattering from an atom with Z electrons, where the electrons in an atom are smeared into a continuous distribution. The electron distribution will be described as a number density, $\rho(r)$ such that

$$Z = \int_V \rho(r) dV. \tag{2.9}$$

The scattered radiation is a superposition of contributions from across the charge distribution; scattering events from various parts of the electron cloud will have different phases as illustrated in Figure 2.3. The following expressions are derived within the Born approximation (otherwise referred to as the kinematic approximation) which neglects multiple scattering events. This simplifies the problem, as within this approximation the scattered x-rays from two points in the electron distribution which are separated by a distance r differ only by a phase factor $\exp^{i\boldsymbol{q}\cdot\boldsymbol{r}}$.

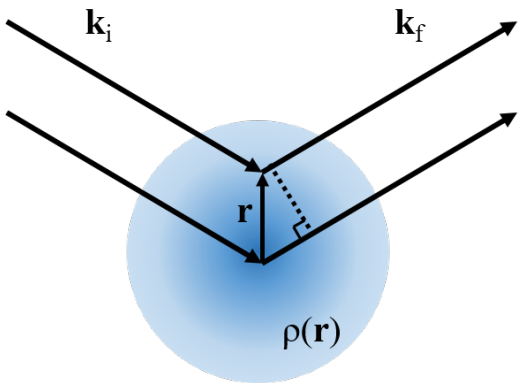

Figure 2.3: A schematic of scattering from an atom with an electron distribution, $\rho(\boldsymbol{r})$. The illustration shows how there is a phase difference between a wave scattered at the origin and one scattered at position $\boldsymbol{r}$.

The atomic scattering factor is the quantity used to describe how efficiently an atom scatters in a given direction. It can be shown that the atomic scattering factor is

$$f^0(\mathbf{q}) = \int \rho(\mathbf{r}) \exp^{i\mathbf{q}.\mathbf{r}} d\mathbf{r} \tag{2.10}$$

which is the *Fourier transform* of the electron density [76]. It will be a frequent feature throughout this work that the scattering length can be calculated from the Fourier transform of the electron distribution. The scattered intensity is then related to the atomic scattering factor and is proportional to $|f^0(\mathbf{q})|^2$.

In a classical model, the electrons are bound in atoms and would behave like a forced harmonic oscillator which is driven by the electric field of the incident x-ray. They would have an associated resonant frequency and damping constant similar to a harmonic oscillator. In this classical model, there are corrections required to the scattering length due to resonance effects. These are f' and f'', the real and imaginary parts of the dispersion corrections which give a total atomic form factor of

$$f(\mathbf{q}, \hbar\omega) = f^0(\mathbf{q}) + f'(\hbar\omega) + if''(\hbar\omega). \tag{2.11}$$

The terms in Equation 2.11 have units of number of electrons per atom. Far from an absorption edge, the dispersion corrections are small and can be considered to be negligible. Note that the Thomson scattering term, $f^0(\mathbf{q})$ is dependent on $\mathbf{q}$ whereas the dispersion corrections are highly dependent on the photon energy with large changes occuring near absorption edges.

2.2.5 Kramers-Kronig Relations

The dispersion corrections $f'(\hbar\omega)$ and $f''(\hbar\omega)$ describing the refraction and absorption respectively are rarely determined independently. The absorption cross-section σ_a can be obtained directly from experiment and the imaginary part of the scattering length f'' is subsequently found from $\sigma_a(E) = (2hcr_0)/Ef''(E)$ where h is Planck's constant, c the speed of light and r_0 is the Thomson scattering length [16]. The real part is then normally calculated using the Kramers-Kronig relation [79]. The relations between the real and imaginary parts of the x-ray scattering factor are given by

$$f'_n(\omega) = \frac{1}{\pi}\mathcal{P}\int_{-\infty}^{\infty} \frac{\omega' f''(\omega')}{(\omega'^2 - \omega^2)} d\omega' \tag{2.12}$$

and

$$f''_n(\omega) = -\frac{1}{\pi}\mathcal{P}\int_{-\infty}^{\infty} \frac{f'(\omega')}{(\omega'^2 - \omega^2)} d\omega'. \tag{2.13}$$

The '$\mathcal{P}\int$' is the principal value integral meaning that the integral is evaluated from $-\infty$ to $(\omega - \epsilon)$ and then from $(\omega + \epsilon)$ to ∞, in the limit that $\epsilon \to 0$. The derivation of the Kramers-Kronig relations is based on Cauchy's theorem, which is used because of the singularity at $\omega = \omega'$ [83].

2.3 Scattering from Surfaces and Interfaces

This chapter has so far outlined some of the theoretical concepts which are needed to describe the interaction of x-rays with matter. It will now go on to look at scattering from thin films and multilayers. In the following sections, $\mathbf{q}$ is taken to be small and so the techniques no longer probe interatomic distances but the scattering is instead determined by the refractive index. Scattering experiments in this regime are sensitive to the effect of surfaces and interfaces; this next section introduces how these are studied. First, Fresnel's equations of reflectivity and transmittivity are given, followed by a description of how these are used for a multilayered material with Parratt's recursive method.

2.3.1 The Refractive Index

In principle, the arguments relating to the interactions of x-rays with matter could be applied to scattering experiments including diffraction, whereby it would be possible to perform scattering studies on atomic scales. This thesis presents the results of scattering experiments carried out at low angles. X-rays in this regime are not

sensitive to the periodic arrangement of atoms but instead the scattering potential is assumed to be constant and defined by the refractive index. The refractive index of a medium can be expressed as

$$n = 1 - \delta - i\beta \tag{2.14}$$

where δ is related to the dispersion within the medium and β is related to absorption [16]. These variables are small positive numbers ($\delta \sim 10^{-5}$ and $\beta \sim 10^{-7}$ for x-rays which have energies of ~ 10 keV) and are given as

$$\delta = \frac{N_A}{2\pi} r_0 \lambda^2 \sum_j \frac{\rho_j}{A_j}(Z_j + f_j') \tag{2.15}$$

and

$$\beta = \frac{N_A}{2\pi} r_0 \lambda^2 \sum_j \frac{\rho_j}{A_j}(f_j'') \tag{2.16}$$

where N_A is Avogadro's number, r_0 is the classical electron radius, λ is the wavelength, ρ_j the density of the jth element, A_j is the atomic mass, Z_j is the atomic number and f_j' and f_j'' are the corrections to the scattering factor required near an absorption edge for the jth element [84]. The values of δ and β are small positive numbers meaning that the refractive index can be slightly less than unity. An illustration of x-rays incident on a surface and being reflected or refracted is shown in Figure 2.4. A beam is incident on a sample at an angle θ_i, it is then either reflected at an angle θ_r or transmitted at an angle θ_t.

Consider these x-ray beams to be plane waves with wavenumbers, $\boldsymbol{k}_i$, $\boldsymbol{k}_r$ and $\boldsymbol{k}_t$ and amplitudes a_i, a_r and a_t for the incident, reflected and transmitted beams

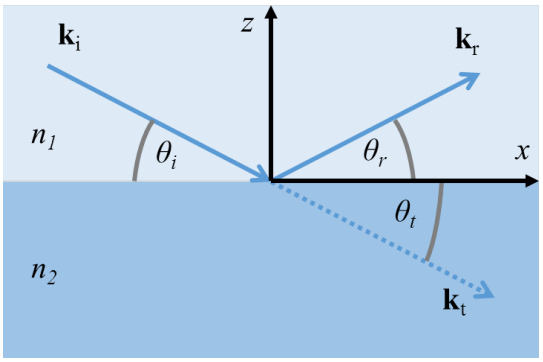

Figure 2.4: A schematic of the reflection and transmission of a plane wave incident on an interface between two materials with refractive indices n_1 and n_2.

respectively. Snell's law and the Fresnel equations can be derived by imposing the conditions that the wave and its derivative at the interface must be continuous and that the amplitudes are related by

$$a_i + a_r = a_t \tag{2.17}$$

and

$$a_i \mathbf{k}_i + a_r \mathbf{k}_r = a_t \mathbf{k}_t. \tag{2.18}$$

Using the wavevector in a vacuum, $k = \frac{|\mathbf{k}_i|}{n_1} = \frac{|\mathbf{k}_r|}{n_1} = \frac{|\mathbf{k}_t|}{n_2}$, and taking the x component of Equation 2.18 this can be combined with Equation 2.17 to give Snell's law, which takes the same form as in the visible range [85]

$$n_1 \cos(\theta_i) = n_2 \cos(\theta_t). \tag{2.19}$$

As the refractive index is less than unity, this implies that below a certain incident grazing angle called the critical angle, θ_c, x-rays exhibit total external reflection. At the critical angle we can set $\theta_t = 0$, $\theta_i = \theta_c$ and for simplicity $\beta = 0$ (absorption is neglected) and substitute these into Equations 2.14 and 2.19 to get

$$\theta_c \simeq \sqrt{2\delta}. \tag{2.20}$$

If we refer back to Equation 2.15, we can see that the critical angle is therefore directly proportional to the wavelength, λ, and to the square root of the mass density.

Fresnel's laws can be obtained by taking the z component of Equation 2.18 and by assuming that at grazing incidence the angles θ_i and θ_f are small. It follows that the coefficients of reflection, F^r, and transmission, F^t, are [79]

$$F^r = \frac{\theta_i - \theta_t}{\theta_i + \theta_t} \qquad F^t = \frac{2\theta_i}{\theta_i + \theta_t}. \tag{2.21}$$

Here the amplitude reflectivity and transmittivity have been introduced whereas the intensity reflectivity or transmittivity are given by the absolute square of these. The Fresnel reflectivity is therefore given as

$$R_F = |F^r|^2 = \left| \frac{\theta_i - \theta_t}{\theta_i + \theta_t} \right|^2. \tag{2.22}$$

According to Snell's law, θ_t can be expressed as $\theta_t = \sqrt{\theta_i^2 - 2\delta - i2\beta}$, which is given as a function of θ_i [84]. Again, if absorption is neglected such that $\beta = 0$, it can then

be shown that *above* θ_c the Fresnel reflectivity follows the relationship $R_F = \delta^2/\theta_i^4$.

The derivations given so far are within the Born approximation which assumes that the interaction between the x-rays and the scattering medium is weak and so the scattered waves have a negligible effect on the incoming beam. It also assumes that multiple scattering events where waves are scattered more than once are neglected. This assumption is not valid at at low q_z because it violates the physical constraint that $R \leq 1$ as $q_z \to 0$ and the Born approximation no longer remains valid close to the critical angle.

2.3.2 Parratt's Recursive Formalism

Parratt derived an iterative process which allows the calculation of the reflectivity from multiple surfaces which allows the reflectivity to be calculated for multilayers [86]. This model is used to generate the simulated specular reflectivity profiles in the software used throughout this work [87]. Unlike the Born approximation, Parratt's recursive formalism takes into account the reflected and refracted beam at each interface. As such, it incorporates multiple scattering and so is valid at all q_z values [79].

Following Parratt, we define the electric vectors at glancing angles as

$$\begin{aligned} E_1(\mathbf{z}_1) &= E_1(0)\exp^{i[wt-(\mathbf{k}_{1,x}\cdot\mathbf{x}_1+\mathbf{k}_{1,z}\cdot\mathbf{z}_1)]} \\ E_1^R(\mathbf{z}_1) &= E_1(0)\exp^{i[wt-(\mathbf{k}_{1,x}\cdot\mathbf{x}_1+\mathbf{k}_{1,z}\cdot\mathbf{z}_1)]} \\ E_2(\mathbf{z}_2) &= E_2^R(0)\exp^{i[wt-(\mathbf{k}_{2,x}\cdot\mathbf{x}_2+\mathbf{k}_{2,z}\cdot\mathbf{z}_2)]} \end{aligned} \tag{2.23}$$

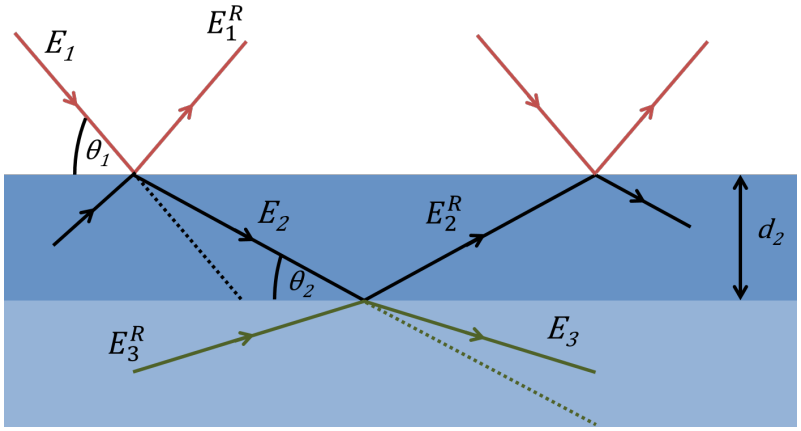

Figure 2.5: Illustration of the reflection and refraction from a layered structure with multiple interfaces. Adapted from [86].

where $\mathbf{k}_1$ and $\mathbf{k}_2$ are the propagation vectors outside and inside the mirror respectively. The propagation of x-rays through a structure with multiple interfaces is illustrated in Figure 2.5, showing the electric vectors as defined above. The Born approximation did not account for refraction of the beam when passing between layers with a different refractive index but, as shown in Figure 2.5, the Parratt recursive formalism does.

Take a theoretical structure comprising N ($N \geq 2$) homogeneous layers with smooth boundaries where the thickness of layer n is denoted by d_n. The thickness of medium 1, d_1, is for air or a vacuum so is disregarded. The continuity equations of the tangential components of the electric vectors for the ($n-1$, n) boundary are given as

$$a_{n-1}E_{n-1} + a_{n-1}^{-1}E_{n-1}^{R} = a_n^{-1}E_n + a_nE_n^{R} \tag{2.24}$$

and

$$(a_{n-1}E_{n-1} + a_{n-1}^{-1}E_{n-1}^{R})f_{n-1}\mathbf{k}_1 = (a_n^{-1}E_n + a_nE_n^{R})f_n\mathbf{k}_1 \tag{2.25}$$

where the amplitude factor, a_n for half the perpendicular depth is $a_n = \exp^{-i\frac{\pi}{\lambda}f_nd_n}$. Here f_n is defined as $f_n = \sqrt{\theta_n^2 - 2\delta_n - 2i\beta_n}$. The solution to the simultaneous equations of Equations 2.24 and 2.25 is obtained by dividing their difference by their sum. The result of this is given as a recursion formula

$$R_{n-1,n} = a_{n-1}^4\left[\frac{R_{n,n+1} + F_{n-1,n}}{R_{n,n+1}F_{n-1,n} + 1}\right] \tag{2.26}$$

where

$$R_{n,n+1} = a_n^2(E_n^R/E_n)$$

and $F_{n-1,n}$, the Fresnel reflection, is

$$F_{n-1,n} = \frac{f_{n-1} - f_n}{f_{n-1} + f_n}.$$

The solution to Equation 2.26 is found by starting at the bottom of the layered system with the last layer assumed to have infinite thickness, so $R_{n,n+1} = 0$. The ratio of the reflected to the incident intensity is then given by

$$\frac{I_R}{I_0} = \left|\frac{E_1^R}{E_1}\right|^2. \tag{2.27}$$

For $N > 3$ where there are many more layers, a matrix approach is commonly used as the algebra, although straightforward, becomes tedious [88].

2.4 Reflectivity

Interactions of x-rays with matter and the reflectivity from multilayered structures have been introduced. Now we look at the scattering geometry used to obtain specular reflectivity scans in practice and how the thickness of layers and roughness between them effect the reflectivity to enable the study of real samples.

2.4.1 Specular Reflectivity

Before continuing, it is necessary to introduce the experimental geometry used when performing a reflectivity measurement. Figure 2.6 shows a schematic of the scattering of an incident x-ray with wave vector $\mathbf{k}_i$ and angle θ. The scattered photon has wave vector $\mathbf{k}_f$ and is scattered at an angle 2θ as indicated. The specular condition is when $\theta = \frac{2\theta}{2}$. The $\mathbf{q}$ vectors are defined as $q_z = (\frac{4\pi}{\lambda})\sin(\frac{2\theta}{2})\cos(\alpha)$ and $q_x = (\frac{4\pi}{\lambda})\sin(\frac{2\theta}{2})\sin(\alpha)$ with $\alpha = (\theta - \frac{2\theta}{2})$. The component of reciprocal space normal to the surface is q_z, and can be probed by scanning the detector and sample angle in a 2 to 1 ratio.

Constructive interference of x-rays reflected from different interfaces gives rise to fringes. The spacing of these fringes is inversely proportional to the layer thickness and constructive interference occurs when

$$d\ \sin(\theta) = n\lambda \tag{2.28}$$

where d is the layer thickness rather than the atomic separation. This effect is

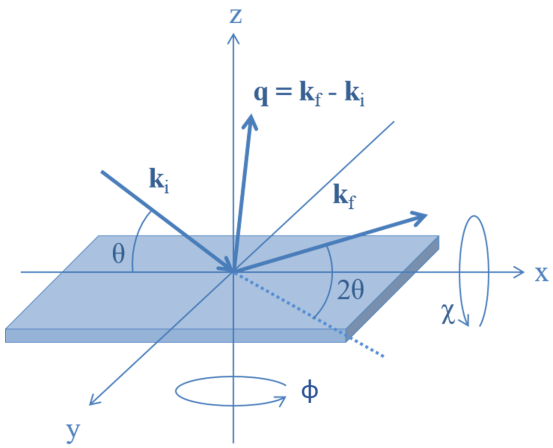

Figure 2.6: Simple schematic of experimental geometry defining $\mathbf{q}$ and its relation to θ and 2θ.

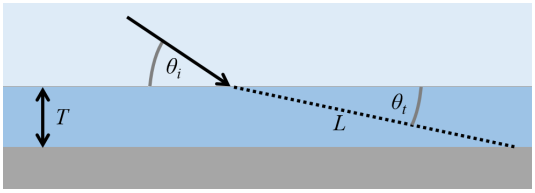

Figure 2.7: The path length, L, of a wave with an incident angle θ_i through a layer of thickness T.

analogous to Bragg's law for diffraction from atomic planes, but is now for multilayer interfaces instead.

Equation 2.28, assumes that the Born approximation is valid, i.e. that the incident wave interacts weakly with the scattering medium. The Born approximation neglects refraction and also assumes a relatively 'thin' sample such that the path length through the medium is small. At the low angles of a reflectivity experiment, however, the path length of the incident wave through the medium can become large. The refraction of an incident beam at an interface between two media is shown in Figure 2.7 illustrating the path length, L, which is given by

$$L = \frac{T}{\sin\theta_t} \tag{2.29}$$

where T is the thickness of the layer and θ_i the transmitted angle. As a result, Equation 2.28 is only valid when $\theta_i \approx \theta_t$, and therefore only in the region where $\theta \gg \theta_c$. This has the consequence that in the reflectivity data presented in this thesis, Equation 2.28 does not strictly hold over the whole range of $\mathbf{q}$, but it can be useful for estimating approximate layer thicknesses from fringe periodicities. This can be useful when setting initial conditions when fitting reflectivity data and it is important to note the reciprocal behaviour.

2.4.2 The Effect of Interfaces on the Reflectivity

Real surfaces and interfaces are not perfectly flat and will have some variations, whether from diffusion of atoms or topographical variations such as terracing. The different types of variations at interfaces and how these are incorporated into models will be discussed in detail in Chapter 3, but this section will introduce how imperfect interfaces are incorporated into the scattering theory.

One of the simplest methods of modelling the variations at an interface is to assume that it is an ensemble of flat surfaces with a distribution about an average surface position. If we assume the distribution of these surfaces to be Gaussian then

the Fresnel reflectivity, R_F, is reduced by an exponential damping factor given by

$$R = R_F \exp^{(q_z^2 \sigma^2)} . \tag{2.30}$$

The $\exp^{(q_z^2\sigma^2)}$ term is the Debye-Waller factor where σ is the width of the interface. This assumes that there is no refraction of the beam at the interfaces [76]. The change in refractive index would cause a beam in one medium with a wavevector of $q_{z,1}$ to be refracted at the interface with a second medium such that it had a new wavevector $q_{z,2}$. The amount of refraction is normally small, in which case the Debye-Waller factor is valid. It ceases to hold at grazing incidence: the factor of q_z^2 in Equation 2.30 can be replaced by $q_{z,1}q_{z,2}$ to give the Névot-Croce factor [89].

Specular reflectivity curves simulated using the Parratt recursive formalism with an interface which is approximated using a Gaussian error function are shown in Figure 2.8 for a single layer of Fe with a thickness of 200 Å on a Si substrate. Figure 2.8(a) shows the simulated specular reflectivity from the 200 Å layer and compares this to a similar layer only 70 Å thick. The width of the Gaussian error function, σ, determines the width of the interface and will be discussed in more detail in Chapter 3. In the simulated data in Figure 2.8(a), the widths of the interfaces were set to $\sigma_{Si} = \sigma_{Fe} = 2$ Å and the electron density was kept the same for both data sets. It is clear from Figure 2.8 that the periodicity of the fringes has increased due to the decrease in layer thickness but the fringe height and shape of the reflectivity is much the same.

To illustrate the effect of changing the interface width on the reflectivity profile, Figure 2.8(b) shows an increase of the Fe layer interface width from $\sigma_{Fe} = 2$ Å to $\sigma_{Fe} = 10$ Å resulting in a reduction of the height of the fringes at high q_z. This can be explained by the Debye-Waller factor in Equation 2.30 which has a decaying exponential as a function of q_z. The reflectivity from the wider interface decays faster than from the narrower interface resulting in a lack of interference at high q_z and hence a lack of well defined fringes.

Figure 2.8(c) compares the reflectivity from the Fe layer to an Al layer with a different electron density, keeping all other parameter the same. The reduced electron density results in a shift of the critical angle. There is also a change in the height of the fringes as the ratio between the electron density of the substrate and the Fe layer is reduced. Figure 2.8(d) shows the effect of increasing the substrate interface width whilst keeping the Fe interface at $\sigma_{Fe} = 2$ Å. As with Figure 2.8(b), there is a loss of definition in the fringes at high q_z except there is not the same increase in definition at lower q_z seen when just the upper surface roughness is in-

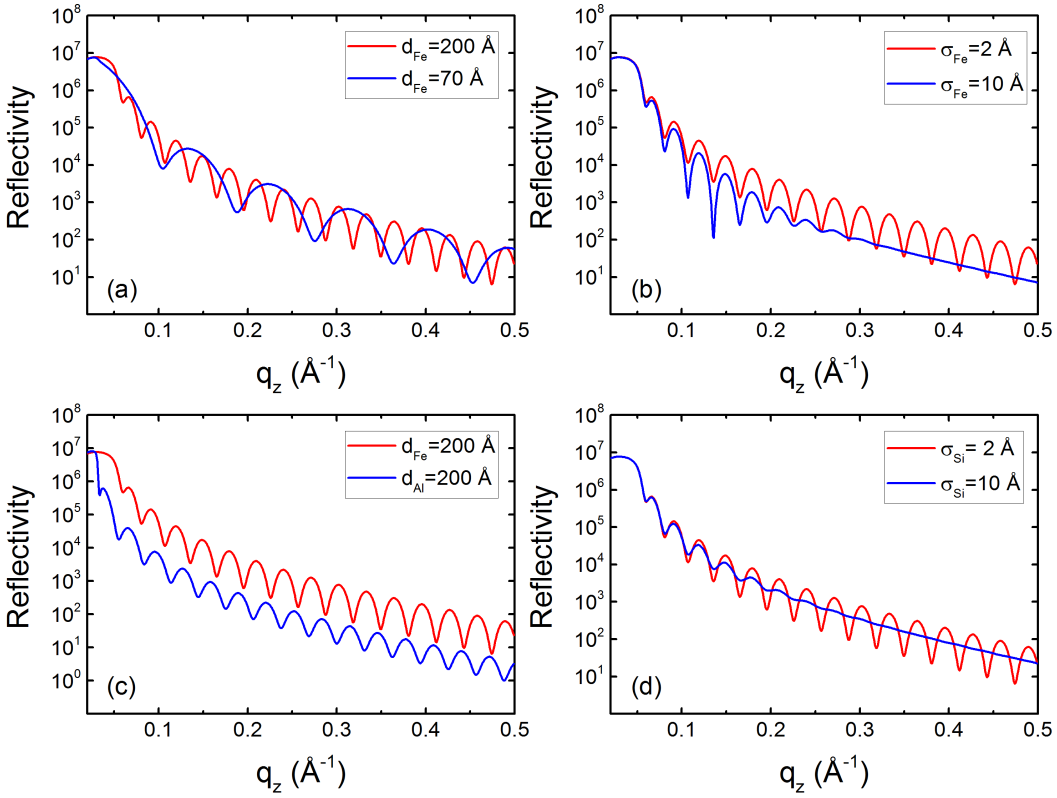

Figure 2.8: Simulated reflectivity of a 200 Å thick Fe layer on a Si substrate. Both interfaces are modelled using a Gaussian error function with a width of 2 Å . A comparison is made to (a) a thinner layer with a thickness of 70 Å, (b) an Fe layer with $\sigma_{Fe} = 10$ Å, (c) an Al layer with the same thickness but different electron density and (d) a substrate interface width of $\sigma_{Si} = 10$ Å.

creased. The effects seen in Figure 2.8 are due to the complex interplay of scattering from the different surfaces. When the reflectivity from one surface decays faster with q_z it can lead to an amplification of fringes. This complex relationship between the reflectivity and the thickness and interface width can make it very difficult to fit reflectivity data from structures with many layers.

2.5 Magnetic Studies Using X-ray Scattering

This section will show that in addition to the charge scattering, x-rays are also sensitive to the electronic spins and, as such, can be used to probe the magnetisation. A quantum mechanical model of scattering will be introduced before going on to discuss how resonant scattering can be used to probe the magnetisation using a band model of magnetism. As an example, the scattering processes are given for a

ferromagnetic $3d$ transition metal to illustrate the transitions occurring during the scattering process.

The section will then go on to introduce x-ray magnetic circular dichroism along with the sum rules, which can be used to calculate the spin and orbital contributions to the magnetic moment. Lastly, resonant scattering is presented and will include the effect of resonance on the dispersion corrections and a matrix formalism of the scattering amplitude.

2.5.1 Magnetic Sensitivity in Scattering Experiments

In the classical description of scattering, an incident photon interacts with the electrons in the sample which behave as a driven harmonic oscillator. X-ray scattering is usually interpreted only through the Thomson scattering mechanism, where the interaction is between the x-rays and the electron charge density only. However, by examining the scattering processes more thoroughly we see that the electronic spin also plays a role: x-rays are electromagnetic waves and therefore have a magnetic component which interacts with the electronic spins.

The possible interactions of the electric and magnetic fields with the electronic charge and spin are illustrated in Figure 2.9. Part (a) of Figure 2.9 shows the mechanism for Thomson scattering, which is the process behind the theory presented so far in this chapter. Figures 2.9(b)-(d), however, show the mechanisms which have a spin dependence and can be used to achieve magnetic sensitivity.

It is possible to probe the magnetisation of a sample using non-resonant x-ray scattering. The scattering amplitude has a non-resonant spin-dependent term f_{spin} which is given as [78, 91]

$$f_{spin} = ir_0 \left(\frac{\hbar\omega}{mc^2}\right) f_D[\tfrac{1}{2}\mathbf{L}(\mathbf{q}) \cdot \mathbf{A} + \mathbf{S}(\mathbf{q}) \cdot \mathbf{B}] \tag{2.31}$$

where

$$\mathbf{A} = 2(1 - \hat{\mathbf{k}} \cdot \hat{\mathbf{k}}')(\hat{\boldsymbol{\epsilon}}' \times \hat{\boldsymbol{\epsilon}}) - (\hat{\mathbf{k}} \times \hat{\boldsymbol{\epsilon}})(\hat{\mathbf{k}} \cdot \hat{\boldsymbol{\epsilon}}') + (\hat{\mathbf{k}}' \times \hat{\boldsymbol{\epsilon}}')(\hat{\mathbf{k}}' \cdot \hat{\boldsymbol{\epsilon}})$$

and

$$\mathbf{B} = (\hat{\boldsymbol{\epsilon}}' \times \hat{\boldsymbol{\epsilon}}) + (\hat{\mathbf{k}}' \times \hat{\boldsymbol{\epsilon}}')(\hat{\mathbf{k}}' \cdot \hat{\boldsymbol{\epsilon}}) - (\hat{\mathbf{k}} \times \hat{\boldsymbol{\epsilon}})(\hat{\mathbf{k}} \cdot \hat{\boldsymbol{\epsilon}}') - (\hat{\mathbf{k}}' \times \hat{\boldsymbol{\epsilon}}')(\hat{\mathbf{k}} \times \hat{\boldsymbol{\epsilon}}).$$

The variables, $\mathbf{L}(\mathbf{q})$ and $\mathbf{S}(\mathbf{q})$ are the Fourier transforms of the atomic orbital and spin magnetic densities respectively and f_D is the Debye-Waller factor. The total scattering amplitude is then given as $f = f^0 + f' + if'' + f_{spin}$. The factor of $\left(\frac{\hbar\omega}{mc^2}\right)$ in Equation 2.31 leads to the amplitude of the magnetic multipole contributions being considerably smaller than the electric dipole and quadrupole transitions. The con-

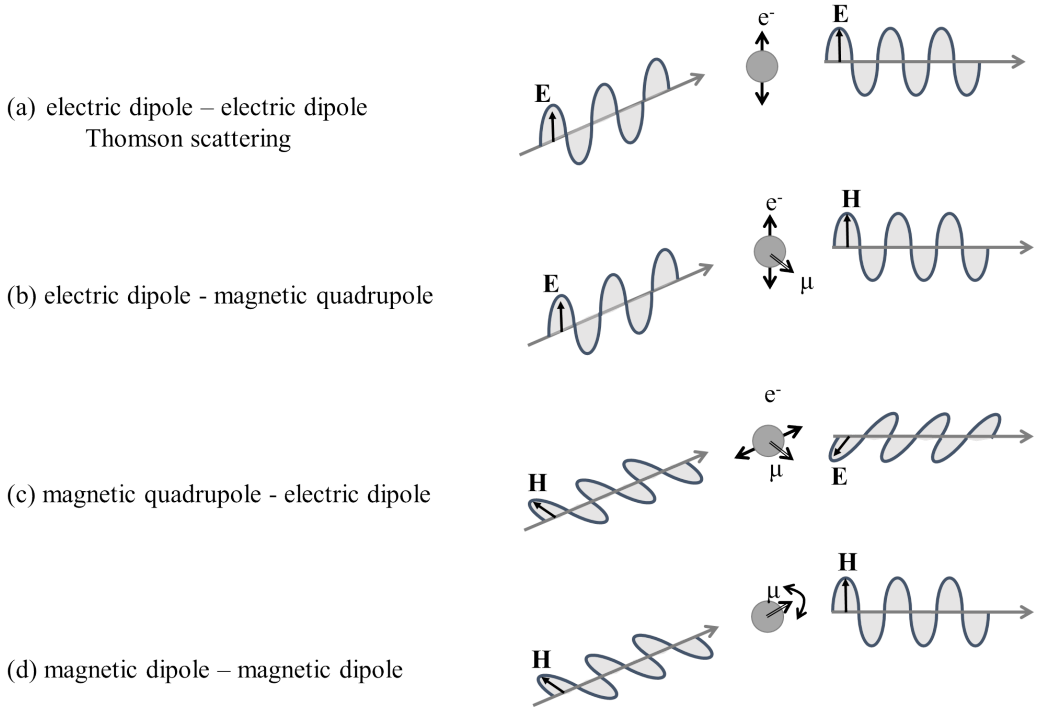

Figure 2.9: Classical description of the four mechanisms of scattering. In each case the electric charge e^- or magnetic moment μ is perturbed by the incident electromagnetic field. Adapted from [90]

sequence is that the non-resonant magnetic scattering signal is very weak, especially when considering that the scattered intensity is proportional to the scattering factor squared. The magnetic scattering is further reduced compared to the Thomson charge scattering because only the unpaired electrons contribute to the scattering process [92]. The non-resonant magnetic scattered intensity is therefore roughly 7 or 8 orders of magnitude weaker than the charge scattering and in the work presented in this thesis, can be ignored. Experiments which probe the non-resonant magnetic signal usually require very good quality single crystal samples and high intensity x-ray beams [93].

2.5.2 Quantum Mechanical Treatment of Scattering

In the quantum mechanical treatment of an atom, electrons are arranged in discrete energy levels. Simple models of atoms consist of positively charged nuclei surrounded by core and valence electrons, each with distinct binding energies. An incident x-ray photon is absorbed by exciting a core electron into a higher empty state; as the

Figure 2.10: Diagram of resonant x-ray absorption showing each energy level with the electronic quantum states.

electron decays back into the core shell, it emits a photon with the same energy. The process is illustrated in Figure 2.10 where an electron in the initial state $|i\rangle$ is excited to an intermediary state $|n\rangle$ and then decays back into a final state $|f\rangle$ with the emission of a photon.

The x-ray absorption and scattering cross-sections are both derived by considering the time-dependent perturbation of the sample by the incident photon. This leads to the transition probability per unit time, T_{if}, from a state $|i\rangle$ to a state $|f\rangle$, which is given (up to second order) as [94]

$$T_{if} = \frac{2\pi}{\hbar}\left|\langle f|\mathcal{H}|i\rangle + \sum_n \frac{\langle f|\mathcal{H}|n\rangle\langle n|\mathcal{H}|i\rangle}{\epsilon_i - \epsilon_n}\right|^2 \delta(\epsilon_i - \epsilon_f)\rho(\epsilon_f). \tag{2.32}$$

The first-order term (which includes transitions directly from $|i\rangle$ to $|f\rangle$ without any intermediary states) is often called *Fermi's golden rule* and the second-order term (which includes intermediary states, $|n\rangle$) is the *Kramers-Heisenberg relation*. Equation 2.32 can be used to obtain the total cross-section by normalisation to the incident photon flux, $\sigma = \frac{T_{if}}{\Phi_0}$.

2.5.3 Resonant X-ray Scattering

As the non-resonant magnetic scattering signal is so much weaker than the charge scattering, it had previously been assumed that magnetic x-ray scattering would not be a suitable choice for studying the magnetic properties of thin films and multilayers. However, whilst studying the magnetic properties of Ho, Gibbs *et al.* [95] found that there was an enhancement of the magnetic signal by a factor of 50 when the incident x-ray energy was tuned to the Ho L_3 edge. The enhancement of the magnetic signal at a resonant edge reveals that the scattered signal is closely related to absorption; this is expected as the quantum mechanical description of scattering introduced in Section 2.5.2 involved the absorption and re-emission of an

x-ray photon. The discovery that the magnetisation can be probed by exploiting these absorption processes to enhance the magnetic signal by tuning to a resonant edge has since opened up a wide and active area of research. The next section will show how scattering processes can be described within the band model of magnetism to study the magnetic properties of materials using resonant x-rays.

X-ray resonant magnetic scattering (XRMS) measures the difference in absorption between left- and right-handed circularly polarised x-rays. In optics, the word dichroism, meaning two-coloured, is the phenomenon of a material having an absorption spectrum which is dependent on the polarization of the incident radiation. This can be seen in polarizing filters where they appear dark in one orientation and allow light to pass in another. In the case of magnetic dichroism the absorption is dependent not only on the polarization of the incident radiation, but also on the magnetisation of the material [96].

The absorption can be described as a two-step process which is shown in Figure 2.11. The first step in the process requires that when an electron is excited by a photon, angular momentum is transferred from the incident circularly polarised x-rays to the excited electrons due to conservation of angular momentum. If the absorption process takes place from a spin-orbit split level like that shown in

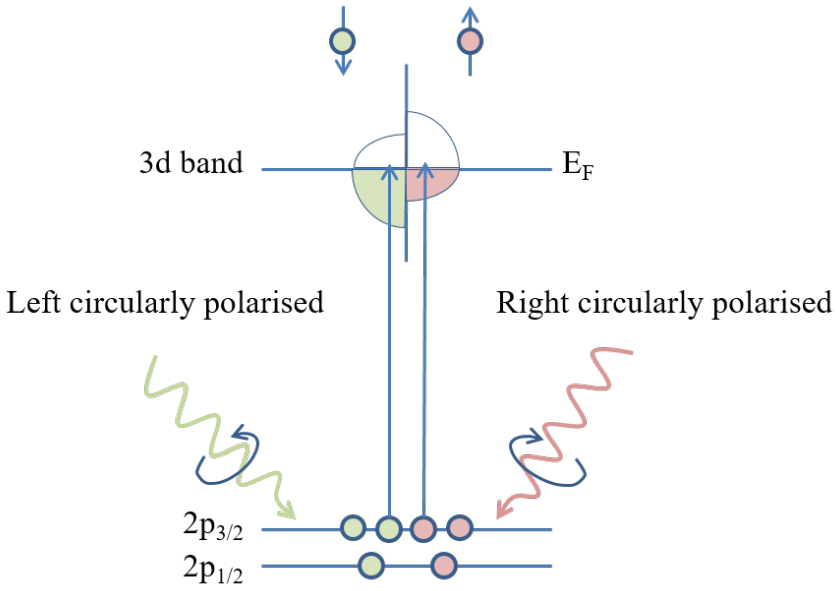

Figure 2.11: An energy level diagram depicting the x-ray magnetic circular dichroism effect at the $L_{2,3}$ edges. Adapted from [16].

Figure 2.11, the angular momentum of the photon couples to the spin and orbital momentum of the electron. The excited electrons are therefore spin polarised. The spin polarisation is opposite for x-rays with left or right circular polarisation such that the helicity can be used to determine which spin-species is predominantly excited. Also, the $2p_{3/2}$ and $2p_{1/2}$ states have opposite spin-orbit coupling and so the spin polarisation is opposite for the L_3 and L_2 edges.

In the second step, there is an asymmetry in the number of available states at the Fermi energy (E_F) between the spin-up and spin-down states which leads to a difference in absorption between left and right circular polarised x-rays. For example, in Figure 2.11, there are more occupied $3d$ states with spin-down than with spin-up which results in a net magnetisation. As the Pauli exclusion principle only allows transitions to vacant states, an incident circularly polarised photon causes an electron to be excited from a core level to an unoccupied valence shell state. As a result, the transition probability for a given energy is proportional to the number of empty d states of a given spin at that energy.

Due to the dipole selection rules, only certain transitions are allowed, and so there are limited absorption edges available that give strong resonance and can be used for magnetic studies. This is of course highly material dependent. For example, transition metals such as Fe have available $3d$ states resulting in $2p \rightarrow 3d$ transitions giving strong absorption effects and magnetic sensitivity at the L_2 and L_3 edges [97]. Alternatively, for the rare-earths, strong resonant scattering will occur at the M_4 and M_5 edges, involving transitions to the $4f$ shell [98, 99].

2.5.4 Resonant Scattering Factors

Previously, the scattering amplitude was introduced as $f = f^0 + f' + if''$ (neglecting f_{spin}) where the dispersion corrections, f' and f'' were negligible away from an absorption edge. At a resonant edge, however, these values become large and cause notable changes to the scattering amplitude. The energy dependence of the real and imaginary parts of the scattering length for Co are shown in Figure 2.12. The energy range in the figure is chosen to include the L edge resonances of Co which are at 0.929 keV (L_1), 0.797 keV (L_2) and 0.782 keV (L_3). Additional to the charge scattering terms, the scattering amplitude contains magnetic terms also which will be discussed in more detail in Section 2.5.6. These terms are called m' and m'' and are the real and imaginary parts of the magnetic scattering length which are analagous to f' and f''.

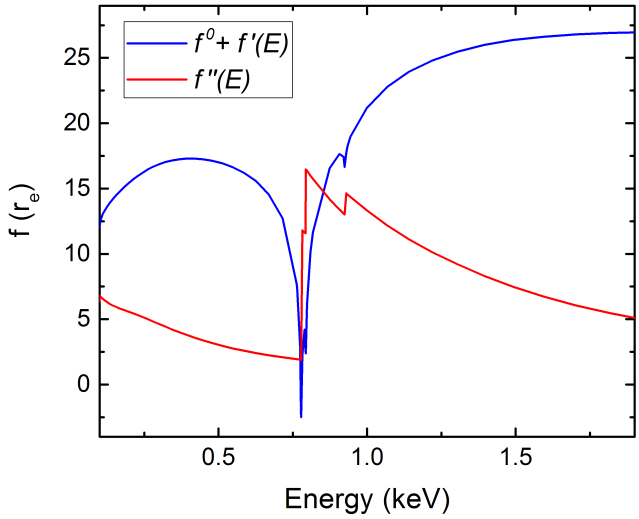

Figure 2.12: Calculated energy dependence of the real and imaginary components of the scattering length for Co across an energy range including the L edge resonances of Co. Data reproduced from the NIST scattering length database [100].

2.5.5 X-ray Magnetic Circular Dichroism

X-ray magnetic circular dichroism (XMCD) uses the same processes as XRMS to measure the dependence of the absorption of x-rays on the helicity and magnetisation. XMCD, however, can be used to calculate the average magnetic moment and the orbital and spin contributions can be extracted. The XMCD signal is given by the asymmetry ratio as defined later in Equation 2.41 and is recorded as a function of energy.

The x-ray absorption signal is recorded by measuring, as a function of energy, the current at the sample surface generated by exciting electrons into the conduction band using circularly polarised resonant x-rays. The XMCD signal is then the difference between the two polarisation channels and is directly proportional to m''. The Kramers-Kronig relations can then be used to derive m'. The magnetic sum rules [101–103] can be used to directly give the spin and orbital contributions to the magnetic moment per atom at fixed q. The charge sum rule for the case of the transition metal L-edges is given as

$$\langle I_{L3} + I_{L2} \rangle = CN_h \tag{2.33}$$

and relates $\langle I_{L3} + I_{L2} \rangle$, the integral of the x-ray absorption spectrum with N_h which is the number of empty valence states per atom and a proportionality constant, C.

For the XMCD spectrum (now taking the difference in the two polarisation channels) then the integral across the L_2 and L_3 edges are commonly denoted A and B as shown in the example XMCD spectrum in Figure 2.13. The spin sum rule is then given by

$$(-A + 2B) = \frac{C}{2\mu_B} m_s \tag{2.34}$$

and the orbital sum rule as

$$-(A + B) = \frac{3C}{2\mu_B} m_o \tag{2.35}$$

where m_s and m_o are the spin and orbital moments respectively. In principle, this provides a simple measurement of the strength of the moments in a system and XMCD can therefore be used to measure the magnetic moment and strength of the spin-orbit interaction.

The energy range in Figure 2.13 is chosen such that the Co L_2 (0.797 keV) and L_3 (0.782 keV) absorption edges are shown. The large changes in the XMCD signal indicate the positions of the absorption edges and these are marked in the figure by dashed lines. The data in Figure 2.13 was recorded by varying the energy of the x-ray beam using a plate with an etched grating, and the angle of this plate is changed to alter the x-ray beam wavelength. More information is given on this in Chapter 4. The nature of this type of monochromator means that an absolute energy calibration is often not possible as changes in the experimental angles result in a drift in the energy recorded. As such, the energies in the figure are not the accepted

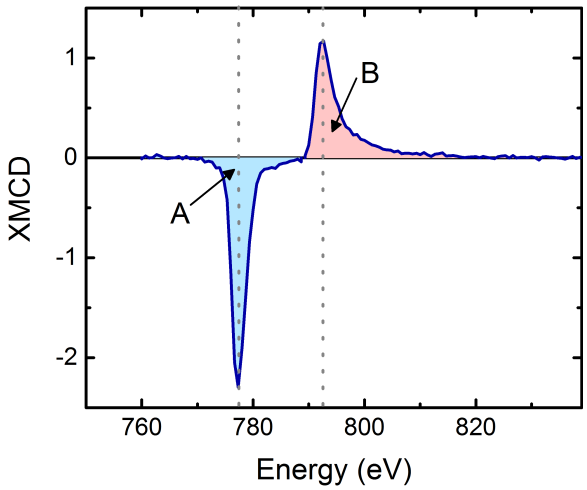

Figure 2.13: Example XMCD scan showing the Co L_2 and L_3 edges for a film of Sm_8Co_{92}.

values of the absorption edges of Co. This is not problematic when performing x-ray magnetic resonant scattering studies, however, as an energy is selected relative to the measured absorption edge.

2.5.6 Matrix Formalism of Resonant Scattering

The remainder of this chapter will introduce a matrix formalism of scattering and show how magnetic sensitivity is achieved from the asymmetry ratio. The resonant scattering is included in the cross section through f' and f''. Both electric and magnetic multipole transitions contribute, but the electric dipole transitions dominate the resonant magnetic cross section and they are the simplest to calculate. We will now go on to show how the resonant scattering amplitude can be written in terms of 2×2 matrices assuming only electric dipole transitions. To start with, the x-ray scattering length within the dipole approximation is written as [104]

$$f(q, E) = (\hat{\boldsymbol{\epsilon}}' \cdot \hat{\boldsymbol{\epsilon}}) F^{(0)}(E) - i(\hat{\boldsymbol{\epsilon}}' \times \hat{\boldsymbol{\epsilon}}) \cdot \hat{\boldsymbol{m}} F^{(1)}(E) \tag{2.36}$$

where the charge scattering amplitude is $F^{(0)}(q, E) = f_0(q) + f'(E) + if''(E)$ and $F^{(1)}$ contains m' and m''. It is therefore the second term in Equation 2.36 that gives rise to the magnetic sensitivity. In Equation 2.36, $\hat{\boldsymbol{\epsilon}}$ and $\hat{\boldsymbol{\epsilon}}'$ are the polarisation unit vectors of the incident and scattered waves respectively and $\hat{\boldsymbol{m}}$ is the unit vector giving the magnetisation direction. Higher order terms, which contain higher harmonic magnetic satellites, are neglected here.

It is often easier to write the dipole operator in Equation 2.36 as a 2×2 matrix, with the polarisation states chosen to be either parallel or perpendicular to the scattering plane. The scattering amplitude is then written in terms of the linear components of the polarisation parallel ($\boldsymbol{\pi}$) and perpendicular ($\boldsymbol{\sigma}$) to the scattering plane for the incident (unprimed) and scattered (primed) beams [105]. This matrix is then written as

$$f(q, E) = \begin{pmatrix} \boldsymbol{\sigma}\text{-}\boldsymbol{\sigma}' & \boldsymbol{\pi}\text{-}\boldsymbol{\sigma}' \\ \boldsymbol{\sigma}\text{-}\boldsymbol{\pi}' & \boldsymbol{\pi}\text{-}\boldsymbol{\pi}' \end{pmatrix}. \tag{2.37}$$

Following Hill and McMorrow [82], the first term of Equation 2.36 is written as a diagonal matrix

$$\hat{\boldsymbol{\epsilon}}' \cdot \hat{\boldsymbol{\epsilon}} = \begin{pmatrix} 1 & 0 \\ 0 & \hat{\mathbf{k}}' \cdot \hat{\mathbf{k}} \end{pmatrix} \tag{2.38}$$

which only contributes to the charge scattering with no dependence on the magnetic moment. This term allows $\boldsymbol{\sigma}$-$\boldsymbol{\sigma}'$ or $\boldsymbol{\pi}$-$\boldsymbol{\pi}'$ scattering which is consistent with the description of charge scattering given earlier in this chapter. The second term,

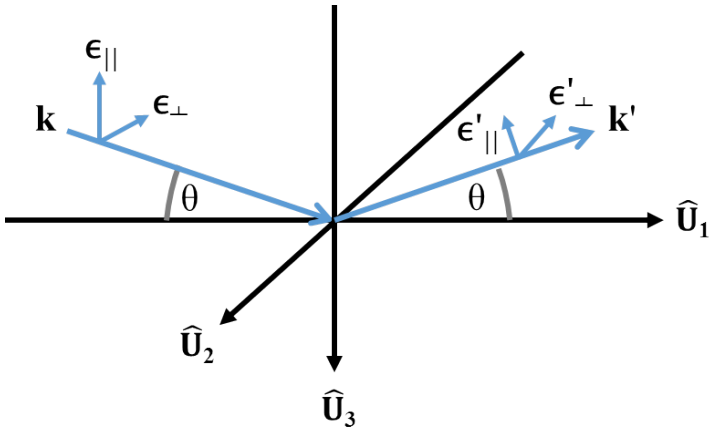

Figure 2.14: The scattering geometry coordinates used to calculate the polarisation dependences.

however, contains a magnetic term and the matrix representation is

$$(\hat{\boldsymbol{\epsilon}}' \times \hat{\boldsymbol{\epsilon}}) \cdot \hat{\boldsymbol{m}} = \begin{pmatrix} 0 & \hat{\mathbf{k}} \\ -\hat{\mathbf{k}}' & \hat{\mathbf{k}}' \times \hat{\mathbf{k}} \end{pmatrix} \cdot \hat{\boldsymbol{m}}. \tag{2.39}$$

This allows $\boldsymbol{\sigma}$-$\boldsymbol{\pi}'$ and $\boldsymbol{\pi}$-$\boldsymbol{\sigma}'$ scattering as well as $\boldsymbol{\pi}$-$\boldsymbol{\pi}'$ but $\boldsymbol{\sigma}$-$\boldsymbol{\sigma}'$ is forbidden.

If the vectors $\hat{\mathbf{k}}'$, $\hat{\mathbf{k}}$ and $\hat{\boldsymbol{m}}$ are resolved into their components as defined in Figure 2.14, this leads to the expression for the resonant dipole scattering amplitude

$$f = F^{(0)} \begin{pmatrix} 1 & 0 \\ 0 & \cos(2\theta) \end{pmatrix} - iF^{(1)} \begin{pmatrix} 0 & m_1 \cos\theta + m_3 \sin\theta \\ m_3 \sin\theta - m_1 \cos\theta & -m_2 \sin(2\theta) \end{pmatrix} \tag{2.40}$$

From Equation 2.40 it is possible to determine which components of the magnetic moment can be measured in a given experimental geometry. When in a geometry where θ is small, the $\sin(\theta)$ terms will be small and so the measured signal is more sensitive to the component of the magnetisation in the $\hat{\mathbf{U}}_1$ direction, i.e. in the sample plane in the direction of the beam, as defined in Figure 2.14.

From Equation 2.40, when using $\boldsymbol{\sigma}$ linearly polarised x-rays, magnetic scattering in the $\boldsymbol{\sigma}$-$\boldsymbol{\sigma}'$ channel is forbidden but the $\boldsymbol{\sigma}$-$\boldsymbol{\pi}'$ channel is sensitive to the magnetic moment in the scattering plane. Similarly for the $\boldsymbol{\pi}$-$\boldsymbol{\sigma}'$ channel, there is sensitivity to the moment in the scattering plane but has an opposite complex phase [106]. Circularly polarised x-rays, however, have both $\boldsymbol{\sigma}$ and $\boldsymbol{\pi}$ components and as such information about the magnetic moment in the scattering plane is con-

tained within the $\boldsymbol{\sigma}$-$\boldsymbol{\pi}'$ and $\boldsymbol{\pi}$-$\boldsymbol{\sigma}'$ channels simultaneously.

The scattered intensity is proportional to the scattering amplitude (given in Equation 2.40) squared. Therefore when using circularly polarised x-rays which have both $\boldsymbol{\sigma}$ and $\boldsymbol{\pi}$ components, the signal contains interference terms between the charge and magnetic scattering. This interference term has the consequence that resonant x-ray scattering can not be used to extract the pure magnetic scattering signal but is instead a combination of the charge and magnetic scattering. The charge-magnetic interference term is obtained by measuring the asymmetry ratio (A.R.). This is the difference in reflected intensity between the two spin channels normalised to the total intensity and is defined as

$$A.R. = \frac{I^+ - I^-}{I^+ + I^-} \tag{2.41}$$

where I^+ and I^- are the reflected intensities for positive and negative helicities respectively. The sum of the two helicities gives structural information only and is usually presented as $(I^+ + I^-)/2$, the average reflectivity. Note that reversing the direction of the moments in the system (by reversing the applied field, for saturating fields) whilst keeping the photon helicity fixed, is equivalent to reversing the helicity whilst keeping the applied field constant.

With the inclusion of the resonant magnetic scattering, the refractive index can then be written in terms of the magnetic scattering lengths m' and m''. For resonant scattering from a magnetic sample with circularly polarised light, the refractive index becomes $n^{\pm} = 1 - \delta^{\pm} + i\beta^{\pm}$ with $\delta^{\pm}((f_0 + f'), \mp m')$ and $\beta^{\pm}(f'', \mp m'')$. The $\pm$ refers to either a reversal of magnetisation or helicity. This can then be incorporated into Parratt's recursive formalism where reversing the magnetisation or helicity results in a change in the simulated reflectivity. This is used to calculate two reflectivity curves corresponding to the $+$ and $-$ states which are in turn used to simulate the average reflectivity and asymmetry ratio.

Conclusion

This chapter has shown that x-rays can be used to study both the structural and magnetic properties of multilayers and patterned arrays. The mechanisms by which x-rays are scattered by matter were introduced, including the scattering factor (which is the Fourier transform of the electron density), and the complex refractive index (which is used to describe reflection and refraction from surfaces and interfaces). It was then shown how the scattering factors and refractive index are

incorporated into Fresnel's equations which can be used to describe the reflection and transmission of an x-ray at an interface between two media. The Fresnel equations did not, however, allow a full description of reflectivity from a multilayer, as refraction and multiple scattering were not accounted for within the Born approximation. As such, the chapter went on to outline the Parratt recursive formalism, which is used to fit the reflectivity data presented throughout this thesis.

The properties of polarised electromagnetic radiation were introduced showing that electromagnetic waves have both electric and magnetic components which can be used to probe the electric charge and/or magnetic moment of a scattering medium, and the chapter introduced how polarised x-rays at energies close to an absorption edge can be used to achieve magnetic sensitivity. The chapter showed how large changes in the scattering length are observed when the x-ray energy approaches an resonant edge. Resonant x-ray scattering was presented in a matrix formalism showing that the resonant scattered signal contains both charge and magnetic terms, and that in order to extract the charge-magnetic signal the asymmetry ratio must be used.

The quantum theory of resonant magnetic scattering was presented before describing how XMCD can be used to extract the spin and orbital contributions of the magnetic moment per atom. The sum rules were introduced, but are not used in x-ray resonant magnetic scattering (XRMS) data as it is the charge-magnetic interference term that is measured and the pure magnetic signal can not be extracted from XRMS data alone. For a full measurement of both the magnetic moment and sample structure, both XMCD (to get $F^{(1)}$) and the reflectivity must be measured. In many cases, however, the absolute quantification of the moments is not necessary and a measurement proportional to the total moment is sufficient, in these cases XRMS can be used.

Chapter 3

Experimental Details

This chapter outlines some of the experimental techniques used throughout this work. It describes the different growth techniques used to produce the samples and introduces magnetic characterisation methods like MOKE and SQUID. It also leads onto resonant x-ray scattering, where the reasons for using synchrotron radiation are given and details of the specific beamlines and equipment used are discussed.

3.1 Sample Growth

The physical properties of magnetic heterostructures are intrinsically linked with their growth method, and as such it is important to consider the details of how to grow them. The growth methods used to produce the samples presented in this thesis are briefly outlined here to provide a background to the kind of structures studied and the effect of growth conditions on the structural and magnetic properties of such materials. All sample growth was carried out by colleagues at the University of Uppsala, Sweden using either D.C. magnetron sputtering or molecular beam epitaxy (MBE).

Control of the growth conditions coupled with the choice of substrate and growth materials allows samples to be grown which are crystalline, poly-crystalline or amorphous. Crystalline structures, require a suitable degree of lattice matching between substrate and film which restricts the combinations of materials available for use. Amorphous materials, however, can be grown on a wide range of substrates, as lattice matching to neighbouring layers is not an issue; this allows growth of alloys with different compositions which have excellent interface quality and layer uniformity [107–110]. Having the capability to produce magnetic materials with an ordering temperature and moment which can be tuned using the composition and

combined into multi-layers opens up a vast number of new possible heterostructures with magnetic properties that could never have been achieved otherwise. The trade off with amorphous materials, however, is that the random distribution of atoms within the film means that magnetic properties which rely on crystalline structure such as magneto-crystalline anisotropy are no longer available (although amorphous materials can be grown with an imprinted anisotropy [111, 112]).

3.1.1 Sputtering

In D.C. sputtering, gaseous ions (usually Ar^+) are bombarded at a target surface, causing particles of the target material to be ejected towards a substrate which is directly opposite the target. A potential difference between the target material and the substrate results in the breakdown of the injected gas particles into ions which are then accelerated towards the target. These ions bombard the target surface causing the release of target atoms which disperse throughout the chamber and adhere to the substrate. D.C. sputtering has the advantage of relatively high deposition rates, good scalability and it can produce excellent quality films.

Unfortunately sputtering requires large voltages (∼kV) to achieve high deposition rates. Increasing the pressure of the Ar gas produces more collisions with the target and increases the deposition rate. Higher gas pressures, however, also increase the risk of sputtered material colliding with the gas atoms. In this case the particles may undergo many inelastic collisions before reaching the substrate instead of high energy sputtered particles travelling ballistically towards the substrate. This can have the adverse effect of reducing the deposition rate and target material can deposit both on the vacuum chamber wall and back onto the target itself.

The sputtering process can be modified to use magnetic fields (magnetron sputtering) as shown in Figure 3.1. The magnetic field is used to confine electrons near the surface of the sputter target material causing gas particles to be ionised and thus increasing the amount of target material being ejected and available for growth [113]. The increase of plasma at the surface leads to higher sputtering rates whilst needing a lower applied voltage and potentially also a lower vacuum. The quality and crystal structure of the deposited films is highly dependent on the kinetic energy of the incident particles, and the substrate temperature. Deposition thickness is controlled by shutters across both the substrate and the sputter target. Samples can be grown using co-sputtering from multiple pure sources but there is also the option to use a target material that is already at the required composition.

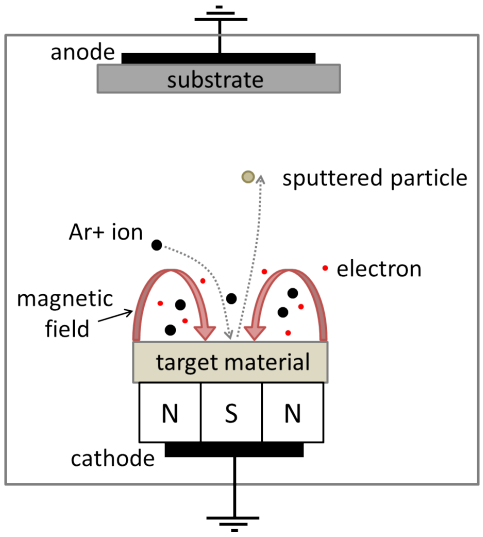

Figure 3.1: Simplified schematic of the D.C. magnetron sputtering process. Ionised Ar bombards a target, releasing atoms which adhere to the substrate. Electrons and Ar^+ ions form a plasma, which is confined near the target surface due to the presence of a magnetic field.

3.1.2 Molecular Beam Epitaxy

Although sputtering can be used to produce excellent quality samples, sometimes a deposition technique like MBE is required which allows the production of highly epitaxial layers. With MBE it is possible to produce single-crystal films with smooth surfaces and well defined film thicknesses which are important features for super-lattice formation. Sample growth using MBE is achieved by evaporating material from effusion cells in a beam towards a heated substrate as shown in Figure 3.2. The effusion cells consist of a crucible of the material to be deposited; this material is heated and the atomic species being ejected from the cell can be controlled using a shutter [114]. The structure of the material is typically monitored during growth using reflection high-energy electron diffraction (RHEED). When using MBE, the composition of the material is controlled by using multiple effusion cells containing different materials and monitoring the deposition rate of each to ensure the correct ratio of the atomic elements are being laid down.

As the beam reaches the surface, the molecules or atoms become weakly adsorbed and they diffuse on the surface, building up the material in atomic layers [116]. In general, the higher the substrate temperature, the more mobile the surface atoms are, which leads to more highly ordered materials but there is likely to be more inter-diffusion at interfaces. On the other hand, lower temperatures can lead

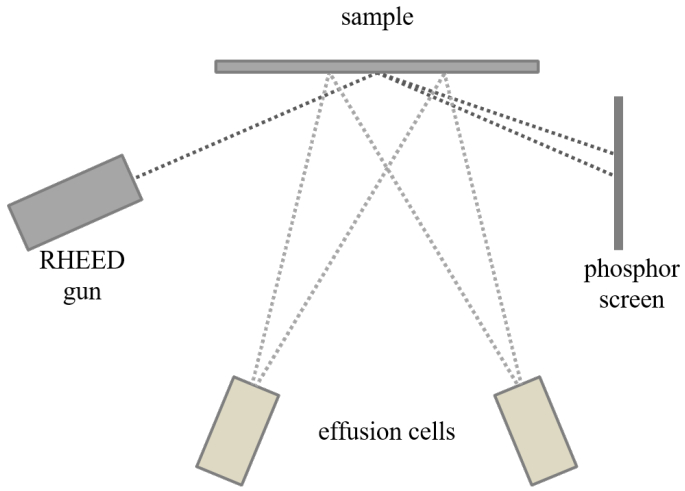

Figure 3.2: Simplified schematic of MBE growth. Material is evaporated from effusion cells in a beam towards the substrate. The sample structure is monitored during growth using reflection high-energy electron diffraction (RHEED). Reproduced from [115].

to sharper interfaces as there is less diffusion of atoms on the surface but a higher probability of defects in the crystal as the atoms have lower mobility and so cannot move around on the surface to sites which would eliminate these defects. Finding the balance between deposition rate and substrate temperature for different types of deposited material is often an involved process, and as such all samples presented in this work were grown by colleagues at Uppsala University, Sweden.

From the growth conditions such as deposition rate and growth time, the nominal structure can be estimated, but to characterise the structural and magnetic properties actually achieved during the growth, we must turn to characterisation techniques such as magnetometry or reflectivity. Often multiple methods are used in tandem to provide a broader understanding of a sample. The advantages and disadvantages of different methods must be considered when choosing a technique to use and when interpreting the data; these are described in the following sections.

3.2 Magnetic Characterisation Methods

A very brief background will now be given on the techniques used to study the magnetic properties of materials in this thesis starting with MOKE and SQUID. These are used as complementary techniques to resonant x-ray scattering (discussed in Section 3.3), which is the main method used to the study magnetic multilayers and patterned arrays in this work.

3.2.1 MOKE

Magneto-optical Kerr effect (MOKE) measurements were used to investigate the magnetic properties of samples throughout this thesis. Polarised optical light reflected from a magnetic material experiences a rotation of the plane of polarisation. The change in polarisation angle is extremely small, typically a few milli-radians but it can be highly sensitive to changes in the magnetisation of a material [117]. The penetration depth is dependent on wavelength, but is normally only around 200 Å so the technique is not suitable for studies of the bulk. The relatively long wavelength of light used means that MOKE has limited spatial resolution and so is not suitable for studying sub-micron structures [16].

The physical origin of the Kerr effect is magnetic circular dichroism whereby exchange and spin-orbit coupling in a magnetic material lead to different absorption for left- and right- polarized light leading to a phase shift and hence elliptically polarised light. The difference in the polarisation of the reflected beam is indicative of the magnetic state of the sample [118,119]. The reflected beam is passed through a polariser and crossed with the polarisation of the incident beam: as the rotation changes, the intensity of the beam passing through the polariser changes [120]. The changing intensity is directly proportional to the magnetisation of the sample. MOKE measurements can be carried out in two main geometries, longitudinal or transverse as illustrated in Figure 3.3. When the incident light is aligned with the sample magnetisation, **M**, the measurement is sensitive to the longitudinal magnetisation only whereas if the optical plane is orientated at 45° to **M**, the measurement is sensitive to the transverse component, which can be useful for studying the anisotropy of a system.

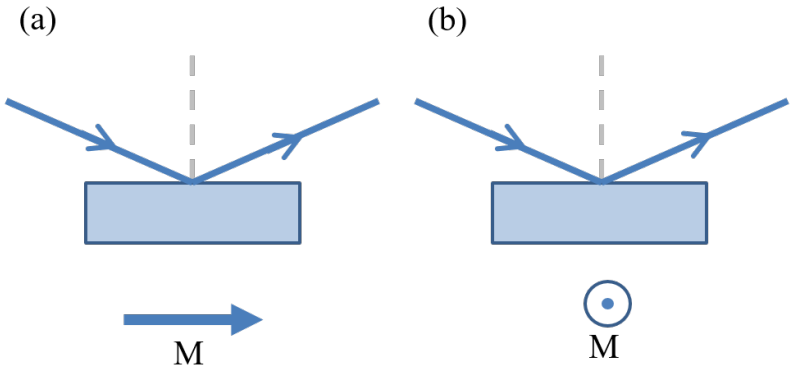

Figure 3.3: Schematic illustrations of MOKE experiments in (a) a longitudinal and (b) a transverse configuration.

MOKE is a dichroism effect whereby the absorption of light in a medium is different depending on whether the the incident light is left- or right-polarised. It stands to reason that this phenomenon should also be seen for higher wavelength radiation, and indeed this is the case. This same principle is used for the x-ray resonant scattering techniques which will be discussed in the next section. MOKE only provides a relative measurement of the magnetisation and can not by itself yield magnetic moment values; this is because the measured signal is proportional to the intensity of the beam, which is also dependent on the polariser angles. Typically saturated states are rescaled to ± 1 and the data is presented as M/M_S.

3.2.2 SQUID

Superconducting quantum interference device (SQUID) measurements are used in Chapter 5 to study Gd-Y superlattices. Unlike MOKE measurements, SQUID gives the total magnetic moment of the sample in μ_B. SQUID magnetometry makes use the Josephson effect whereby two superconducting materials are separated by a thin insulating layer, superconducting electrons can tunnel through the barrier with the critical current density which is affected by the presence of a magnetic field [121]. The change in current is used to detect the change in field and these devices are capable of achieving very high levels of sensitivity [118].

Unlike MOKE, SQUID gives a measurement of the total moment and probes the whole sample, which is particularly important when studying thicker samples in which MOKE would not probe the entirety of the magnetically active region. As SQUID probes the whole sample, this also means that the SQUID measurement will contain the signal from the substrate, often as a diamagnetic background. In very thin films this signal can dominate making analysis of the magnetic film difficult.

3.3 X-ray Scattering

So far, it has been shown that only through precise control of the growth conditions can good quality samples be produced. Characterisation techniques like MOKE and SQUID provide information about the total magnetisation of a sample, but they do not give the magnetic structure. To be able to explore the structure of a sample as a function of depth, we must turn to x-ray scattering techniques. In particular, to study the magnetic structure requires a depth dependent technique such as resonant reflectivity, where polarised x-rays tuned to a resonant edge are used. The reasons for using polarised x-rays and for tuning to an absorption edge were given in Chapter 2. This chapter will explore how x-rays are produced, including how the energy and

polarisation are controlled. It will also give details of the specific beamlines that were used to collect the data presented in this work.

3.3.1 X-ray Production

Traditional laboratory sources of x-rays can be used for reflectometry and diffraction experiments. Laboratory based sources have the advantage of being relatively quick and simple to use. Reflectivity data can be used to characterise densities, thicknesses and roughnesses of layered materials.

X-rays are produced by bombarding a metal target in an x-ray tube with high speed electrons which causes electrons in the inner core shells to be excited and electrons from higher energy levels then drop down to fill the vacancies [122]. This process results in the emission of a photon, with some characteristic energy which is dependent upon the type of material that is used as the target. Additionally there is Bremstrahlung, or 'braking' radiation which is produced when the electrons striking the target rapidly change velocity resulting in the emission of a spectrum of x-rays [123].

One consequence of producing x-rays using a traditional laboratory source is that to get high enough flux to be able to perform scattering studies with enough sensitivity, the x-rays at the characteristic energies must be used. Using a traditional laboratory source means that the range of energies available for practical use is very limited and is highly dependent on the type of metal target used. For these reasons, laboratory sources of x-rays have only been used to aid in the initial characterisation of the structural properties of samples, but they do not allow the study of a material's magnetic properties.

Probing the magnetisation of a sample using x-rays requires the use of polarised x-rays and the ability to tune the energy of the x-rays to perform resonant scattering, as outlined in Chapter 2. To tune the energy to the resonant energies of an element whilst maintaining a high flux, we must turn to synchrotron radiation.

Synchrotron radiation is produced when electrons travelling at very high speeds change direction leading to the emission of photons. A simplistic diagram of a typical synchrotron is given in in Figure 3.4. Electrons are produced (normally by thermionic emission from a hot filament) and are accelerated using a linear accelerator (LINAC). The electrons then enter a booster ring and are accelerated further before being periodically injected into the main storage ring. The storage ring is a series of curved sections containing bending magnets and straight sections used for insertion devices. Electrons are lost continuously during operation and so the source regularly tops up the electrons in the storage ring, the frequency of which

varies from facility to facility. All stages of electron production and storage are kept under ultra-high vacuum to reduce interactions with air [79].

Bending (or dipole) magnets are used to keep the electrons on their trajectory around the storage ring. These apply a Lorentz force to the electrons perpendicular to the direction of motion which changes the direction of the electrons. As per classical electromagnetic theory, accelerating a point like charge in this manner emits electromagnetic waves and this is the source of synchrotron radiation. A consequence of this is that the electrons lose energy and so this is replenished using a radiofrequency cavity. Each bending magnet used to keep the electrons in their trajectory is a source of synchrotron radiation and this radiation is used on the beamlines.

Experimental beamlines run off tangentially to the storage ring. The front end of the beamline isolates the vacuum from that of the storage ring, it also monitors the position of the photon beam and defines the angular acceptance of the beam using an aperture. The beam is focused and/or monochromated in the optics hutch and then enters the experimental hutch where the configuration of equipment will be dependent on the particular experiment [96]. Most high energy x-ray beamlines are shielded using lead-lined, concrete walls to protect users from harmful radiation. Often, Beryllium windows are used to isolate the vacuum as they allow x-rays to be transmitted. The transmission of x-rays through Beryllium is highly energy

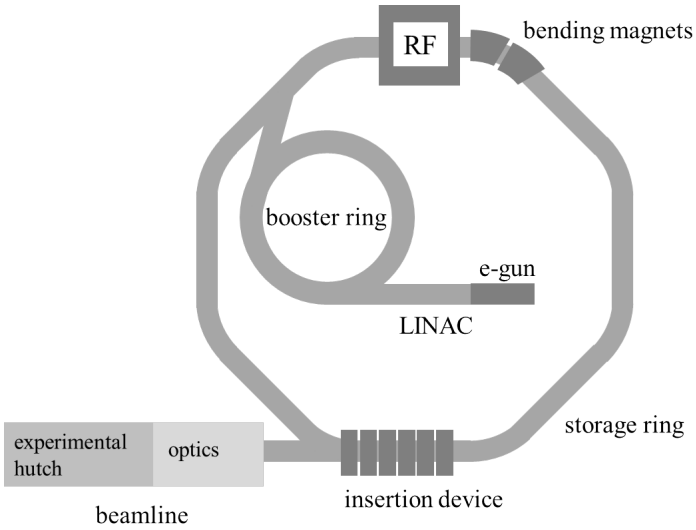

Figure 3.4: Schematic of a synchrotron. The electrons are produced at the e-gun and then accelerated in the booster ring before being injected into the main storage ring. The RF source accelerates electrons in the storage ring. Bending magnets and insertion devices produce synchrotron x-rays for use on experimental beamlines.

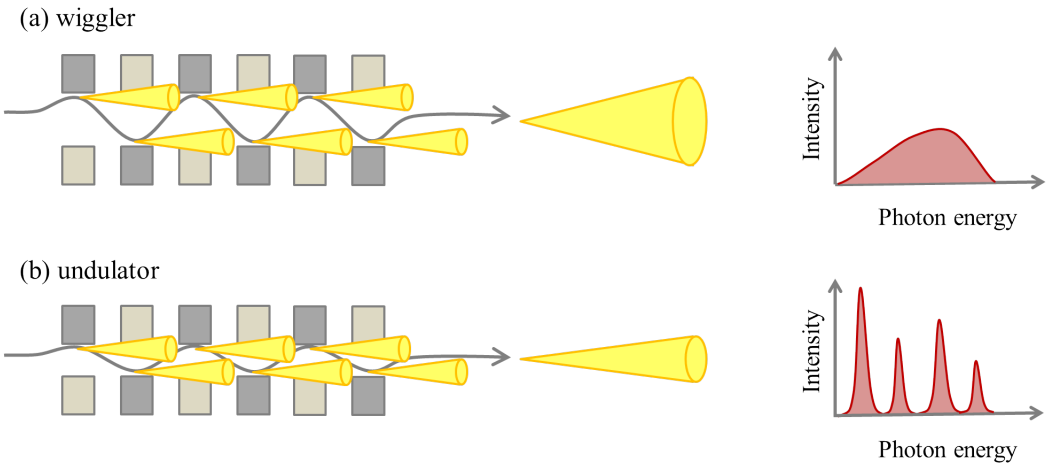

Figure 3.5: (a) Schematic of a wiggler showing that at each successive bending magnet, synchrotron radiation is produced that does not interfere with subsequent emissions producing a continuous emission spectrum. (b) An undulator in which radiation from previous emissions interferes resulting in peaks in the emission spectrum at wavelengths which interfere constructively.

dependent and so is not suitable for very soft energy x-rays (below approximately 4 keV) [96].

Other than bending magnets, another method of producing synchrotron radiation is with insertion devices which come in two main classes, 'undulators' or 'wigglers'. Both of these are constructed from a series of magnets which each cause a change in direction of the electrons and thus produce x-rays. Wigglers produce x-rays at each consecutive bend which do not interfere with each other and the total intensity produced is the sum of that from each of the bends. In an undulator, the x-rays produced at each consecutive bend overlap and constructively interfere with those from previous bends. Wigglers produce a continuous emission spectrum as in Figure 3.5(a) whereas undulators only interfere constructively at certain wavelengths and so the emission spectrum has peaks where constructive interference occurs as shown in Figure 3.5(b). The consequence of using a wiggler is the high loading on the monochromator as the majority of the beam is absorbed with only the energy required being diffracted meaning that the monochromator must be cooled.

A natural consequence of producing synchrotron radiation using bending magnets or an insertion device is that the radiation produced is polarised. This polarisation is a crucial feature to be able to do magnetic resonant scattering studies. Some methods of modifying the polarisation to suit certain experimental requirements are discussed in the next section.

3.3.2 Polarisation

Polarised x-rays are an essential tool for resonant scattering techniques and a fine level of control is needed over the degree of circular polarisation, P_{C}. There are several ways in which circularly polarised x-rays can be created but the method of production is highly dependent upon the x-ray energy required for the experiment. Undulators naturally produce polarised light when the radiation generated at each bending magnet interferes constructively with those from previous bends. If the oscillations in the undulator are confined to a plane, then linearly polarised radiation is produced. A helical arrangement of magnets within the undulator, however, will result in an electron trajectory which produces elliptically polarised synchrotron radiation.

Beamline X13A, (discussed in Section 3.3.3) uses a helical undulator of this type to generate elliptically polarised radiation with a degree of P_{C} of $\sim$70%. A helical undulator allows the energy of the synchrotron radiation produced to be tuned by either changing the relative position of the magnets in the undulator or the strength of the magnets. There are limits on the maximum change in position and strength of the magnets which define the operating energy of a helical undulator, and for X13A this range is $\sim$250-1600 eV.

To produce polarised x-rays at harder energies, we must turn to phase retarders as a method of generating circularly polarised x-rays and these were used on beamlines 4-ID-D and XMaS (discussed in Section 3.3.3). Phase retarders transform linear to elliptically polarised radiation by changing the angle of the phase plate. As the angle of the phase plate is changed, the degree of ellipticity changes as there is different absorption of the σ and π components, a phenomenon called birefringence. Circular polarization is achieved by inducing a $\pm\pi/2$ phase shift between equal amounts of incoming σ and π polarized radiation [124]. Phase retarders need to have low absorption and a low lattice parameter because they work in transmission [125]. Diamond is commonly used because of its low absorption up to $\sim$10 keV beyond which it needs to be so thick that the cost becomes prohibitively expensive. Diamond is not used below about 3 keV because of the absorption and relatively large lattice parameter so silicon monochromators are often used in the energy gap 2-3 keV.

The degree of polarisation for a diamond phase retarder as a function of angular offset ($\Delta\theta$) is shown in Figure 3.6 at an energy of 3.174 keV. The asymmetry ratio (A.R.), which is defined in Chapter 2, is directly proportional to P_C and Figure 3.6 shows how the polarisation changes from negative to positive helicity as the phase retarder is rotated across the Darwin width at the Bragg peak. The

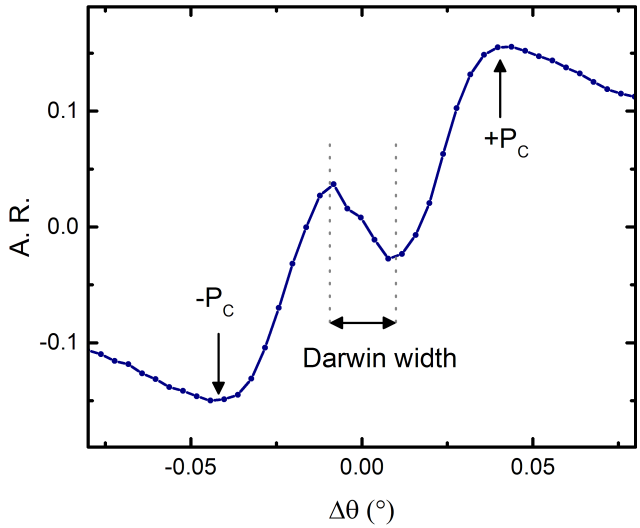

Figure 3.6: The asymmetry ratio (which is directly proportional to the degree of circular polarisation (P_C)) from a diamond phase retarder as a function of angular offset ($\Delta\theta$).

points at which the maximum circular polarisation is achieved are indicated in the figure and are equal and opposite. The angular positions of the phase retarder that give positive and negative helicity are used whilst performing experiments where the helicity is flipped during operation in order to obtain the asymmetry ratio instead of flipping the applied field.

In reality, the P_C achieved is rarely 100% but this is dealt with when the difference between the signals recorded at the two helicities is taken as any discrepancy is cancelled out. It is important to check that the signals are equal and opposite: if this is not the case the discrepancy would not be corrected for in the difference signal. Alternatively, if $+P_C$ and $-P_C$ are not equal and opposite (as is normally the case with a Si phase retarder) the data must be corrected with a scaling factor which is proportional to the ratio between the two helicities. Additionally, the intensity of the beam after the phase retarder is not the same for the two helicities and must be corrected for e.g. by counting to the same monitor counts. This difference occurs because there is higher absorption when the beam travels through more of the phase retarder at higher angles.

3.3.3 Beamlines

When designing an experiment, consideration must be given to specific beamline capabilities. The energy of x-rays available and the experimental equipment vary hugely between beamlines. In this section we highlight the main features of the

different the beamlines used to collect the experimental data presented in this thesis and why they were chosen for the experiments.

XMaS

The resonant scattering studies on Gd-Y and Gd-Y-Ho-Y superlattices reported in Chapter 5 were carried out at beamline XMaS (BM28) at the ESRF, Grenoble, France [126]. XMaS is a beamline situated on a bending magnet which has an energy range of 2.5 keV to 15 keV. The L_3 resonant edges of Gd and Ho are at 7.211 keV and 8.046 keV respectively which sit well in the middle of the energy range possible at XMaS. The L_3 edge of Y is at 2.079 keV and lies outside the practical operating range of XMaS. Indeed, it would be very difficult to find a single beamline that could cover the range of energies needed to study both Gd and Y on the same beamline.

XMaS has the option to work with white beam or with focussed or unfocussed monochromatic beams. The data presented in this work was recorded using a focussed monochromatic beam produced with a double-crystal monochromator which is constructed from two, plane silicon (111) crystals [125]. The first crystal is water cooled and absorbs most of the incident synchrotron radiation. This is followed by a toroidal mirror, which is uncooled and made from single crystal silicon with a very slight curvature produced by a pneumatically actuated bending mechanism. The mirror is coated in Rhodium to increase the reflectivity, and is responsible for focussing the beam to a small spot (<0.5×0.5 mm).

A schematic of the XMaS optics hutch is provided in Figure 3.7. The beamline has an 11-axis Huber diffractometer which allows operation in both vertical and horizontal scattering geometries. The samples were kept under vacuum during operation using the in-vacuum magnet cryostat nicknamed 'Zebedee'. There are

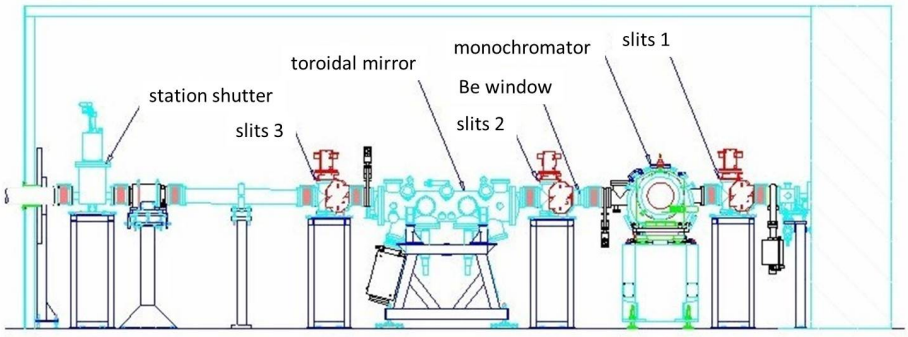

Figure 3.7: Schematic of the optics hutch at the XMaS beamline, showing the positioning of the slits, toroidal mirror and monochromator. Adapted from [127].

harmonic rejection mirrors and the beam can be further conditioned by phase-plates and an in-vacuum polarisation analyser [127].

4-ID-D

4-ID-D is located at the Advanced Photon Source (APS), Chicago, USA and was designed for x-ray magnetic circular dichroism, magnetic x-ray scattering and x-ray magnetic reflectivity studies [128, 129]. The beamline is mainly involved with polarisation dependent spectroscopic and scattering studies of magnetic materials and has an energy range of 2.5 keV to 30 keV. The beamline was used to collect data on patterned arrays of FePd circular islands in Chapter 8. The Pd L_3 resonant edge is at 3.187 keV, which falls within the range of energies produced on 4-ID-D. The Fe L_3 edge is at a much softer energy of 0.708 keV which is not produced on this beamline. It was therefore not possible to investigate both the Fe and Pd in the samples during the same experimental run on this beamline. The beamline is equipped with an 8-circle Huber diffractometer which again allows operation in both vertical and horizontal scattering geometries. The polarisation is controlled using crystal phase retarding optics that allow linear to circular polarisation with $P_c \sim 0.98$.

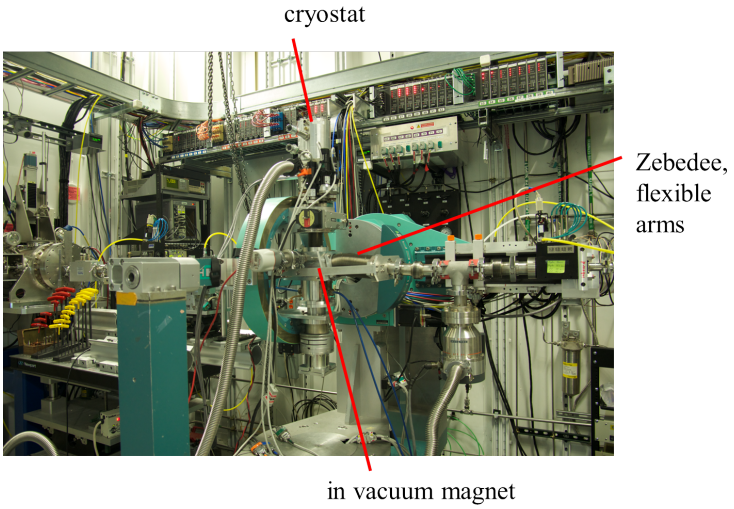

Figure 3.8: Photo of beamline 4-ID-D during experimental run showing how the in-vacuum magnet, 'Zebedee', is used with the cryostat and the 8-circle diffractometer.

Zebedee

At XMaS and 4-ID-D, a flexible vacuum chamber nicknamed 'Zebedee' was used [126]. A photo of Zebedee in use at beamline 4-ID-D is shown in Figure 3.8 and shows how the in-vacuum sample environment is used with the 8-circle diffractometer and cryostat. Soft energy x-rays are easily absorbed in air, therefore it is necessary to operate under vacuum to reduce scattering by air. Reducing the absorption of soft x-rays by air presents challenges for scattering techniques as the geometries involved require a large range of angles to be achievable whilst maintaining a sample environment under vacuum.

This challenge was resolved with the use of an in-vacuum magnet, 'Zebedee', designed to perform magnetic reflectivity measurements at low energy and low temperatures (down to approximately 20 K). It is constructed from Aluminium and is windowless to avoid entry and exit window absorption. A magnetic field of up to ± 0.2 T is applied (using an electromagnet) in the plane of a sample and along the beam direction. The chamber uses two flexible bellows attached to the main sample housing to allow changes in angle when recording reflectivity measurements whilst maintaining a vacuum ($< 10^{-6}$ Torr).

X13A

The work on SmCo single layers and SmCo/CoAlZr trilayers was carried out at X13A, at the NSLS, Brookhaven National Laboratory, New York, USA [130]. The beamline was primarily designed for x-ray magnetic circular dichroism and resonant magnetic scattering experiments at soft energies. It has an elliptically polarising wiggler consisting of five permanent magnet vertical poles and six electromagnetic horizontal poles which allows fast switching (at 22 Hz) of the polarisation by reversing the current of the horizontal electromagnets.

The beamline operates at energies in the range 0.25 keV to 1.6 keV, making it a good candidate for studies of the L_3 resonant edge of Co at 0.782 keV and the M_4 and M_5 resonant edges of Sm at 1.106 keV and 1.081 keV respectively. A water cooled focussing mirror was used after the first aperture from the insertion device and the beamline used a spherical grating to monochromate the beam, allowing a large range of energies to be achieved depending on the groove density (800 or 1600 grooves/mm). The main difference to the optics on the other beamlines is that as the helicity is flipped during operation, a chopper is needed to block the linearly polarised part of the beam that is created when the helicity is reversed. The fast switching technique allows the $\pm P_C$ signals to be recorded simultaneously.

Conclusion

In this chapter, the main growth and characterisation techniques used in to produce the samples and data throughout this work were introduced. Sputtering and MBE were introduced as the main growth techniques. Sputtering produces samples over larger areas and grows high quality layers at relatively fast deposition rates. MBE is used when a epitaxial growth is needed as with layers in a superlattice. MOKE and SQUID are used to characterise magnetic properties of the structures. MOKE is surface sensitive and therefore often used to study thin films whereas SQUID measures the whole sample, which is better for studies of the bulk properties. Finally, various methods of x-ray production were described, including the reasons for choosing the particular beamlines for each of the different experiments.

Chapter 4

Data Collection and Analysis

This chapter outlines how the data presented throughout this thesis was collected, including the different types of scans in reciprocal space and magnetic hysteresis loops. The chapter illustrates how the asymmetry ratio is obtained and its dependence on the helicity and **q** *vector. The methods used to analyse data are also introduced, starting with a description of the fitting software, GenX, which outlines the fitting algorithm and functions used to assess the 'goodness of fit'. The chapter then goes on to describe how real samples may have roughness at interfaces or differences between the magnetic and chemical structures such as magnetic dead layers. How the samples are modelled using the available techniques within the limits of the software is discussed.*

4.1 Scanning Methods

The beamlines described in the previous chapter all had essentially the same operation in regards to performing scans and the details of this will now be given briefly. In principle, it is only necessary to be able to scan in θ and 2θ which are defined in Chapter 2, assuming that the sample is perfectly flat, aligned in the beam and that the sample is positioned in the correct orientation (which is particularly important for patterned arrays). This is very unlikely to be the case when the sample is first placed in the sample holder and so the user must be able to fine tune the position and rotation in all three dimensions to achieve good alignment.

When performing a scattering experiment, the sample must first be aligned with the beam; this is performed by first moving the sample into the beam and finding the point where the signal is cut in half (half cut scan). The next step is to perform a θ scan and set the centre of the peak to be the new $2\theta/2$. It may also be

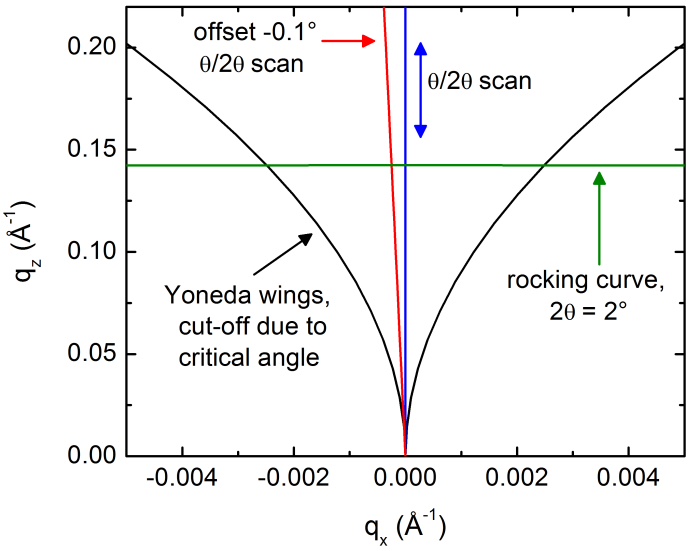

Figure 4.1: A reciprocal space representation of experimental scans showing (blue) a specular scan, (red) an off-specular scan and (green) a rocking curve. Reproduced from [131].

necessary to rotate the sample in ϕ, which was defined in Figure 2.6 in Chapter 2. This process must be iteratively repeated until good alignment is reached and there is no longer any change between scans.

Once the sample is aligned in the beam, there are a number of scanning geometries that can be adopted, each giving different information about the sample. A scan which is on the specular condition, where $\theta = \frac{2\theta}{2}$, $q_x = 0$, records the reflectivity as a function of q_z from which a depth dependent profile can be obtained, and this will be referred to as a *specular* scan ($\theta/2\theta$ scan in Figure 4.1). By off-setting the specular scan by a small amount in q_x but keeping $\theta + \delta\theta$ and 2θ in a 2 to 1 ratio, the diffuse scatter is probed as a function of q_z. Scans of this type will be referred to as *off-specular* scans. Additionally, a *rocking curve* or *transverse diffuse scan*, is a scan of the in-plane component of reciprocal space, q_x. The detector angle, 2θ is fixed whilst the sample angle, θ is varied. There is a small change in q_z in these scans, but it is typically negligible and can be ignored. A representation in reciprocal space of these different types of scans is shown in Figure 4.1.

With *resonant* scattering experiments, the energy of the incident x-rays is tuned to just below the absorption edge of a particular element. By tuning just below the edge this avoids strong absorption effects, which would reduce the penetration depth, but still remains sensitive to the magnetic signal. The energy of the beam is tuned to the edge using a reference sample that is known to be magnetic and noting

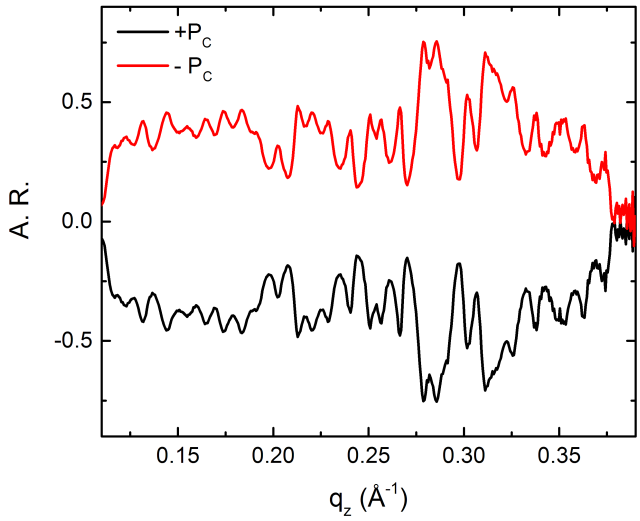

Figure 4.2: An example asymmetry ratio recorded as a function of q_z, with $\pm P_C$ for a SmCo/CoAlZr trilayer.

where the signal is maximised. It is important to work under vacuum not only because soft x-rays are scattered by air, but also whilst working at low temperature to avoid the formation of ice on the surface of the sample. Ice on the surface of the sample would produce a scattered signal in which the features would be obscured by those from the ice layer. To avoid ice build up, the sample is cooled with the heater on so that cryo-pumping acts on the cold-finger and not the sample surface.

Element specific hysteresis loops were recorded using resonant x-ray scattering; the sample is held at a **q** value at which the asymmetry ratio (A.R.) is large to maximise the signal to noise ratio and the A.R. is measured as a function of applied field. When measuring with the sample in an applied field, the helicity must be reversed rather than the applied field to obtain the A.R. In this case it is important to account for any remanence of the magnet. Remanence is often observed as an offset of the loops in the applied field and can be accounted for by fitting the loops and subtracting this offset. An example of reversing the helicity on the recorded A.R. is shown in Figure 4.2 and shows how the signal is equal and opposite with the two helicities.

As the A.R. is dependent on **q**, the amplitude of the hysteresis loops recorded using resonant x-ray scattering are directly proportional to the magnetisation but do not give an absolute value of the magnetic moment. Figure 4.3 shows some examples of hysteresis loops measured at different q_z values as marked on the A.R. in Figure 4.3. It is clear that even small changes in **q** can result in large changes in the shape and magnitude of the measured hysteresis loops, and for this reason

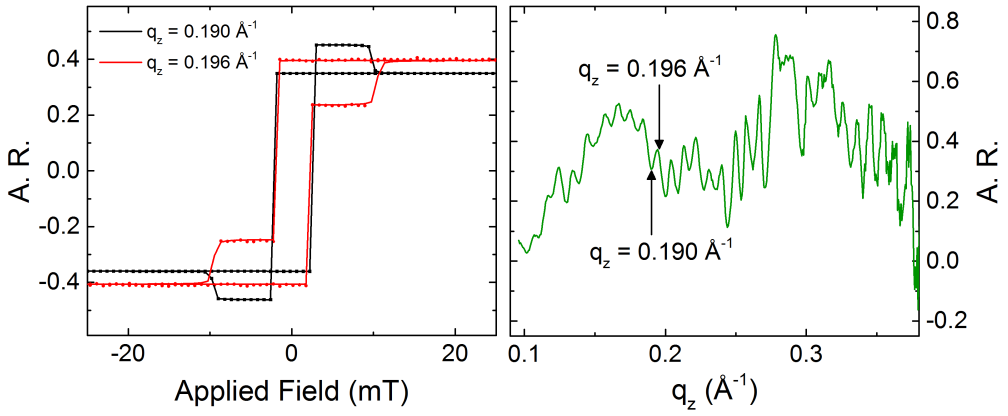

Figure 4.3: (left) Example hysteresis loops recorded with resonant x-ray scattering, flipping the helicity at each point and tuned to the Co L_3 edge for a SmCo/CoAlZr trilayer. The two loops are measured at different q_z values as indicated on the A.R. scan (right).

caution must be applied when investigating properties such as the position of domain wall boundaries and relative magnetisation of layers using this technique.

4.2 Fitting Hysteresis Data

Hysteresis loops give information about the magnetic reversals in a material. Key properties of interest are remanence, saturation magnetisation, coercivity and loop shape. Throughout this work, hysteresis loops will appear for a variety of different thin films and multilayers, and so, to enable faster, more accurate processing of these hysteresis loops, python scripts were written to fit the data.

For single, thin films, where one reversal is observed, the A.R. as a function of applied field was fitted to a modified Langevin equation of the form

$$A.R. = A\left(\frac{1}{\tanh(H')} - \frac{1}{H'}\right) + y_0 \tag{4.1}$$

where A is the amplitude of the loop, y_0 a constant offset and $H' = ((H \pm H_c) + H_0)/\zeta$ with H the applied field, H_c the coercive field, H_0 a constant offset and ζ a shape parameter defining the 'squareness' of the loop. Several functions were tried including modified forms of *atan* and *tanh* but the modified Langevin function was found to allow enough variation in shape to provide a good fit to the variety of loops throughout this work and was chosen for this reason. The modified Langevin formula in Equation 4.1 was fitted to the data using a Levenberg-Marquardt algorithm

to minimise χ^2. An example of a single hysteresis loop fitted with this modified Langevin function is shown in Figure 4.4(a).

The modified Langevin formula in Equation 4.1 is suitable for fitting loops as long as there is just a single reversal. When multiple layers are combined into new and complex heterostructures, however, this is often no longer the case and a method of fitting hysteresis loops from different kinds of structures was devised. The scripts were extended to fit other types of magnetisation reversal. For example, SmCo/CoAlZr trilayers as described in Chapter 6 have layers that undergo magnetisation reversals at different applied fields leading to steps in the hysteresis curve. To accommodate this in the model, data was fitted to a function which used a sum of several Langevin equations (the number of which was equal to the number of steps in the loop) as is shown in Figure 4.4(b). The sum of loops used the same offset values, H_0 and y_0.

Also, magnetisation reversals which had a steep gradient at first, but then a more gradual change in magnetisation, could not be accounted for by a simple

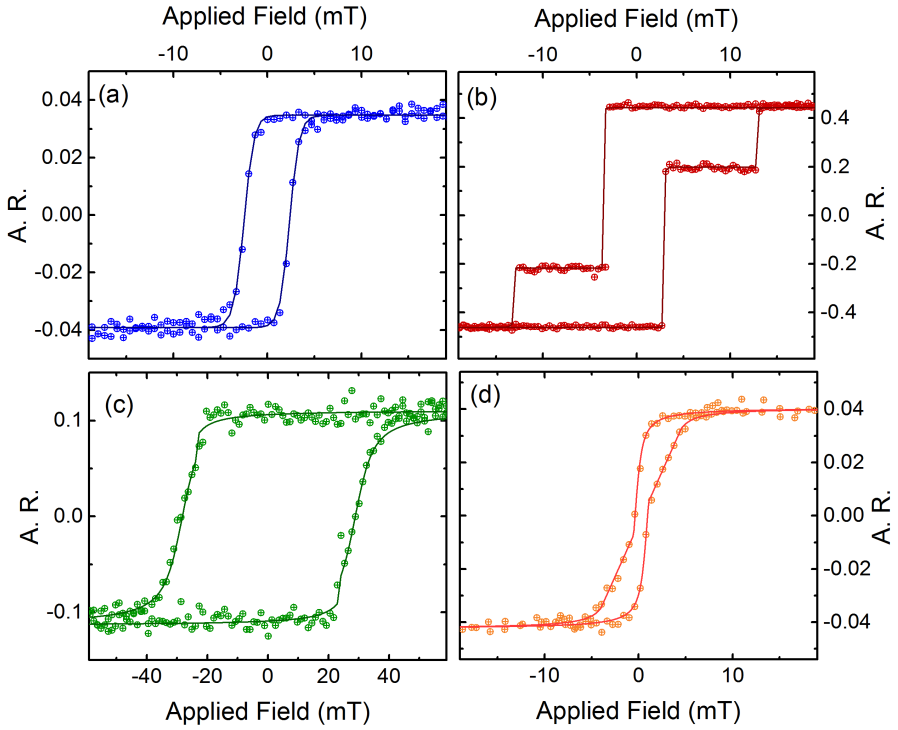

Figure 4.4: Some example hysteresis loops for (a) a single loop, (b) a loop with multiple reversals, (c) one with different shape parameters and (d) a loop for a patterned array of circular islands which form vortices. Error bars are excluded for clarity.

Langevin equation. An example of such is the Sm sub-network in SmCo/CoAlZr trilayers where part of the curve had a different shape to the other. This was modelled using a point H_{shape} where the curve switched from shape factor ζ to ζ' as shown in Figure 4.4(c). Loops where magnetic vortices were induced in circular islands proved to be another challenge to fit and this was done by inserting a linear section of the form $A.R = mH + c$ into the loop between points H_{in} and H_{ej} which are the field values at which the vortex is injected and ejected respectively. An example of a hysteresis loop for a patterned array containing magnetic vortices is shown in Figure 4.4(d). Note that all the functions used to fit the hysteresis data assumed that the hysteresis loops were symmetrical and that any features observed for an increasing applied field would also be included for a decreasing applied field.

The Marquardt-Levenberg algorithm provides a fitting method which is robust and effective at fitting data. It combines a method of steepest descent, optimising the parameters to rapidly progress towards the best fit when the trial solution is far from the optimum values. Once closer to the best fit, it then switches to an expansion method [132]. The Marquardt-Levenberg algorithm has proved highly successful for fitting the data sets presented in this work and is used widely in other fitting programs. The Marquardt-Levenberg algorithm was also chosen as it provides a weighted fit using the error bars on the data. One of the disadvantages to using the Marquardt-Levenberg algorithm is that if the initial parameters are very far from the optimum values, it can find a minimisation that is not at the true optmimum solution, but instead at a point where there is a local minimum on the error surface. For this reason, it was often important to give a set of initial parameters that were relatively close to the optimum values.

4.3 Reflectivity Simulations

The software used to fit the reflectivity spectra throughout this work is a package called GenX [87]. In this section some of the parameters and main concepts involved with using the software are discussed.

4.3.1 Introduction to GenX

In Chapter 2, it was shown that the phase information is lost in reflectivity scans, and as such it is not possible to obtain the sample structure by performing a Fourier transform on the reflectivity data. As a result, reflectivity measurements can only be used to calculate values of thicknesses, roughnesses and densities by producing a simulated reflectivity scan and then refining the parameters to achieve a match be-

tween the data and simulation. When dealing with many coupled fitting parameters in samples with many layers, this soon becomes a challenging task. To fit reflectivity data we need a program that is capable of dealing with a large number of fitting parameters. For each layer the minimum number of fitting parameters necessary to achieve a fit are the thickness, roughness and electron density but the number of parameters can rapidly grow as properties such as resonant scattering factors or composition are added.

GenX uses a differential evolution algorithm for fitting x-ray and neutron reflectivity data. The differential evolution algorithm is a robust optimization method which avoids local minima but at the same time is highly effective. GenX allows modelling of the scattering length density (SLD) of a sample using the thickness d, roughness σ, electron density $dens$ and scattering factors f (real and imaginary parts). The structure is built up in slabs from the substrate upwards. The SLD is the electron density multiplied by the scattering length. In GenX these are given as $dens$ and f respectively and GenX allows the user to define the real and imaginary parts separately. The SLD is generated as the product of these parameters on a slab by slab basis with a Gaussian error function of width σ allowing for roughness between slabs. GenX then uses the total SLD profile to generate the simulated reflectivity.

The model used throughout this work will be one called 'mag_refl' which allows resonant terms to be included for the fitting of resonant x-ray scattering data. The model is capable of fitting both x-ray and neutron data but the description here will only be concerned with x-rays. The total non-magnetic scattering length is given as $(f + f_r \times resdens) \times dens$ where f is the non-resonant scattering length per formula unit in electrons, f_r the resonant x-ray scattering length of the resonant species in electrons, $resdens$ the fraction of resonant species and $dens$ the electron density, as before. Chapter 2 also showed that when doing resonant magnetic scattering there are additional terms to the magnetic scattering length, m and m'. In GenX, the total magnetic scattering length is given as $f_{m1} \times resmag \times mag \times resdens \times dens$. f_{m1} (real and imaginary parts) is the resonant magnetic part of the scattering length and has the same units as f, $resmag$ is the fraction of magnetic resonant species, mag the magnetic moment per formula unit and $resdens$ and $dens$ as before.

Figure 4.5(left) illustrates how GenX builds up the sample structure slab by slab in the z direction for a Co layer on a Si substrate and with a CoO layer on top. The resulting SLD profile as a function of height from the substrate is shown in Figure 4.5(right) and shows well defined layers with a roughness between layers set to 2 Å for every layer. It is clear that the SLD of the Si substrate changes by very

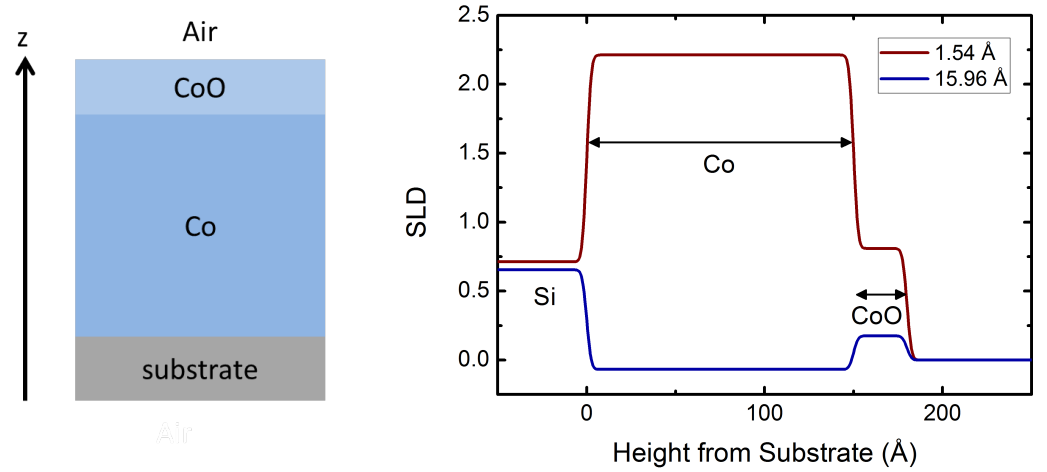

Figure 4.5: (left) Schematic of a Co layer on a Si substrate and a CoO oxide layer on top. (right) The corresponding scattering length density (real parts only) profiles at 1.54 Å (the wavelength of a Cu K_α laboratory source) and 15.69 Å (The Co L_3 resonant edge) as produced using GenX.

little at the Co L_3 edge compared to the laboratory source, but the effect of tuning to an absorption edge on the SLD value of the layers containing Co is dramatic. When fitting reflectivity data recorded at multiple energies, it therefore important that the changes to the scattering lengths must be carefully considered, as tuning to a resonant edge can have a large impact on the SLD profile, and also on the reflectivity simulation.

4.3.2 The Differential Evolution Algorithm

The differential evolution algorithm used in GenX to fit reflectivity data takes an individual, which is defined by a vector $\mathbf{p}_i$ that contains the values for the M parameters to be optimised. $\mathbf{p}_i$ defines one point in the parameter space that defines the optimisation problem. A collection of several vectors make up a population. The program takes a population $P = \{\mathbf{p}_0, \mathbf{p}_1 ... \mathbf{p}_{N-1}\}$ and initialises it by setting each parameter to a random number between its minimum and maximum allowed values which are chosen by the user. A trial population $T = \{\mathbf{t}_0, \mathbf{t}_1 ... \mathbf{t}_{N-1}\}$ is formed from the parent population P, through the application of mutation and recombination operators. Then each vector, $\mathbf{t}_i$, is compared which its parent vector, $\mathbf{p}_i$, through the figure of merit (FOM) value which is an indicator of the 'goodness of fit'. The population which gives the lowest FOM is selected to become the next parent population and the process repeats. To summarise, the basic idea is that the parameters are changed randomly, if the fit is better, it sets them as the new parameters [133].

4.3.3 Figure of Merit

The Figure of Merit (FOM) is the function that compares how well the simulation matches the data. The quality of the fit produced is highly dependent on the FOM chosen and different FOM functions will be sensitive to different parts of the data. The following section will briefly outline the FOM functions used for fitting the data in this work, although others are available, these are the ones that proved most useful for the particular data sets recorded.

The first is called 'diff' which is the absolute difference between the simulation and data, and is given by

$$FOM_{diff} = \frac{1}{(N-p)} \sum_i (Y_i - S_i) \tag{4.2}$$

where Y is the merged data set consisting of all data sets and S the corresponding simulation. Each element within the super data set is denoted by i. The total number of data points is N and p is the number of free parameters in the fit. This FOM is useful when all parts of the data set lie within the same order of magnitude. When fitting reflectivity sum and asymmetry ratio data sets it is sometimes necessary to rescale the sum spectrum so that both data sets can be fitted simultaneously using the same FOM.

Other FOM functions that work well with data sets which are within the same order of magnitude are 'R1', given by

$$FOM_{R1} = \sum_i \frac{\sqrt{Y_i} - \sqrt{S_i}}{\sqrt{Y_i}} \tag{4.3}$$

which is often called the residual factor, gives the percentage of the summed structure factor residuals (the absolute difference between the data and simulation) over the entire data set with respect to the total sum of measured structure factors. Additionally there is 'R2', given by

$$FOM_{R2} = \sum_i \frac{(Y_i - S_i)^2}{Y_i^2} \tag{4.4}$$

which in contrast to 'R1', gives the ratio of the total sum of squared deviations to the total sum of squared structure factors. Using the square of any deviations has the consequence of amplifying the FOM at regions where the simulation is furthest from the data. This can be useful for bringing in parts of the fit that were not recognised as being particularly far from the simulation using other FOM functions.

If only the sum signal is to be fitted it may be more appropriate to use a logarithmic FOM as given by

$$FOM_{\log} = \frac{1}{(N-p)} \sum_i (\log_{10} Y_i - \log_{10} S_i) \tag{4.5}$$

Figure 4.6 illustrates how the goodness of fit scan changes for 'R2', 'R1' and 'diff' with the reflectivity rescaled by q_z^4 so that the data is all within the same order of magnitude. The data and simulation are shown in the upper part of each section and the goodness of fit scan in the lower part. The total FOM value is the sum of the goodness of fit scan in the lower part of each figure. The three FOM functions ('R2', 'R1' and 'diff') have visibly different sensitivity to certain parts of the reflectivity data. Figure 4.6(d) shows the 'log' FOM with the data unscaled by the q_z^4 factor. All of the simulations in the figure are produced with exactly the same parameters.

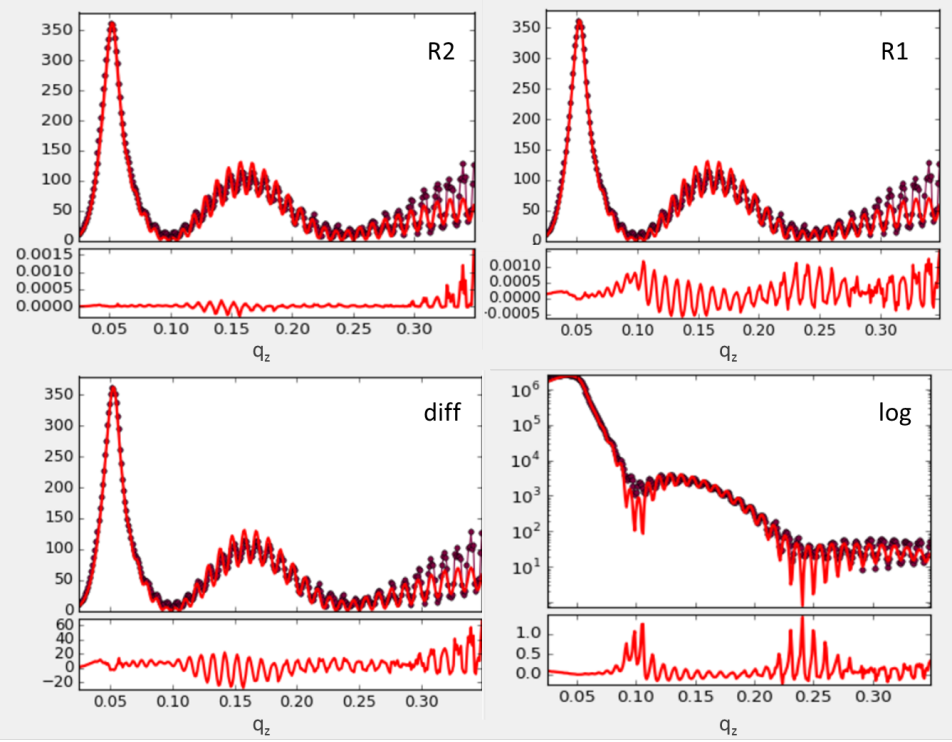

Figure 4.6: Examples of data sets and simulations (upper parts of each section) with the corresponding goodness of fit scan as a function of $\mathbf{q_z}$ (lower part of each section). These are shown for 'R2', 'R1' and 'diff' with the data scaled by q_z^4 and for 'log' with the unscaled data. All plots shown are for the same data simulated with the same parameters.

4.4 Modelling Real Samples Using GenX

Defining the thickness, density, scattering factors, roughness etc. of the layers in a thin film or multilayer to model samples in GenX will provide a good estimate of the reflectivity profile for simple structures with very few layers. When dealing with more complex structures with multiple layers and thick oxides, however, there are some subtleties to getting a good fit to the data, and it is important to remember that the model can only go so far to approximating the real structure. Some of the methods used to achieve a suitable fit will be outlined in this section.

4.4.1 Diffusion at Interfaces

Real samples will always have some imperfections at interfaces between different layers. Whether this is caused by interdiffusion of atomic species or variations in the interface, it is extremely unlikely that the interface will be perfectly flat. This section explores the effect of diffusion at interfaces on reflectivity data and how we can model it using the available software. It starts by exploring roughness caused by the diffusion of particles across an interface. The interface is considered to be two layers of different materials where particles diffuse across with a diffusion flux, J. An illustration of such a system is shown in Figure 4.7(left) and the corresponding concentration gradient (right). In a solution with a concentration gradient, there will be a net flux of atoms from regions of high to low concentrations. The net flux

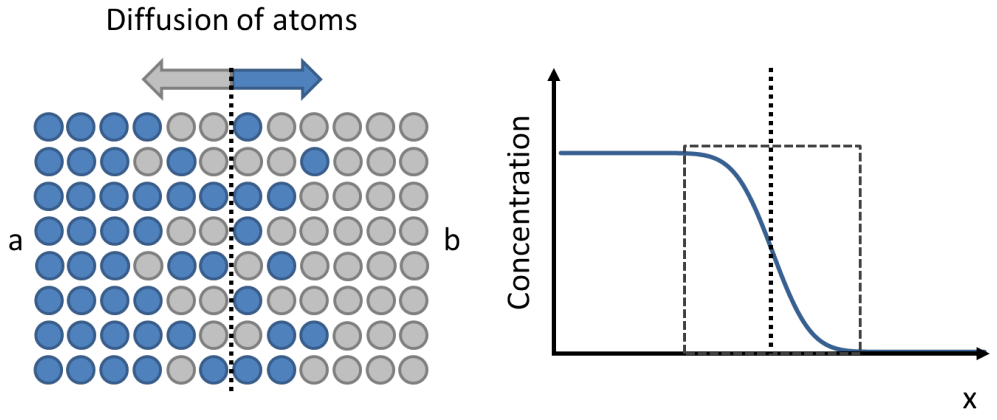

Figure 4.7: (left) Illustration of diffusion across an interface and (right) the resulting concentration profile.

of particles is given by Fick's first law as

$$J = -\mathcal{D}\frac{dc}{dx} \tag{4.6}$$

with concentration gradient, c and diffusion coefficient, $\mathcal{D}$ [134].

Equation 4.6 assumes that the diffusion is steady-state and the conditions do not change with time which is not commonly encountered in real systems. It is more realistic that the concentration of particles at any point in the material will change with time [135]. Fick's second law takes into account the concentration changes with time and is given by

$$\frac{dc}{dt} = D\frac{d^2c}{dx^2}. \tag{4.7}$$

If two materials are put in contact with one another where the diffusing particles have a uniform initial concentration, c_0, the surface concentration of diffusing particles is c_s, and the concentration of the diffusing particles at distance x from the interface is c_x. This leads to the solution to Fick's second law

$$\frac{c_x - c_0}{c_s - c_0} = 1 - \text{erf}\left(\frac{x}{2\sqrt{Dt}}\right) \tag{4.8}$$

where erf is the Gaussian error function.

GenX models roughness between layers using a Gaussian error function which provides a good approximation of the variation across an interface assuming that the roughness is as a result of diffusion and Fick's second law holds. GenX uses a

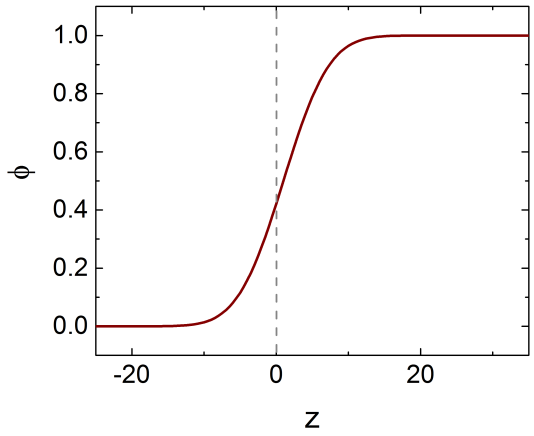

Figure 4.8: A simulated interface between two layers which is modelled as a lateral variation in the electron density.

function of the form $\exp^{-1/2\sigma^2 q_z^2}$ where σ is the interface width and q_z the scattering vector. This results in an interface profile described by ϕ_i

$$\phi_i(z) = \frac{1}{2}\left(1 + \text{erf}\left(\frac{z}{\sqrt{2}\ \sigma_i}\right)\right). \tag{4.9}$$

where the interface width is σ_i which is centred on the interface position z_i as shown in Figure 4.8.

Modelling the interface profile as a Gaussian error function in this manner works well to model many different types of multi-layered materials and can be used to determine the thickness of the layers and the width of the interfaces. It has the benefit of requiring relatively light computational power and works well as long as the layer thicknesses are much greater than the roughness.

4.4.2 Topographical Variations Versus Diffusion at Interfaces

Specular reflectivity scans are only sensitive to variations in the SLD in the z direction. At each z value, the measurement is sensitive to the average SLD throughout the 'slice' integrated across the sample in x and y which makes it impossible to distinguish between an interface which is rough due to interdiffusion of atoms or one which varies topographically (e.g. terraced). For example, see Figure 4.9 (a), which has no intermixing of the chemical species of the two layers, but has a variation in the interface. If instead, the sample was sliced across the region of roughness, and the average density was calculated for each slice, this would look very similar in the SLD profile to Figure 4.9 (b) which does have chemical intermixing.

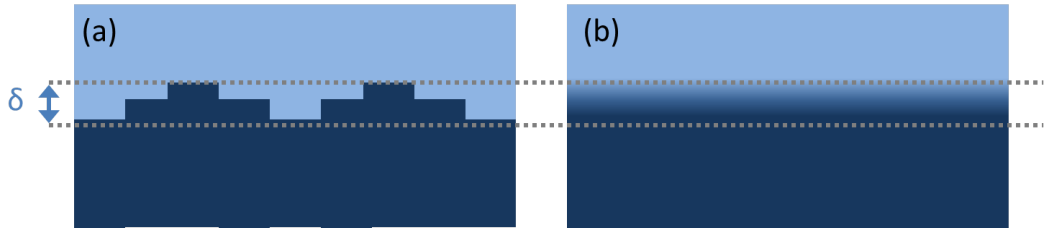

Figure 4.9: A comparison between (a) surface variations such as terracing and (b) chemical intermixing at an interface.

With roughness caused by atomic diffusion, the Gaussian error function is a good approximation of the intermixing/roughness between layers, but what about when there is topographical roughness? Sample growth using MBE or sputtering involves depositing particles onto the surface which can then move around to find an optimal position. To create a simple model of this, consider a particle on a

one-dimensional lattice undergoing a random walk. The particle is originally at $x = 0$, and at every moment in time, the particle moves one site randomly up or down $|x(t+1) - x(t)| = 1$ with equal probability $p = 1/2$. The coordinate $x(t)$ is recorded as a function of time resulting in a probability of the particle being found at a distance x from the origin at time t of

$$P(x,t) = \frac{1}{\sqrt{2\pi t}} \exp -\frac{x^2}{2t} \tag{4.10}$$

which is a Gaussian distribution [136]. This is a much simplified model of the kinetics of particles on a surface during growth but this basic Gaussian distribution model provides a good approximation of the z profile of an interface with topographical variations.

The Gaussian error function used in GenX ceases to hold when the structure of the interface is more complex, for example asymmetric variations or when a chemical element is more easily diffused in one layer than another leading to asymmetric chemical profiles across an interface. Additional challenges are present for structures like arrays of islands where the average across slices is taken. These can be fitted in GenX by allowing the density or scattering factors to be reduced to allow for air spaces in between islands which would bring the average SLD in each slice down. If it is assumed that the whole island is made of the same material, it is possible to estimate the average shape of structures in patterned arrays like these by assuming that a reduction (increase) in SLD is directly proportional to the loss (gain) of material due to the change in shape.

4.4.3 Slicing

When dealing with very thin layers, the Gaussian error function method outlined above no longer holds. The error functions from neighbouring layers can overlap causing unphysical electron density profiles to occur as in Figure 4.10 (b). This has been overcome in GenX by slicing up the electron density profile into many small layers so that it approximates a continuous function [104]. The effective electron density profile, Φ_i, of an isolated layer i is the combination of the interface profiles $\phi_i(z)$ and $\phi_{i+1}(z)$ from the adjacent i and $i+1$ layers,

$$\Phi_i = \begin{cases} \phi_i(z - z_i) & z \leq \zeta \\ \phi_{i+1}(-(z - z_{i+1})) & z \geq \zeta \end{cases} \tag{4.11}$$

where ζ is a parameter which defines where the SLD profile switches from ϕ_i to ϕ_{i+1}

$$\zeta = \frac{\sigma_{i+1} z_i + \sigma_i z_{i+1}}{\sigma_i + \sigma_{i+1}}. \tag{4.12}$$

It is necessary to to set $\phi_i(\zeta - z_i) = \phi_{i+1}(-(\zeta - z_{i+1}))$. To ensure physically realistic profiles, the effective density of the i^{th} component ρ_i must be normalised so that the total composition $\varrho_i = \Phi_i / \sum_i \Phi_i$ never exceeds 1. The final scattering length is then given by $\rho(z) = \sum_i \rho_i \varrho_i(z)$. The slicing model requires that the slice thickness is low, typically 1 Å or less, for the profile to approach a continuous function. Reducing the slice size is more computationally taxing and so when fitting using GenX, a balance between a fine level of sampling and run speed must be found. One way to combat this is to merge layers that have a similar SLD to reduce the total number of layers. GenX allows the user to select the value which the SLD of two layers must be within for them to be merged.

A simulated layer modelled using this slicing method is shown in Figure 4.10. Figure 4.10(a) shows the simulated SLD profile when using the original model (without slicing), the roughness is low ($\sigma = 1$ Å) compared to the thickness ($d = 10$ Å) and so the model copes well. Figure 4.10(b), however, shows how the original model breaks down when the upper roughness is increased such that it approaches the thickness of the layer. We can clearly see that there is now a sharp step in the

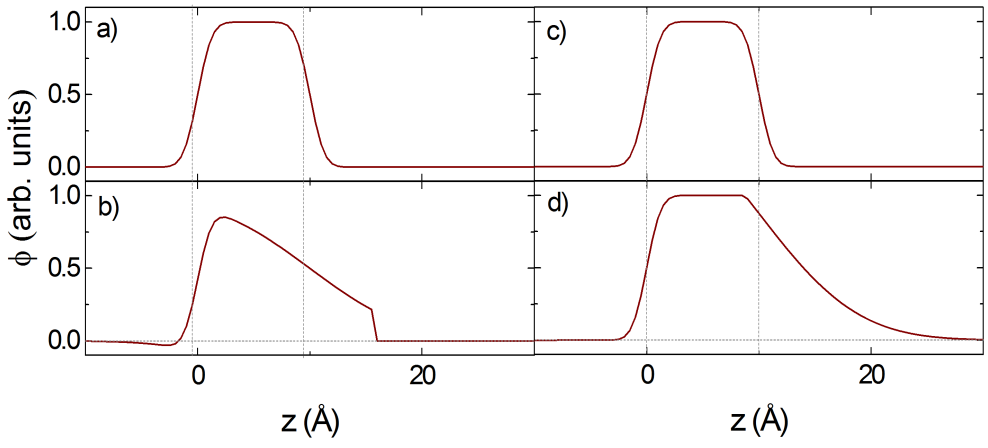

Figure 4.10: A simulated SLD profile for a single layer with roughness modelled as a Gaussian error function. (a) and (b) are calculated using a model which allows error functions to overlap causing un-physical features when the roughness becomes large compared to the thickness. (c) and (d) are calculated using an updated slicing model which resolves the issues with large roughnesses.

upper part of the SLD profile that would not represent a real sample. Additionally, there is a section in the lower part of the SLD that has become negative due to overlap of the error functions. The updated model is shown in Figure 4.10(c) and (d) for the same given parameters as (a) and (b) respectively. Figure 4.10(c) appears identical to (a) which is as expected for cases when the roughness is low compared to the thickness. Figure 4.10(d), however, shows a much improved SLD profile for the high roughness case with the updated slicing model.

4.4.4 Non-symmetric interfaces

What if the the composition across an interface is more diffuse in one direction than the other? The samples are grown from the bottom up so this is likely to be the case. The incident particles during growth have high energies meaning the deposited material is likely to be more mobile than the material it is deposited on to. There could be some implantation in the surface and also temperature gradients during growth, both of which could lead to an interface that is not well described by the solution to Fick's second law. This can be accounted for in GenX by writing a bespoke function, but this can be fairly difficult to implement, plus there is still the problem of choosing a suitable function to use. The easier thing to do (although more computationally intensive) is to split the interface up into multiple layers with different σ values. Figure 4.11(left) shows an example of an interface split into two layers where the lower layer has a lower σ value than the upper layer and Figure 4.11(right) shows a single layer for comparison.

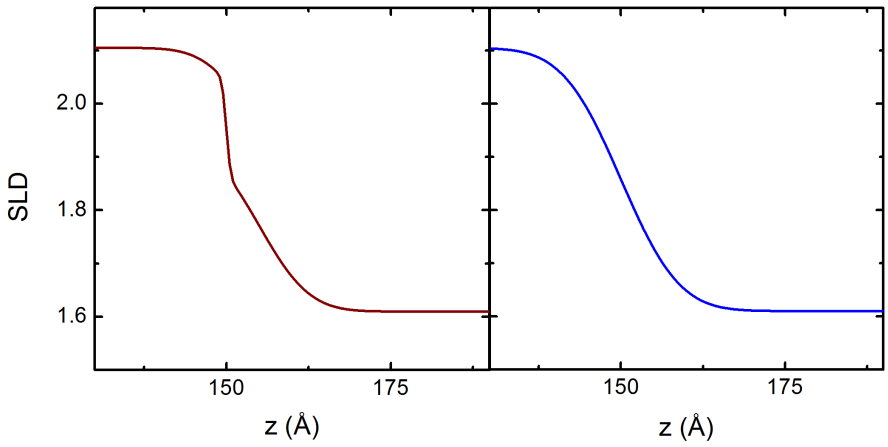

Figure 4.11: (left) An interface between modelled using two layers to give an asymmetric profile and (right) a normal Gaussian error function profile for comparison.

4.4.5 Magnetic interfaces

When materials are combined into multilayers and patterned arrays, the resulting magnetic interactions can lead to the magnetic and chemical SLDs not necessarily being the same. Multiple layers in proximity to one another can have magnetic interactions that extend far further than chemical mixing at an interface. To account for differences between the chemical and magnetic structure, GenX has been adapted to be able to modify the magnetic SLD (MSLD) profile. As indicated in Figure 4.12, the MSLD can be altered to move the magnetic interface position by an amount Δd_{mag}, the MSLD is multiplied by a factor ΔM over the region Δd_{mag} and an additional roughness can be added, σ_{mag}. Note that unless the roughness is modified using these parameters, it will exactly match that of the chemical SLD.

The additional parameters allow the user to modify the MSLD to account for enhancement or reduction of the magnetisation at magnetic interfaces. Accounting for this is important when modelling samples with features such as magnetic dead layers where the magnetic structure differs from the chemical structure due to a layer with a reduced magnetic moment. Alternatively, there could be enhancement of the magnetic moment in one material when in contact with another and GenX allows the user to model this. For example, a readily polarised material such as Pd, in contact with a ferromagnet such as Fe can result in an extended region of magnetisation into the Pd induced by the Fe layer.

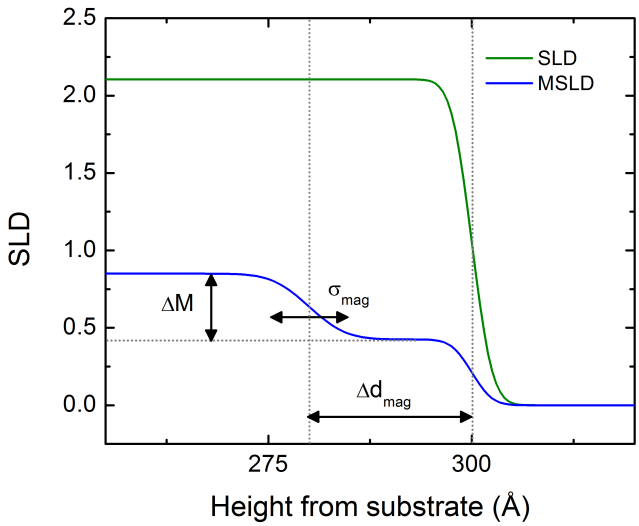

Figure 4.12: Illustration of how GenX models the magnetic SLD profile by multiplying a region Δd_{mag} by a factor ΔM and adding a roughness σ_{mag}

Conclusion

This chapter first introduced the basics of aligning a sample and the types of scans used to collect the data that will later be presented. This included a reciprocal space representation of the most common scans which were specular and off-specular reflectivity, and rocking curves. The **q** dependence of the asymmetry ratio was shown and made clear that dichroism experiments can not be used to obtain absolute values of the magnetisation from hysteresis loops. This will later become important when trying to determine the exact position of magnetisation reversals within a sample, which can not be determined using hysteresis alone. Details were outlined of the method used to fit magnetic hysteresis data including the various forms of the modified Langevin equation used throughout this work.

An introduction to GenX was given, stating the parameters available in the software and how they relate to scattering theory. The genetic algorithm that GenX uses to fit the data was briefly discussed and the advantages of the different figure of merit functions. The specifics of how the algorithm works, what the parameters mean and how to use the functions to best effect is important to being able to achieve a good fit for complicated multilayers and other structures.

Details were given about how real samples may differ from the idealised slab model and how to account for roughnesses, chemical mixing and magnetic enhancement or dead layers at interfaces. Issues associated with what happens to an SLD profile when real samples deviate from the nominal structure expected from the growth conditions will be a recurring theme in the rest of this work.

Chapter 5

Gd-Y Superlattices

This chapter presents a study of the effect of substrate temperature during growth on the physical and magnetic properties of Gd-Y superlattices. The effects of growth temperature on structure will be investigated using x-ray diffraction and reflectivity and the magnetic properties probed using resonant scattering and MOKE. The Y layers can not be probed using resonant scattering as the absorption edge lies outside the available experimental range and so a Ho 'tagging' layer was grown inside the Y layers in the superlattice to enable the study of any Y polarisation.

5.1 Introduction

The term superlattice is used to describe an epitaxial periodic structure of layers with typical thicknesses of only a few nanometres. Development of MBE techniques led to the creation of the first superlattices as it was then possible to achieve the high level of control needed to create very thin layers with good quality interfaces. The use of rare-earth materials has been extensive in superlattices and they have been combined with either materials with very different magnetic properties or alternatively a non-magnetic material, such as Y [137].

The heavy rare earth metals such as Gd, Dy, Ho and Er have been shown to have an indirect exchange coupling between localized $4f$ electron moments which is mediated by conduction electrons, and is known as the Ruderman-Kittel-Kasuya-Yoshida (RKKY) interaction. Early work investigating Dy-Y systems [54] and Gd-Y systems [138] found that the rare earth $4f$ electron moments spin polarise the Y conduction band. This results in a coupling between the magnetic layers in the superlattice which is a modified version of the RKKY interaction. The $4f$ electrons mediate the coupling through the spacer layer although Y itself is non-

magnetic [139]. These heavy rare earths are often combined in a superlattice with Y which is ideal as it is well lattice matched to the heavy rare-earths. A variety of magnetic structures can be achieved in these superlattices including collinear, ferromagnetic or antiferromagnetic states [140]. Non-collinear structures are also possible such as helical ordered states, for example in Dy-Y superlattices [141, 142].

Superlattices have been studied with a wide range of combinations of materials [143–147], and are of interest because properties observed in thin films such as proximity effects, exchange coupling and effects due to restriction in geometry are enhanced by the increased number of layers [4]. Also, the interfaces within the multilayer are well protected from surface oxidation or contamination which is a common issue with rare earths as they tend to oxidise easily.

The observed magnetic structures are strongly dependent on the topography/ roughness of the interfaces between layers throughout the superlattice [148] for example from chemical interdiffusion or variations at the interface such as terraces or a mosaic topography. It is therefore important to study these interfaces to be able to determine the effect of growth parameters on the resulting magnetic structure.

A large number of structural studies exist of rare-earth superlattices but the majority of these are in the form of diffraction data from highly crystalline layers, references [53, 142, 145, 149] are just some examples. Diffraction studies are useful for investigating the crystal structure, strain relaxation in the layers, thin-layer tilting, lattice distortion, mosaicity and interfacial roughness [150]. Also, studies of superlattices using neutron diffraction are sensitive to the magnetisation and have been used to determine the magnetic ordering in superlattices [151, 152]. There are, however, relatively few reflectivity studies investigating the magnetic properties of such superlattices. Fits to reflectivity data give a layer-by-layer model of both the chemical and magnetic structures which diffraction does not provide. By combining information from a range of techniques, we can hope to build up a full picture of the properties of interfaces in superlattices. As such, this chapter presents the influence of growth temperature on the structural and magnetic properties of Gd-Y superlattices studied by x-ray resonant magnetic scattering in combination with x-ray diffraction and MOKE magnetometry.

5.2 Sample Details

Gd-Y superlattices were grown on $(11\bar{2}0)$ sapphire (Al_2O_3) using a molecular beam epitaxy (MBE) system with a base pressure of 4×10^{-11} Torr. A Nb buffer and Y

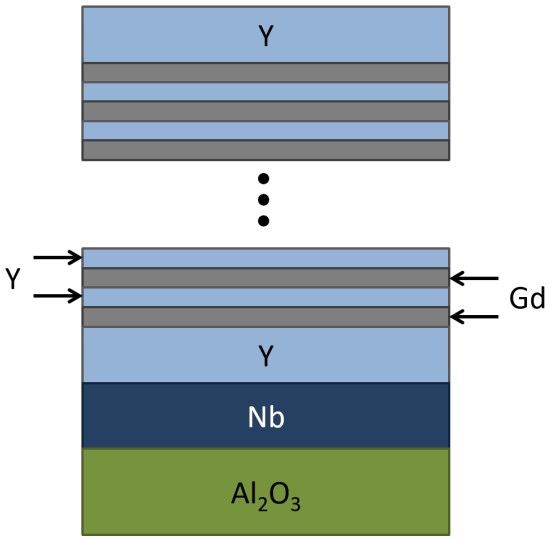

Figure 5.1: A schematic of the Gd-Y superlattice sample structure. A Nb buffer layer is grown on sapphire $(11\bar{2}0)$, followed by a thick Y slab before the superlattice. An Y capping layer is deposited at the end to protect the sample from oxidation.

seed layer were grown below the superlattice to ensure epitaxial growth of the Gd-Y bilayers [53]. A schematic of the sample structure is shown in Figure 5.1.

The Nb deposition was carried out using an e-beam source at a rate of 0.2 Å/s and the deposition rates for Gd and Y were 0.1 and 0.2 Å/s, respectively. The quality of the layers was studied in-situ using a reflection high-energy electron diffraction (RHEED) system; the Gd and Y displayed characteristic streak patterns, indicating good crystallinity with stepped surface profiles. The nominal thicknesses of the layers from the growth conditions are Nb(150 Å)/ Y(200 Å)/ $[$Gd(12 Å)/Y(12 Å)$]_{\times 10}$/ Gd(12 Å)/ Y(50 Å). With these thicknesses in the multilayer we would expect ferromagnetic coupling between the Gd layers, as predicted from RKKY calculations [153] and from previous experimental work [138].

Epitaxially grown Nb (110) on Al_2O_3 $(11\bar{2}0)$ has previously been shown to be coherent at the interface when the thickness of the Nb layer is below some critical value, i.e. the Nb lattice is strained so that a perfect match with the substrate is achieved [154]. The lattice parameter of the Al_2O_3 is 2.392 Å and is close to that of the Nb, which is 2.334 Å resulting in a mismatch of $\sim 2\%$. Above the critical thickness value, however, stress at the interface due to the lattice mismatch leads to relaxation by the formation of misfit dislocations as illustrated in Figure 5.2(a). The interface becomes semi-coherent, with coherent regions in between the misfit dislocations [155]. The critical thickness is typically less than 10 ML; we therefore expect the thickness of the Nb layers in our samples to be above the critical value.

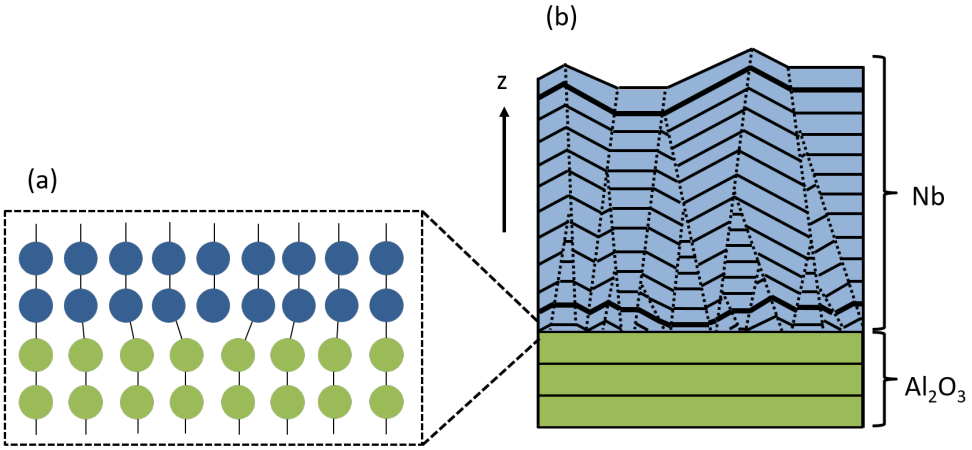

Figure 5.2: (a) Misfit strain between the Al_2O_3 and Nb layers is accommodated by the formation of misfit dislocations. Coherent regions exist between dislocations and a mosaic structure is created. (b) Model of a Nb epitaxial film with two orientational length scales indicated by the thicker black lines. As the film thickness is increased, crystal domains merge so that the roughness in the upper and lower parts of the layer is partially correlated. Adapted from [156].

The relaxation due to the formation of misfit dislocations results in the formation of crystal domains in the Nb which are orientated at slightly different angles to each other resulting in a mosaicity at the interface between the substrate and the Nb. The lateral domain size close to the interface is small but with increasing film thickness the domains merge as shown in Figure 5.2(b) [156]. In reflectivity studies this would appear as a roughness at the Nb-Al_2O_3 interface which is partially correlated with the roughness at the Nb-Y interface. It may even be expected that the crystal domains would influence the Gd-Y superlattice with correlations between interfaces extending throughout the multilayer.

The choice of growth temperature used to produce geometrically smooth and chemically sharp interfaces in the superlattice such that there is minimal interdiffusion, must give consideration to the balance between interdiffusion and mobility. At high temperatures, interdiffusion of the materials could lead to mixing at the interfaces reducing the chemical sharpness. At temperatures which are too low, however, mobility at the surface would not be sufficient to allow the atoms to find energetically favourable positions and form a smooth interface. Therefore, it is necessary to deposit Gd and Y layers at the lowest temperature possible to minimise interdiffusion whilst still maintaining good order.

Previous work has suggested that the optimal growth temperature of a superlattice is related to the melting temperature T_m of the materials with an upper limit on the optimum temperature set at $3T_m/8$ and a lower limit as $T_m/8$ [157]. The melting temperature of Gd and Y are 1,314°C and 1,525°C respectively [158] suggesting an optimal growth temperature range of approximately 190°C to 500°C. It is also necessary to choose two materials which have similar melting points. Examples of Gd-Y superlattices which have been previously studied have been grown at 220°C, where they claim to minimise diffusion [53] and 250 ± 20°C is suggested in [140]. This chapter presents x-ray scattering data from Gd-Y superlattices grown at 280°C, 330°C and 400°C which are all within the suggested optimum temperature range.

5.3 Results

The structural properties of the Gd-Y superlattices are first investigated with x-ray diffraction and combined with additional x-ray reflectivity studies. The reflectivity is recorded using both a Cu $K_{\alpha 1}$ laboratory source and also using synchrotron radiation at the Gd L_3 resonant edge. The resonant data was used to extract both the chemical and magnetic structure of the superlattices as a function of z. The chapter then looks at MOKE magnetometry and compares this to the reflectivity measurements.

5.3.1 XRD

Samples were characterised by x-ray diffraction using a Philips PW1820 diffractometer, with a Bragg-Brentano geometry and Cu $K_{\alpha 1}$ radiation ($\lambda = 1.54018$ Å). The diffraction data is shown in Figure 5.3. The main peak at $2\theta \simeq 31°$ (as marked by a dashed line in Figure 5.3) corresponds to a lattice parameter of 5.73 Å which is approximately the c axis lattice parameter of Gd and Y. There are no observable fringes around the main peak which would correspond to the total thickness for any of the samples, and is indicative of substrate roughness. Previous work on the growth of Nb on Al_2O_3 suggests that this roughness most likely results from stress relaxation in the Nb film leading to misfit dislocations at the interface [159]. The peak at 38° (marked by a dashed line in Figure 5.3) corresponds to a lattice parameter of 4.75 Å from the Al_2O_3 substrate.

The fringes with periodicity of approximately 1.2° which are marked by the arrows in Figure 5.3, are a result of the total thickness of the Nb buffer layer, and show this layer to have a thickness of 70 Å. This is much thinner than expected from the growth conditions but is confirmed later using fits to reflectivity data. The

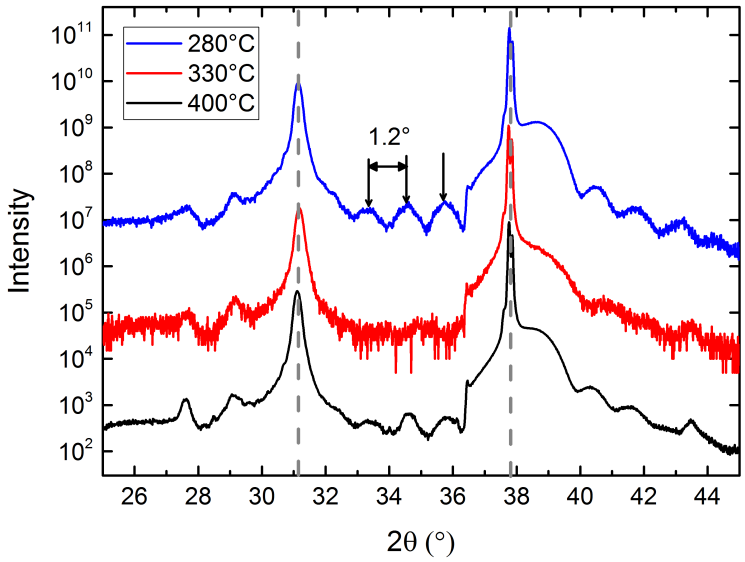

Figure 5.3: X-ray diffraction pattern ($CuK_{\alpha 1}$ radiation) for three samples having different superlattice growth temperature. The bilayer thickness in both is 5 ML Gd and 5 ML Y. The main peak is the (002) diffraction from the superlattice structure. Satellite peaks are visible left and right of the (002) peak, arising from the chemical repetition inside the superlattice structure. (Data sets are offset vertically.)

Nb fringes are not clearly observed in the data for the sample grown at 330°C, this most likely due to high roughness at the interface between the substrate and Nb buffer layer. The Bragg peak from the multi-layer is still clearly visible in the data for the sample grown at 330°C showing that the multi-layer is unaffected. The XRD data recorded for the sample grown at 330°C is noisier than those at the other temperatures. To determine whether the noise and loss of definition in the Nb peaks is a consequence of experimental conditions or truly reflective of roughness at the substrate/Nb buffer interface this data would need to be re-recorded. Without further studies which reproduce these results, some uncertainty remains around our conclusions regarding the roughness at the substrate/Nb buffer interface for the sample grown at 330°C.

Rocking curves were used to investigate the effects of misfit dislocations and the resulting structure at the interface between the substrate and the Nb. To record a rocking curve, the detector is set at a specific Bragg angle and the sample is tilted as illustrated in Figure 5.4(left). Defects like mosaicity, dislocations and curvature distort the atomic planes such that they are no longer parallel and this is observed as broadening of the peak. The rocking curves recorded for the samples grown at 440°C, 330°C and 280 °C are shown in Figure 5.4(right), and are normalised for an

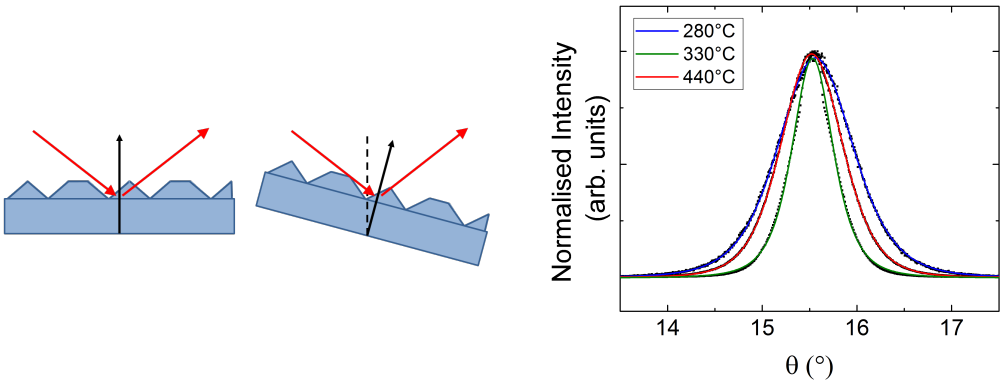

Figure 5.4: (left) Illustration of scattering geometry showing how a sample is tilted to record a rocking curve. (right) Resulting rocking curve data from Gd-Y superlattices grown with different substrate temperatures.

easier comparison of the peak widths.

The peaks in Figure 5.4(right) are fitted using a Pearson VII function to obtain the full width at half maximum, w. The width of the peak is directly related to the crystal mosaicity and the values of w found from the fits are given in Table 5.1. w is smallest for the sample grown at 330°C, the middle of the three temperatures, which shows that the mosaic spread is smallest for this sample. The middle growth temperature therefore produces the sample with the least mosaicity at the interface between the substrate and Nb layer despite there being a high roughness at this interface shown by the XRD in Figure 5.3. These findings suggest that the sample grown at the middle temperature of the three perhaps has more interdiffusion leading to high roughness, but then does not form the semi-coherent interface as a result of misfit dislocations to the same extent.

Growth Temperature	280°C	330°C	400°C
w	0.765 ± 0.001°	0.5140 ± 0.0003°	0.935 ± 0.002°

Table 5.1: Peak widths of the rocking curves recorded for Gd-Y superlattices grown with substrate temperatures of 280°C, 330°C and 400°C.

5.3.2 X-ray Reflectivity

XRD allowed predictions to be made about the sample structure and quality, but to probe the structure of the samples as a function of z we must turn to reflectivity. Before the experimental data is presented, a *simulated* x-ray reflectivity profile was generated to highlight some of the expected features. The simulated x-ray reflectiv-

ity profile was generated assuming x-rays with a wavelength of $\lambda = 1.54$ Å which is that of a Cu $K_{\alpha 1}$ laboratory source and it was produced using the nominal structure from the growth conditions. The simulation is shown in Figure 5.5(a), with the corresponding scattering length density (SLD) profile in Figure 5.5(b). The roughnesses between all layers in the modelled structure were set to be low (1 Å).

The simulated profile shows fringes which arise from the total thickness and have separation 0.01 $Å^{-1}$ which are marked in Figure 5.5(a). These fringes correspond to a layer thickness of 630 Å, the total thickness of the modelled sample. Fringes from the Nb layer with separation 0.04 $Å^{-1}$ are also marked in Figure 5.5(a) and correspond to a layer thickness of 150 Å. The fringes from the Nb layer are well defined even to high q_z because of the large difference in the scattering length density between Nb and the other elements in the multilayer and also due to the low roughness between the Nb and neighbouring layers.

At $q_z = 0.27$ $Å^{-1}$, as marked in Figure 5.5 by a dashed line, there is a peak which is due to the repeating Gd-Y bilayer, which corresponds to a layer thickness of approximately 23 Å, the total thickness of the repeating bilayer. The peak is

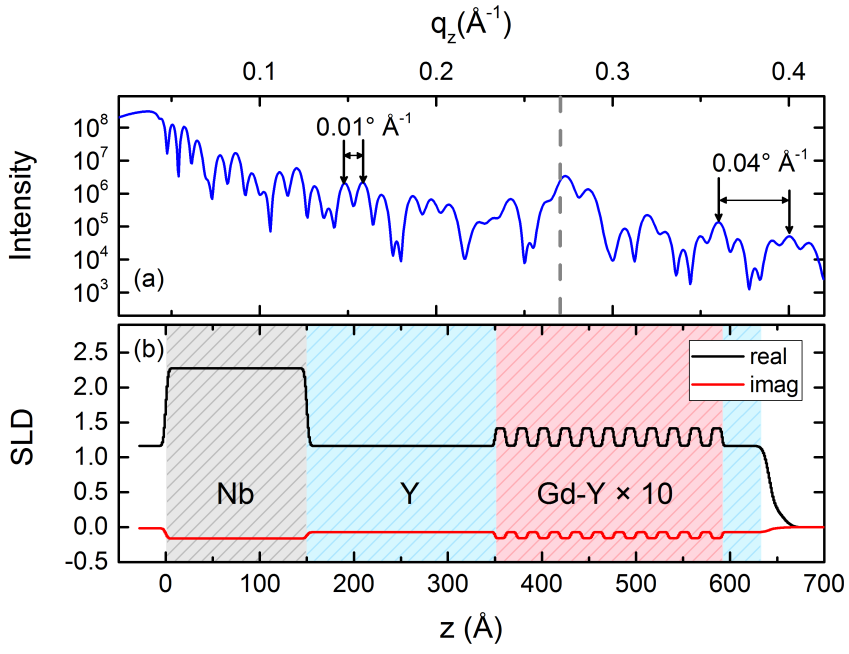

Figure 5.5: Simulated reflectivity spectrum (a) and SLD profile (b) generated using nominal structure comprising a 150 Å Nb buffer layer, a 200 Å Y seed layer followed by a 10× [Gd(11.5 Å)/Y(11.5 Å)] and finally a 50 Å Y capping layer. Layer roughnesses are 1 Å and an oxide is included at the surface. The simulation was produced with a wavelength of 1.54 Å.

not well defined due to the relatively small difference in scattering length density between Gd and Y. Even with low roughness between layers in the multilayer (1 Å) as used in this simulated data, there is not a well defined peak. With a larger roughness between these layers, as will likely be the case with real samples, this definition will only get worse.

Sometimes it is possible to increase the contrast between layers in the SLD profile by tuning to an absorption edge and changing the resonant scattering factors of certain layers. For example it might be expected that by tuning to the Gd L_3 edge, we would change the scattering factors of the Gd only and so increase the contrast between the Gd and Y in the multilayer thus making the Bragg peak in the data more apparent. It is unfortunate, however, from looking at the tables of scattering factors [100] that tuning to the Gd L_3 edge actually makes this definition worse. We are still able to obtain resonant scattering data and use it to extract the chemical and magnetic profiles, but we would expect the Bragg peak from the repeating bi-layer to be difficult to distinguish in the specular data.

5.3.3 Resonant Structural Studies

The chemical and magnetic structure of the Gd-Y superlattices were studied using resonant x-ray scattering tuned to just below the Gd L_3 edge (7.243 keV) on beamline BM28 (XMaS) at the ERSF, Grenoble. Additionally non-resonant reflectivity data was recorded with a Cu $K_{\alpha 1}$ laboratory x-ray source for the same samples to allow simultaneous fitting of the data at multiple energies which would give greater confidence in the fit.

It is expected that changing the growth temperature will change the structure of the interfaces in the superlattice. This change could be due to the buffer layer and substrate interface relaxing, forming a mosaic structure which then propagates through the multilayer. If this is the case, the multilayer interfaces would follow the same structure as the substrate interface and would be correlated. Correlated roughness can be observed by measuring off-specular reflectivity scans.

The roughness of an interface can be characterised as a function of lateral position R using a height-height correlation function given as $C(R) = \sigma^2 \exp\left(-[R/\zeta]^{2h}\right)$ where σ is the rms value of the surface roughness, h is a roughness exponent and ζ is a roughness correlation length. The scattering cross section for the diffuse scattering is dependent on this height-height correlation function and as such off-specular scans are sensitive to the in-plane variations in a surface and any correlations between surfaces in a multilayer. The mathematical expressions associated with this will not be presented here but can be found in [160, 161].

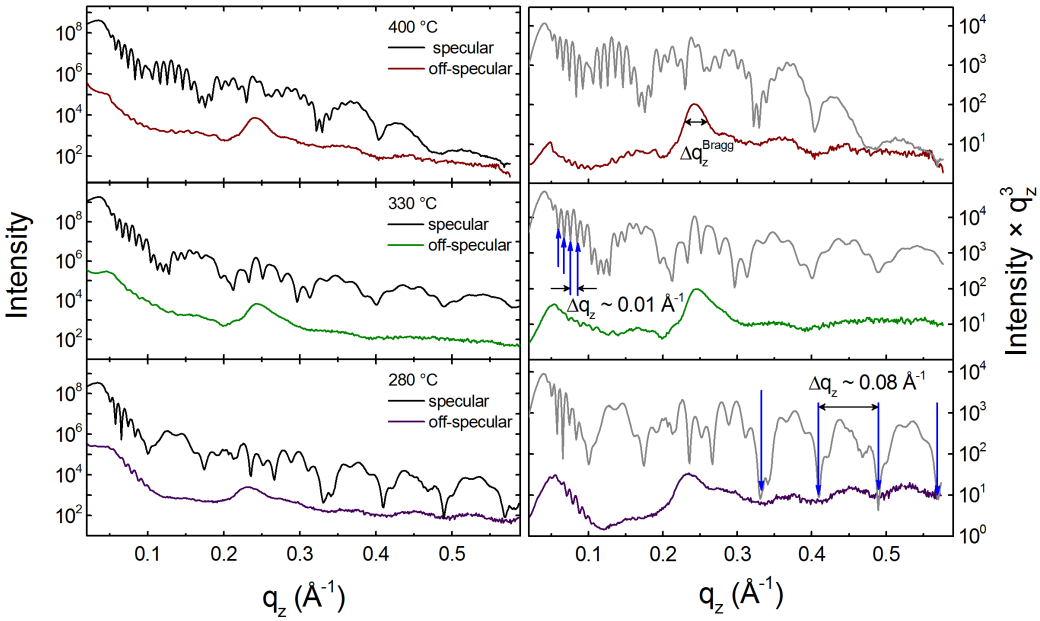

Figure 5.6: Specular and off-specular reflectivity scans recorded at the Gd L_3 edge for samples with multi-layers grown at 400 °C, 330 °C and 280 °C. (left) are the scans as recorded and (right) are the same scans multiplied by q_z^3 for the purposes of making the features easier to see.

Figure 5.6 shows the specular and off-specular reflectivity data for the Gd-Y superlattices where the multi-layer was grown with the substrate held at three different temperatures 400 °C, 330 °C and 280 °C. To highlight the features in the data, the right hand side of Figure 5.6 shows the data multiplied by q_z^3. Without fitting the data, some initial observations can be made. As in the simulated data, there are narrow fringes in all 3 sets of data with a periodicity of approximately 0.01 Å^{-1} corresponding to a layer thickness of 630 Å which is the total thickness of the sample. The fringes become less defined at higher q_z which is an indication of roughness between layers. The fringes extending over the whole q_z range with periodicity of approximately 0.08 Å^{-1} correspond to a layer thickness of 80 Å and are from the Nb layer which is approximately half the thickness predicted by the growth conditions. This supports the XRD data, which also found the Nb layer thickness to be much lower than expected. The features in both the specular and off-specular at approximately 0.25 Å^{-1} are Bragg peaks due to the repeating bi-layer.

The existence of the Bragg peak in the off-specular data indicates that the interfaces between layers in the multi-layer are correlated in the z direction and vari-

ations at the interface between the Gd and Y layers are dependent on the variations in lower layers. The correlated roughness most likely originates from the mosaic structure formed due to the misfit dislocations at the substrate/ Nb buffer interface. This mosaic structure propagates through the Nb buffer and Y seed layers and is then inherited by the Gd-Y multi-layer. The schematic in Figure 5.7 illustrates how this correlated roughness may propagate through all the layers as in (a), or there may be a partially correlated structure whereby the interfaces are sensitive to those above and below but the interface structure does not propagate through the whole of the multi-layer as in (b). For comparison, Figure 5.7 (c) shows a system where the roughness between layers has no correlation.

The extent of the out-of-plane correlation between the interfaces through the multi-layer can be estimated from the width of the Bragg peak in the off-specular data. The Bragg peaks from the off-specular data in Figure 5.6 for each sample were fitted with a Gaussian and the width of the peak found. The width of the Bragg peaks are 0.021 ± 0.001 Å^{-1}, 0.022 ± 0.001 Å^{-1} and 0.028 ± 0.001 Å^{-1} for the samples with the multi-layer grown at 400°C, 330°C and 280°C respectively. These peak widths correspond to out-of-plane correlation lengths of 300 ± 10 Å, 290 ± 10 Å and 224 ± 8 Å. The total thickness of the multi-layer is nominally about 240 Å which suggests that the roughness in the multi-layer is correlated throughout the entire thickness for the samples grown at 400°C and 330°C but there is only a partial correlation for the sample grown at 280°C. The sample grown at the lowest temperature has a partially correlated structure where variations in the interfaces follow those directly below but this is gradually lost over the total thickness of the multi-layer. Additionally, the other fringes both from the total sample thickness and from the Nb buffer layer seen in the off-specular suggest that there is a correlated roughness between the substrate and the buffer layers.

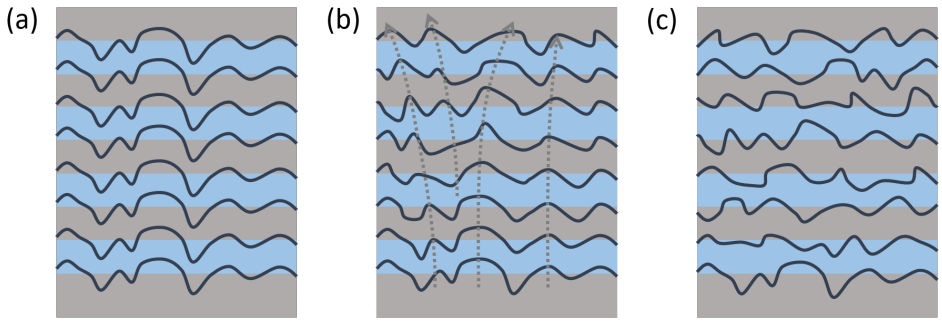

Figure 5.7: Schematic illustrations of (a) correlated roughness, (b) partially correlated roughness (with arrows to guide the eye) and (c) uncorrelated roughness.

5.3.4 Resonant Magnetic Scattering

XRMS data recorded at the Gd L_3 edge were fitted, both the sum and asymmetry ratio (A.R.), at a range of temperatures. This section will now present fits to the data and compare the SLD profiles for the samples grown with different substrate temperatures. To give confidence in the fits, reflectivity measured using a Cu $K_{\alpha 1}$ laboratory source were included and fitted simultaneously. The reflectivity data and fits are shown in Figures 5.8, 5.9 and 5.10 for the samples grown at 400 °C, 330 °C and 280 °C respectively.

Looking first at Figure 5.8(a), the reflectivity recorded using a Cu $K_{\alpha 1}$ laboratory source is shown for the sample grown with the substrate held at 400 °C, we see that many of the features are not well defined, particularly the Bragg peak from the multilayer, which is difficult to distinguish from other features. Indeed the SLD profile in Figure 5.8(b) indicates that there is very little definition between the individual Y and Gd layers in the multilayer. There is strong contrast from the Nb buffer layer, however, as expected from the simulated profiles. The fringes caused by the Nb layer lose definition at high q_z and the shape becomes slightly distorted. To achieve a suitable fit to the data, an extra layer was inserted into the model between the substrate and the Nb layer. This could be a strained layer or a region of intermixing but was found to be needed to give the Nb fringe shapes at high q_z.

Figure 5.8(c) and (d) then show the specular and off-specular reflectivity recorded at the Gd L_3 edge and the resulting SLD profile. The reflectivity data was recorded by measuring the sum of the two helicities of circularly polarised x-rays. The fits to the data require the layers in the superlattice to have a high roughness. The lower parts of Figure 5.8(c) and (d) show the asymmetry ratios recorded at 50 K, 150 K and 180 K and the resulting magnetic SLD profile at 50 K only. The data at 150 K and 180 K were fitted by only changing the magnetic moment from the fit at 50 K whilst all other parameters were kept the same.

As indicated by the XRD data and the off-specular reflectivity there is correlated roughness in the multilayer. It follows that the high roughness in the simulated SLD profiles and the evidence that this roughness is correlated demonstrates that there is most likely a mosaic structure which propagates through the multilayer. It is not possible with reflectivity to distinguish between chemical intermixing and surface variations. In the models here, the high roughness is of the same order as the layer thickness which is accounted for by using the slicing model which was discussed in Chapter 4. The slicing model prevents unphysical discontinuities in the SLD profile when the layer roughness approaches the layer thickness.

The same data is presented for the sample grown with the substrate held at

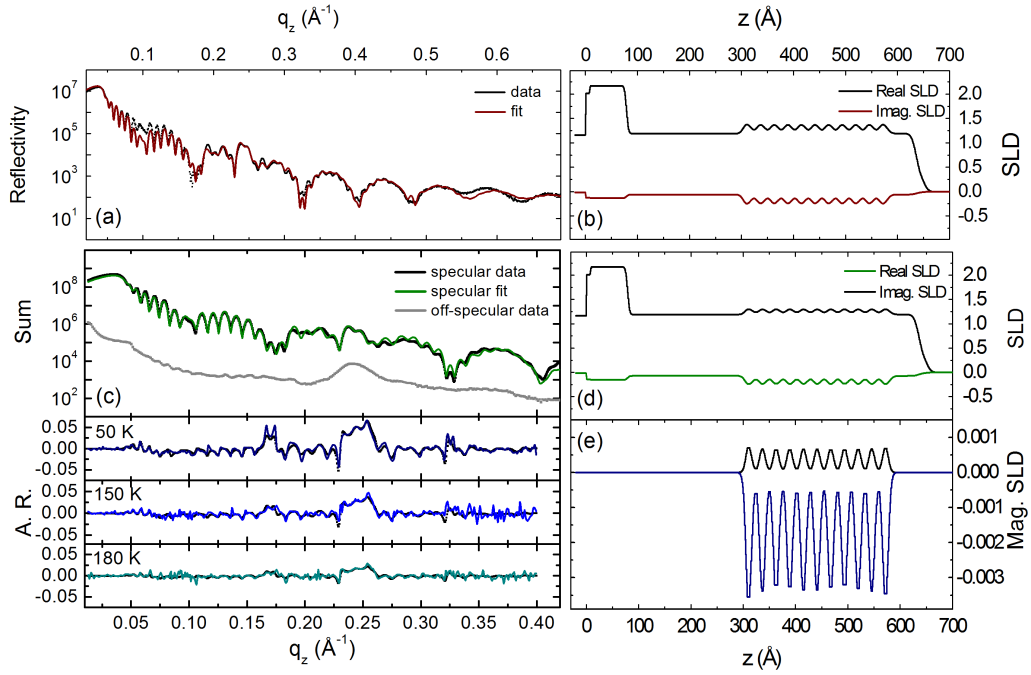

Figure 5.8: Reflectivity data for the sample grown at 400°C. (a) Specular reflectivity data (points) and fit (line) measured at using a Cu $K_{\alpha 1}$ laboratory source and (b) the SLD profile obtained from the GenX fit. (c)(upper) Specular reflectivity data (black points) and fit (line) and off-specular reflectivity data (grey points) recorded at the Gd L_3 edge. (c)(lower) asymmetry ratio recorded at the Gd L_3 edge at 50 K, 150 K and 180 K. (d) SLD and (e) magnetic SLD profiles obtained from GenX fits to the XRMS data.

330°C in Figure 5.9 and at 280°C in Figure 5.10. In each, only the magnetic SLD recorded at 50 K is shown. As the growth temperature decreases, the roughness between layers in the multilayer increases. This is not directly introduced in the roughness parameter in GenX but as a combination of thickness and roughness, and it was modelled using the bilayer thickness as a fitting parameter to fix the Bragg peak position. The roughness is included in GenX as a Gaussian error function, and although this is often very accurate at modelling the shape of an interface it does sometimes fall short, reasons for which were given in Chapter 4. When modelling the Gd-Y superlattice here, by changing the thickness of the Gd whilst keeping the bilayer total thickness the same, it allows the fit to have more freedom to change the shape of the SLD profile through the multilayer whilst locking in the position of the Bragg peak.

The SLD profiles in Figures 5.8-5.10 are not easily comparable in separate figures so these are shown for the superlattice only in Figure 5.11. It is clear in this

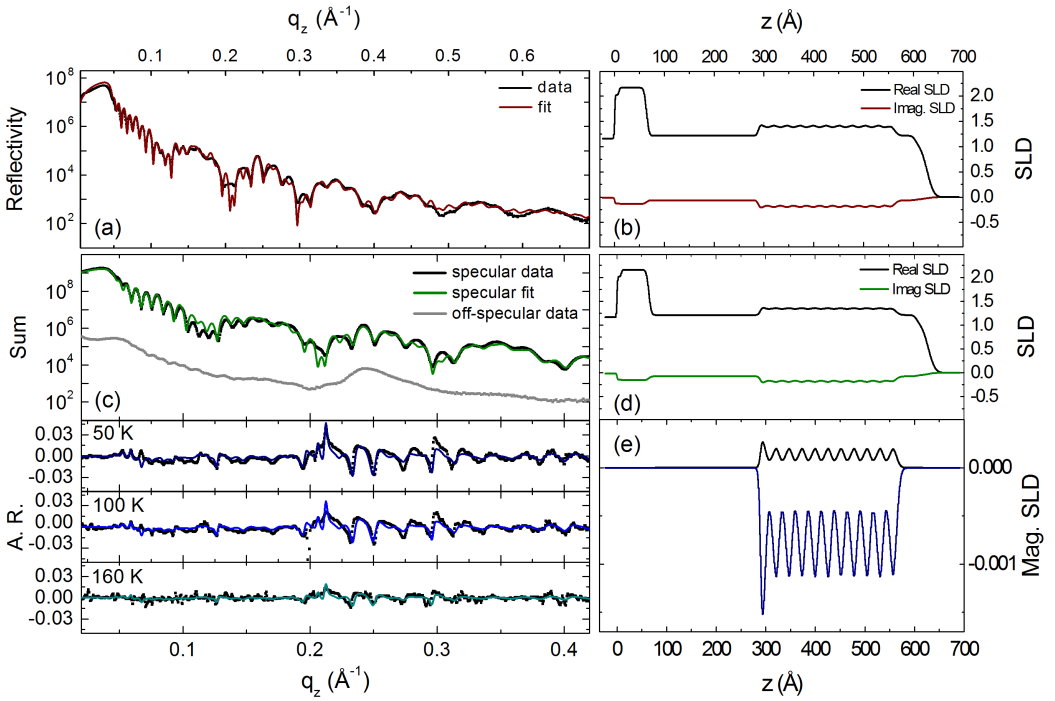

Figure 5.9: Reflectivity data for the sample grown at 330°C. (a) Specular reflectivity data (points) and fit (line) measured at using a Cu $K_{\alpha 1}$ laboratory source and (b) the SLD profile obtained from the GenX fit. (c)(upper) Specular reflectivity data (black points) and fit (line) and off-specular reflectivity data (grey points) recorded at the Gd L_3 edge. (c)(lower) asymmetry ratio recorded at the Gd L_3 edge at 50 K, 150 K and 180 K. (d) SLD and (e) magnetic SLD profiles obtained from GenX fits to the XRMS data.

figure that decreasing the growth temperature results in the whole multilayer having a higher average SLD value. In fact, the reflectivity data for the samples grown at 330°C and 280°C have features that correspond to the total thickness of the Gd-Y superlattice, which is caused by the multilayer appearing more like a single layer due to this rise in average SLD value. The SLD profile for the sample grown at 330°C has the least well defined individual layers throughout the superlattice and this sample also had high substrate roughness but low mosaicity from the XRD data.

The total increase in SLD value across the superlattice was modelled by allowing the resonant correction to the Gd scattering factors to vary slightly and allowing the roughness to go higher than the layer thickness. This resulted in the SLD throughout the multilayer as a whole to be higher with less definition between the Gd and Y. Note that the increase in SLD value of the bottom layer in the Gd-Y

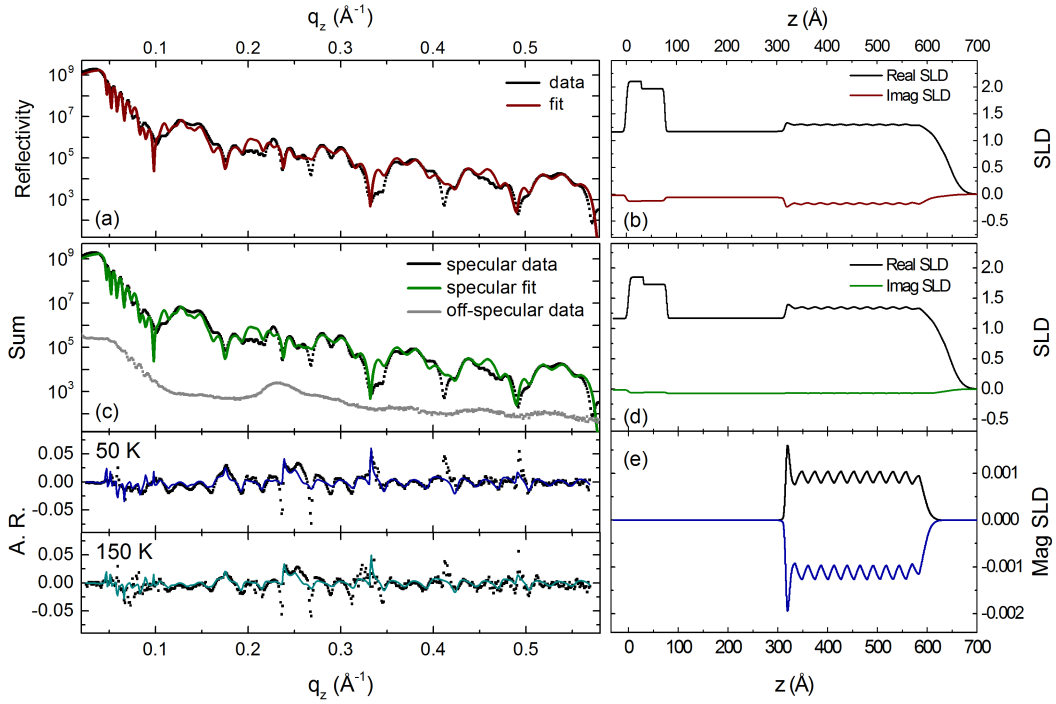

Figure 5.10: Reflectivity data for the sample grown at 280°C. (a) Specular reflectivity data (points) and fit (line) measured at using a Cu $K_{\alpha 1}$ laboratory source and (b) the SLD profile obtained from the GenX fit. (c)(upper) Specular reflectivity data (black points) and fit (line) and off-specular reflectivity data (grey points) recorded at the Gd L_3 edge. (c)(lower) asymmetry ratio recorded at the Gd L_3 edge at 50 K, 150 K and 180 K. (d) SLD and (e) magnetic SLD profiles obtained from GenX fits to the XRMS data.

superlattice is due to the Y seed layer having a low roughness compared to the Y in the multilayer, and is just an artefact of the slicing model within GenX. The fit is not particularly sensitive to the SLD value of this lowermost layer but it is sensitive to the interface roughness between the Y seed layer and the bottom of the superlattice.

It would generally be expected that the Gd scattering factors would be the same for all three samples as the measurements were taken with the same energy x-rays. It is unlikely that the energy of the x-rays drifted enough during the experiment to cause such a large change in scattering factor, although, near an absorption edge small changes in energy could result in large changes to the scattering factors. It is possible that the higher roughness at the interfaces could lead to more contact between Gd and Y atoms in the multilayer. The scattering factors of atoms are highly dependent on their local environment [162] and intermixing of Gd and Y

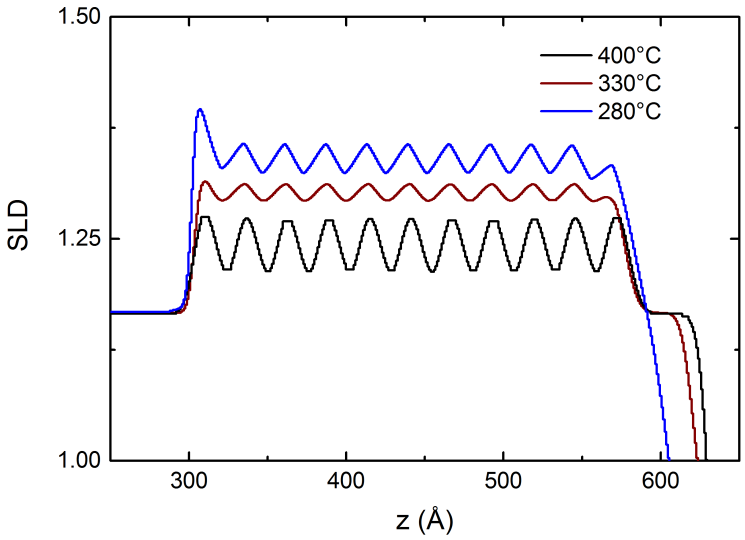

Figure 5.11: Sections of SLD profiles obtained from fits to reflectivity data for Gd-Y superlattices grown at different temperatures. The Y seed layer had different thicknesses in the three samples so these are shifted in z to show the multilayer in the same place for comparison.

could be the cause of the change in scattering factor. Alternatively, as the total SLD is the product of density and scattering factor, it could be that the density of the Gd is higher in those samples grown at lower temperatures, but the model has incorporated this as a change to the scattering factors.

The raise in SLD across the whole multilayer seen in Figure 5.11 can be explained when we consider that these layers of Gd and Y are only approximately 5 monolayers thick. The SLD profile can be modelled by taking slices through the sample as a function of z. When there are only small variations at the interface between the layers as in Figure 5.12(a), it is possible to take slices which allow the individual layers to be discerned. For example, in Figure 5.12, slice (1a) cuts through a section which is entirely composed of Y and (3a) is entirely Gd. This leads to an SLD profile with good definition between layers in the multilayer with both the Y and Gd having SLD values closer to the bulk values. There are still small variations at the interface, however, and slice (2a) probes a mixture of Y and Gd. As the variations across the interface increase, it is no longer possible to take slices of the same thickness which only contain Y or Gd, as illustrated in Figure 5.12(b). Instead each slice will contain a mixture of the two leading to an SLD value which is a combination of both; this results in the SLD profile appearing less well defined throughout the multilayer, even though on atomic length scales there are still clearly distinct layers of Gd and Y.

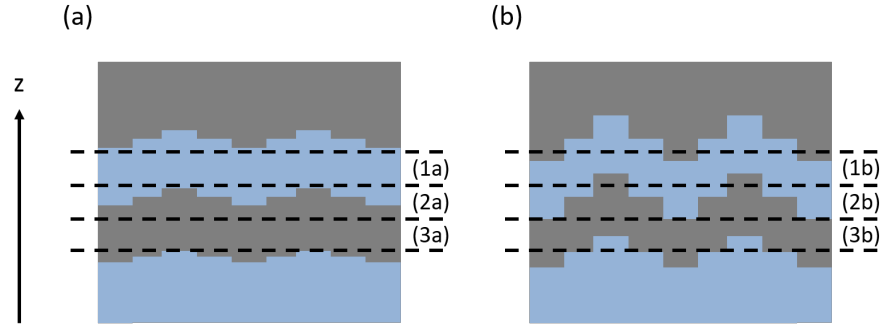

Figure 5.12: Schematic illustrations of how interface variations could lead to fitted SLD profiles obtained from GenX fits. (a) shows small variations and how taking slices in z allows distinct layers to be probed whereas in (b) the increased interface variations mean that slices will take both Gd (grey) and Y (blue) into the total SLD value of that slice.

The increased interface variations observed in the chemical SLD profiles are echoed in the magnetic SLD profiles. For the samples grown at lower temperatures, there is less definition between layers in the magnetic SLD across the superlattice and there is a reduction in the magnetic SLD value. This is particularly clear in the imaginary part. The next question is whether this loss of definition between layers and the reduction in magnetic SLD value can be explored further using magnetometry such as MOKE and whether comparisons can be made between this and the XRMS data.

5.3.5 Magnetometry

Thus far, x-ray reflectivity has been presented showing a decrease in interface roughness as the growth temperature was increased. Similarly, the magnetic SLD profile has revealed an increase in roughness between layers as the growth temperature is decreased such that the multilayer no longer appears to be a series of magnetic/non-magnetic layers but instead as one magnetic layer with deviations across it. It would therefore be useful to compare the findings from the magnetic reflectivity results with a complementary technique such as MOKE. This section will give MOKE magnetisation as a function of temperature for each of the samples grown at different temperatures and compare these to values from the fitted reflectivity data.

MOKE

Magnetic hysteresis loops were recorded for each of the three samples using MOKE, as a function of temperature. Selected hysteresis loops are shown in Figure 5.13 as a function of temperature for the sample grown at 280°C to illustrate the changing shape and coercivity of the loops as a function of temperature. The hysteresis loops at low temperature exhibit a more rounded shape and higher coercivity. As the temperature is increased, the shape becomes more square, and the coercivity decreases. Additionally, as the temperature is increased, the saturation magnetisation also increases showing that the magnetic structure is changing in such a way that the total in-plane component of the magnetisation becomes larger. At temperatures approaching T_C, the more square shape is maintained and the lower coercivity value, whilst the saturation magnetisation decreases.

Matlab scripts were used to extract the saturation and remanent magnetisation as a function of temperature from hysteresis loops recorded for all three Gd-Y superlattice samples and the normalised values are shown in Figure 5.14. Both the remanent and saturation magnetisation are shown, given as M_r and M_s respectively. The data sets are normalised to the value of M_s at 50 K to allow a comparison to the XRMS data in Figure 5.15. The values of both M_s and M_r decrease at low temperatures suggesting that there is a mechanism which acts to reduce the total in-plane magnetisation. The data for the saturation magnetisation shows a tail at temperatures just above T_C which is typical of a magnetisation curve as a function

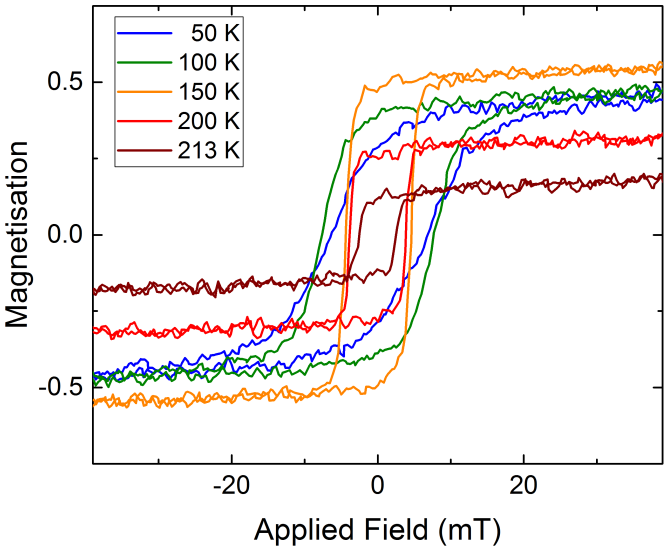

Figure 5.13: Hysteresis loops recorded from a Gd-Y superlattice grown at 280°C using MOKE as a function of temperature.

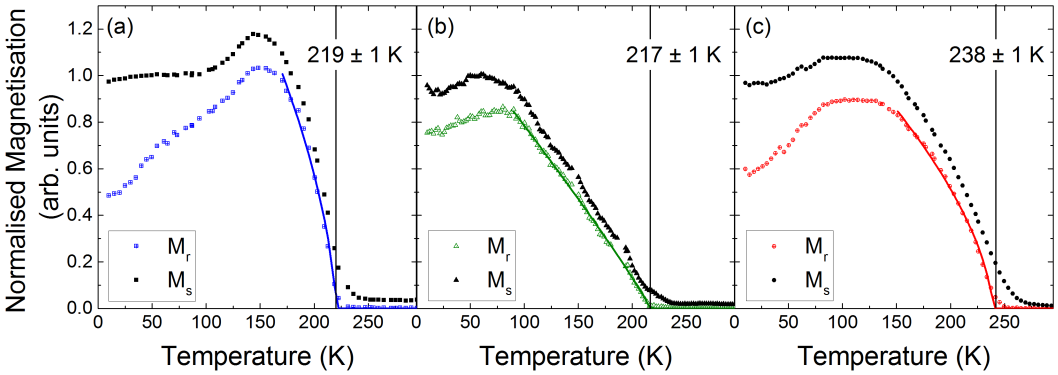

Figure 5.14: MOKE measurements of the magnetisation as a function of temperature for Gd-Y superlattices grown with substrate temperatures of (a) 280°C, (b) 330°C and (c) 400°C. All curves are normalised to the saturation magnetisation at 50 K. The solid lines were fitted to the data using a Curie-Weiss formula and are only fitted for the upper portion of the curve.

of temperature for a sample in an applied field. As such the ordering temperatures were found from the M_r curves and are marked in Figure 5.14.

A decrease in magnetisation at low temperatures has been previously observed in Gd-Y superlattices with the Gd layers ordered anti-ferromagnetically where it was attributed to slight canting of the Gd moments resulting in a net reduction of the magnetic moment [138]. Other work with ferromagnetically aligned layers has shown this reduction in average magnetic moment to be consistent with a reduction in the projected moment near the interfaces between the Gd and Y [163]. Unfortunately, the high roughness in the superlattice of the samples studied here makes it difficult to investigate whether this is the case, but the reduction we see could very well be due to a rotation of the moments at the interfaces leading to a decrease in the projected moment. The decrease in magnetisation observed at low temperatures occurs as the maximum applied field used to perform the MOKE experiments was not large enough to fully saturate the sample. If the sample was fully saturated then all moments would point in the direction of the applied field and there would be no canting.

The shape of the magnetisation curves as a function of temperature in Figure 5.14 are not well described by a Curie-Weiss law, which would be expected if the samples could be described by mean-field theory in a bulk magnetic material. The deviation from mean-field theory reveals that there are additional mechanisms at work in the Gd-Y superlattices. The superlattices are constructed of very thin layers, and as such there are surface effects which change the exchange interactions at the surface and it is no longer correct to describe the curve with an ordering

exponent β, but instead by an effective ordering exponent β_{eff} which will not typically take a value from mean-field theory [40]. Due to edge effects, the values of β_{eff} would be expected to be larger than observed in bulk materials.

In order to facilitate a comparison to the XRMS data, the curves (solid lines) in Figure 5.14 were fitted with a Curie-Weiss formula for only the upper sections which were approaching T_C. No constraints were set on the effective critical exponent in each case and were found to be $\beta_{eff} = 0.60\pm0.03$, 0.92 ± 0.02 and 0.62 ± 0.02 for the samples grown at 280°C, 330°C and 400°C respectively. The ordering temperatures indicated in Figure 5.14 were obtained from the fits. The values of β_{eff} found are all larger than would be expected in bulk Gd, suggesting that the interactions in the Gd layers are dominated by edge effects. The value of β_{eff} found for the sample grown at 330°C is nearly unity, which suggests that the structure of this sample is different from the others and has consequently altered the magnetic interactions. Perhaps the high substrate roughness observed in the XRD data for this sample propagates through to the multilayer; this could result in less distinct individual magnetic layers and instead the superlattice acts more as a dilute alloy with weakly interacting moments. This theory would fit with the SLD profiles in Figure 5.11 where the sample grown at 330°C shows less clearly defined layers throughout the superlattice.

The ordering temperature is highest for the sample grown at the highest temperature, 400°C. From the data in Figure 5.14, it is also clear that the point at which the magnetisation starts to reduce as the temperature is decreased is different for the three samples. The reduction occurs first in the sample grown at 280°C at ∼150 K as can be seen in Figure 5.14(a). The sample grown at the highest temperature then has a decrease in magnetisation at ∼80 K and then lastly the sample with the middle growth temperature decreases at ∼50 K.

Alloys of Gd-Y have been found to have ferromagnetic or helimagnetic configurations depending on the composition [164]. It is possible that mixing at the interfaces forms regions of Gd-Y alloys. These alloys may result in a rotation of the magnetic moments and lead to different shaped magnetisation versus temperature plots and different canting temperatures. This theory would fit with the XRMS fits that suggest there are less distinct individual layers across the multilayer in the sample grown at the middle temperature, as seen in Figure 5.11. Alloys of Gd-Y have been shown to have increasing ordering temperatures as the Gd content increases [165]. If the sample grown at the lowest temperature has more mixing of Gd with Y, this could account for the higher ordering temperature.

XRMS

The fits to the asymmetry ratio presented earlier in this chapter used the total magnetic moment as a variable with the value of the magnetic moment set to 1 for the data recorded at 50 K. The normalised moment as a function of temperature is plotted in Figure 5.15 for the Gd-Y superlattices grown at (a) 280°C, (b) 330°C and (c) 400°C. Plotting the normalised magnetic moment obtained from the fit in this way is equivalent to plotting the normalised magnetisation. As the measurements are taken in an applied field, they show the saturation magnetisation, M_s. As such, a direct comparison cannot easily be made between the XRMS and MOKE data, but can be used to give some information on the temperature dependence observed using XRMS.

As there are only a very small number of data points for each of the samples recorded using XRMS, the solid lines in Figure 5.15 are included as a guide to the eye only. The solid lines were calculated using a Curie-Weiss law with the same value of β_{eff} and T_C as was found for the MOKE data. The fits found for the MOKE were only taken for the upper portion of the data due to the complex relationship between the magnetisation and temperature. The decrease in magnetisation at low temperature, however, is not observed for the XRMS data (even though there are only very few data points). The trend line was therefore allowed to extend over the whole range to provide a comparison, and appears to run very close to the data.

The resonant x-ray scattering technique used here is element specific, and as such only probes the magnetisation of the Gd, whereas the MOKE data measures

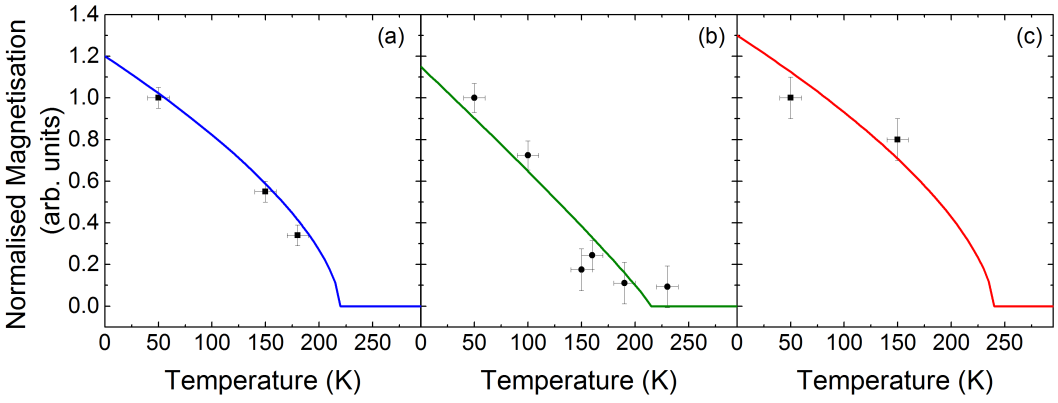

Figure 5.15: Magnetisation as a function of temperature for samples grown at (a) 280°C, (b) 330°C and (c) 400°C. The hysteresis loops are obtained by taking the value of the magnetic moment from the GenX fits normalised to the fit measured at 50 K. These are fitted with the function given in Equation 1.4 with $\beta = 0.33$ for all.

the total magnetisation. Both techniques are based on the same principle whereby the angular momentum of the incident radiation couples to the spin of the scattering medium, but the techniques use different wavelength radiation to achieve this. MOKE studies have a limited penetration depth of around 200 Å but this should mean that the magnetisation of the whole of the superlattice region of the samples would be measured. The x-ray energy is tuned to just below the Gd L_3 edge to avoid strong absorption effects to ensure the whole of the multilayer is measured. We can therefore conclude that both techniques record the signal from the whole of the superlattice.

SQUID magnetometry was also obtained from these samples and measured a similar reduction in magnetisation at low temperatures. A logical assumption would therefore be that the difference observed in shape of the magnetisation curves between the MOKE and the XRMS data is due to the element specificity of the x-ray scattering. If the differences in the curves are caused by XRMS being element specific, it suggests that the MOKE data is sensitive to a magnetic moment from an element other than Gd, i.e. an induced moment in the Y layers. It is possible that the Y moments rotate such that the net magnetisation is reduced but this is not measured by the XRMS.

Without further data, it is difficult to determine the cause of the discrepancy between the data sets recorded using MOKE and XRMS. It would therefore be ideal if the Y layers could be investigated further to get a better understanding of the interactions taking place throughout the superlattice, and record any induced polarisation in the Y. This could in principle be done by tuning to an Y resonant edge. The next section will present work undertaken to attempt to study the properties of Y in Gd-Y superlattices in more detail.

5.3.6 Addition of a Ho tagging layer

Studying the magnetic properties of the Gd was possible as the Gd L_3 edge is at 7.24 keV which is easily achievable on the XMaS beamline. To study the properties of Y, however, we would need to go to 2.08 keV which is outside the realistic operating energy range of most soft energy synchrotron beamlines. To address this issue, a thin layer of Ho was added as a 'tagging' layer with a sample structure as shown in Figure 5.16. Ho would normally be non-magnetic but when in contact with the polarised environment in the superlattice, it will develop a small moment through the spin-polarised conduction electrons. The Ho becomes polarised by the Y and therefore measurements of the magnetisation of the Ho act as a proxy measurement of the induced Y moment. Using the Ho as a tagging layer in this way means that

the magnetic properties of the Y can be indirectly studied by tuning to the Ho L_3 edge (8.05 keV).

Resonant reflectivity data was measured at both the Gd and Ho L_3 edges and are shown in Figure 5.17. The Bragg peak is clearly visible at roughly 0.06 $Å^{-1}$ in both data sets and so too are the fringes caused by the Nb layer. The data were fitted and are shown in Figure 5.17 along with the resulting chemical and magnetic SLD profiles. The roughness is high enough compared to the thickness of the Ho layer in the multilayer such that it is not possible to distinguish distinct layers of Ho. The presence of Ho, however, has an effect on the shape of the SLD profile of the layers throughout the superlattice, and there is a visible change in the structure between the data at the Gd and Ho edges.

There is a low signal to noise ratio in the Ho L_3 edge asymmetry ratio (shown in Figure 5.17(d)) and unfortunately it was not possible to fit this data as any features were obscured by noise. The feature at $q_z = 0.13$ $Å^{-1}$ is an artefact caused by the low signal. It occurs at a minimum in the sum signal leading to an amplification of noise at this point. Due to the weak magnetic signal, the chemical SLD is shown but not the magnetic SLD. The low signal to noise and very high roughness compared to the layer thickness makes it nearly impossible to study the magnetic behaviour of the Ho tagging layer itself. In future work, the aim would be

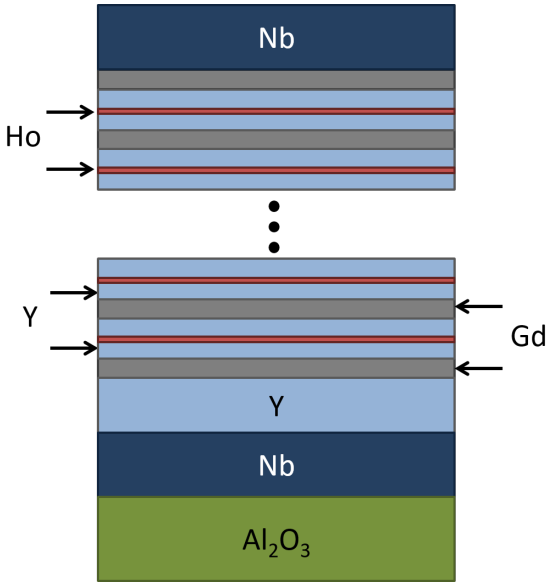

Figure 5.16: A schematic of the Gd-Y superlattice sample structure with Ho tagging layers. The structure is as before but with thin layers of Ho grown in the Y layers and a Nb capping layer rather than Y.

to grow samples with lower roughness between layers in the multilayer so that the magnetic behaviour of the Ho tagging layer could be investigated. It would also be useful to explore a way to improve the signal to noise ratio, maybe by counting for longer or taking repeated measurements.

Due to the low signal to noise ratio encountered when recording the asymmetry ratio at the Ho edge, it was not possible to get detailed layer-by-layer structural information about these samples. Hysteresis loops were recorded to investigate whether there was polarised Ho present and whether using Ho as a tagging layer could be a viable method of investigating the magnetic properties of Y in Gd-Y superlattices. The hysteresis loop measured at the Gd L_3 edge to confirm that the Gd was indeed magnetic and behaving as expected is shown in Figure 5.18(a). Hysteresis loops were then recorded for the same sample at the Ho L_3 edge. The signal to noise ratio was again very low so multiple loops were recorded at the same q value and averaged to provide the data shown as the solid line in Figure 5.18(b).

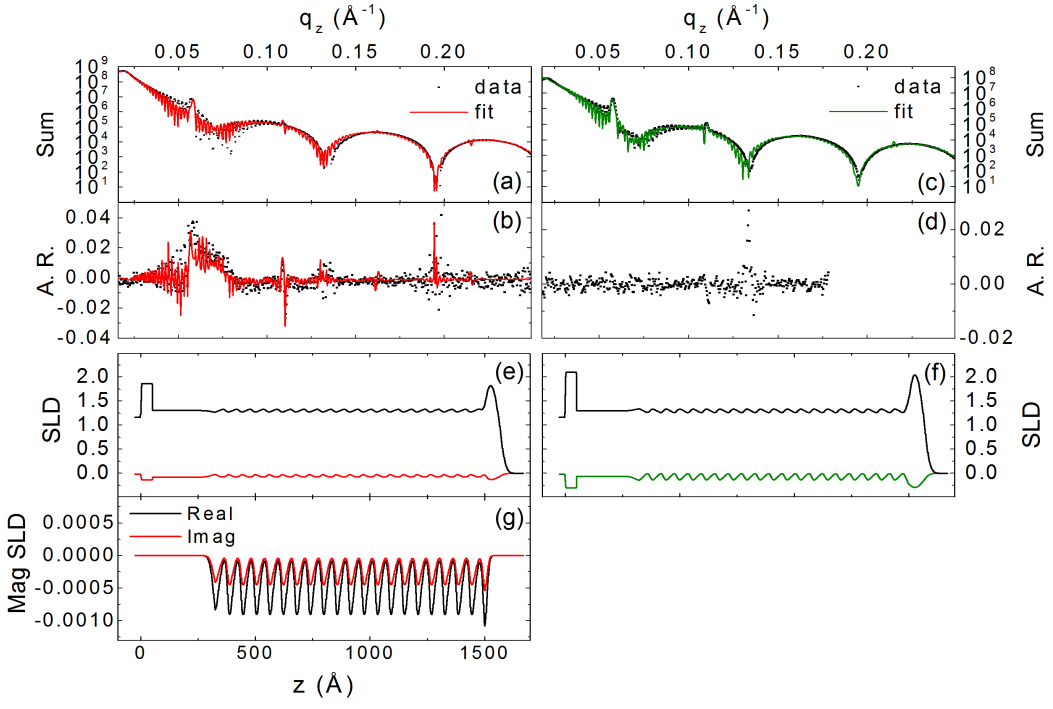

Figure 5.17: Specular reflectivity, sum and asymmetry ratio for superlattices grown with a Ho tagging layer. (a) and (b) are recorded at the Gd L_3 edge and (c) and (d) at the Ho L_3 edge. For each, the fit obtained using GenX is shown as a solid line. (e) and (f) are the chemical and (g) the magnetic part of the scattering length density.

The signal from the Ho is weak but there is clearly a magnetic response showing that both the Ho and Y are weakly polarised. Resonant magnetic x-ray scattering measurements at the Ho L_3 edge should therefore be possible if the signal to noise issue could be overcome.

The hysteresis loops were fitted using a modified Langevin function, details of which can be found in Chapter 4. As the Ho loop has a low signal to noise ratio, the loops measured at the Gd and Ho edges were fitted using the same shape parameter and coercivity to give confidence in the fit. It would be expected that these parameters be the same, as the Ho is only magnetic through proximity effects. The free fit obtained when the shape parameter and coercivity are not constrained is also shown in Figure 5.18(b) by the dashed line. The free fit indicates that the coercivity of the Ho is higher than that of the Gd.

The higher coercivity observed in the Ho hysteresis loops is possibly just due to the noise on the data but could potentially be indicating that there is pinning occuring in the superlattice which causes the Y magnetisation reversal to occur at a higher field value than the Gd. If there is canting of the moment as expected, this could provide a mechanism for pinning. Also, if the multilayer has a mosaic topography, the correlated variations in the layers could have a notable effect on the orientation of the magnetic spins at the interfaces and could provide a mechanism for the pinning of the Ho, similar to 'orange peel' coupling [166,167]. An alternative

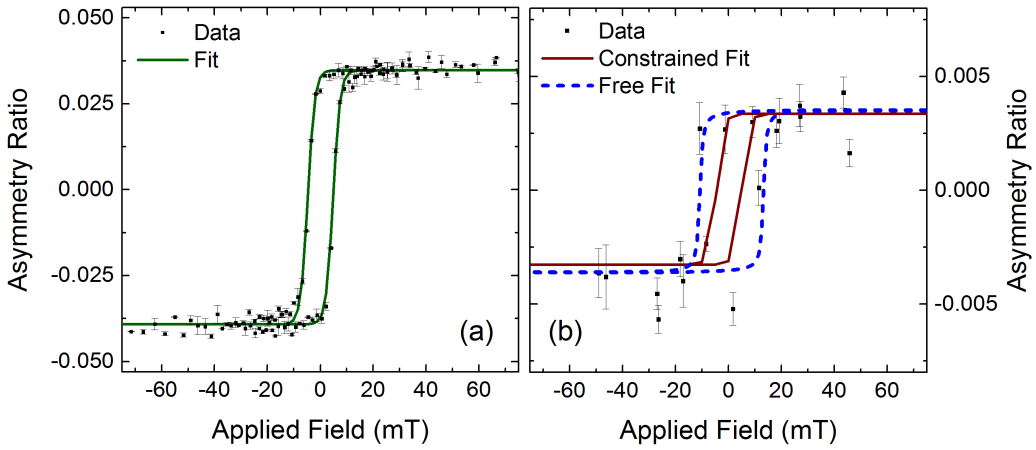

Figure 5.18: Hysteresis data (points) measured at (a) the Gd L_3 and (b) the Ho L_3 resonant edges. Both loops are fitted with a modified Langevin function with the same coercivity and shape parameter (solid line). The data at the Ho edge is also fitted without the parameters constrained (dashed line).

explanation to canting of the magnetic moments could be that there is intermixing of Gd and Y at the interface. Gd-Y alloys have been shown to have helical magnetic structures and so there is possibly some rotation of spins at the interfaces resulting in the pinning of the Y [168, 169].

This section has shown that using resonant x-ray magnetic scattering with the addition of a Ho tagging layer could potentially be used to measure the induced magnetisation in Y layers within a Gd-Y superlattice. This would be conditional on the signal to noise ratio being improved and growth of samples with lower roughness between layers. Hysteresis loops obtained at the Gd and Ho edges show different coercivities which hints at there being pinning of the Ho spins, possibly caused by correlated variations in the interfaces or by intermixing.

Conclusion

This chapter presented a study of the physical and magnetic properties of Gd-Y superlattices grown with different substrate temperatures. The effects of growth temperature on structure were investigated using x-ray diffraction which showed that the sample grown at the middle of the three temperatures had high substrate roughness but rocking curves showed this sample to have the lowest mosaicity. XRMS showed an increase in the average SLD value across the superlattice as the temperature was decreased but it is not possible to tell whether this is caused by interface variations or intermixing. The roughness in the multilayer was due to relaxation at the substrate/ Nb interface in the form of misfit dislocations resulting in a mosaic structure which was inherited by the upper layers. The roughness in the multilayer was echoed in the magnetic SLD and the profile across the superlattice no longer reached zero for the Y layers due to the high roughness. Additionally, with decreased growth temperature, there was a reduction in magnetic SLD value observed.

The sample grown at the middle of the three temperatures exhibited the highest roughness in the XRD data, and also the lowest mosaicity. Similarly, in the SLD profiles obtained from the XRMS reflectivity, the data from the sample grown at the middle temperature has the least well defined individual layers throughout the superlattice.

MOKE measurements were then presented giving the ordering temperatures for the three samples. The MOKE showed a reduction in moment at very low temperatures which was attributed to a canting of Gd moments causing a reduction in the net in-plane component of the magnetic moment. The reduction in magnetisation at low temperatures was not observed in the XRMS data which was assumed

to be due to the element specific nature of the technique. As the XRMS was element specific and so only measured the magnetisation of the Gd, it was proposed that there was an induced moment in the Y which experiences a rotation at low temperatures.

Studies of the properties of Y within the superlattice were attempted by using a Ho tagging layer which would act as a magnetic proxy for the Y moment. High roughness between layers and a low signal to noise ratio meant that these measurements did not provide the detailed information on the Y layer properties as expected. It was possible to obtain hysteresis data at the Ho L_3 edge, which suggests that the use of Ho as a tagging layer could be a viable technique. Hysteresis data recorded at the Ho L_3 edge showed a different coercivity to that at the Gd L_3 edge which supports the hypothesis that there is canting or intermixing of Gd and Y at the interfaces. To conclusively determine if Ho could be used in this way, improvements in the signal to noise ratio and growth of samples with lower roughness would be needed.

Chapter 6

Magnetisation Reversal Processes in Amorphous SmCo-CoAlZr Trilayers

This chapter presents an element specific study of the magnetisation reversal processes in an amorphous trilayer of SmCo and CoAlZr. Hysteresis loops recorded using x-rays at the Co L_3 and Sm M_4 edges are presented at 100 K and 300 K. Minor hysteresis loops at these energies and temperatures are also given and are indicative of a complex, randomly distributed magnetic structure existing in the trilayer. The chapter then goes goes on to look at the effect of changing composition and interaction strength by modelling amorphous alloys using a randomly distributed lattice with nearest neighbour interactions.

6.1 Introduction

The ability to tailor the properties of thin films and heterostructures so that novel materials can be created is highly valuable in many applications in modern technology. To overcome issues with lattice matching in crystalline multilayers, amorphous materials can be used. Amorphous alloys allow materials with a large range of compositions to be grown [111, 170, 171] and they can be created in multilayers with materials of widely different compositions [172]. Layers of amorphous material can be highly uniform with low roughness between layers which makes them ideal for use as magnetic multilayers; they also allow material properties such as the magnetic moment, anisotropy, coercivity and ordering temperature to be manipulated through composition and structure [173].

Previous work has shown that the magnetic ordering temperature of amorphous layers of FeZr is highly dependent on the composition [174]. Additionally, the replacement of the Fe by Co has been shown to increase the ordering temperature [175,176]. It follows from these findings that $Co_x(AlZr)_{100-x}$ is expected to be a material that allows very fine control of the magnetic properties by varying the composition. Crystalline alloys of Co and Sm are well known for their large coercivity and anisotropy [177, 178] and although smaller than in the crystalline case, a large uniaxial in-plane anisotropy can be imprinted in amorphous layers during growth by applying a magnetic field [179]. By combining a magnetically hard layer of SmCo with softer CoAlZr layers with different ordering temperatures, we aim to create a heterostructure which allows fine control over the layer interactions with composition and temperature.

6.2 Sample Details

The films were deposited by D.C. magnetron sputtering on Si(100) substrates with the in-plane easy axis of the samples set by an in-situ magnetic field applied during growth [107]. Amorphous trilayer samples were grown with the structure as illustrated in Figure 6.1(a). The first magnetic layer being a hard $Sm_{0.09}Co_{0.91}$ layer (20 nm), in a single domain state [181]. This SmCo layer acts to pin the two subsequent $Co_x(Al_{0.7}Zr_{0.3})_{1-x}$ layers with $x = 0.6$ and $x = 0.85$. These layers have nominal thicknesses of 40 nm and 15 nm respectively. The anticipated behaviour when the sample is placed in an applied field is that of an exchange spring whereby the soft upper $Co_{85}AlZr_{15}$ layer undergoes a magnetisation reversal at a lower field

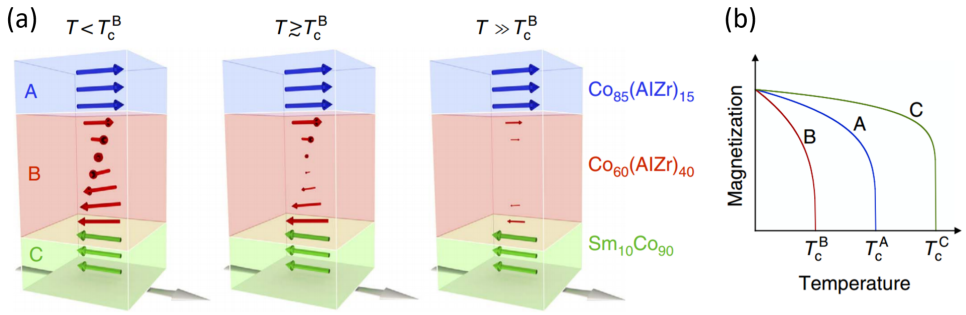

Figure 6.1: (a) A simplified schematic of the layer structure of the trilayer, showing the three different magnetic layers. (b) An illustration of the temperature dependence of the magnetisation in the three layers showing that they each have a different ordering temperature. Adapted from [180].

value than the SmCo layer. The hard SmCo pins the upper soft layers inducing an exchange spring structure in the middle $Co_{60}AlZr_{40}$ layer as shown in Figure 6.1(a).

The composition of the layers is chosen to give relative ordering temperatures as shown in Figure 6.1(b) where the middle layer orders at a much lower temperature than the other layers. This allows the magnetic properties to be altered using temperature as the magnetisation in the middle layer is directly controlled by heating or cooling. In a parallel growth run, thin films (nominally 20–50 nm) of the individual magnetic layers were deposited. In all cases, the magnetic layers were seeded and capped by 2 nm thick layers of $Al_{0.7}Zr_{0.3}$. The buffer layer eliminated any crystallization occurring at the substrate/film interface whilst the cap protected the active layers from post growth oxidation [182, 183].

All samples were studied using grazing incidence diffraction, x-ray reflectivity and transmission electron microscopy (TEM) which confirmed the layer structure, low roughness ($\sigma \lesssim 0.5$ nm) and amorphous nature of the films. Figure 6.2(a) shows TEM of a single film of SmCo confirming the uniform thickness and low roughness of the layer. Figure 6.2(b) and (c) are selected area electron diffraction images from the substrate and the SmCo layers respectively and show that the substrate is crystalline (well defined diffraction spots) and the SmCo is amorphous (diffuse ring pattern). Non-resonant reflectivity from the trilayer sample is shown in Figure 6.3(a) and the

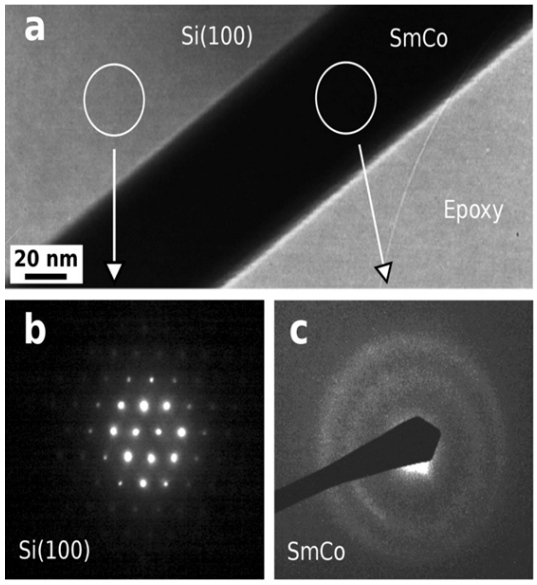

Figure 6.2: (a) A cross-sectional TEM image of the single layer of $Sm_{11}Co_{89}$. The SmCo has a uniform thickness with well defined interfaces. (b) and (c) Selected area electron diffraction from the Si substrate (crystalline) and SmCo film (amorphous), respectively [107].

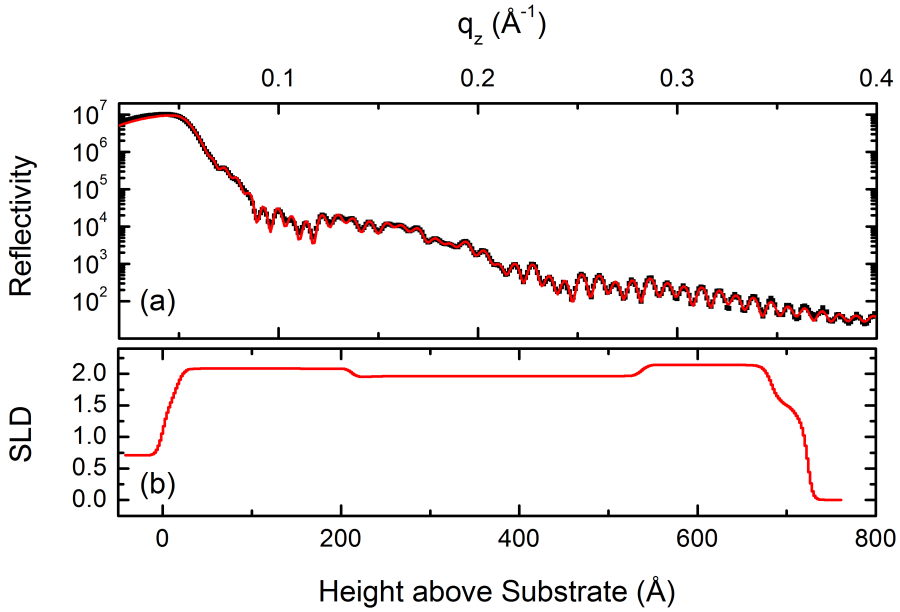

Figure 6.3: (top) Non-resonant x-ray reflectivity for an amorphous SmCo-CoAlZr trilayer. Data (black points) and best fit (red line). (bottom) Scattering length density profile obtained from best fit.

SLD profile of the chemical structure is shown in Figure 6.3(b). The fit shows that there are three well defined layers with uniform density and low roughness (∼5 Å) plus an AlZr capping and buffer layer plus an oxide at the surface. Previous studies including more details of the magnetic structure can be found in [107, 184].

Element specific studies were then conducted using resonant x-ray scattering on beamline X13A at the NSLS, Brookhaven National Laboratory, details of which can be found in Chapter 3. To avoid strong absorption, the x-ray energy was tuned to just below (by roughly ~ 0.25 eV) the Co L_3 and Sm M_4 edges [185]. Reflectivity and spectroscopy data, synchronized to the helicity reversal, were recorded as a function of scattering vector, incident energy, temperature and magnetic field ($\pm$ 100 mT). Reflectivity data at all energies showed strong Kiessig fringes with a period corresponding to the expected sample thickness demonstrating that the x-rays probed the entire sample [186].

6.3 Results

This chapter will now go on to present hysteresis data recorded using resonant x-ray scattering at both 100 K and 300 K. Hysteresis data recorded using resonant x-rays provides an element specific technique for observing magnetisation reversals. In the

case of the SmCo-CoAlZr trilayers investigated here, it allows the measurement of the Co and Sm separately and will give information on the separate magnetisation reversal mechanisms at work in such a structure. The hysteresis loops are recorded by fixing **q** at a value at which the signal is maximised and recording the asymmetry ratio (A.R.) as a function of applied field. As it is not possible to reverse the sign of the magnetic field whilst recording a hysteresis loop, the helicity of the circularly polarised x-rays is flipped during operation to obtain the asymmetry ratio.

6.3.1 Single Films

We begin by considering the magnetisation reversals of single films of SmCo and CoAlZr. Figure 6.4(a) shows the magnetisation as a function of temperature for a $Co_{60}(AlZr)_{40}$ film measured using MOKE. The sample is ferromagnetic at low temperatures with a phase transition at the ordering temperature 103 ± 1 K. The hysteresis loop of a $Co_{85}(AlZr)_{15}$ film measured at room temperature with the field aligned with the easy axis is in the inset of Figure 6.4(a) and reveals that the material is clearly ferromagnetic at room temperature with a square hysteresis loop and low coercivity, $H_C^{Co_{85}} = 0.44 \pm 0.05$ mT.

Element specific hysteresis loops for the SmCo film are shown in Figure 6.4(b)

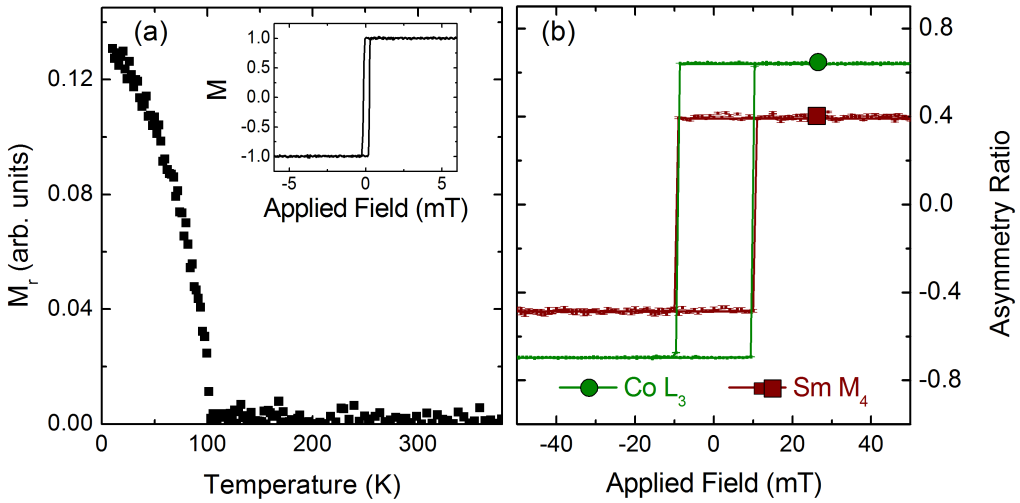

Figure 6.4: Magnetisation of single films: (a) MOKE measurements of the remanence M_r as a function of temperature for a $Co_{60}(AlZr)_{40}$ film and inset, normalised hysteresis loop recorded at 300 K for a $Co_{85}(AlZr)_{15}$ film. (b) Element specific hysteresis loops recorded at 300 K for the Sm_8Co_{92} film at both the Sm M_4 (red, square) and the Co L_3 (green, dot) edges. Experimental data (points) are fitted to a modified Langevin function (line).

and reveal that the SmCo is also ferromagnetic at room temperature. Data from both edges have identical behaviour, with the unscaled A.R. for both the Sm and Co sub-networks reversing at $H_C^{Sm} = H_C^{Co} = 9.5 \pm 0.5$ mT, more than ten times that of the softer CoAlZr films.

6.3.2 Trilayer Magnetisation Reversals at Low Temperature

When these materials are combined into a trilayer, the field dependence of the magnetisation reflects not only the properties of the individual layers, but also any coupling between them. Element specific hysteresis loops recorded at the Co L_3 and Sm M_4 edges for a $Sm_9Co_{91}/Co_{60}(AlZr)_{40}/Co_{85}(AlZr)_{15}$ trilayer are shown in Figure 6.5. The measurements are performed at 100 K where all three layers are at or below their respective ordering temperatures, but the middle $Co_{60}(AlZr)_{40}$ is expected to be very soft with its magnetisation dominated by the proximity induced magnetisation from the adjacent layers. Immediately obvious in Figure 6.5 are the different shapes and coercivities of the Co and Sm data when compared to the data for the single, isolated layers.

The Co sub-network shows a two-step hysteresis curve consistent with an

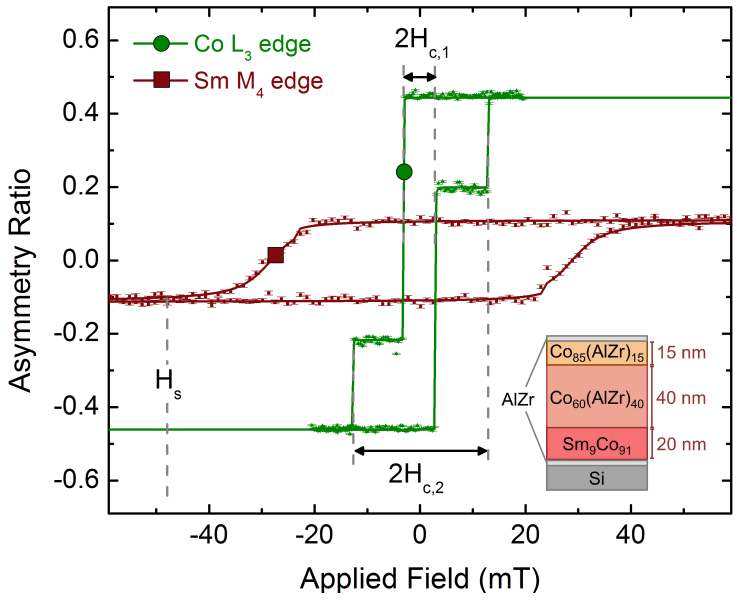

Figure 6.5: Element specific hysteresis loops obtained for the trilayer at 100 K at both the Sm M_4 (red square) and the Co L_3 (green dot) resonant edges. Experimental data (points) are fitted to a modified Langevin function (line). The sample was held at ±100 mT prior to each measurement. (inset) Schematic of the trilayer structure showing nominal layer thicknesses and composition

apparent separate switching of the hard and soft magnetic layers. The first switch at $H_{c,1}$ we attribute to a reversal of the Co in the softer CoAlZr layers and the second switch at $H_{c,2}$ to the Co in the hard SmCo layer. Sm edge data shows the expected single switch behaviour as the data is only sensitive to the reversal of the Sm within the SmCo layer. The coercivity, however, far exceeds any switching seen in the Co data indicating that the Sm and Co sub-networks are no longer magnetically locked as in the single layer, Figure 6.4(b). The shape of the reversal is also different for the Sm, extending over a wider field range than the sharp Co reversals, further supporting that the interactions between the two sub-networks are not as strong as the inter-layer Co interactions. The saturation field of the Sm sub-network is $H_S^{Sm} = 46 \pm 1$ mT. No third switching event was observed in the Co data at any scattering vector over the range 0.2 Å^{-1} to 0.25 Å^{-1} at the same switching field as the Sm reversal.

To further explore the observation of weaker interactions between the Sm and Co sub-networks compared to the inter-layer Co interactions, minor loops with increasing positive fields were recorded after the sample had been held in a negative saturating field of -100 mT. Figure 6.6(a) shows the minor loops recorded at the Co L_3 edge. On increasing the value of the positive field for the minor loops, the Co loops evolve; at $H_{sw,1}$ the upper Co layer switches sharply and the minor loops are vertically shifted single square loops with low coercivity, but with a field offset H_{ex}. This behaviour continues until the upper switching field $H_{sw,2}$ at which point the second step is observed in the minor loops as the Co in the harder layer reverses. There is no longer a vertical offset in the A.R. suggesting that all the Co has reversed. With increasing field, the coercivity increases further and there is a steady reduction in the field offset. The evolution of the coercivity is shown in Figure 6.6(b) and (c) for $H_{c,2}$ and $H_{c,1}$ respectively. $H_{c,2}$ increases slightly on increasing field but shows larger changes above 40 mT, in the vicinity of H_s^{Sm}. The effect is more clearly demonstrated in the $H_{c,1}$ data, Figure 6.6(c), where a rapid rise from a plateau of $\sim$1.5 mT is observed close to H_s^{Sm}. This plateau forms above $H_{sw,1}$, below which a steady increase in the coercivity was observed.

The changes in the coercivity are mirrored in those seen in the offset field, H_{ex}, which is shown in Figure 6.6(d). We see a rapid fall-off in H_{ex} at $H_{sw,2}$ but pinning remains until the applied field exceeds H_s^{Sm}. The offset field H_{ex} can be considered as an exchange interaction, acting on the Co network. The presence of such an exchange bias suggests that although the Sm and Co sub-networks interact less strongly, some interaction between the two sub-networks remains and the dependence on H_s^{Sm} shows that this biasing is related to the switching behavior of the

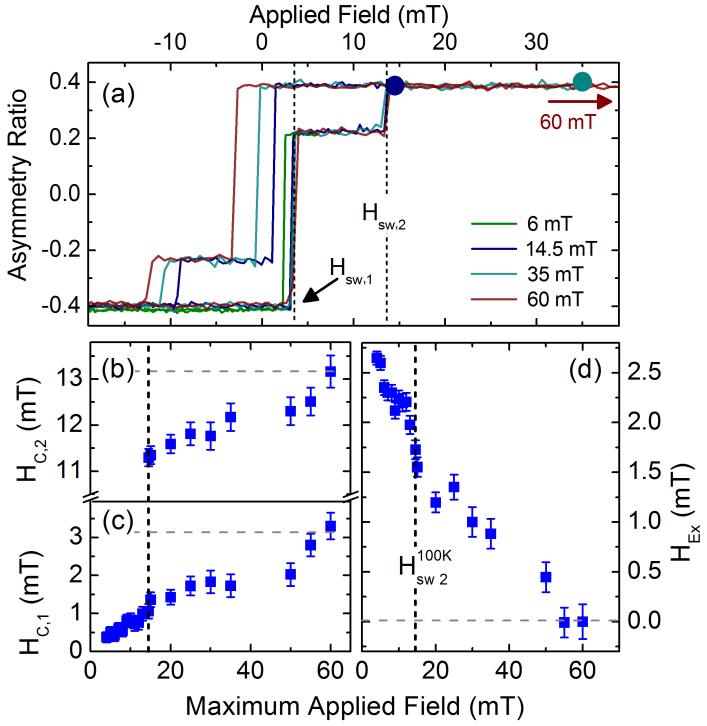

Figure 6.6: (a) Minor hysteresis loops at 100 K at the Co L_3 edge. The circles mark the maximum field value for each minor loop. The samples were held at -100 mT before each field measurement and show a two step switch for fields above $H_{\mathrm{sw},2}$. (b) and (c) Coercivities $H_{\mathrm{c},2}$ and $H_{\mathrm{c},1}$. The vertical dashed line marks $H_{\mathrm{sw},2}$. (d) Exchange field, H_{ex}, for the loops as a function of maximum applied field. Horizontal dashed lines in (b), (c) and (d) are the asymptotic values determined from fully saturated loops.

Sm sub-network within the lower SmCo layer.

Minor loops were also obtained at the Sm M_4 edge and are shown in Figure 6.7(a). As a function of increasing field, the amplitude of the minor loop increases as more of the Sm reverses. The percentage of Sm reversed is shown in the cumulative plot in Figure 6.7(b) and is fitted to a skewed normal distribution to yield the switching field probability distribution shown in the inset of Figure 6.7(b). The distribution has a mean and variance of 29.5 mT and 23.9 mT respectively.

6.3.3 Trilayer Magnetisation Reversals at Room Temperature

So far, all three of the layers have been below or at the ordering temperature of the middle layer. Now the properties of the system are considered when the temperature is raised well above the ordering temperature of the middle $Co_{60}(AlZr)_{40}$ layer so

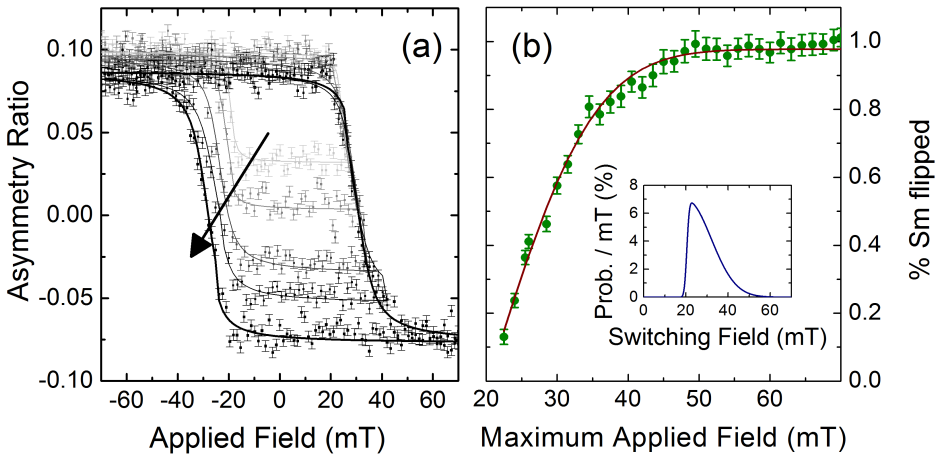

Figure 6.7: (a) Minor hysteresis loops at 100 K at the Sm M_4 edge, measured as the maximum applied field is increased for each loop. (b) Percentage of total Sm reversed calculated from the minor loops. (inset) Probability distribution of switching fields determined from a fit of a skewed normal distribution to the cumulative data.

that in principle the magnetic structure comprises two magnetic layers separated by a ∼40 nm thick layer of paramagnetic material. It would be expected that a similar two-step reversal would be observed with the magnetisation extending some way into the middle layer at 300 K, but the middle layer would have a much lower magnetic moment. As such, there would be no mechanism for coupling between the upper and lower layers leading to no observed exchange bias.

Element specific hysteresis loops recorded at the Co L_3 and Sm M_4 resonant edges were measured are shown in Figure 6.8. As with the data recorded at 100 K, there is a two-step magnetisation reversal of the Co sub-network and a single, more gradual reversal in the Sm sub-network. Here the coercivity of the Co hysteresis curve is $H_{c,1}^{300\ K} = 2.0 \pm 0.3$ mT and $H_{c,2}^{300\ K} = 9.99 \pm 0.04$ mT which are approximately 1/3 lower than the values recorded at 100 K of $H_{c,1}^{100\ K} = 3.0 \pm 0.4$ mT and $H_{c,2}^{100\ K} = 12.89 \pm 0.08$ mT. The coercivity of the hysteresis curve measured at the Sm edge was $H_c^{Sm,100\ K} = 28.5 \pm 0.2$ mT compared to the room temperature value of $H_c^{Sm,300\ K} = 15.1 \pm 0.1$ mT which is a reduction in coercivity of nearly a factor of two. The reduced coercivity is as expected as there is increased thermal energy assisting the reversals.

The shape of the first reversal in the Co hysteresis curve is much the same as that at 100 K with a sharp, square loop, but the second reversal at $H_{c,2}^{300\ K}$ (which was previously attributed to the Co in the hard SmCo layer) has a more extended reversal than previously seen at low temperature. This more gradual second reversal

shows that there is a mechanism acting to pin the Co and prevent the remaining Co reversing simultaneously. This more extended shape to the hysteresis curve seen in the Co sub-network combined with the drop in coercivity of the Sm edge hysteresis data indicate that the regions of Co and Sm in the lower SmCo layer are now interacting more strongly with each other than at 100 K. Additionally, the Co in the SmCo layer is now interacting less strongly with the Co in the other layers. The result is that the top and bottom layers behave more like two independent magnetic layers.

Although the behaviour is more similar to that of two individual layers, there is still a difference in the reversal fields of the Co and Sm sub-networks as shown in Figure 6.8, implying that the Co inter-layer interactions are still strong compared to those between the Co and Sm sub-networks even across ∼40 nm of supposedly paramagnetic material. As a result of these layers acting more independently, it is expected that the magnetic properties would be more similar to those of the single films and in fact the coercivity of the higher field reversal in the Co loop is closer to that of the individual SmCo film at 300 K ($H_C^{Sm} = H_C^{Co} = 9.5 \pm 0.5$ mT).

Minor loops were recorded at both the Sm and Co resonant edges at 300 K. Those recorded at the Co edge are shown in Figure 6.9(a) as a function of increasing

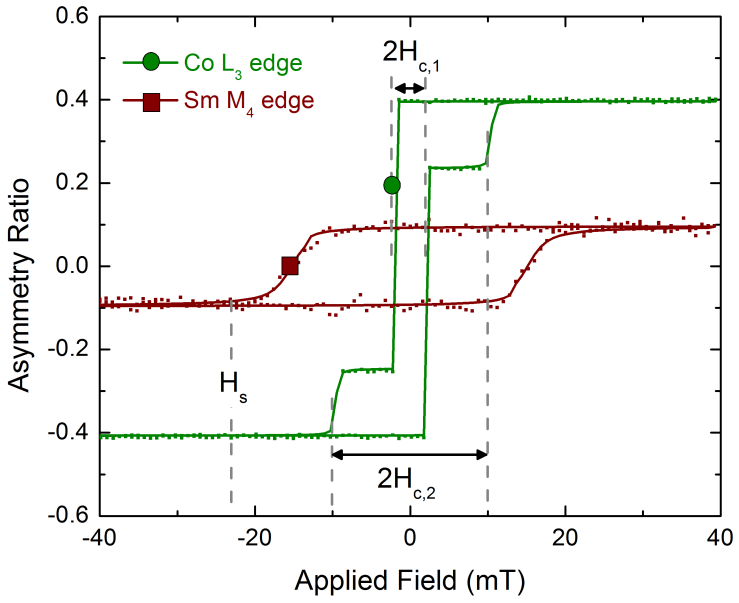

Figure 6.8: Element specific hysteresis loops obtained for the trilayer at 300 K at both the Sm M_4 (red square) and the Co L_3 (green dot) resonant edges. Experimental data (points) are fitted to a modified Langevin function (line). The sample was held at ±100 mT prior to each measurement.

maximum field. Again, a single square hysteresis curve is seen which is vertically offset. These evolve as the maximum applied field is increased until 10.8 ± 0.1 mT, when a second reversal is introduced as the rest of the Co reverses. Unlike the low temperature data, however, the second reversal shows a more extended shape as is seen in the full hysteresis curve at this temperature. $H_{c,2}$ and $H_{c,1}$ increase as the maximum applied field of the loops is increased, and the evolution of these is shown in Figure 6.9(b) and (c) respectively. $H_{c,2}$ shows a steep increase at first until approximately 15 mT where it gradually levels off until it reaches the value of the full hysteresis curve of 9.99 ± 0.04 mT. The levelling off of $H_{c,2}$ at 15 mT coincides with the saturation field of the Sm. $H_{c,1}$ increases gradually, until reaching the

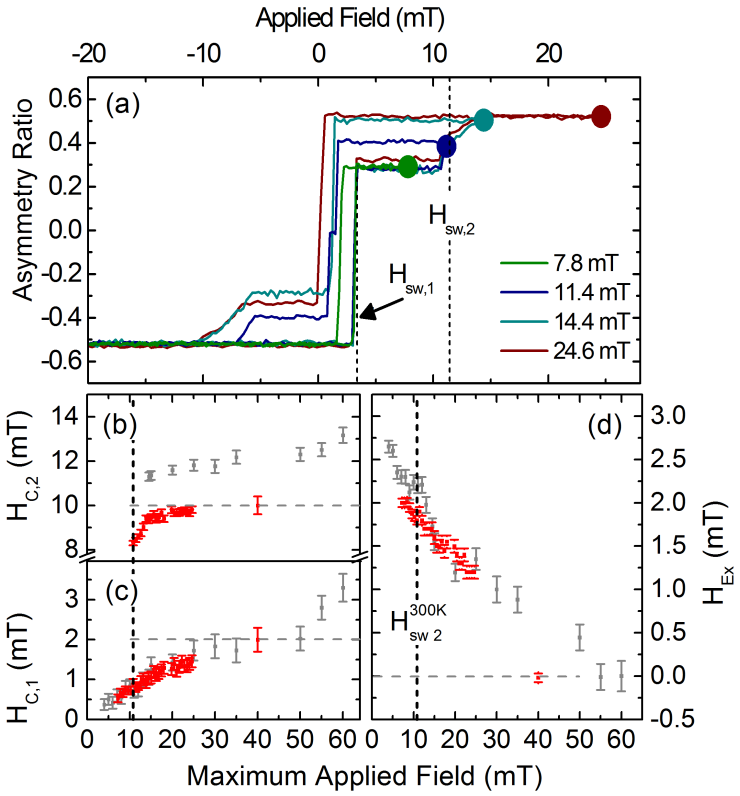

Figure 6.9: (a) Minor hysteresis loops at 300 K at the Co L_3 edge. The circles mark the maximum field value for each minor loop. The samples were held at -100 mT before each field measurement and show a two step switch for fields above $H_{sw,2}$. (b) and (c) Coercivities $H_{c,2}$ and $H_{c,1}$. The vertical dashed line marks $H_{sw,2}$. (d) Exchange field, H_{ex}, for the loops as a function of maximum applied field. Horizontal dashed lines in (b), (c) and (d) are the asymptotic values determined from fully saturated loops. The data measured at 100 K is shown in light grey to aid in the comparison between the behaviour at the two temperatures.

saturation value marked by the dashed horizontal line in Figure 6.9(c). The initial steep increase in $H_{c,2}$ which levels off at the Sm saturation field is evidence that the Sm and Co within the lower SmCo layer are more strongly interacting at this temperature than the inter-layer coupling between the Co. Lastly, Figure 6.9(d) shows that while the maximum applied field value of the loops is low, H_{ex} is approximately the same as for the 100 K data indicating that there is similar coupling between the layers even when 200 K above the ordering temperature of the middle layer. H_{ex} does, however, drop to zero sooner than it does in the data at 100 K (see the value of H_{ex} at 40 mT in Figure 6.9 (d)).

Minor loops were obtained at the Sm M_4 edge and are shown in Figure 6.10(a). As a function of increasing field, the amplitude of the minor loop increases as more of the Sm reverses, similar to the minor loops observed at low temperature. The percentage of Sm reversed is shown in the cumulative plot in Figure 6.10(b). The 100 K data is shown in grey for comparison. It is clear that at 300 K there is a much more rapid rate of Sm reversal compared to the low temperature data before levelling off at the saturation value; this provides further evidence that the intra-layer interactions between the Co and Sm sub-networks are more strongly interacting at 300 K than the inter-layer Co interactions.

The relative amplitudes of the two parts of the hysteresis loops recorded at

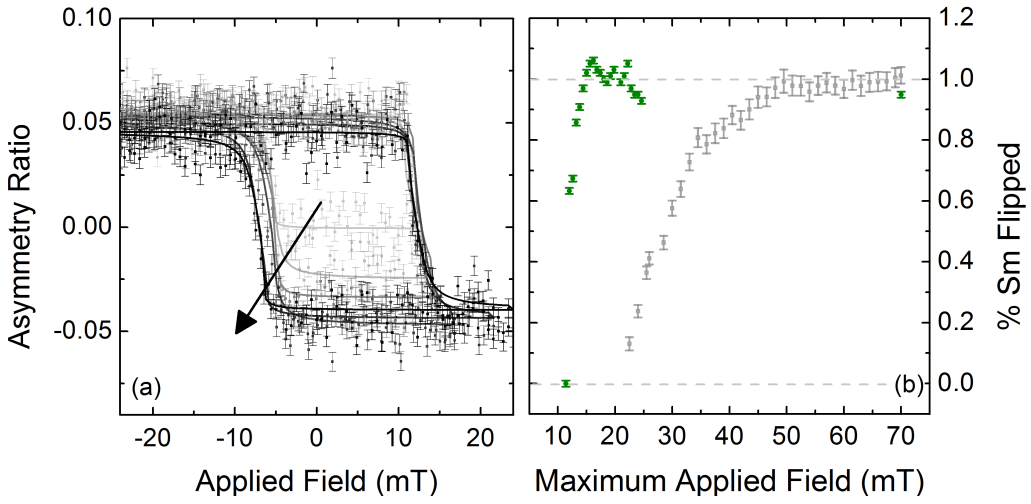

Figure 6.10: (a) Minor hysteresis loops at 300 K at the Sm M_4 edge, measured as the maximum applied field is increased for each loop. (b) Percentage of total Sm reversed calculated from the minor loops (green). The data recorded at 100 K is shown in grey for comparison.

the Co edge change as the maximum applied field is increased. This must be treated with some caution as changing amplitudes could be caused by changing **q**, but as this is not observed in the Co minor loops at 100 K it is highly unlikely that this is caused by the alignment drifting by a large enough amount to cause the changes in amplitude seen here. Figure 6.11(a) and (b) show the changing amplitudes of the minor loops as the maximum applied field is increased, recorded at 300 K and 100 K respectively.

At 300 K we see that $A_{\mathrm{Co},1}$, the amplitude of the first Co reversal, remains constant at first and then steadily increases after approximately 20 mT (which is the saturation field for the Sm hysteresis loops). $A_{\mathrm{Co},2}$, however, which is the amplitude of the second Co reversal, steeply increases until approximately 15 mT, and then steadily decreases. A_{Sm} corresponds to the magnetisation amplitude of the reversal of the Sm in the SmCo layer. At 300 K the amplitudes $A_{\mathrm{Co},2}$ and A_{Sm} both increase at first, as the bottom layer reverses independently of the upper layer. Above 20 mT, the total amplitude $A_{\mathrm{Co},1} + A_{\mathrm{Co},2}$ remains constant whilst the ratio of the two individual amplitudes changes.

When the upper layer reverses, there is a point in the middle layer at which the magnetisation changes sign which will loosely be termed a domain wall here. When the ratio of the two amplitudes, $A_{\mathrm{Co},1}$ and $A_{\mathrm{Co},2}$ changes, this could possibly be explained by the position of the domain wall moving. Due to the dependence of the asymmetry ratio on **q**, to be able to determine the absolute position of this

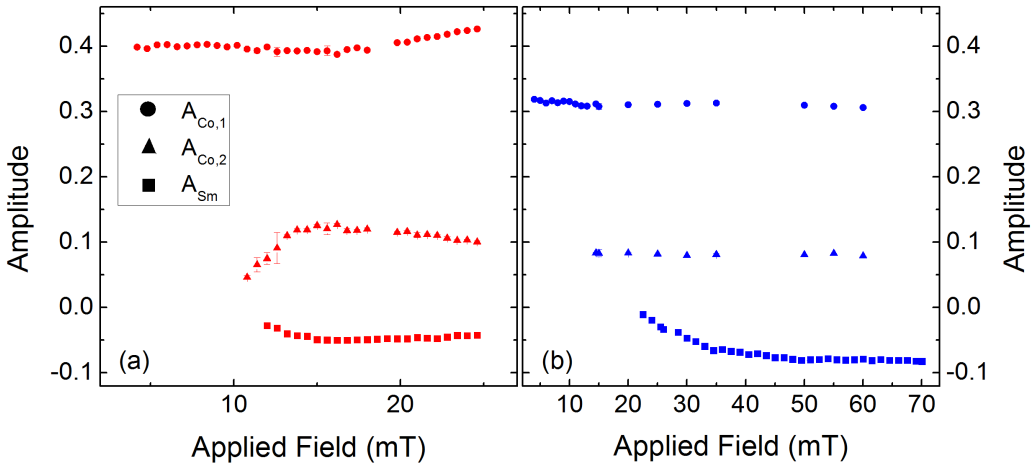

Figure 6.11: Amplitude of minor hysteresis loops as a function of maximum applied field at (a) 300 K and (b) 100 K.

domain wall within the structure and better understand the magnetic profile, the specular reflectivity must be fitted and a model created of the scattering length density, both chemical (from the sum signal) and magnetic (from the asymmetry ratio). At 100 K, there is no change in the amplitude of $A_{\mathrm{Co},1}$ or $A_{\mathrm{Co},2}$ suggesting that there is no movement of the domain wall position.

These amorphous trilayers clearly have a complex internal structure that results in the observed exchange bias in the minor loops. The next sections will present modelling of the Co distribution which is used to investigate the random distribution of amorphous alloys which leads to coupling across a layer that would be paramagnetic if grown as a single thin film rather than in a multilayer.

6.4 Modelling

Previous work on samples of this kind often describe the observed behaviour as being like an exchange 'spring', which is wound up similar to a torsion spring [49, 50, 187, 188]. We see similar magnetic properties in the samples presented here from hysteresis loops recorded using MOKE which exhibit a continuous, gradual magnetisation reversal as seen in Figure 6.12(a). At 100 K, the middle layer is below its ordering temperature and there is a gradual reversal in the magnetisation of the soft upper part of the sample which is consistent with an exchange spring being induced in the middle layer. The data at 300 K which is well above the ordering temperature of the middle CoAlZr layer, shows a sharp reversal indicative of two layers flipping independently. There is a very slight rounding of the second switch, similar to that seen at room temperature in the hysteresis loops recorded with XRMS.

As shown so far in this chapter, this simple exchange spring model does not go far enough to explain the element specific data as we do not see a gradual change in magnetisation in the Co data consistent with an exchange spring. In principle MOKE and XRMS use the same mechanism to probe the magnetisation whereby the absorption is dependent on the magnetisation of the sample and polarisation of the incident light. MOKE, however, is typically only sensitive to the top 200 Å of material whereas the x-ray energy is chosen to limit absorption effects such that the whole sample is probed (this is confirmed from specular reflectivity as the Kiessig fringe thickness corresponds to the total expected thickness of the trilayer sample). It is therefore likely that the MOKE data does not give a measurement of the whole sample which could mean that the gradual change observed in the MOKE hysteresis loops is only for the upper part of the sample. When measuring the whole sample,

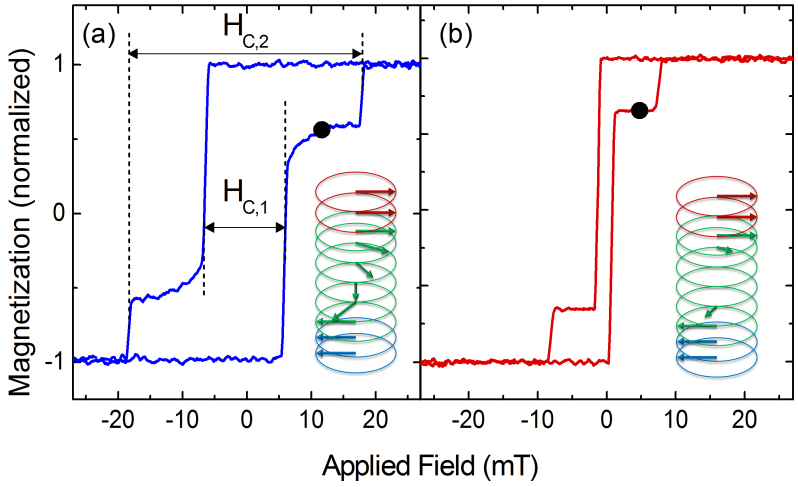

Figure 6.12: MOKE hysteresis loops of the trilayer structure recorded at (a) 100 K and (b) 300 K. Potential magnetic structures at the points on the hysteresis curves marked by black dots are shown (insets).

as with the XRMS data, the gradual change in magnetisation in the upper part of the sample is perhaps counteracted by the lower part of the sample and so the apparent spring behaviour is not observed.

The exchange spring model also falls short of explaining the exchange bias observed in the minor hysteresis loops and does not address the complex internal structure that is believed to exist within the amorphous alloys. To further aid understanding of the trilayer systems, modelling of the distribution of the Co sub-network throughout the layers was carried out and will be presented in the next sections.

6.4.1 A Simple Square Lattice Model

To attempt to understand the mechanisms at work in the Co sub-network, it would be useful to be able to create a model to investigate the interactions between Co atoms in a randomly distributed alloy such as those in this chapter. The model chosen needs to represent the samples, which are amorphous alloys with the interacting magnetic elements randomly distributed within the layers. Firstly, we consider just the Co sub-network and ignore any other interactions (from the Sm atoms) and model this as a lattice on which each site is assigned either a Co atom (represented as a 1) or not a Co atom (represented as a 0). The Co sites are randomly distributed across the lattice in a probability corresponding to the composition of the layer.

The model first looks at the effect of reversing the spins in the top layer

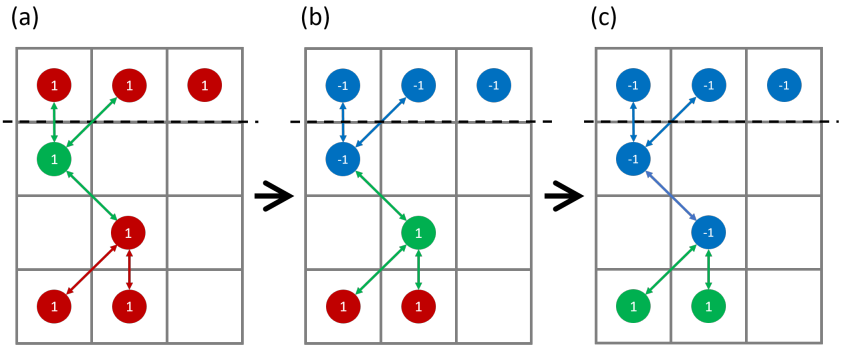

Figure 6.13: Illustration of modelling of interactions between Co atoms on a square lattice. Red circles mark sites with Co atoms, blue circles are Co atoms whose spin has been flipped. The nearest neighbours to the green circle contribute to the total interaction strength. The dashed line marks the interface between two layers with different Co concentrations where the magnetisation of the top layer is flipped (b) and (c). Blue represents negative spins and red are positive spins.

(85% Co), and allowing any spin in contact with a reversed spin to also reverse. See Figure 6.13(a) for a representation of the Co sites on the lattice; it shows the interface between a higher Co density layer with a lower one similar to the interface between the $Co_{85}AlZr_{15}$ and the $Co_{60}AlZr_{40}$ in the trilayer. Consider the Co atom highlighted in green, it is in contact with positive spins only and so remains positive. Figures 6.13(b) and (c) then show the effect of reversing the magnetisation of the uppermost layer by setting all Co spins to -1 in the layer. This simple model then reverses any spin in contact with another negative spin and the reversals percolate through to all spins in contact with another reversed spin resulting in chains of negative spins extending through the layers.

The point at which the concentration is high enough that interconnected

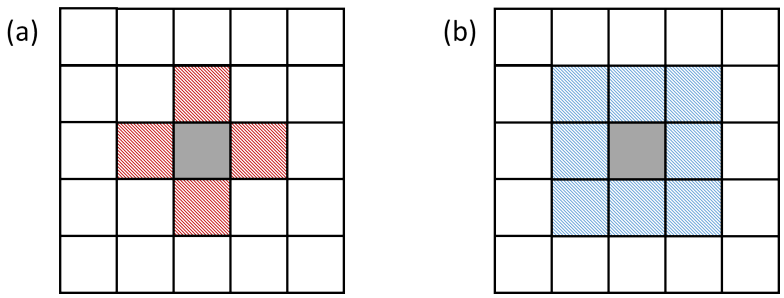

Figure 6.14: Illustration of interactions in different percolation models showing (a) the NN and (b) the NN + NNN models.

paths appear throughout the whole structure is called the *percolation threshold* [189]. The percolation effect is highly dependent on the concentration of interacting atoms. The 2D percolation threshold for a square lattice of this type is about 0.59 for interactions directly up/down and left/right on a square lattice (the NN model) as shown in Figure 6.14(a) [190]. When the number of nearest neighbours is increased to 8 and the diagonal interactions are taken into account (the NN + NNN model) as shown in Figure 6.14(b), then the percolation limit drops to about 0.4 [191]. The 8 nearest neighbours model presented in Figure 6.14(b) gives all highlighted sites equal weighting whereas the model in this work weights the diagonal sites with a $\frac{1}{\sqrt{2}}$ factor. The resulting percolation threshold would therefore be expected to be somewhere in the region 0.4–0.59.

6.4.2 Changing Co Concentration

The effect of changing the Co concentration in the middle layer is shown in Figure 6.15 where spins are flipped when in contact with reversed spins only. The Co concentration in the middle layer is increased and shows that as it passes the 2D percolation limit, paths of flipped spins emerge through the Co lattice. The higher the Co concentration the more likely a chain of interacting sites will penetrate through the middle layer and cause a coupling between the upper and lower layers.

The purpose of the model created here is purely to study the probability that chains of interacting spins exist through an amorphous material such as the middle $Co_{60}AlZr_{40}$ layer in the trilayer studied in this chapter. This could build a foundation

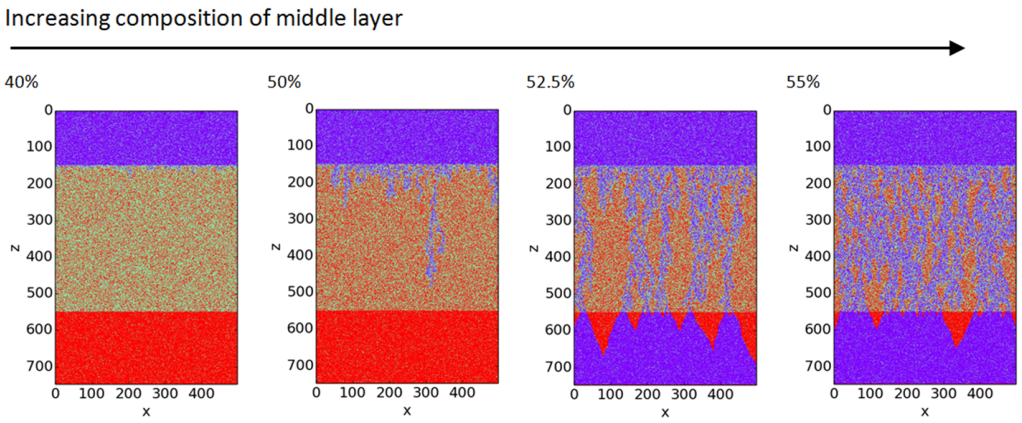

Figure 6.15: Models of randomly distributed alloys illustrating the effect of reversing the upper layer whilst changing the Co concentration of the middle layer. As the Co concentration passes the 2D percolation limit, paths of flipped spins emerge through the middle layer. Red are +1 spins, blue are −1 spins and green are 0, i.e. non Co.

on which to start to understand the mechanisms behind the long range magnetic interactions in the trilayer, which were observed experimentally as exchange bias. This is a simplified model and is not intended as an accurate representation of the system, but it does indicate that small changes in the Co concentration around the percolation limit of amorphous alloys could lead to large changes in the coupling between layers.

6.4.3 Nearest Neighbour Interactions

The model was then altered to calculate the nearest neighbour interactions from the surrounding Co atoms at each of the Co sites according to the full Ising model where the exchange energy is

$$H = -\sum_{<ij>} J_{ij} s_i s_j - \mu_0 \mu_B \sum_i H_i s_i \tag{6.1}$$

where $< ij >$ indicates that the spins are nearest neighbours, s_i and s_j take the values ± 1 depending on the spin configuration and H_i is the applied field acting on spin i [192]. The exchange interaction, J_{ij}, is negative for parallel spin configurations and positive when antiparallel. The Ising model therefore can not account for any x-y deviation such as rotation of spins, the only available spin configurations are represented by $s_i = \pm 1$ ($\uparrow$ or $\downarrow$).

The nearest neighbour model calculated the energy acting on each spin (ΔH) as per Equation 6.1 from all of the nearest neighbour spins. If the total energy acting on that spin was less than zero (i.e. if it was surrounded by negative spins or if the applied field was large enough to reverse the spin) then that site was flipped from

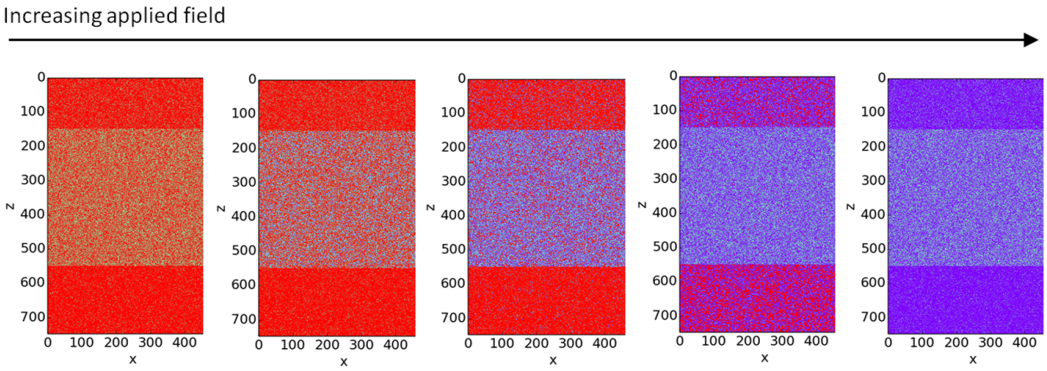

Figure 6.16: Models of randomly distributed alloys illustrating the effect of increasing the applied field within an Ising model. More of the Co reverses as the magnitude of the applied field is increased.

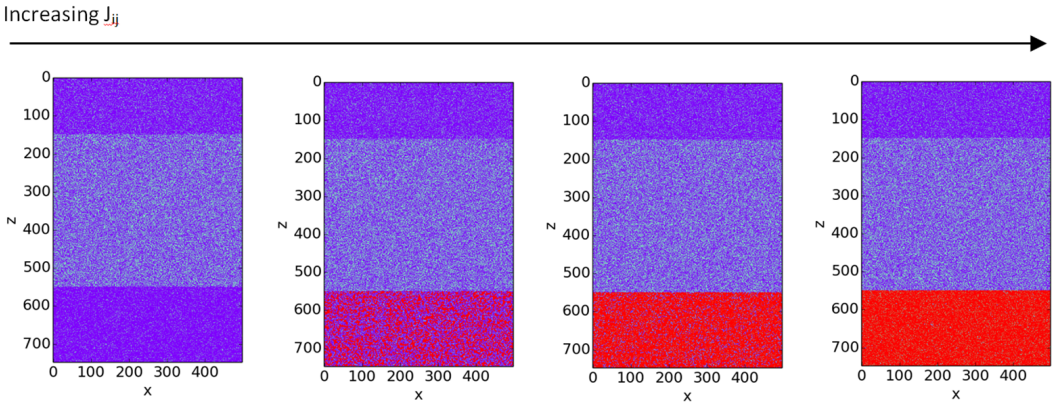

Figure 6.17: Models of randomly distributed alloys illustrating the effect of increasing the interaction strength, J_{ij}, of the bottom layer within an Ising model.

+1 to −1. The effect of increasing the applied field within this Ising model is shown in Figure 6.16 with J_{ij} set to -1 for all three layers. The middle layer, which has the lowest Co concentration, reverses before the other two; this is because the exchange interaction is weaker due to the sparser distribution, meaning that the applied field can cause spins to reverse more easily than in the denser layers.

By changing the value of J_{ij}, the switching field can be changed. In the trilayer, the bottom SmCo layer was magnetically harder than the upper CoAlZr layers. To illustrate how this could be incorporated into the model, the value of J_{ij} was changed for just the bottom layer. The results of this are shown in Figure 6.17, the applied field was kept constant whilst J_{ij} of the bottom layer was increased. It is clear that as J_{ij} is increased, the applied field is no longer sufficient to cause the layer to reverse. It would take a much higher field to cause the reversal. As $T_C \sim J_{ij}$, changing the interaction strength within a particular layer in this manner is similar to changing the ordering temperature of the layer.

6.4.4 Nearest Neighbours and Percolation Effects

The models were then combined to include both percolation effects and the exchange interaction in a field. Instead of using the model where any spin in contact with another negative spin is flipped, the model was updated to calculate the change in energy, ΔH, associated with the reversal of a spin when in an applied field. This change in energy is given as

$$\Delta H_i = -\sum_{<ij>} J_{ij}^{\uparrow\downarrow} s_i^{\uparrow} s_j^{\downarrow} - \sum_{<ij>} J_{ij}^{\uparrow\uparrow} s_i^{\uparrow} s_j^{\uparrow} - \mu_0 \mu_B \sum_i H_i s_i \tag{6.2}$$

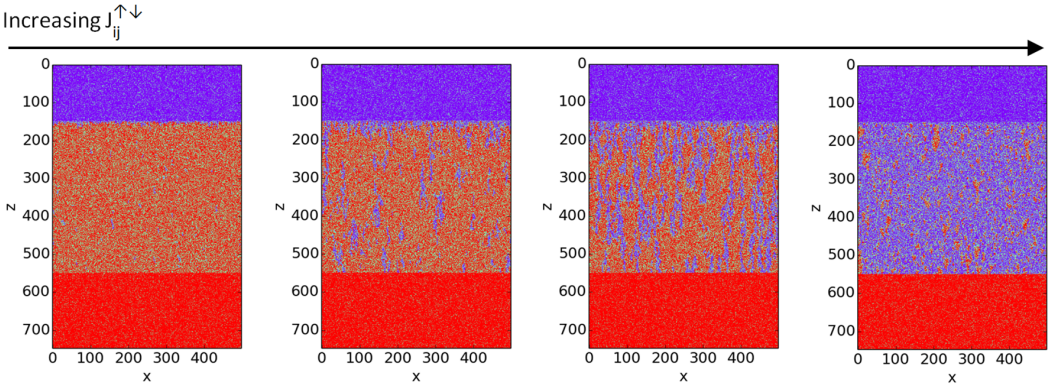

Figure 6.18: Models of randomly distributed alloys illustrating the effect of reversing the upper layer whilst changing the coupling strength of the middle layer. The concentration of the middle layer was set to 60%, above the percolation threshold.

where $J_{ij}^{\uparrow\downarrow}$ and $J_{ij}^{\uparrow\uparrow}$ are the exchange parameters between anti-parallel and parallel spins respectively. If $\Delta H_i < 0$ then spin i is flipped. This can in turn destabilise the surrounding spins and causes an avalanche effect resulting in paths of flipped spins similar to those seen earlier in Figure 6.15. These paths of flipped spins are still highly dependent on the percolation threshold. ΔH in Equation 6.2 assumes that the exchange coupling between parallel spins is different to anti-parallel ones. So by increasing one of $J_{ij}^{\uparrow\downarrow}$ or $J_{ij}^{\uparrow\uparrow}$ the system is weighted towards a particular configuration.

The results of increasing $J_{ij}^{\uparrow\downarrow}$ so that the system is weighted towards flipping spins is shown in Figure 6.18. As before, paths of flipped spins appear through the material. The largest difference now is that regions of spins are flipped throughout the layer and any of these areas of reversed spins could act as a nucleation point for a path of negative spins.

Magnetic properties such as ordering temperature vary with composition; this combined with the effect of composition on percolation effects through the middle layer show that even small changes in Co concentration could have a large impact on the coupling between layers. This has the potential for highly sophisticated design of amorphous heterostructures with complex and varied properties.

6.5 The Model and Hysteresis Data

It has been shown that by using a simple Ising model on a square lattice, increasing the concentration of interacting atoms has a large impact on the distance over which coupling can exist in a randomly distributed alloy. We attribute the exchange

bias observed in minor hysteresis loops recorded at the Co L_3 edge to an exchange coupling between the upper and lower layers which is mediated by Co rich regions which propagate through the middle layer. According to these models, the coupling observed experimentally should be highly dependent on Co concentration. It would be interesting in further work to look at whether Co concentration in the middle layer changes the observed exchange bias and whether reducing Co concentration reduces the interlayer coupling.

All models here assumed a 2D lattice for simplicity and to limit the computational power needed. To more accurately reflect real samples, the models would need to be extended to 3D. The percolation threshold in 3D drops to approximately 0.31 for a simple cubic lattice [193, 194] so for real samples we would expect the concentration of Co needed for exchange coupling across the layers to be much lower than that introduced in this chapter.

The effect of applying an external field to the material was introduced into the model and combined with percolation effects. The result was that additional regions of reversed spins appeared in the middle layer which acted as nucleation points for interacting paths through the middle layer which would act to increase the interlayer coupling. This could potentially explain the strong coupling observed between the upper and lower parts of the sample observed as exchange bias in the minor hysteresis loops.

Note that the percolation models presented here use a 'top down' method which gives a snapshot of the system after a single pass through the lattice. To extend this model such that simulated magnetic hysteresis loops could be produced, a probabilistic method would be needed in which the system develops with time. This would most likely make use of Monte Carlo simulations but this is beyond the scope of this work.

Further work could also be carried out including the effect of the Sm in the lower layer. The models used here took the Co sub-network only and did not incorporate the Sm sub-network at all. It did not account for the layers having different magnetic moments and the resulting proximity effects. We would expect to see regions of reversed Sm spins, which would account for the spread in the distribution of reversed Sm observed in the minor hysteresis loops recorded at the Sm M_4 edge. This would provide a mechanism for both the weaker interactions between the Sm and Co sub-networks compared to the Co inter-layer interactions and also for the pinning which is observed in the minor loops as exchange bias. To incorporate this into the model would involve significantly more effort and is therefore beyond the scope of this work.

As an additional point, these models only account for a plus or minus spin but in an exchange spring we would expect the spins to rotate in plane. To take this study further and look at exchange spring behaviour, the rotation angle and the subsequent in plane component of the moment due to this rotation would need to be accounted for.

Conclusion

We have observed element specific hysteresis loops at 100 K and 300 K at the Co L_3 and Sm M_4 edges for a trilayer of $Sm_9Co_{91}/Co_{60}(AlZr)_{40}/Co_{85}(AlZr)_{15}$. At 100 K and 300 K, a two-step hysteresis loop is observed in the Co data indicating that there are two magnetic reversals rather than three as would be expected from the chemical structure. There being only two reversals was attributed to weak interactions between the Co and Sm sub-networks compared to stronger inter-layer Co interactions resulting in magnetically interacting regions which spanned the chemical interfaces.

An extended reversal was observed in the Sm hysteresis loop indicating that there are regions of high Sm density throughout the amorphous layer which have a range of switching fields resulting in the hysteresis shape observed. The Sm hysteresis loop also reversed at a different switching field to that at the Co edge, again indicating that the intra-layer Co and Sm interactions are weaker than the inter-layer Co-Co interactions resulting in the sub-networks being slightly decoupled from each other.

It was suggested that the overall magnetic structure of the trilayer presented in this chapter consisted of connected, interacting regions with high Co density. These localised regions with high Co density existed as a result of the random distribution of the amorphous layers. This model of interconnected regions of magnetic material which span the interfaces and extend into the other layers deviates from the conventional model of an exchange spring where the magnetic structure is described as having planes of rotating spins similar to a torsion spring. This model results in magnetic behaviour which is highly dependenet on the concentration of the magnetic species in the alloy.

The interconnected regions of Co mediate a long range interaction between the upper and lower layer which is observed in minor loops as a shift in applied field; this has been loosely termed here as an exchange bias. This exchange bias is seen at both temperatures showing that there is coupling between the upper and lower layers even 200 K above the ordering temperature of the middle layer.

Modelling of the distribution of Co throughout the amorphous alloy was

carried out to illustrate how interactions may be mediated by interconnected regions of high Co concentration. The effect of Co concentration was investigated near the 2D percolation threshold and also the effect of the coupling strength. The models showed how an amorphous multilayered system such as this is highly dependent on composition.

Chapter 7

Resonant X-ray Reflectivity Studies of Amorphous SmCo-CoAlZr Trilayers

This chapter presents a study of the SmCo-CoAlZr trilayer discussed in the previous chapter which determines the layer-by-layer chemical and magnetic structure using resonant x-ray scattering. A discussion is given of the effect of tuning to an absorption edge on the scattering length density. The details of the fits to the reflectivity data are given including how oxide layers at the surface and changes in chemical composition at interfaces were incorporated into the models.

7.1 Introduction

The previous chapter presented element specific hysteresis data which demonstrated that the expected magnetic structure in the SmCo-CoAlZr trilayer of an exchange spring did not fully describe the complex internal structure that must exist in the amorphous layers. To determine the magnetic profile as a function of depth, it is not enough to just use hysteresis data. As such, to take the investigation of the SmCo-CoAlZr trilayers further, a technique is required which allows a layer-by-layer study of the chemical and magnetic properties, and for this we turn to resonant x-ray reflectivity. This chapter will present the chemical and magnetic structures, as determined by fitting resonant x-ray reflectivity data, for a SmCo-CoAlZr trilayer at 100 K which is just below the ordering temperature of the middle layer and at 300 K which is well above the ordering temperature of the middle layer.

As mentioned in the previous chapter, the exact magnetic structure and in

particular the position of the magnetisation reversal point when one layer reverses with respect to the other, can not be exactly determined from the hysteresis data recorded using x-ray resonant magnetic scattering (XRMS) because of the dependence of the asymmetry ratio (A.R.) on **q**. This information can, however, be extracted from specular reflectivity studies as it provides information on the chemical and magnetic structure as a function of z. In these studies, the field is held constant whilst the sum and A.R are recorded as a function of q_z. The field is held at values which correspond to points on the hysteresis loops to enable a study of how the magnetic structure is altered by an applied field.

This chapter will start by explaining how the scattering factors are incorporated into the model of the trilayer in GenX, especially when the x-rays are tuned to resonant energies. Some of the subtleties of using a genetic algorithm to fit the data are outlined before fits to the data are presented for single layers of SmCo and then SmCo-CoAlZr trilayers.

7.2 Resonant Scattering Factors

In Chapter 2, the scattering of a photon was described as being a process where the electrons in the scattering medium act as a driven harmonic oscillator. As such, the scattering length of the material is highly dependent on the local environments of the atoms. Alternatively, in a quantum mechanical picture, the transition probability changes based on the available empty states which is directly determined by the electronic structure of the material and so will vary between alloys even measuring at the resonant edge of a chemical element which is common to both materials.

The change in the x-ray absorption for different compounds at a resonant edge is used as a spectroscopic technique, called X-ray Absorption Spectroscopy (XAS), for studying changes in composition and is used, for example, to study the composition of corrosion layers in copper [195]. There are large differences observed in the XAS spectra of different Cu compounds recorded at the Cu L_3 edge [196]. The differences in the band structure between materials of different compositions can be exploited to study a wide range of compounds [197–199].

To take an example, there are clear differences observed between the shape and position of the absorption edges of pure Co and CoO. These differences are driven by the local environments within these materials resulting in changes to the electronic band structure, even though the XAS is recorded at the same absorption edge [200]. The XAS spectra for Co and CoO have been shown to have a shift in the absorption edge of approximately 1 eV. If we refer back to Chapter 2, it

was shown that the scattering factors vary hugely across the resonant edge. It could therefore be expected that materials with different chemical compositions could have small differences in the absorption edge resulting in large changes in the resonant scattering factors. XAS has been used to study many materials containing Co at the L edges indicating clear changes in the absorption [201–203].

The total scattering length density (SLD) of a material will therefore not only be the average value of the different chemical species but will also be an average of the different local environments of these elements. For example, a Sm atom surrounded by Co atoms will have a different resonant scattering factor to Sm surrounded by Al. Therefore, an alloy where two different species are arranged in a material together would be expected to behave differently from the two elements individually when in their pure form.This makes it very difficult to estimate the SLD values of complex alloys, particularly if there is any oxidation or chemical mixing.

When it comes to the samples investigated here, the scattering factor for the three layers in the trilayer would be expected to be

$$f_{Co_{85}(AlZr)_{15}} = f_{Co} \times 0.85 + f_{Al} \times (0.7 \times 0.15) + f_{Zr} \times (0.3 \times 0.15) \tag{7.1}$$

$$f_{Co_{60}(AlZr)_{40}} = f_{Co} \times 0.6 + f_{Al} \times (0.7 \times 0.4) + f_{Zr} \times (0.3 \times 0.4) \tag{7.2}$$

$$f_{Sm_9Co_{91}} = f_{Sm} \times 0.09 + f_{Co} \times 0.91. \tag{7.3}$$

The f values in principle could be taken straight from recorded values for the pure materials such as those from the Henke tables [100]. It would normally be logical to assume that f_{Co} would have the same value for all three layers. Taking the model of the driven harmonic oscillator, however, this is not necessarily the case. This has the consequence that the scattering factors for the three layers could be very different even when recorded using x-rays from just the one energy and this adds extra complexity to the fit.

The theoretical values of the scattering factors obtained from the Henke tables also have large uncertainties associated with them when at soft energies and close to an absorption edge. When the energy is within 15% of the $L_{2,3}$ or $M_{4,5}$ edges, f' has an uncertainty of approximately 30% and the uncertainty on f'' is in the range 20-40% [100]. These large uncertainties give further justification for allowing the scattering factors to vary by large amounts within the fit.

Fitting data sets recorded at multiple energies can result in each layer, at each energy, having a different scattering factor which rapidly increases the number of fitting parameters needed. This is where the use of a genetic evolution algorithm really comes into its own as it is robust enough to cope with many data sets and

parameters. The down side is that the more variables that are added, the slower the fitting runs and so a balance was needed between having enough parameters to accurately represent the sample structure without slowing the fit down excessively.

The genetic evolution algorithm used in GenX was discussed in Chapter 4. The user assigns the parameters a range over which random numbers are chosen. If the new set of randomly selected numbers gives a lower figure of merit than previously achieved, these are taken as the new parameter set. Whilst the algorithm is searching within the parameter set, however, the range available for each parameter is reduced. The consequence of having many parameters when using a genetic evolution algorithm is that it takes a long time to search within the parameter set for a better solution, during which time the available range for each individual parameter is reduced. It is sometimes the case that the range can be reduced to the extent that the program can not find the best solution.

Additional complications occur in the fitting process because it is not possible to know the exact electron density, *dens*, in the alloys used to construct the multilayer. The value of *dens* is calculated using the material density in kg/m^3, but the exact value is not known for each of the layers, especially for the ternary CoAlZr alloys. However, the value of *dens* should be the same for all data sets regardless of the x-ray energy used. The SLD is calculated by the product of f and *dens* and this introduces a challenge when fitting these parameters as it is necessary to fix one of f or *dens* to ensure that the fit is accurate. Without fixing one of these parameters, they can be altered such that the product remains the same but the ratio varies. This is problematic when fitting multiple data sets as the fit becomes prohibitively complex.

Not only do the scattering factors change for individual layers when on resonance which causes complications when trying to fit reflectivity data recorded at multiple energies, but this presents a bigger challenge when there is chemical mixing or oxidation. The next section will introduce XRMS from a single layer of SmCo; it will illustrate some of the challenges presented when fitting data at multiple energies and how these were dealt with using the available tools within the GenX software.

7.3 Single SmCo Layers

The logical starting point for investigating the trilayer structures, is with a single layer. This should provide information on the resonant scattering factors, oxidation of the capping layer and whether there is high roughness between the interfaces at the substrate and buffer layer. This information would then in principle be useful

for restricting some of the parameters when fitting the trilayer to help reduce the number of variables included in the fit. As such, specular XRMS data was recorded for single films of SmCo capped with AlZr. The data was fitted using GenX and used to check the quality of the SmCo single layer samples including interface roughness and uniformity. The single layers of Sm_xCo_{1-x} were grown as described in Chapter 6.

Reflectivity from a Sm_8Co_{92} film (which is the single film with the closest composition to that in the trilayer) was recorded on beamline X13A at the NSLS, Brookhaven National Laboratory. Figure 7.1(a) shows the sum reflectivity signal recorded at the Co L_3 and Sm M_4 edges and also using a Cu K_α laboratory source. Figures 7.1(b) and (c) show the A.R. obtained at the Co L_3 and Sm M_4 edges respectively. All specular reflectivity data for the single film samples were recorded at 300 K. These were fitted simultaneously which was intended to constrain the parameter set to provide confidence in the fit. As the value of the SLD is given by the product of the density and scattering factors, it is possible when fitting single data sets to find a solution where the parameters can vary by large amounts as long as the total product is the same. By using multiple data sets, the individual values of the scattering factors and densities should be restricted to give more accurate values. It is also important to highlight that many solutions can exist which give very similar looking fits, but they can often give unphysical results in the SLD profile. This must be monitored whilst fitting the data and parameters should be restricted such that they can only take values which give meaningful SLD profiles.

The chemical and magnetic SLD profiles obtained from the GenX fits are presented Figure 7.1(d) and (e) respectively. The chemical SLD shows that the SmCo is uniform across the layer in the z direction. The resonant scattering factors of the Sm and Co were large and negative resulting in notable changes in the chemical SLD values at the resonant edges. The capping and buffer layers of AlZr are clearly visible, with the dashed lines serving as a visual guide indicating the upper and lower boundaries. To achieve a good fit, it was necessary to add in extra layers between the SmCo and AlZr layers both at the top and bottom where the scattering factors were allowed to vary slightly from those of either the SmCo or AlZr. These layers are approximately 20 Å thick and it would be logical to assume that these are regions of chemical intermixing. As a Gaussian error function is unlikely to account for variations in the chemical profiles, this goes some way towards allowing flexibility in the fit. Fitting without these extra layers was very unsuccessful and gave poor fits. The very uppermost layer was assumed to be ice, and as such was allowed to vary slightly ($\leq$ 5 Å) in thickness and roughness between data sets to account for small amounts of ice build up during experiments.

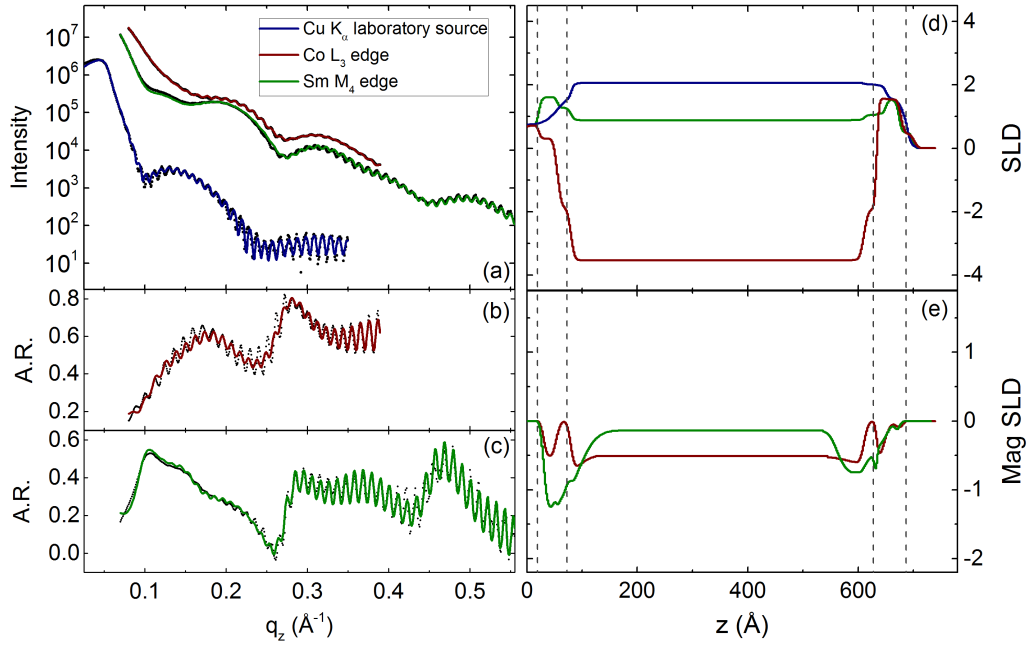

Figure 7.1: Reflectivity data for a single film of Sm_8Co_{92} with a buffer and capping layer of $Al_{70}Zr_{30}$ on a Si substrate. (a) Specular reflectivity data recorded using (blue) a Cu $K_{\alpha 1}$ laboratory x-ray source. Additionally the sum signal is shown which was recorded using synchrotron radiation tuned to (red) the Co L_3 edge and (green) the Sm M_4 edge. A.R. recorded at (b) the Co L_3 edge and (c) the Sm M_4 edge. The points are the data and lines are the fit obtained using GenX. The SLD profiles obtained from the fits are shown for (d) the chemical and (e) the magnetic parts.

The magnetic SLD profiles in Figure 7.1(e) give unexpected results, with a magnetic moment clearly visible in the capping and buffer layers when AlZr should be non-magnetic. Quite often it is possible that there are not unique solutions for fits like these and so many attempts were made to fit the data with the magnetisation restricted to the SmCo layer only, trying different initial conditions. None of these attempts to fit the data could achieve the fringe periodicity in the A.R. necessary for a good fit which suggested that the magnetic layer needed to be thicker whilst the chemical SLD needed to remain unchanged. The lack of success at fitting the data when the model included a distinct layer of SmCo with a non-magnetic capping and buffer layer showed that the layers in the sample were possibly not exactly of the composition expected from the growth. To account for this in the model, the scattering factors were allowed to vary and the capping and buffer layer were given a magnetic moment of 1, whilst the magnetic scattering factors were fitted.

Both the real and imaginary parts of the SLD profiles obtained from the fits

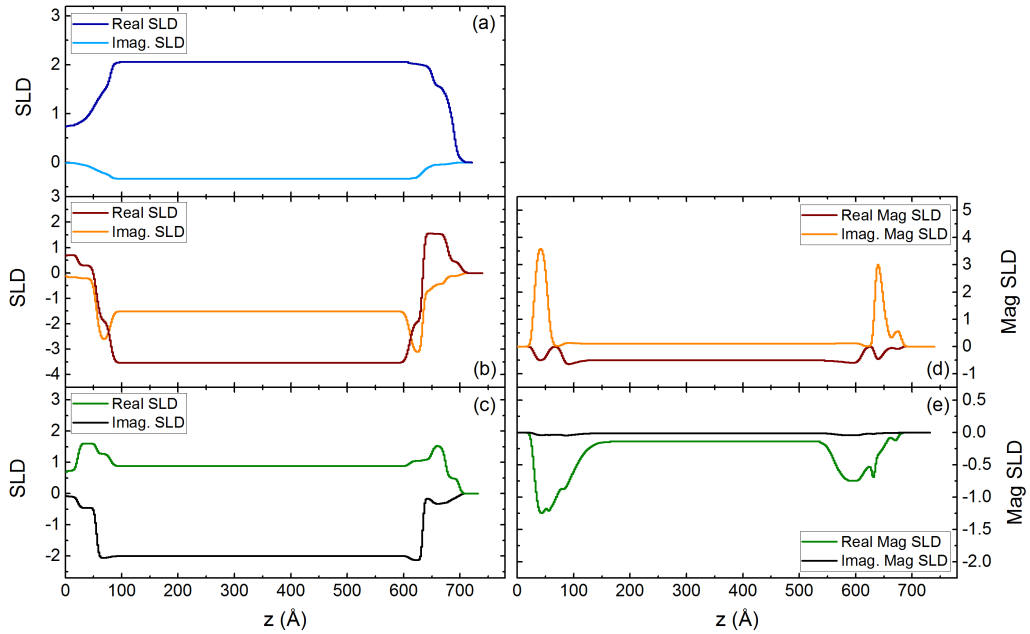

Figure 7.2: SLD profiles obtained from fits to reflectivity data for a single film of Sm_8Co_{92}. (a) Real and imaginary parts of the SLD from data recorded using a Cu $K_{\alpha 1}$ laboratory x-ray source. (b)-(c) Real and imaginary parts of SLD profiles from data recorded at the Co L_3 edge and Sm M_4 edge respectively and (d)-(e) are the corresponding magnetic SLD profiles.

to the single layers are shown in Figure 7.2. There are differences between the values of the real and imaginary parts but the structural information is much the same in both. As all the necessary information is contained in the real part and not much more is gained from the imaginary part, Figure 7.1 only shows the real SLD for simplicity. Henceforth, all SLD profiles presented from here on in this chapter will only show the real part. This helps to make a comparison between different SLD profiles easier.

To illustrate why it was that the magnetisation was allowed to extend into the capping/buffer layers, the best fit achieved with the magnetisation in the these layers set to zero is shown in Figure 7.3. In Figure 7.3(a) the data and fit is given and (b) shows the corresponding real parts of the chemical and magnetic SLD. This model allowed the magnetic SLD at the upper and lower interfaces of the SmCo layer to change by increasing or reducing the magnetic SLD value but did not allow it to extend into the capping/buffer layers. The details of how this is incorporated into the model in GenX were given in Chapter 4. No matter how the magnetic SLD was changed at the upper and lower interfaces in the SmCo, however, a suitable fit could not be achieved across the entire q_z range.

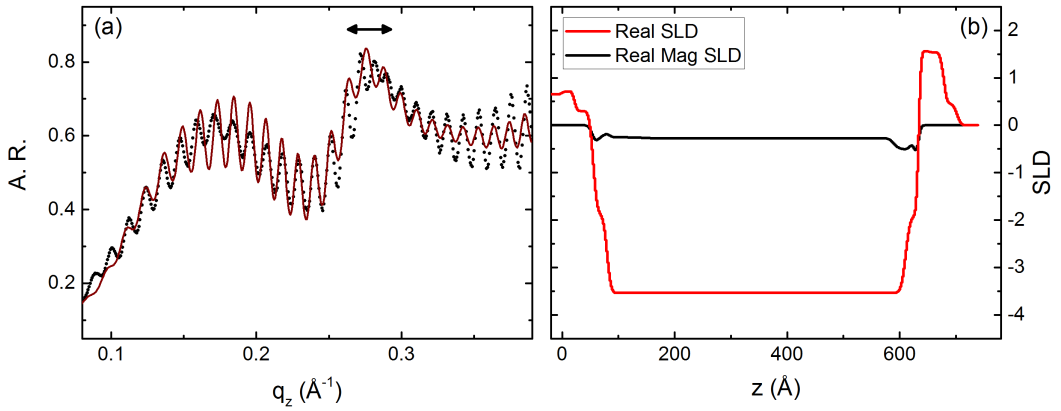

Figure 7.3: Asymmetry ratio for a single film of Sm_8Co_{92} recorded at the Co L_3 edge with data (points) and fit using a model which did not allow magnetisation in the buffer/capping layers.

Particular difficulties were had with fitting the fringes in the region marked by the arrow in Figure 7.3 at around 0.27 $Å^{-1}$, which indicated that a feature of approximately 25 Å thickness would be needed to change the phase of the fringes to be able to achieve a good fit in this region. In the SLD profile from the fit in Figure 7.1, the magnetic feature observed in the AlZr layer at the bottom of the sample is 25 Å thick which corresponds directly to the feature predicted to achieve the necessary fringe thickness. Attempts to include a feature like this at the bottom of the SmCo layer without extending into the buffer layer were unsuccessful at fitting the fringes in the region marked by the arrow in Figure 7.3. Although there was not the same evidence for a similar magnetic layer at the top of the sample, it was logical that the same could be assumed for the capping layer.

A similar example is given for the data recorded at the Sm M_4 edge with the data and fit shown in Figure 7.4(a) and the chemical and magnetic SLD profiles from the fit in Figure 7.4 (b). Again, the best fit achieved whilst keeping the magnetisation in the capping/buffer layers set at zero is shown and shows that the overall shape of the simulated A.R. does not match the data well. The magnetic SLD was allowed to vary at the upper and lower interfaces of the SmCo to try and achieve a suitable fit but was unsuccessful. The particular feature in the data that was difficult to fit was in the region marked by the arrow at around 0.27 $Å^{-1}$. To fit this feature, the magnetic SLD required the surface regions to be altered significantly and in particular, the magnetisation needed to be extended into the capping/buffer layer to move the feature to higher q_z whilst retaining the shape of the rest of the data.

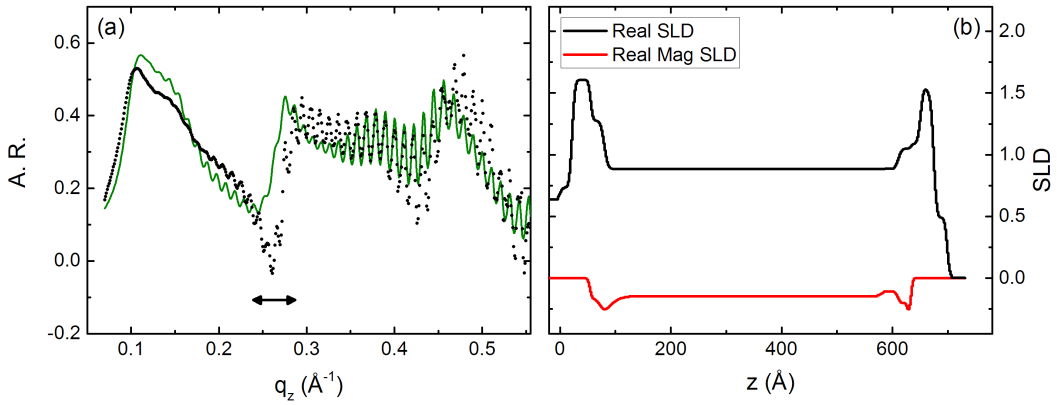

Figure 7.4: Asymmetry ratio for a single film of Sm_8Co_{92} recorded at the Sm M_4 edge with data (points) and fit using a model which did not allow magnetisation in the buffer/capping layers.

The magnetic SLD from the fit to the data recorded at the Co L_3 edge as presented in Figure 7.1 shows that the magnetisation extends uniformly across the SmCo layer and drops to zero as would be expected. There is then, however, a distinct magnetic layer at the top and bottom suggesting that there is Co in the capping and buffer layers with a magnetic moment. The data recorded at the Sm M_4 edge does not show the drop to zero magnetisation at the upper and lower edges of the SmCo layer but instead increases to a magnetic SLD value that is much larger than that for the SmCo layer itself. This suggests there is either an increased amount of Sm in the buffer layers or that the composition of the layer has Sm with an enhanced magnetic scattering factor. It appears that there may have been some issues with the growth of the capping and buffer layers for this SmCo single layer sample which has resulted in mixed layers incorporating Sm, Co and AlZr. Although there are issues with the capping/buffer layers, it should be possible to use the resonant scattering factors for the Co and Sm obtained from the fits to the single layers in the fitting of the trilayer data. It will likely be necessary to account for chemical mixing in the trilayer model as well.

Modelling the oxide has also presented many challenges whilst fitting this data and the simulated reflectivity is very sensitive to the SLD profile of the surface region, particularly for the resonant energies due to absorption effects. Initial attempts to fit these with a single layer of AlZr with a thin oxide layer on top using published scattering factors obtained from [100] were unsuccessful. The fit suggests that there is a complex oxide formed at the surface of the samples which is not well described by a Gaussian error function. This was modelled by setting the AlZr

layer to actually be three thin layers and allowing the composition to vary for each of these layers. The scattering factors at each energy were then allowed to deviate from the tabulated values slightly to account for the chemical variations in such a layer. As the scattering factors of the mixing layers were allowed to vary to account for different local environments of chemical species as the composition changed, it was difficult to determine the exact chemical profiles. Fits were attempted where the scattering factors were kept constant for each element at each energy and the ratio of elements changed, but produced very poor results.

Work looking at similar amorphous AlZr films showed that the alloy formed regions of polycrystalline Al resulting in other regions of the material becoming Zr rich [204]. This would fit with the AlZr capping layer on the samples in this work exhibiting a complex chemical composition profile. It was also found that the AlZr films had an oxide of up to ∼6 nm formed on the surface. This would be the entirety of the 2-3 nm capping layer on the samples presented here. This oxide was shown to have gradients of Zr-enrichment and O-deficiency throughout, plus a mixture of Al and Al_2O_3 near the surface [205]. This adds extra complications for fitting as it is unlikely that the oxidation of the AlZr will be well represented by a Gaussian error function, especially when fitting data recorded at multiple energies. This also suggests that the SmCo layer is not necessarily protected from oxidation by the capping layer. This information about mixing layers and complex oxides can be carried forward to help with fitting the data from the trilayer.

7.4 Reflectivity from a SmCo-CoAlZr Trilayer at 100 K

X-ray resonant specular reflectivity measurements were performed on the SmCo-CoAlZr trilayer structure described in the previous chapter. At 100 K, it was expected that the middle $Co_{60}AlZr_{40}$ layer was just below its ordering temperature. From the full hysteresis data we saw that the magnetisation reversals for the Co and Sm sub-networks occurred at different field values and thus revealed that the sub-networks within the SmCo layer were less strongly interacting than the inter-layer Co interactions. Fits to specular reflectivity should provide a layer-by-layer depth profile of the chemical and magnetic structure which can be used to understand the processes behind this apparent 'decoupling'.

7.4.1 XRMS at the Co L_3 Resonant Edge

Specular scans were recorded at the Co L_3 edge at 100 K with the sum signal shown in Figure 7.5(a) and the A.R. recorded at different values of applied field in

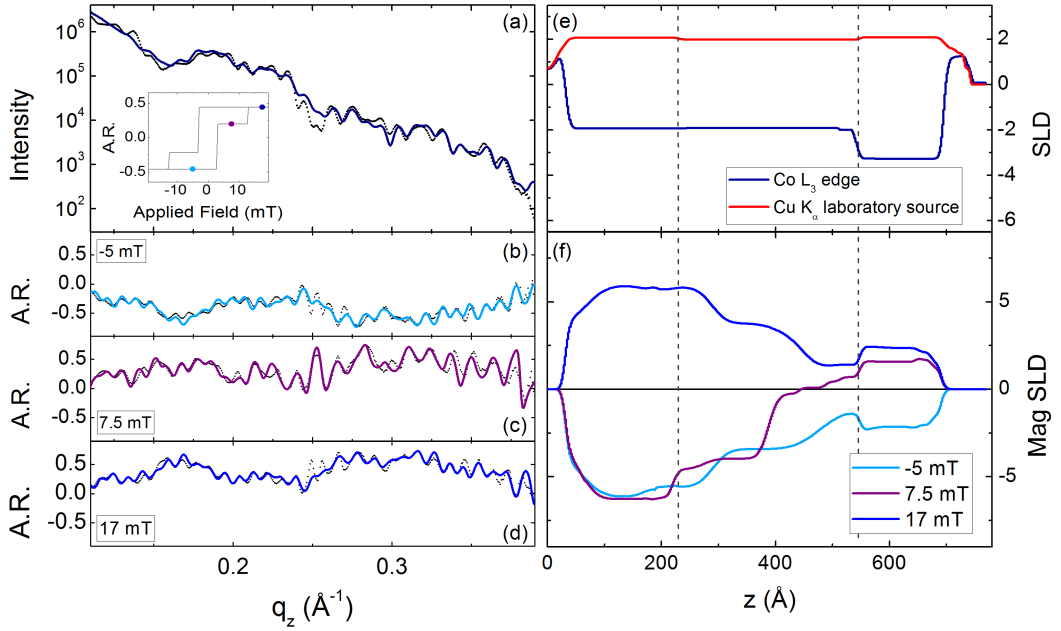

Figure 7.5: Specular reflectivity data (points) and fit obtained using Genx (line) for a SmCo-CoAlZr trilayer. (a) Sum and (b)-(d) A.R. were recorded in different applied fields at the Co L_3 edge at 100 K. The inset indicates the field values on the hysteresis loop. The corresponding SLD profiles for (e) the chemical and (f) the magnetic structure. The SLD profile recorded using a Cu K_α laboratory source is shown in (e) for comparison.

Figures 7.5(b)-(d). The data and the fits obtained using GenX are shown and also the corresponding SLD profiles from the fits with the chemical SLD in Figure 7.5(e) and the magnetic SLD in Figure 7.5(f). Additional reflectivity data was recorded using a Cu $K_{\alpha 1}$ laboratory source, the data for which was presented at the start of Chapter 6 and also using synchrotron x-rays at the Sm M_4 edge. Similar to the single layers, these data sets were included in the fitting to constrain the parameters and give confidence in the fit. The SLD profile from the fit to the data recorded using the laboratory source is shown in Figure 7.5(e) for comparison.

With the single layers, it was found that the fits were highly sensitive to the oxide structure, and this was also the case for the trilayer. Similar methods were used to fit the trilayer data as were used for the single layers, using multiple oxide layers and allowing the scattering factors to vary. As the data was recorded at low temperature, a small ice layer was included in the model on the upper surface. The chamber was kept under high vacuum during the scattering experiment so ice build up would be expected to be minimal. Therefore the ice layer was restricted to be less than 10 Å.

The scattering factors for Co varied quite significantly at the Co L_3 edge compared to those for the laboratory source. A difference in scattering factors was previously observed for the single layer sample and is somewhat expected as according to the Henke tables, for pure Co, the scattering factor can vary from approximately 20 to -20 across the L_3 absorption edge [100]. The scattering factors could be further altered because these layers are amorphous alloys and so it is not possible to exactly calculate the expected scattering factor as it would be highly dependent on the local environment of the Co atoms throughout the alloy. The altered scattering factors were accounted for in the GenX model by fitting the values of the real and imaginary part of the Co scattering factor at the Co L_3 edge for the upper $Co_{85}AlZr_{15}$ layer. The scattering factors for the Co in the $Co_{60}AlZr_{40}$ and SmCo layers were then allowed to vary by a ratio which was set as a fitting parameter. Fits that were carried out without allowing these ratios to vary were unsuccessful, highlighting the importance of accounting for the changes to the scattering factors caused by alloying. The ratio of the real part of the scattering factor for the bottom SmCo layer was found to be almost three times that of the $Co_{85}AlZr_{15}$ layer.

The chemical SLD profile at the Co L_3 edge is shown in Figure 7.5(e) and has the same low roughness between layers seen in the data recorded using the laboratory source with good uniformity throughout each layer. The magnetic SLD profile, however, presented in Figure 7.5(f) shows a completely different story. The inset in Figure 7.5(a) is provided to clarify where on the hysteresis curve the asymmetry ratio data sets are recorded, with measurements taken at the positive and negative saturated states and also at the point where the only first reversal had taken place.

One of the clearest features in the magnetic SLD profiles is the extension of the magnetisation of the lower layer into the middle layer. The magnetisation extends into the $Co_{60}AlZr_{40}$ by approximately 50 Å before gradually reducing to a much lower SLD value. The dashed lines indicate the position of the chemical interfaces to make a comparison easier. In the hysteresis data, there was an exchange bias observed in the minor hysteresis loops, which can be explained by the enhanced magnetisation extending into the middle layer creating a strong coupling between the upper and lower layers. The Co in the soft upper layers is then pinned by the Co in the hard lower layer which leads to the observed exchange bias.

The extension of the SLD into the middle region suggests that the Co nearest the bottom layer has an enhanced moment due to proximity with the SmCo. The proximity effects are far reaching, more than can be explained with a nearest neighbour model alone. This could take the form of interconnected Co atoms as modelled in the previous chapter whereby the enhanced moment is mediated by

regions of high Co concentration which span the interface. The strongly interacting Co rich areas would provide a mechanism for the different switching fields between the hysteresis loops recorded at the Sm and Co edges.

All three magnetic SLD profiles indicate a decrease in the SLD value at the very lower interface between the SmCo and the AlZr buffer layer. The fit was very sensitive to the exact shape of this lower region which extends over roughly 50 Å. This region could be caused by intermixing at the interface, similar to that observed in the single layers, leading to the formation of a layer with a different magnetic moment to SmCo. Any compositional change would have to be slight though as there is no change observed in this region in the chemical SLD and there was also no noticeable chemical or structural difference observed in the cross-sectional TEM images in the previous chapter. The composition of this mixing layer must be a material for which the magnetic properties are very sensitive to small chemical changes.

The magnetic SLD recorded at 7.5 mT was taken at the point when the top part of the sample had reversed. Although it was assumed that the soft upper part of the sample underwent a magnetisation reversal first, it was not actually possible to tell this from the hysteresis curves. The fit confirms that when the first reversal takes place, the whole of the top $Co_{85}AlZr_{15}$ layer reverses and part of the middle $Co_{60}AlZr_{40}$ layer. The portion of the middle layer that had an enhanced moment from proximity to the SmCo layer still has a larger SLD value than the upper part of the middle layer but to a lesser degree than in the saturated state. The lessened enhancement could be due to competing interactions between the upper and lower parts of the sample. When the magnetisation of the upper part of the sample reverses, this causes a reduction in the moment of the middle layer.

There is a large region over which the magnetisation gradually reverses in the middle layer which is consistent with an exchange spring model. The magnetisation reversal position, i.e. the point at which the magnetisation reverses in the middle layer, is at approximately 100 Å from the upper layer. It is difficult to estimate the accuracy of this value, or whether the fit is sensitive to large changes in the position of the magnetisation reversal point. Changing the parameter which controls the position by even a few Angstroms or changing the slope or shape of the profile in the middle layer, had a large effect on the quality of the fit. This does not mean, however, that the position at which the magnetisation reverses is well defined, as the position could be fixed at another value, the fit re-run, and it is possible that a new solution could be found that also gives a suitable fit. It is common that there are not unique solutions for complicated fits like these which have many parameters.

To fully investigate the effect of moving the magnetisation reversal position, multiple fits would ideally be carried out from different initial conditions and the SLD profiles compared. Alternatively, the parameters could be set to new values and the fitting algorithm re-run, but both methods would be lengthy processes. Running multiple fits with different initial conditions presents problems as the parameters initially used need to be relatively good approximations for a fit to be successful, so care must be taken when selecting which parameters to change and by how much.

GenX allows a scan of the figure of merit to be performed across the maximum allowed range of a parameter. Scanning a parameter can often have an oscillatory behaviour as the interference patterns become constructive/destructive. Performing a parameter scan can illuminate whether this parameter has got restricted to a local minimum but this method must be treated with caution as it only scans within the current parameter set, which would change if the fit were re-run. Some attempt was made to investigate the accuracy of the reversal position by scanning it across its full possible range and noting the oscillatory behaviour. The reversal position was changed to another value at a point where the figure of merit was at a local minimum and then the fitting algorithm was run once more from this new starting point. The SLD profile was found to return to that shown in Figure 7.5 consistently. It is difficult to tell, however, whether this is a good indication of the quality of the fit or whether it was due to the rest of the parameter set constraining the fit.

7.4.2 XRMS at the Sm M_4 Resonant Edge

Data was recorded at the Sm M_4 resonant edge and is presented in Figure 7.6. The left of Figure 7.6 shows the data as the points and the fits obtained from GenX as the solid lines. The resulting SLD profiles from the fits are shown on the right with the chemical SLD shown in Figure 7.6(e). The SLD profile obtained from the fit to the data recorded using the laboratory source is also shown for comparison. The chemical SLD profile indicates a large change in the scattering factor for the Sm in the SmCo layer at the M_4 edge. The chemical SLD is otherwise much the same as that recorded using the laboratory source.

To enable a good fit, a background was applied to the simulated A.R. and was included by creating a constant α_{bckg} which was applied as $\alpha_{bckg} \times q_z^4$. A background signal of this type could be needed if there were differences in intensities between the left- and right-handed polarised photons reaching the sample. Slight variations in beam positions between the two helicities could result in differences in intensity causing the background observed in the A.R. to shift up or down from the normal zero value.

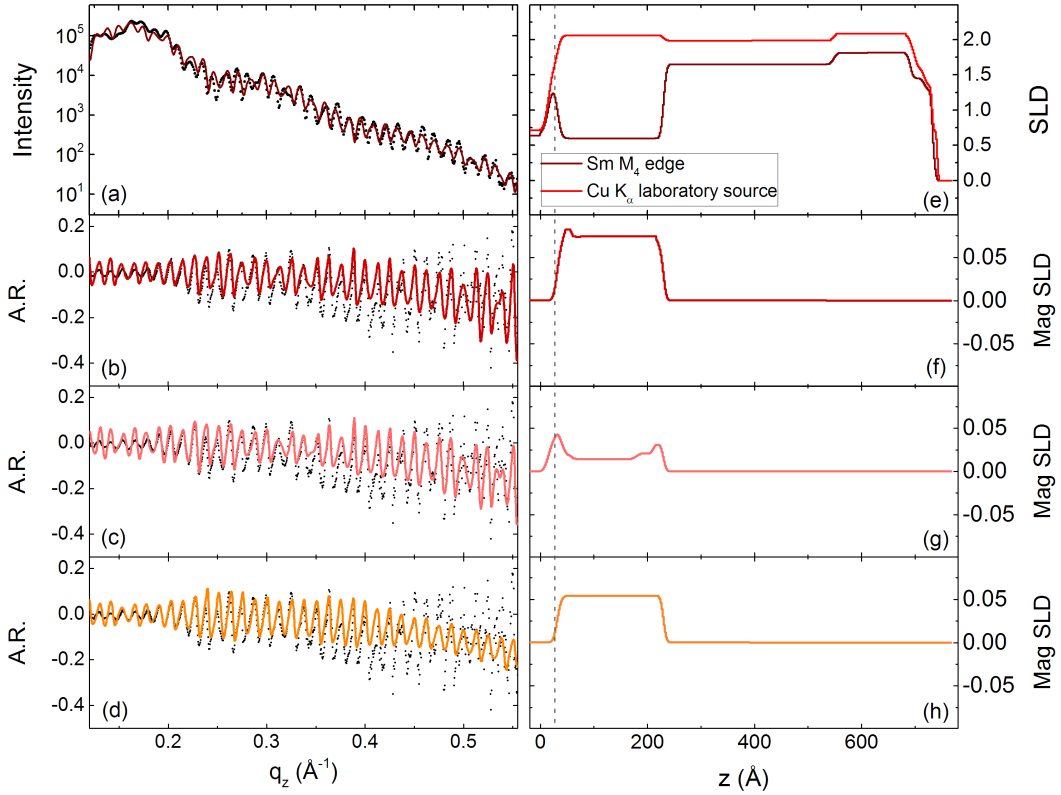

Figure 7.6: Specular reflectivity data (points) and fit obtained using GenX (line) for a SmCo-CoAlZr trilayer. The data is recorded at the Sm M_4 edge at 100 K. (a) Sum and (b)-(d) A.R. signals with the corresponding SLD profiles for (e) the chemical and (d)-(h) the magnetic structure. Different models were used for fitting the A.R. with (upper) no magnetisation in the AlZr layer, (middle) no magnetisation plus no changes to the magnetic SLD at the interfaces and (lower) the magnetisation extends into the AlZr layer.

Multiple models were used to attempt to fit the A.R. data recorded at the Sm M_4 edge, the first restricted the magnetisation to the SmCo and bottom mixing layer only which are the layers which should contain Sm. This model resulted in the A.R. shown in Figure 7.6(b) and corresponding magnetic SLD in Figure 7.6(f). The magnetic SLD shows a mostly uniform magnetisation across the layer with a region with a slightly increased magnetisation at the lower interface. The fit to the data gives the correct fringe periodicity but the simulation does not match the fringe amplitude well in the higher q_z range. This suggested that there was something lacking in the fit and this prompted the use of alternative magnetic structures.

Referring back to the fits to the data recorded for the *single* SmCo layers, these suggested that the magnetisation extended into the buffer layer and so to

investigate whether this would give a better fit, a model was used which set the lower buffer layer to have a magnetic moment. The fit to the data with a magnetic buffer layer is shown in Figure 7.6(c) and the corresponding magnetic SLD in (g). The fit is much the same as that shown in Figure 7.6(b) with a similar figure of merit value, even though the magnetic SLDs between the two fits are very different. This suggests that the simulated A.R. at the Sm edge is not particularly sensitive to changes in the magnetic SLD profile.

As there was very little sensitivity to changes in the shape and thickness of the magnetisation in the SmCo layer, another model was tried which had uniform magnetisation across the layer with no changes in magnetic SLD at the interfaces. The aim of trying another magnetic structure was to illustrate how sensitive the fit was to changes in the magnetic SLD at the Sm edge for this sample. The fit is shown in Figure 7.6(d) and the corresponding magnetic SLD in (h) and these indicate that although the fit is fairly similar to those in Figures 7.6(b) and (c), there is a decrease in fringe height at high q_z. The decrease in fringe height is related to the region with a higher magnetic SLD value at the lower interface of the SmCo layer. This gives some confidence that there needs to be some magnetically enhanced region between the substrate and the SmCo as was observed for the single layers, but this technique does not provide enough sensitivity at this energy, for this sample, to determine the exact magnetic structure of this region.

The increase in magnetisation at the lower interface is in contrast to the rounded shape and drop in the magnetic SLD profile observed between the AlZr buffer layer and the SmCo which is observed for the trilayer at the Co L_3 edge. The difference between the data recorded at the two energies suggests that any variation due to intermixing or strain, effects the Co and Sm sub-networks differently, and gives possible evidence for a mechanism behind the 'decoupling' of the sub-networks observed in the Co and Sm hysteresis data.

7.5 Reflectivity from a SmCo-CoAlZr Trilayer at 300 K

X-ray resonant specular reflectivity data were also recorded at 300 K. It was expected that the magnetic SLD would show that the upper and lower magnetic layers were separated by a layer with very low, if not zero, magnetisation as the middle $Co_{60}AlZr_{40}$ layer was well above its ordering temperature. Recall from the previous chapter, however, that coupling was observed between the upper and lower layers as an exchange bias in the minor hysteresis loops. Reflectivity data should illuminate the magnetic structure and help to explain why this exchange bias occurs.

7.5.1 XRMS at the Co L_3 Resonant Edge

The reflectivity data are shown in Figure 7.7, where again the data and fits are shown at a range of applied fields with the corresponding SLD profiles obtained from the GenX fits. As with the data recorded at 100 K, the fits were carried out with the data recorded using the laboratory source, and those at the Co and Sm edge simultaneously to give confidence in the results.

To fit the sum signal which is shown in Figure 7.7, the scattering factors were allowed to vary by only a small amount from those recorded at 100 K. It is possible that the measurements at the two temperatures were recorded at slightly different energies and this could alter the resonant scattering factors. The thickness and roughness of the ice layer which was added for the 100 K sample were reduced and all other layer thickness and roughness values were allowed to vary by up to 5 Å to allow for any expansion at the higher temperature. The chemical SLD profiles are therefore very similar to those found from the data recorded at 100 K with low roughness between layers and a large negative value for the real part of the resonant scattering factor for Co.

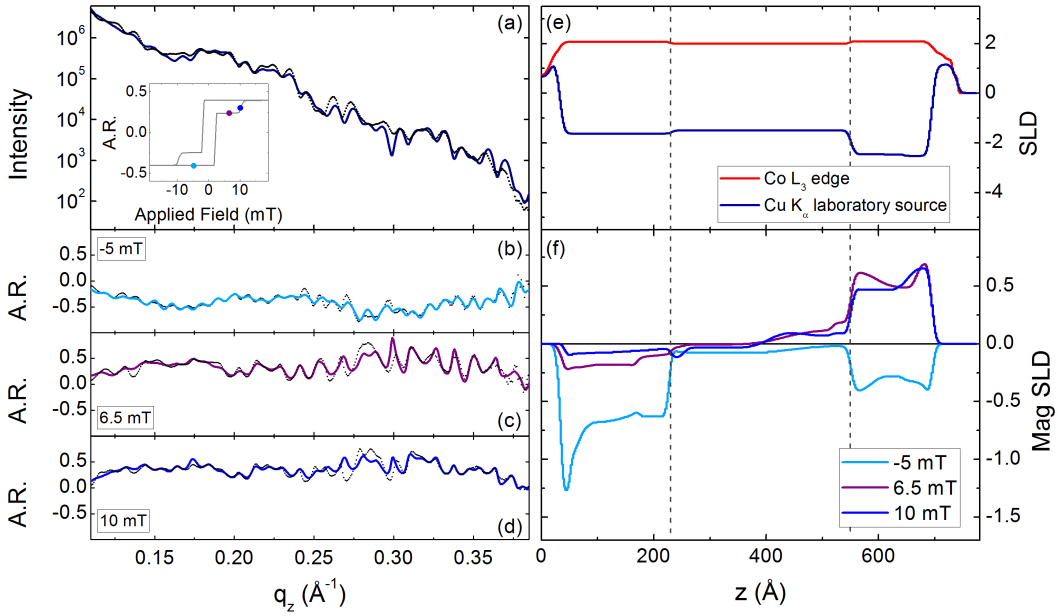

Figure 7.7: Specular reflectivity data (points) and fit obtained using Genx (line) for a SmCo-CoAlZr trilayer at 300 K. (a) Sum and (b)-(d) A.R. were recorded in different applied fields at the Co L_3 edge. The inset indicates the field values on the hysteresis loop. The corresponding SLD profiles for (e) the chemical and (f) the magnetic structure. The SLD profile recorded using a Cu K_α laboratory source is shown in (e) for comparison.

The magnetic SLD data was recorded at values of the applied field of -5 mT, 6.5 mT and 10 mT as marked on the hysteresis loop in the inset in Figure 7.7(a). These points were chosen as they give a point at full saturation, then a state where the first reversal has taken place but not the second, and then also a point where the second switch has started but has only partially reversed. This should be able to provide information on the nature of the second reversal at 300 K which has a more rounded shape than that at 100 K. The A.R. recorded in a positive saturating field was also recorded but is neglected here as it does not add to the discussion and is just the total reversal of that shown in Figure 7.7(b).

The magnetic SLD profiles shown in Figure 7.7(f) indicate that when the sample is in a negatively saturating applied field the upper and lower layers are still strongly magnetic but the middle has a much lower magnetisation as expected. From the fit, the magnetisation in the middle layer is a factor of 0.1 of that of the upper $Co_{85}AlZr_{15}$ layer. The magnetisation in this middle layer is low but non-zero which could explain the exchange coupling observed in the minor hysteresis loops.

There is an increase in the magnetisation at the lower interface between the AlZr buffer layer and the SmCo approximately 30 Å thick which could be due to intermixing. This was observed in the data at 100 K as a region with a decrease in the magnetic SLD. A layer of different composition at the bottom could have a different magnetic moment to the SmCo layer and also a different temperature dependence of the magnetisation. As the scattering factors were allowed to vary to account for this mixing layer, and because the resonant scattering factor is so highly dependent on local environment, it is impossible to say from the reflectivity data presented here exactly what the composition of this mixing layer is. It is, however, clear that there is very minimal change to the chemical SLD, but a large change in the magnetic SLD, suggesting that the chemical composition of this layer is not significantly different to the SmCo layer. One possibility is that a layer of SmCoZr is formed, with dilute amounts of Zr. Work on alloys like these has shown that even a few percent of Zr in SmCo can have quite a large impact on the magnetic properties including changes to the temperature dependence of the magnetisation [206, 207]. The specular reflectivity presented here is not capable of giving a detailed chemical composition profile, and without further chemical analysis it is not possible to directly identify the exact details of why this layer has enhanced magnetisation.

At 6.5 mT, the upper layer has reversed and the position at which the magnetisation changes sign in the SLD profile is at approximately 400 Å from the substrate which is the same as was observed at 100 K. Additionally, the point at which

there is a change of sign in the SLD at 300 K does not change as the applied field value is increased. The fixed position of the SLD switching point shows that the model that was suggested previously where the changing ratios of the two reversals in the Co hysteresis loop were explained by a moving domain wall, must not be valid. Instead, the changing ratios of the hysteresis loops must be due to the net magnetisation changing, possibly from the Co in the lower SmCo layer as shown in Figure 7.7(f). The value of the magnetic SLD of the lower layer has dropped, indicating that the magnetisation of the Co within the SmCo layer is reduced.

The full hysteresis loop recorded at 300 K showed a gradual reversal on the second switch and the asymmetry ratio in Figure 7.7(d) was recorded at a field of 10 mT, this is at the point on the hysteresis loop which is directly on the curved part of the hysteresis loop. It was previously suggested that the gradual reversal observed for the second switch was due to intra-layer coupling between the Sm and Co sub-networks in the lower SmCo layer causing the Sm and Co within the layer to undergo a reversal together. At 10 mT the magnetic SLD profile shows that the magnetisation of the Co in the SmCo layer has dropped significantly, whilst the rest of the SLD profile remains mostly unchanged, which would support this theory.

To illustrate the reversal processes occurring, modelling of the randomly distributed Co lattice was carried out using the same methods as presented in Chapter 6. The exchange integral and interaction strength for each layer were set such that the top layer was magnetically soft and reversed first. As can be seen in Figure 7.8, as the applied field is increased, the magnetisation in the upper layer

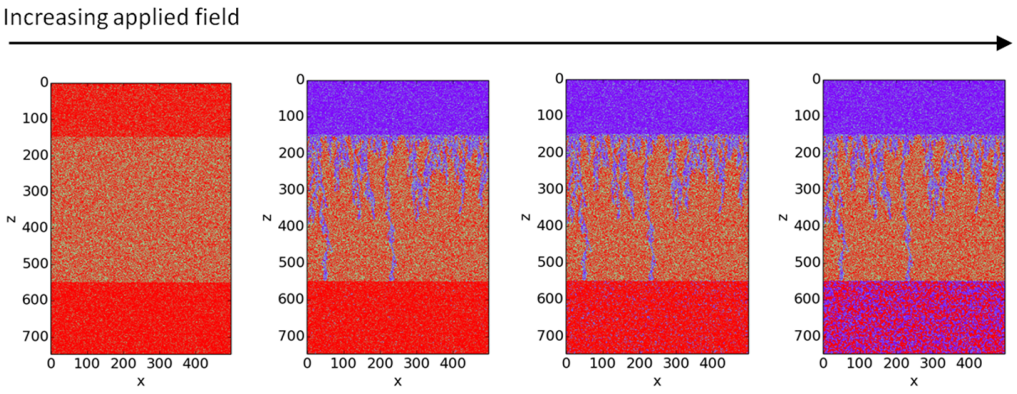

Figure 7.8: Model of randomly distributed alloys illustrating the effect of increasing the applied field on the magnetisation reversal processes. The applied field is increased, causing the upper layer to reverse followed by regions of high Co concentration in the middle layer. As the applied field is increased further, regions of high Co concentration in the bottom layer switch.

reverses and causes regions of high Co concentration near to the interface to also undergo a reversal. This would result in the reversal of the upper region of the middle $Co_{60}AlZr_{40}$ layer as observed in the magnetic SLD profiles. As the applied field is increased further, regions of high Co concentration in the lower layer gradually start to reverse magnetisation resulting in a reduction of the magnetic SLD value of the Co in the entire SmCo layer which is also observed in the magnetic SLD profiles.

Once again, it is important to note that this modelling is meant as more of a visual aid to explain the magnetisation reversal mechanisms at work in an amorphous multilayer which has a complex internal structure. There would be much more work required to accurately reproduce the full range of interactions at work to fully model these systems. In further work it would be ideal if the models could be used to produce simulated hysteresis curves to compare to experimental results.

7.5.2 XRMS at the Sm M_4 Resonant Edge

Data was again recorded at the Sm M_4 edge with the measured sum signal shown in Figure 7.9(a). The data are the points and the fits obtained from GenX are the solid lines. The resulting chemical SLD profile from the fit is shown in Figure 7.9(d) alongside the fit to the data recorded using a Cu K_α laboratory source for comparison. The fit at the Sm M_4 edge shows less change in the scattering factor for the Sm in the SmCo layer than at 100 K. This could be due to the x-ray energy being slightly different for this data set, resulting in a change to the scattering factors. The oxide layer also appears different in this figure but this is likely due to fitting the data over a larger range of q_z. As data were available at lower q_z which is more sensitive to the surface regions, it was possible to refine the fit for the surface region.

Figures 7.9(b) and (c) show fits to the A.R. data at the Sm M_4 edge with no magnetisation in the buffer layer and then also allowing a magnetisation respectively. Similar to the low temperature magnetic SLD profile, there is a single magnetic layer with an enhanced magnetisation at the lower interface which again would be consistent with chemical intermixing at the interface. As before with the data at 100 K, the increase in magnetic SLD was needed at the lower interface to achieve the larger fringe amplitude at high q_z. Again, the simulated A.R. is not particularly sensitive to changes in shape of the magnetic SLD profile for this sample at the Sm M_4 edge and the fits in Figures 7.9(b) and (c) are very similar despite the apparent differences in the SLD profiles. There is also some enhancement of the magnetisation at the upper surface although there is probably not sufficient sensitivity to determine whether this is a true representation of the magnetic structure in the sample. The

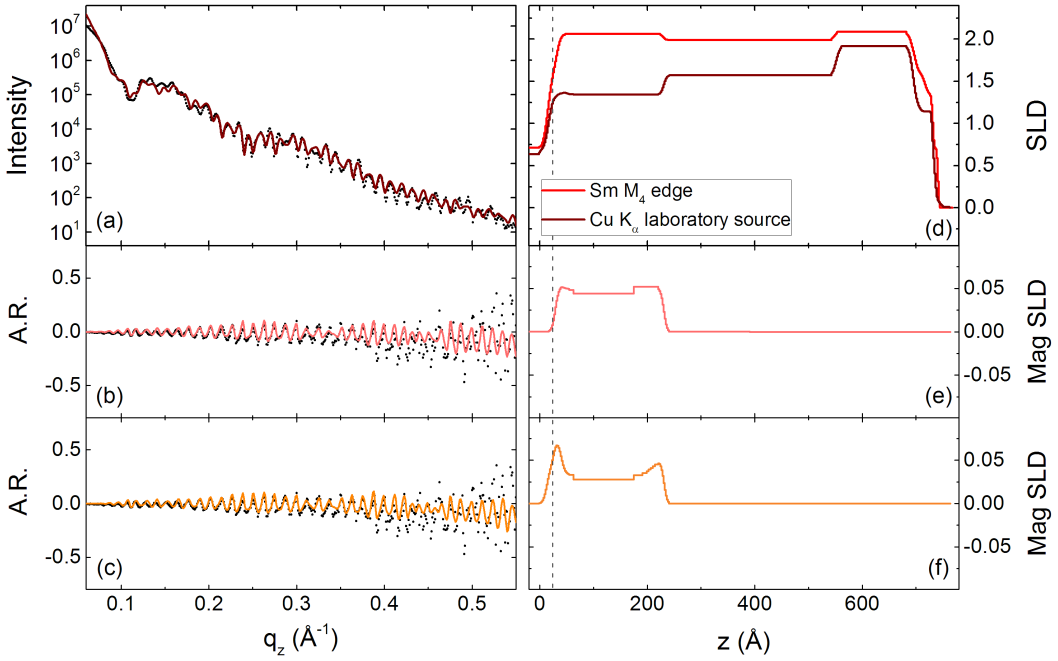

Figure 7.9: Specular reflectivity data (points) and fit obtained using GenX (line) for a SmCo-CoAlZr trilayer. The data is recorded at the Sm M_4 edge at 300 K. (a) Sum and (b)-(c) A.R. signals with the corresponding SLD profiles for (d) the chemical and (e)-(f) the magnetic structure. Different models were used for fitting the A.R. with (upper) no magnetisation in the AlZr layer and (lower) allowing the magnetisation to extend into the AlZr layer.

sharp steps observed in the magnetic SLD are an artefact of the slicing model. The steps can be removed by reducing the slice thickness; this does not noticeably alter the simulated reflectivity but is more computationally intensive.

Conclusion

This chapter introduced how scattering factors change at resonant absorption edges and how the scattering length density is altered by large amounts when tuning to a resonant energy of a particular element. The scattering length is also different depending on the composition of the material containing the resonant element because the local environments of the chemical elements throughout the layer change the resonant scattering factors.

Fits to x-ray resonant magnetic reflectivity data for single layers of Sm_8Co_{92} were presented at the Co L_3 and Sm M_4 resonant edges and the challenges of fitting oxides and mixing layers with complex chemical profiles were discussed. It was

shown that these single layers which appear to have smooth, well-defined interfaces with TEM microscopy and laboratory x-ray reflectivity, have large changes in chemical and magnetic scattering length density at the interfaces when using resonant scattering. The challenge that this poses when fitting multiple data sets recorded at different energies was discussed.

The investigation was then taken further by studying trilayers of SmCo-CoAlZr using the same techniques. Resonant reflectivity at 100 K at the Co L_3 edge revealed that there was a region of enhanced magnetisation which extended from the SmCo layer into the middle of the $Co_{60}AlZr_{40}$ layer in the trilayer which was most likely caused by proximity to the lower SmCo layer. The observation of a proximity induced enhanced magnetisation is consistent with a model where regions of high Co concentration span the interface and the enhanced moment is propagated via these interconnected regions. Magnetic data recorded at different applied field values showed that the top $Co_{85}AlZr_{15}$ layer reversed first with a portion of the middle $Co_{60}AlZr_{40}$ layer which again could be supported by a model with interconnected Co rich regions. At 300 K, a similar magnetic structure was found, but this time with a much reduced magnetisation in the middle layer.

Data recorded at the Sm M_4 edge showed that there was a single magnetic layer at both temperatures with an enhanced moment at the lower interface. The magnetisation in the lower region was shown to possibly extend into the buffer layer which was also the case for the single layers and was explained by chemical intermixing. There was not, however, sufficient sensitivity to changes in the magnetic SLD to determine the exact shape, SLD value and thickness of this mixing layer at the Sm M_4 edge.

In the previous chapter, the magnetisation reversals observed in the hysteresis data recorded at the Sm and Co resonant edges showed that the Co and Sm sub-networks were 'decoupled', with reversals occurring at different applied fields. The decoupling was attributed to there being stronger inter-layer coupling between Co regions than intra-layer coupling between the Sm and Co sub-networks. The extension of the magnetic moment into the middle layer observed in the Co edge SLD profiles, and partial reversal in the middle layer when the upper layer reverses, provides evidence for the decoupling of the sub-networks and also explains why only two reversals were ever observed in the hysteresis data. The reflectivity data presented in this chapter gives further evidence that there exists a complex internal structure in amorphous multilayers which has potential to be manipulated and tuned for use in both basic research and technological applications.

Chapter 8

Patterned Arrays of FePd Islands

This chapter introduces the theory of scattering from patterned arrays including the link between scattering and Fourier transforms, an introduction to how the convolution theorem can be used to simulate a rocking curve and also how the shape of elements in the array affects the form factor. It goes on to present results of resonant scattering from first a continuous FePd film and then a square array of circular FePd islands. These results are then compared to simulations which are generated using the theory introduced in the start of the chapter.

8.1 Introduction

The work so far has presented a study of the magnetic properties of a superlattice, where the geometry was restricted by growing thin films, and a multilayer where the magnetic properties were altered by combining layers with different compositions. In this chapter, the magnetic interactions in a thin film which is patterned such that the magnetism is confined within nano-scale elements are investigated. We present an example of how magnetic materials can be engineered by patterning a thin film into an array of circular islands, and observe how confining the moments in a nano-scale element changes the magnetic properties of a thin film.

Many new phenomena come about by imposing geometric restrictions upon magnetic materials. Such patterned media have wide ranging applications such as in high density data storage [208], integrated magnetic-electronic devices [209] and even in biotechnological applications [210]. These geometrically constrained nanomagnets provide a unique opportunity to study magnetism in confined systems

and form an excellent platform for testing fundamental theorems in magnetostatics and micromagnetics [211–213].

Ferromagnetic materials generally form magnetic domain structures to minimise the magnetostatic energy. When the dimensions of these systems are reduced to the sub-micrometre scale, however, the formation of domains is often no longer energetically favourable and a single domain state is formed [60]. The formation of domains is highly dependent on the width of the domain walls, with small domain walls being much more likely to allow multiple domains to form in a nano-scale magnet. The width of domain walls is determined by the balance between the exchange energy and the magnetic anisotropy. It can be shown that the width of a Bloch wall is given by [17]

$$\delta = \pi S \sqrt{\frac{2J}{K_u a}} \tag{8.1}$$

where S is the spin, J the exchange constant, K_u the anisotropy constant and a the lattice parameter. Thus, a larger exchange interaction yields a wider domain wall and higher anisotropy gives thinner walls.

Much of the early work investigating patterned arrays was carried out using permalloy ($Ni_{80}Fe_{20}$) which is a widely studied material and so the parameters in Equation 8.1 are well-known [214–216]. Permalloy has a low anisotropy giving a domain wall width of the order of hundreds of nanometres depending on the thickness of the film. The low anisotropy means that relatively large (of the order of hundreds of nanometres up to several microns) magnetic structures can be patterned which will form a single domain state. Materials with low anisotropy are desirable when creating patterned arrays because then the shape anisotropy becomes the dominant driving mechanism defining the magnetic state. FePd has a similarly low anisotropy and this is one of the reasons it has been chosen for this work, along with its soft magnetic properties.

Permalloy has an ordering temperature of $\sim 560°C$ and so it is necessary to perform AC demagnetisation which involves rotating the sample whilst reducing the applied field to reduce the magnetisation to zero. The ordering temperature of FePd is highly dependent on composition [217] but is generally much lower than for permalloy and so the sample can be demagnetised relatively simply by heating. This makes experiments on FePd patterned arrays easier to perform than for permalloy.

Reducing the thickness of the island compared to the radius, causes the spins to tend to align in-plane. In a circular island of ferromagnetic material the moments align parallel to the edges of the island creating magnetic states such as vortices, or leaf structures [218]. The most energetically favourable state when a magnetic

vortex is induced in an island is often where the central spins turn out-of-plane [219]. Changing the inter-island separation influences magnetostatic interactions and affects the formation of the vortex state [220]. By tuning island thickness, radius, spacing and composition there is scope for producing highly tunable nanomagnetic structures such as the patterned array of FePd islands presented in this chapter.

This chapter presents a study of an array of circular islands on a simple square lattice using x-ray magnetic resonant scattering, but in principle, this technique could be used to study more complex arrays. Artificial spin ice is one particular area of current research that makes use of patterned arrays of nano-scale magnetic islands. The term spin ice was initially used to describe geometrically frustrated magnetic systems where atomic magnetic moments mimic the frustration of hydrogen positions in water ice [63]. By instead using arrays of nanoscale magnets rather than atomic moments, systems can be engineered to study magnetic frustration in detail [221]. Reducing the dimensions of a magnetic material into a nano-scale structure with an ellipsoidal or rectangular shape can force the magnetisation to align along the long axis and increase the dipole interactions between the elements. This results in the islands behaving as macrospins parametrized by the Ising variable $S = \pm 1$. This can be exploited by arranging the magnetic nano-structures into an array on a square [61] or honeycomb (Kagome) lattice [222].

Microscopy techniques such as magnetic force microscopy and Lorentz microscopy are well suited for providing images in real space of the magnetic configurations of the islands in an artificial spin ice array [223]. Photoemission electron microscopy with X-ray magnetic circular dichroism (PEEM-XMCD) can also be used to determine real space images of the magnetisation of the individual elements in the arrays, providing a highly sensitive, element specific technique for obtaining information on the vertex configurations and ordering [64, 224]. PEEM-XMCD has the added advantage that synchrotron radiation can be used to record time-resolved data to study magnetisation dymnamics. Microscopy techniques, however, probe a relatively small area of the sample and are only sensitive to the very surface of the material so thick capping layers or oxides can obscure the signal. To overcome these limitations and investigate the magnetic interactions across a large area of the surface whilst measuring the entirety of the islands, we can turn to x-ray resonant magnetic scattering.

This chapter presents data obtained using x-ray resonant magnetic scattering both as a function of q_z on the specular condition and of q_x to produce rocking curves. Rocking curves can be used to extract in-plane, structural information of the islands in a patterned array and by tuning to a resonant edge we can also probe the

element specific magnetic structure. Previous work fitting rocking curves measured at grazing incidence with x-rays has been carried out using simple patterned samples [225] and even using the sum and difference signals [226] but there is very little work on modelling complicated magnetic structures using this technique. For these reasons, this chapter presents a preliminary study of a simple square array of circular islands. It is hoped that the results of this work motivate and provide the technical underpinning for future research towards accurately fitting rocking curves, with the goal of forming detailed models of the magnetic structure within patterned arrays in a wide variety of shapes, sizes and magnetic configurations.

8.2 Theory of Scattering from Patterned Arrays

To analyse and interpret the scattering data, the link between experimental results and theory must be made. This section outlines some principles of scattering from patterned arrays.

8.2.1 Scattering and Fourier Transforms

To begin, consider a diffraction experiment as outlined in Figure 8.1. A plane wave is incident on a set of slits and interference of the transmitted waves results in a modulated intensity $I(q)$ observed on a distant screen or detector. The apertures are assumed to be one-dimensional and are described by an aperture function, $A(x)$. This function takes the values of ones and zeros corresponding to areas where there is, or is not a slit respectively [81].

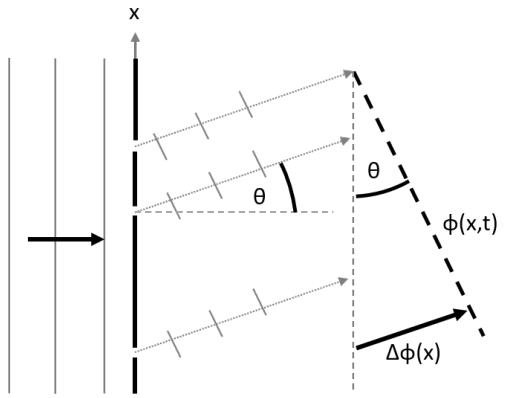

Figure 8.1: Illustration of geometry of a typical diffraction experiment and the resulting interference pattern, $I(q)$.

To calculate the interference pattern, using the principle of superposition, the waves that emerge from the aperture are summed. In the region between x and $x + \Delta x$ the amplitude of the contribution is proportional to $A(x)\Delta x$. The change in phase relative to the incoming wavefront, $\Delta\phi$, depends on the distance, x, and the angle relative to the incident wave, θ, and is given as

$$\Delta\phi = \frac{2\pi}{\lambda} x \sin\theta. \tag{8.2}$$

The complex contribution to the resultant wave is

$$\Delta\psi = \psi_0 A(x) \exp^{iqx} \Delta x \tag{8.3}$$

where $q = \frac{2\pi}{\lambda}\sin\theta$ and ψ_0 is a constant. The total diffracted wave is the sum of these terms in the limit $\Delta x \to 0$

$$\psi(q) = \psi_0 \int_{-\infty}^{\infty} A(x) \exp^{iqx} dx \tag{8.4}$$

which is the *Fourier transform of the aperture function.* The measured signal, the intensity, is then the modulus-squared of the complex function $\psi(q)$

$$I(q) = |\psi(q)|^2 = \psi(q)\psi(q)^* \tag{8.5}$$

Note that the phase information is lost in Equation 8.5. This is significant as it has the consequence that one can not simply take the inverse Fourier transform of a reflectivity profile to obtain structural information. It is for this reason that we must use a model to obtain a best fit to the data, implemented using programs such as GenX.

8.2.2 A Single Aperture

The next question is how to start to apply this to an array of islands. In fact, we can think of these islands as being similar to the picture in Figure 8.1 except now instead of a series of slits, we have reflective islands with each island acting as a source of waves. For now, the islands will be considered to be completely flat, and they either reflect or do not reflect x-rays, similar to the slits introduced before. There is assumed to be no reflection from the substrate; this is a reasonable assumption as the substrate for the samples in this work is relatively rough due to the patterning process, which results in a weak reflected signal.

First, consider the reflection from a single island. Take an aperture which is

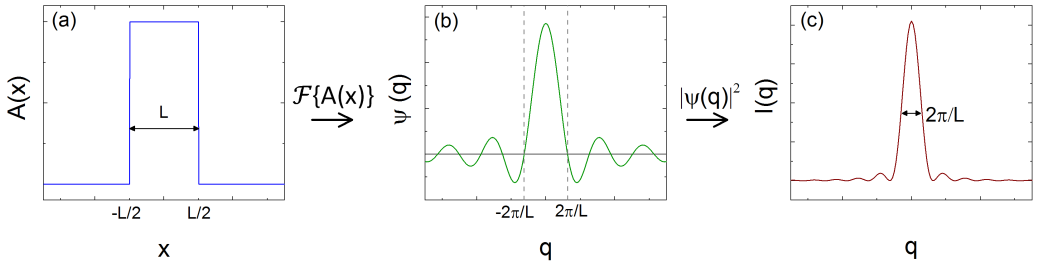

Figure 8.2: (a) Aperture function of a single slit of width L, (b) Fourier transform of the single slit aperture function and (c) the modulus-squared of the Fourier transform which gives the intensity.

a slit of width L, giving an aperture function of

$$A(x) = \begin{cases} 1, & \text{if } |x| \geqslant L/2 \\ 0, & \text{otherwise} \end{cases} \tag{8.6}$$

as shown in Figure 8.2 (a). The Fourier transform, $\psi(q)$, of a boxcar function of this kind is a sinc function ($\text{sinc}(x) = \frac{\sin(x)}{x}$), shown in Figure 8.2 (b). The intensity is the modulus-squared of $\psi(q)$

$$I(q) \propto \left| \frac{1}{q} \sin(\frac{qL}{2}) \right|^2 \tag{8.7}$$

which is shown in Figure 8.2 (c) where the width of the peak is inversely proportional to the width of the island.

Note that this work assumes we are in the Fraunhofer regime, i.e. the detector is sufficiently far from the sample that at any point across the detector surface the waves can be considered to be parallel. If this assumption does not hold, the equations become much more involved and we are said to be in the Fresnel regime.

8.2.3 Fourier Series

This chapter will make extensive use of Fourier series to describe the scattered signal recorded from patterned arrays. The fundamental principle behind Fourier transforms is that they are an infinite sum of periodic, sinusoidal functions. Any periodic function $f(x)$ can be represented as an expansion of *sine* and *cosine* terms such as

$$f(x) = a_0 + \sum_{m=1}^{\infty} a_m \cos \frac{2\pi m x}{L} + \sum_{n=1}^{\infty} b_n \sin \frac{2\pi n x}{L} \tag{8.8}$$

where a_0, a_m and b_n are the coefficients of the Fourier series. Figure 8.3 represents a periodic square wave as a sum of sinusoidal functions which is analagous to the arrays of islands that will be the subject of study in this chapter.

As more sinusoidal terms are added into the sum, the Fourier series better represents the original function. The square function in the figure can be represented by sine terms with the following conditions:

$$a_0 = \frac{1}{2}$$
$$a_m = 0, \quad m = 1, 2, ...$$
$$b_n = \begin{cases} \frac{2}{\pi n}, & \text{n odd} \\ 0, & \text{n even} \end{cases}$$

Figure 8.3 shows a sum terms with (a) n=1, (b) n=3 and (c) n=15 and as higher terms are included, the function becomes better described by the sum of terms.

The scattering experiments that will be introduced later in this chapter include reflectivity scans both as a function of q_z (on the specular condition) and of q_x (rocking curves), as described in Chapter 4. In a rocking curve, at larger q_x, higher order Fourier components are included in the scattered signal. Satellite peaks at higher q_x in the rocking curve contain information from higher order Fourier series terms and the higher the Fourier series terms, the better the island shapes are de-

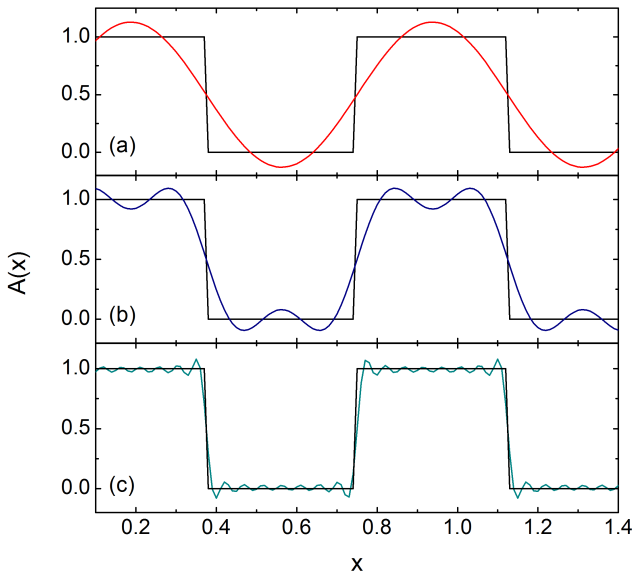

Figure 8.3: A square waveform represented as a Fourier series with increasing numbers of sinusoidal terms for (a) n =1, (b) n = 3 and (c) n = 15.

scribed. We therefore get more information about the magnetic structure towards the edges of the islands at higher q_x.

8.2.4 Lattices and the Convolution Theorem

So far, we have considered a single aperture, so the question is, how do we extend this to an array of apertures? For this, we need to use the convolution theorem. To aid with the discussion Figure 8.4 gives an illustration of the convolution theorem and shows how convolving two functions and then performing a Fourier transform produces the same result as performing a Fourier transform on the original functions and multiplying these together.

An array of islands can be modelled as an infinite array, $h(x)$, with separation between elements d, convolved with an aperture function, $g(x)$, with width L. The functions $h(x)$ and $g(x)$ are shown in Figures 8.4(a) and (b) respectively and the convolution $h(x)*g(x)$ is shown in Figure 8.4(e). To generate the simulated scattered

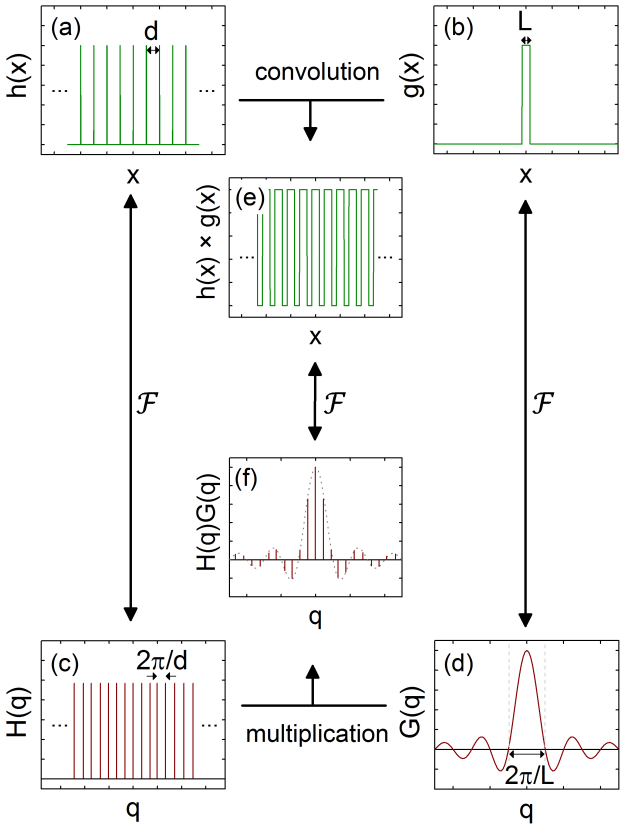

Figure 8.4: Illustration of an example application of the convolution theorem. The vertical arrows represent a Fourier/inverse Fourier transform. Adapted from [227].

signal, the Fourier transform of the convolved function is taken, giving $H(q)G(q)$ as shown in Figure 8.4(f) [227]. An equivalent method to calculate the simulated scattered signal is to take the Fourier transform of $h(x)$ and $g(x)$ independently, respectively giving $H(q)$ and $G(q)$ as shown in Figures 8.4(c) and (d). Multiplying these together produces the simulated scattered signal, $H(q)G(q)$, which is shown in Figure 8.4(f).

The simulated scattered signal shown in Figure 8.4(f) consists of peaks at periodicities of $2\pi/d$ contained within an envelope function called the form factor which has a shape determined by $2\pi/L$. The experimental rocking curves will therefore contain information about the island spacing in the peak separation and about the island shape and size in the form factor. Note that it is assumed that the function $h(x)$ shown in Figure 8.4(a) is an infinite array, which in reality is some finite region constrained by the projected coherence length of the beam. To accommodate the finite coherence length, the signal must be multiplied by an additional term, the Fourier transform of the coherence length, which would take the form of another $sinc(q)$ function.

8.2.5 The Form Factor

The slits considered so far have been assumed to be an aperture function that is either 0 or 1 but this could, however, be any complex function where $0 \leq A(x) \leq 1$. For example, the structure investigated in this chapter is an array of circular islands, on a square lattice where the islands have been shown to be domed. The aperture function for this structure is therefore a function that represents the shape and size of the islands. As the form factor is given by the Fourier transform of the aperture function, the shape of the disks directly affects the shape of the rocking curve.

Some examples of the effect of changing the aperture function, $A(x)$, on the form factor are shown in Figure 8.5, where the aperture function gives a one-dimensional projection of the island shape and can give some insight into how the doming may effect the experimental scattered signal. The aperture functions presented here do not, however, incorporate the full scattering length density or the total, three-dimensional island shape. In all aperture functions shown, the width of the island is kept constant, resulting in the peaks in all simulated data sets also having the same widths. Figures 8.5 (a)-(c) show how the islands becoming increasingly more domed would lead to a change in the heights of the peaks, becoming more smoothed with increased doming. Figure 8.5 (d) shows that a more complex island shape could lead to a very different shape to the form factor with the ratio between the height of the central peak and those at higher $|q_x|$ being different to

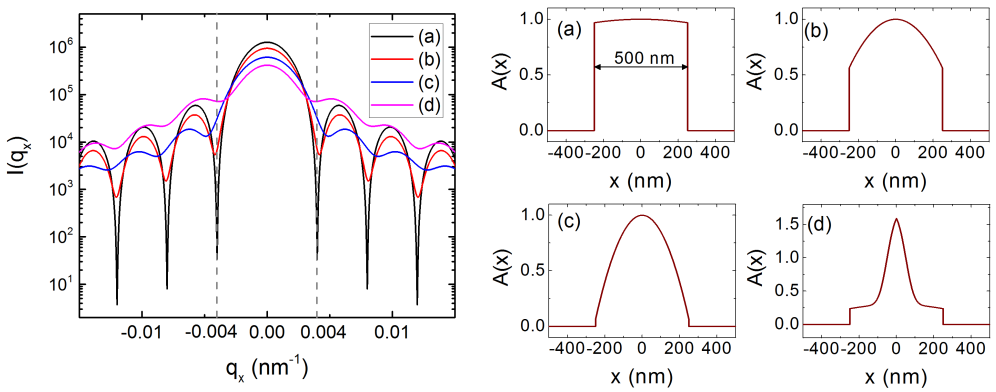

Figure 8.5: (left) Simulated form factors for (right) different aperture functions.

the simpler domed structures.

It is important to note that the structures shown in Figure 8.5 are a one-dimensional projection along x and not a full representation of the islands in 3D. This modelling allows an insight into the relationship between island shape and the resulting form factor observed in the experimental data. To be able to fully model the patterned array, however, it would be necessary to model the structure of the islands in three dimensions and calculate the resulting three-dimensional Fourier transform and would also rely on knowledge of the projected coherence lengths.

8.2.6 Modelling Real Samples

The modelling was intended to give a basic overview of the aspects involved in simulating rocking curves, but is not intended to be able to fit the measured data. There is significant work involved modelling the experimental data which is beyond the scope of this work. Not only would this involve using a suitable fitting algorithm, probably a genetic evolution algorithm similar to that used in GenX, but there are additional factors such as the detector resolution function, the shape of the islands in three dimensions (plus the subsequent three-dimensional Fourier transform) and the coherence of the beam. We must also consider that in real data there will also be a background caused by diffuse scattering from interface roughness, this is not included in these simple models.

Modern synchrotron sources make it possible to obtain intense x-ray beams with a high degree of coherence. In practice, however, most experiments use radia-

tion that is only partially coherent [228] with the coherence length is given by [229]

$$\xi = \frac{\lambda L}{s}. \tag{8.9}$$

The coherence length given here assumes that the source is not point-like, but has some lateral extension where s is the spatial extent of the source and L is the distance from the source to the scattering medium. These parameters are defined relative to the beam direction and sample plane as shown in Figure 8.6. Additionally, the beam is not symmetrical and as such will have different coherence lengths in the x, y and z directions. In reciprocal space, this forms what is commonly referred to as the resolution ellipsoid.

When scattering from a sample, we must consider that the coherence lengths are projected onto the surface as shown by the shaded area in Figure 8.6. Reflectivity measurements are sensitive to the in-plane component in the direction of the beam, i.e. the x component, of the scattered signal. As such, the projected coherence length in the x direction onto the sample surface needs to be taken into account and is given as

$$\xi_x^{proj} = \frac{\xi_x}{\sin\theta} \tag{8.10}$$

where θ is defined in Figure 8.6. Equation 8.10 shows that at low angles, ξ_x^{proj} can become very large.

The coherence length in the x direction is usually of the order of tens of microns for synchrotron radiation with a much larger projected coherence length at low angles, whereas the coherence of the beam in the y direction is lower, typically about a micron. Combined with the instrument resolution, this means that the data

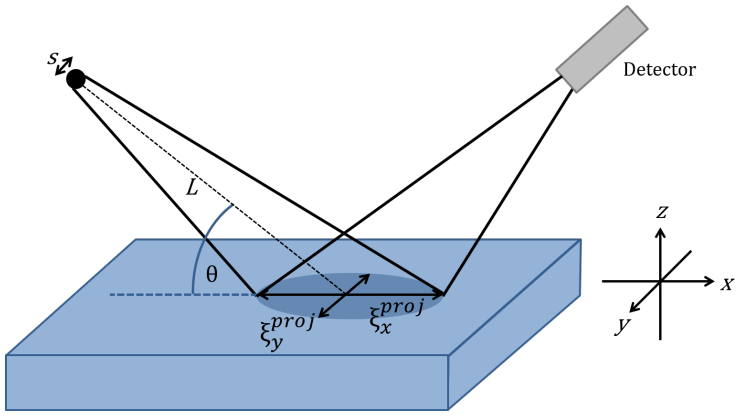

Figure 8.6: The projection of the coherence lengths onto the sample surface from a source of size s at a distance L from the sample.

is assumed to not be sensitive to the periodicity of the array in the y direction [186]. A coherence length which is larger than the in-plane periodicity of the array elements is required for interference to occur which is fundamental to a scattering experiment.

The signal is also dependent on the detector acceptance which depends on the detector slit width and the distance from the sample to the detector. The angular resolution of a scattering experiment can be estimated by calculating the area in reciprocal space that is simultaneously illuminated by the incident beam and accepted by the detector [122]. The detected signal is highly dependent on this resolution function and as such when simulating rocking curves, a convolution with the resolution function must also be included if experimental data is to be accurately modelled [161].

8.3 Results

This chapter now goes on to look at x-ray resonant magnetic reflectivity and element specific hysteresis of a continuous film and a patterned array of FePd. FePd alloys are used because the ordering temperature and magnetic moment can be directly controlled using the composition [230]. This makes them an ideal choice for designing new systems as the magnetic properties are easily altered by a changing the Fe concentration.

8.3.1 Continuous FePd Films

Firstly, resonant magnetic x-ray scattering studies will be presented for a continuous film of FePd alloy so that a comparison can be made between this and the patterned array. Pd has the largest paramagnetic susceptibility among the non-magnetic transition metals and it is easily spin-polarised by proximity to a magnetic moment. Pd has a Stoner enhancement factor of $S \simeq 9.4$ and as such is close to the ferromagnetic instability [231]. The large Stoner enhancement factor of Pd means that the magnetic moment of a $3d$ impurity can easily polarize the conduction electrons. The presence of an Fe atom in Pd causes a moment of approximately 12 μB [232] which extends out to a distance of almost 10 Å [233]. In Fe_xPd_{1-x} alloys these moments overlap and create a nominally uniform magnetisation throughout the layer with properties that are highly dependent on x, the Fe content.

Continuous films of $Fe_{0.05}Pd_{0.95}$ were grown using ultra-high vacuum sputtering on a Si(100) substrate with a nominal thickness of 500 Å. As the Pd is easily polarised, it is possible to perform x-ray scattering with the energy tuned to the Pd L_3 resonant edge and measure the magnetisation of the material. Resonant x-ray

scattering studies were performed on beamline 4-ID-D at the APS, Chicago. The Pd L_3 edge (3.187 keV) was used rather than the Fe L_3 edge (0.708 keV) as it was within the energy range of the beamline. Figure 8.7(a) and (b) show x-ray resonant sum and A.R. reflectivity data respectively measured just below the Pd L_3 edge (to avoid strong absorption effects) and lines of best fit obtained using GenX. The chemical SLD shown in Figure 8.7(c) indicates that the film is uniform throughout with very low roughness both at the substrate interface and the surface. The magnetic SLD from the best fit is shown in Figure 8.7(d) to have a uniform magnetic moment throughout the entirety of the layer. This confirms that the composition is the same throughout the whole thickness of the film and the Pd is polarised throughout.

Element specific hysteresis loops measured just below the Pd L_3 edge were recorded as a function of temperature and are shown in Figure 8.8(a). The loops were obtained by keeping the scattering vector fixed and varying the applied magnetic field whilst flipping the helicity of the circularly polarised x-rays. The loops collapse as they approach the ordering temperature at 266 ± 1 K but maintain the square shape without any rounding as the loops collapse. To facilitate analysis, the loops were fitted using a modified Langevin function using scripts as described in Chapter

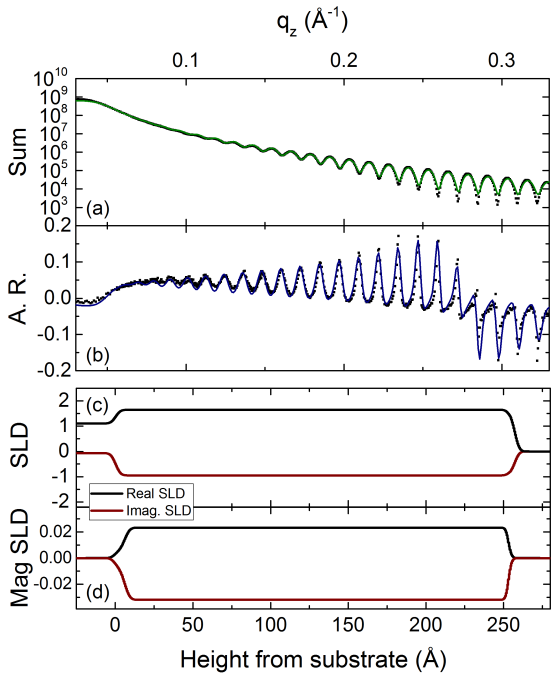

Figure 8.7: ((a) Sum and (b) A.R. reflectivity data (points) and fit (line) for a continuous $Fe_{0.05}Pd_{0.95}$ film recorded at the Pd L_3 edge. (c) Chemical and (d) magnetic SLD from fits.

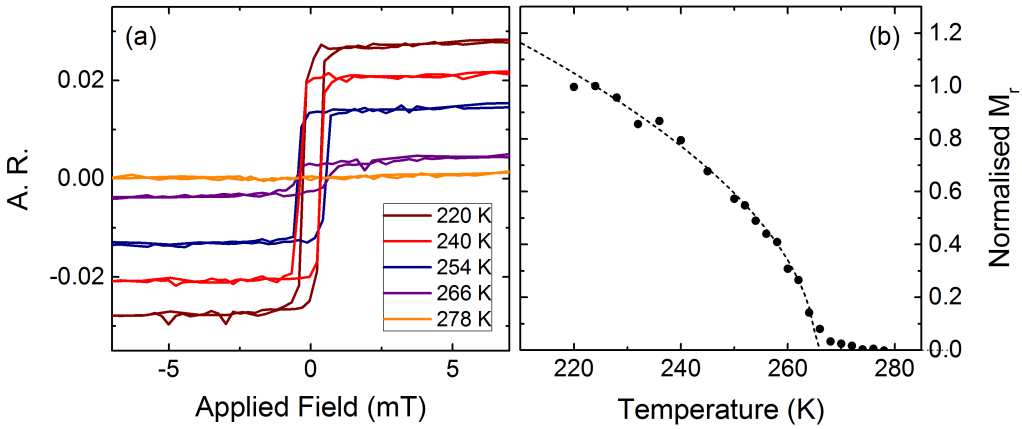

Figure 8.8: (a) Hysteresis loops obtained from a continuous film of FePd alloy recorded at the Pd L_3 edge and (b) the normalised remanent magnetisation as a function of temperature.

4. The asymmetry ratio at zero field is proportional to the remanent magnetisation. This is calculated from the fits to the data and plotted as a function of temperature in Figure 8.8(b).

The data in Figure 8.8(b) are fitted using a Curie-Weiss law. In the fit, the value of β_{eff} was found to be 0.53 ± 0.01. The error on β_{eff} was found by obtaining multiple fits, with different initial conditions and taking the average and standard deviation of β_{eff}. This value of the critical exponent is consistent with mean field theory but is much larger than the value of ~ 0.33 which is normally observed in ferromagnetic materials. This increase in the value of the critical exponent has been previously observed in similar alloys [234] but the physical mechanism causing the increase is currently not well understood. Work is ongoing between the University of Warwick magnetic x-ray scattering group and the materials physics group at the University of Uppsala to attempt to explain this observation.

8.3.2 FePd Patterned Arrays

In the previous section, data was shown for an FePd continuous film revealing that the Pd is polarised and it has a uniform composition and magnetisation throughout the layer. It had clearly ferromagnetic hysteresis loops which collapsed at the ordering temperature. This chapter will now present a study of the structural and magnetic properties of an FePd film which is patterned into an array of nano-scale islands.

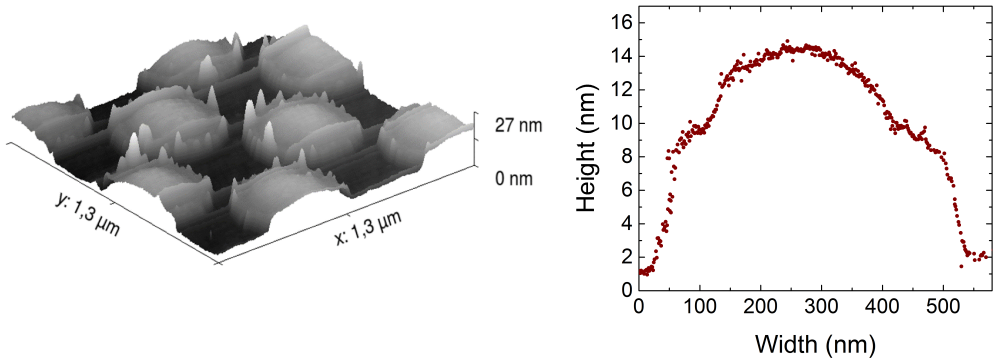

Figure 8.9: (left) AFM image of a selected area of the patterned array of FePd dots. (right) Average shape of dots obtained by taking line profiles from AFM data indicating domed structures.

Nano-imprint lithography was used to pattern a fused silica substrate [235]. The FePd layer was then deposited with a nominal composition of $Fe_{13.5}Pd_{86.5}$ onto the pre-patterned substrate at room temperature whilst the sample was rotated. The samples were co-sputtered using elemental Fe (99.95 at.%) and Pd (99.95 at.%) targets in an ultra-high vacuum magnetron sputtering system. Post deposition, the mask was removed using a lift-off process leaving behind a square lattice of circular FePd islands. This process results in highly uniform, polycrystalline circular disks over an area of 30 × 30 mm^2 [236]. SEM revealed the sample to have an in-plane periodicity of 513 nm giving an inter-disk separation $d_{[10]} = 63$ nm in the [10] direction and $d_{[11]} = 275$ nm in the [11] direction.

AFM images were taken and are shown in Figure 8.9(left). Line profiles were taken across the AFM image and the average profile is shown in Figure 8.9(right). The averaged line profile reveals a slight doming of the disks which is a direct result of the growth method. The island height is small compared to the depth of the holes in the pre-patterned substrate (approximately 1/10). As the holes were only partially filled, there were shadowing effects which led to a larger amount of material accumulating in the centre of the islands, and hence resulted in the observed domed shape. The samples were rotated during the deposition of the FePd to minimise the doming and to attempt to make the islands as symmetrical as possible.

Resonant reflectivity data were recorded as a function of scattering vector q_z just below the Pd L_3 resonant edge (3.187 keV). The sum and asymmetry ratio are shown in Figure 8.10(a) and (b) respectively where the black circles are the data

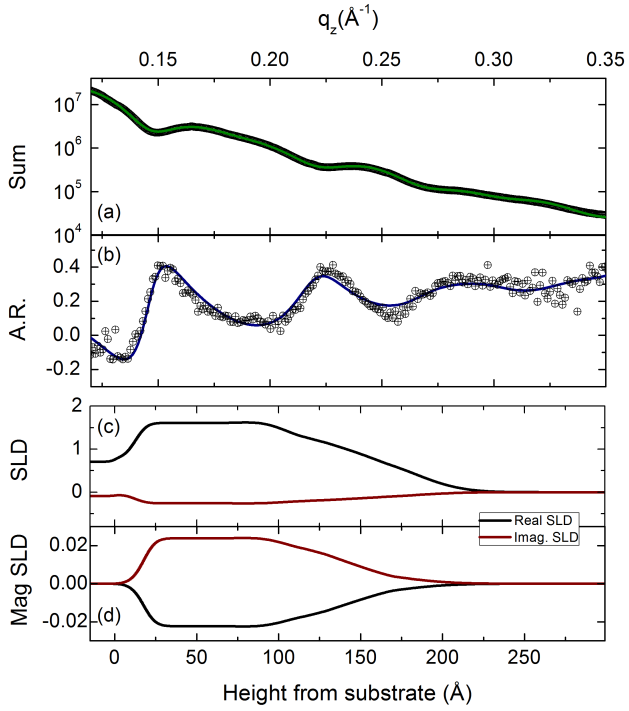

Figure 8.10: Resonant x-ray reflectivity data from an array of FePd circular islands. (a) Sum and (b) asymmetry ratio with data (black circles) and best fit (red line). (a) inset shows slicing model used to achieve best fit. (c) chemical and (d) magnetic SLD profiles obtained from best fit.

and the red line is the best fit obtained using GenX. The resulting SLD profile from the fit is shown in Figure 8.10(c) for the chemical and (d) the magnetic structures.

Specular reflectivity scans of this type are sensitive to the average SLD area as a function of z and so in principle, these islands can be modelled as a single layer thin film with a slightly reduced density to account for air spaces between islands. As the islands were domed, however, simulating the structure as being a single layer does not achieve a good fit as the structure is not accurately modelled. The structure was therefore modelled as being a series of layers with decreasing density as the height from the substrate, z, increased. This can be visualised using Figure 8.11 which illustrates how slices through a domed island would sequentially have less material and result in each slice having a lower density than the last. Each 'slice' was modelled as having the same scattering factors as the bottom layer but the density was set to be a ratio of the density of the bottom layer. The result of this is the SLD profile seen in Figure 8.10(c) which exhibits a constant SLD to approximately 100 Å corresponding to the straight sides of the islands giving no

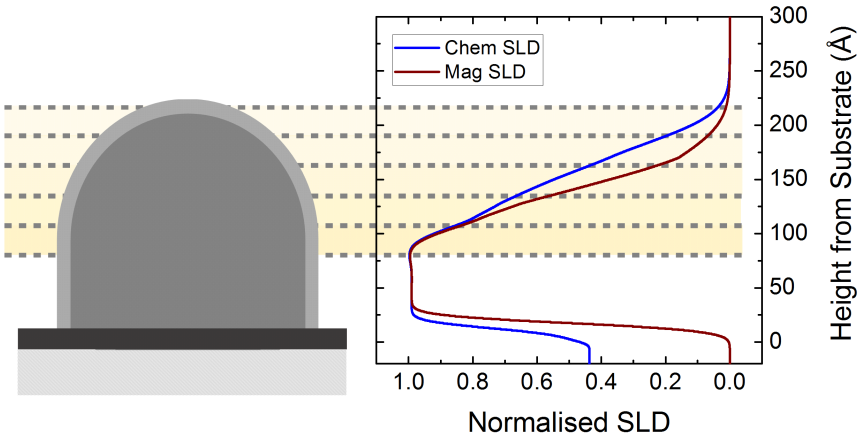

Figure 8.11: Schematic of the slicing model employed to model the domed islands. Progressively higher slices contain less material leading to the long, extended tail in the SLD seen.

change in density. There is then a gradual decrease in the SLD as the domed shape decreases the amount of material in each slice.

Additional to the effect that the doming has on the profile, any change of density due to oxidisation of the FePd at the edges of the islands will also result in a reduction of the SLD. This is illustrated in the schematic in Figure 8.11 as a layer around the outside of the island in a lighter colour. This could account for the extent of the tail on the SLD profile from the fit. There is a possibility that the SLD tail could also be caused by variations in height between islands. If the islands are slightly different heights, then slices taken across the upper parts of the islands would appear to give an SLD profile similar to a large roughness.

The data here were recorded whilst the sample was in a fully saturated magnetic state. The magnetic SLD profile as shown in Figure 8.10(d) follows the chemical structure almost exactly suggesting that the majority of the sample is magnetic and the magnetisation direction is in one direction throughout the whole of the island in this saturated state. In the normalised SLD in Figure 8.11 it is more apparent that there is a magnetic dead-layer both at the surface and at the interface between the substrate and FePd. The dead-layers are due to non-magnetic oxides on the FePd and the native oxide on the substrate.

8.3.3 Hysteresis

Element specific magnetic hysteresis loops were obtained for the patterned array of circular islands with x-rays tuned to just below the Pd L_3 edge. The scattering vector was held constant whilst the applied field was varied. A negative field was applied to saturate the islands fully, as is shown in the schematic in Figure 8.12(a). The data are fitted to a modified Langevin function as described in Chapter 4. In addition to the amplitude, shape and coercivity parameters, the modified Langevin function chosen to fit the hysteresis data included a linear section to represent the magnetisation reversal curve of the sample when in the vortex state.

The hysteresis data shown in Figure 8.12 is recorded on the specular condition and as such this provides a measurement of the average magnetisation across the entirety of the islands. As the applied field was reduced from negative saturation, the net magnetisation across the islands remained at the saturation value, until a field slightly below zero, when nearly all the net magnetisation was lost. The loss of magnetisation just below zero field is characteristic of a flux closure configuration, the simplest of which is a vortex [60]. The vortex results in the measured in-plane component being reduced to zero. In a vortex state the magnetisation is aligned parallel to the edges of the circular island which acts to lower the magnetostatic energy by reducing stray fields. The value of the field at which the vortex state forms will be labelled the 'injection field', H_{in} and is marked on Figure 8.12 as point (b).

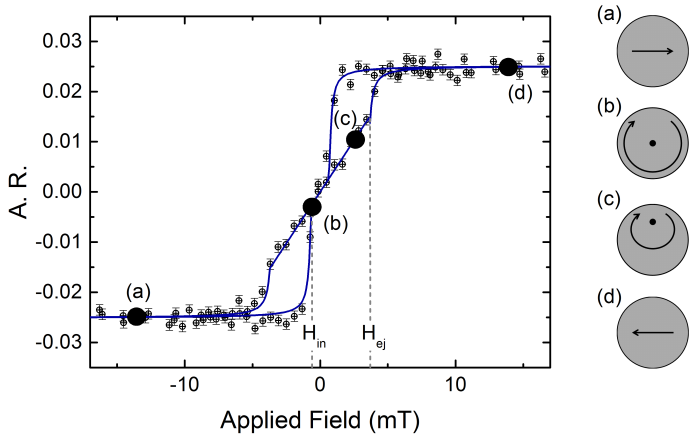

Figure 8.12: Hysteresis loops recorded at 100 K using x-ray magnetic scattering. Experimental data (black circles) are fitted using a modified Langevin function (blue line). (a) - (d) Schematic illustrations showing the magnetization within a circular island.

The formation of a vortex state leads to the central moment pointing out of the plane as shown in the schematics in (b) and (c) on the right of Figure 8.12. The vortex is defined by two main parameters, the chirality (the direction of the in-plane moments) and the polarity (the direction of the out-of-plane moments). The magnetisation reappears as the applied field is increased, during this process the vortex is deformed by pushing its core away from the centre of the island as illustrated in the schematic in Figure 8.12(c). At a critical field value, the vortex becomes unstable and is annihilated from the islands. This point is labelled as H_{ej}, the 'ejection field', in Figure 8.12. The magnetisation continues to align with the field as the value is increased until the whole island is completely saturated, as is the case at point (d) in Figure 8.12 and is shown in the schematic.

Previous work on these samples using photoemission electron microscopy (PEEM) found that there is no preferential chirality observed across the islands [236]. As the scattering techniques used here are sensitive to the components of the magnetisation in the beam direction, both chiralities are recorded as being equivalent. If we consider two islands with opposite chirality as illustrated in Figure 8.13, and measure the components of the magnetisation in the beam direction as indicated by the dashed lines, it can be seen that the total signal measured is the same for the two islands.

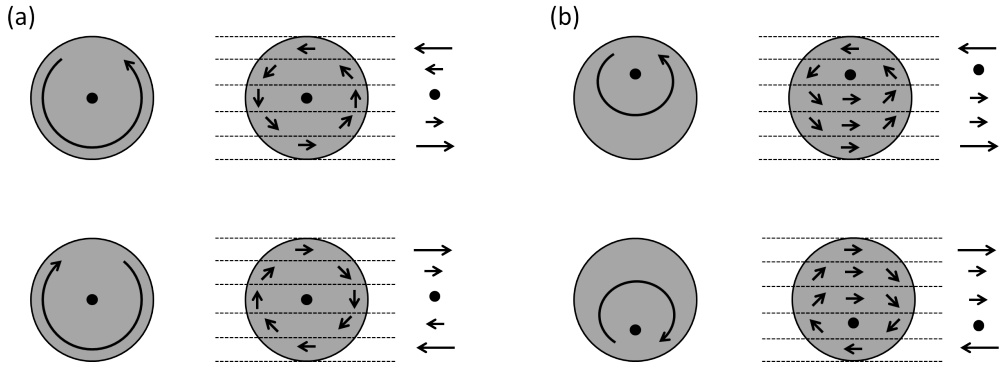

Figure 8.13: Illustration indicating how vortices with opposite chirality are measured as equivalent using x-ray reflectivity. (a) A vortex with the core at the centre and (b) where the vortex core is moved across the circular island by the applied field. The components in the direction of the field are indicated by arrows on the right hand side. Both chiralities give the same total magnetisation as would be recorded by the detector.

8.3.4 Temperature Dependence

Thus far, it has been shown that a patterned array of circular islands can be investigated using specular reflectivity scans and hysteresis loops with a clear change in gradient at points where a vortex is created and annihilated. The relationship of the injection and ejection fields with temperature recorded using PEEM studies at the Fe L_3 edge and MOKE has previously been reported in [236], and this next section will present temperature dependent hysteresis at the Pd L_3 edge.

Figure 8.14 shows hysteresis loops recorded as a function of temperature. At 40 K there is insufficient thermal energy for fluctuations of the vortices to occur and such the loop exhibits hysteresis at every point along the curve. At 100 K, however, thermal fluctuations start to have a more notable effect and the hysteresis collapses in part of the loop. As the temperature increases further, thermal fluctuations play a larger role and the hysteresis of the loops collapses over a larger region. At approximately 200 K, the bifurcation temperature, the hysteresis collapses completely and the injection and ejection fields are now the same. For temperatures between the bifurcation temperature and the ordering temperature of the material there exists a hysteresis-free transition between collinear and vortex states. The features of the loops are still typical of vortex injection and ejection, with the change in gradient

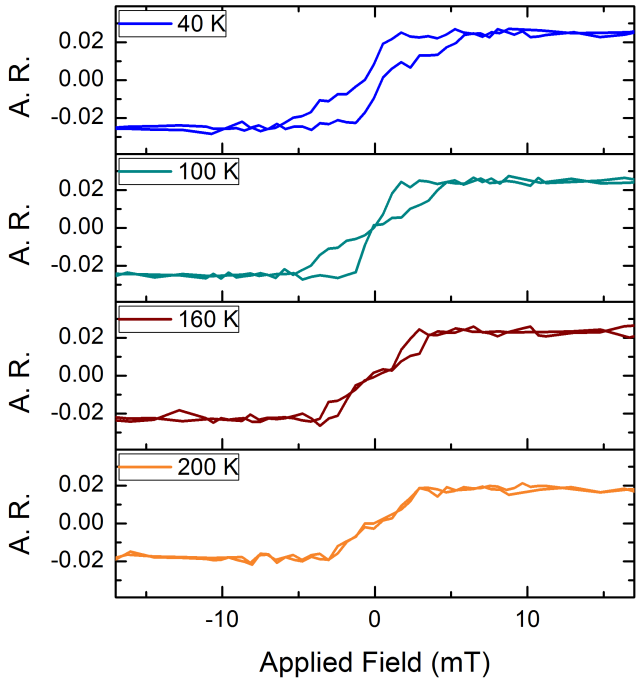

Figure 8.14: Magnetic hysteresis loops recorded for an FePd patterned array as a function of temperature.

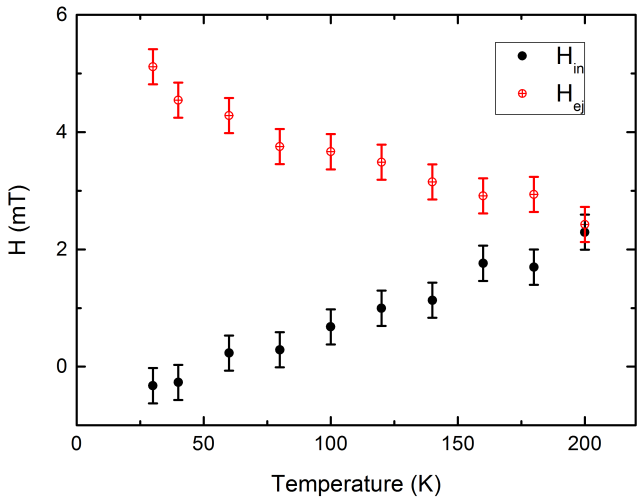

Figure 8.15: H_{in} and H_{ej} recorded as a function of temperature. They collapse at the ordering temperature at ∼200 K.

of the loop still clearly visible.

All loops were fitted to a modified Langevin function in which the values of H_{in} and H_{ej} were fitted. The evolution of H_{in} and H_{ej} with temperature are shown in Figure 8.15. The injection and ejection fields collapse at around 200 K. This point is the bifurcation temperature and it occurs below the ordering temperature, which is approximately 300 K. The field required to inject (eject) the vortex state decreases (increases) as the temperature is increased. The change in H_{ej} and H_{in} with temperature is attributed to a decrease in M_s, the saturation magnetisation [237], and thermal excitations causing fluctuations of the vortex core [238].

The effect of temperature on H_{in} and H_{ej} is discussed in previous work on these samples, see ref [236] for details. Although the evolution of the hysteresis loops and parameters has been presented before, it is reassuring that the results are replicated here at the Pd L_3 edge when previous work was carried out using MOKE and resonant studies at the Fe L_3 edge. This means that the assumption that the Pd is polarised throughout the entirety of the islands is correct and we can have confidence in the data that are presented in the following sections.

8.3.5 Rocking Curves

Rocking curves are a useful tool for investigating the in-plane structure of patterned arrays. They are highly sensitive to the shape, size and separation of the elements in the array. The size of the islands that can be resolved using this technique varies depending on the energy and coherence length of the beam, and also the scattering

geometry used. To improve the resolution, rocking curves can be recorded at lower detector angles. Typically it is difficult to study islands which are less than about 100-200 nm in size, because smaller islands result in broader peaks and require longer counting times to get a large enough signal to noise ratio to resolve the satellite peaks.

Rocking curves recorded using resonant techniques can be used to study the magnetic structure within islands in a patterned array. Fitting the sum and asymmetry ratio rocking curves, however, is a very involved process especially for islands with complicated shapes or magnetic structures.

Figure 8.16 shows the rocking curve obtained by scanning q_x at 30 K in zero field after applying a large saturating field. The rocking curve displays periodic peaks with separation $\sim$0.0012 Å^{-1} corresponding to the separation of the circular islands of approximately 5160 ± 60 Å which is as expected. The form factor is the envelope waveform indicated by the dashed line in Figure 8.16 and contains information about the shape and size of the islands. Hysteresis loops were then obtained at scattering vectors corresponding to each of the satellite peaks of the rocking curve and these can be seen in Figure 8.16(a)-(d). The hysteresis loops recorded at higher satellite peaks show that the loops collapse and then switch sign.

As introduced in the theory section at the beginning of this chapter, the

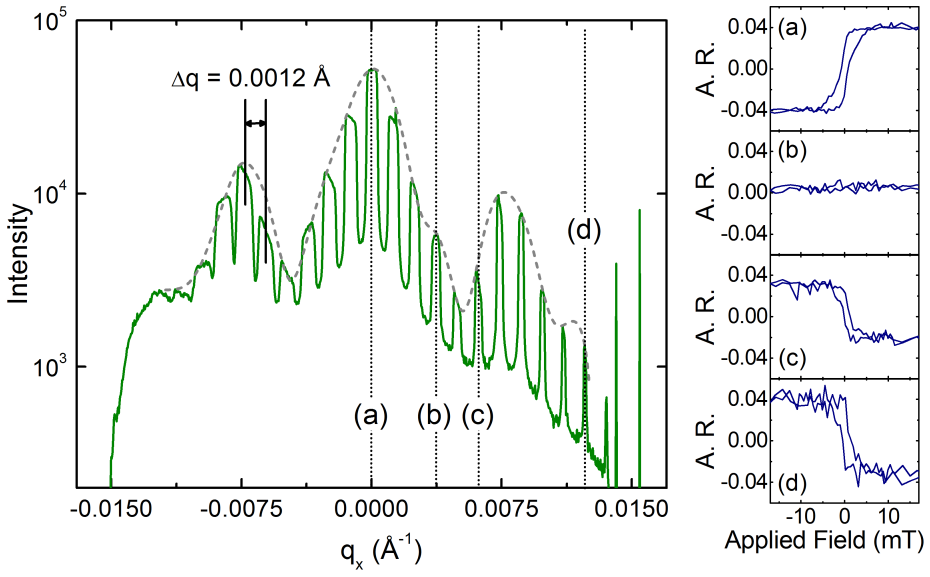

Figure 8.16: (left) Rocking curve measured at 30 K with hysteresis curves recorded at satellite peaks marked (a)-(d) shown (right). The light grey dashed line is intended as a guide to the eye marking the approximate form factor.

scattered signal is a Fourier transform of the aperture function which is dependent on the island shape, size and spacing. As a result, satellite peaks at higher q_x are made up of higher order Fourier components and so contain information about the magnetic structure further towards the edges of the islands. Unfortunately, it is not possible to obtain the exact structure from these rocking curves without simulations, and such simulations would require in depth modelling of the island structure and scattering factors plus experimental parameters such as detector resolution. Development of such a fitting program is beyond the scope of this work, but a qualitative approach can provide some information about the magnetic state of these structures.

Hysteresis loops in Figure 8.17 are recorded at different q_x values corresponding to the specular, first and sixth satellite peaks to illustrate the effect of changing q_x on the magnetisation reversal data. The fits to the data are shown instead of the data for easier comparison. The shape of the hysteresis loops are different when recorded at different satellite peaks as those at higher q_x probe the edges of the islands more than those near the specular condition. We can therefore make some inferences about the magnetic structure. The hysteresis loop recorded at the specular condition shows that a vortex state is induced in the islands marginally sooner than that at the first and sixth satellite peaks. This could indicate that the centre of the islands reverse first. The loop obtained at the specular condition has a steeper

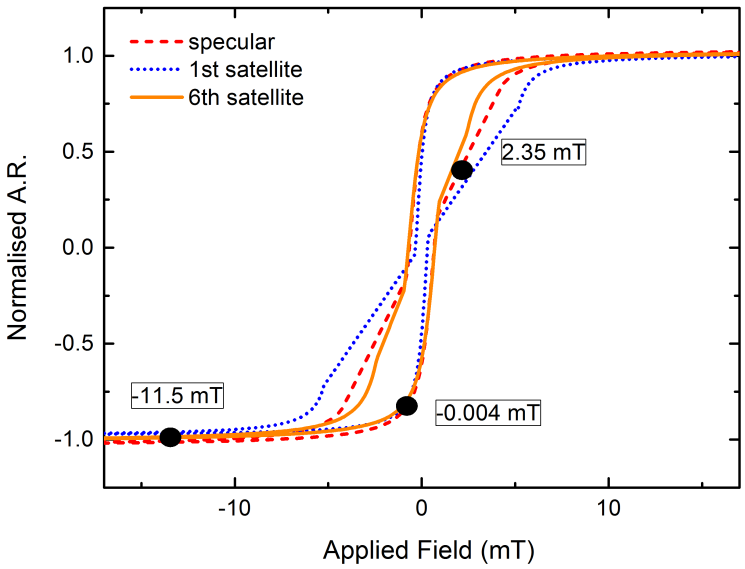

Figure 8.17: Simulated normalised hysteresis loops measured at q_x values corresponding to the specular, first and sixth satellite peaks. All loops have been normalised to facilitate in the comparison of loop shapes. The simulated curves reproduced from fits to the original data are shown.

gradient in the region associated with the vortex state suggesting that the central spin is driven across the island more easily than the rotation of the outer spins.

The ejection field also changes in each loop which shows that the spins in different regions of the islands reverse at different rates to other areas. To illustrate a possible explanation for the variations in the ejection fields at different satellite peaks, see Figure 8.18, where the centre of the vortex is displaced from the centre of the island just before the point at which the vortex state in the whole island would be annihilated. In Figure 8.18(a), the scattered signal is sensitive to the centre of the island as indicated by the red shaded area and as such the measured signal is large, which would appear in the hysteresis loop as though the vortex had been annihilated and approaching positive saturation. At higher satellite peaks, the scattered signal may be sensitive to other areas of the islands, for example as shown by the blue shaded areas in Figures 8.18(b) in which the scattered signal would be very small, and would appear as though the vortex state was still fully induced in the island. Alternatively, if the scattered signal was sensitive to only very edges of the island as indicated by the yellow shaded areas in Figure 8.18(c), the scattered signal would again be very small and appear as though the vortex was still partially present. The measured hysteresis loops which are sensitive to these shaded areas would therefore appear to have different ejection fields due to the sensitivity to different parts of the islands, despite having the same overall magnetic structure.

As seen in previous sections, by tuning the energy of the incident photons to a resonant edge of one of the elements in the material, the magnetic structure of the material can be probed. The same is true when scattering from patterned arrays like those in this chapter and measurements can be sensitive to changes in

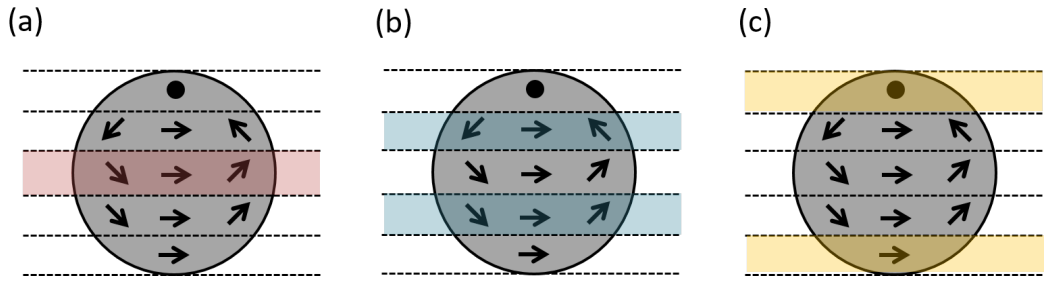

Figure 8.18: Illustration of a magnetic vortex where the core has been displaced from the centre. (a) At the specular condition, the signal is most sensitive to the magnetisation in the centre of the island as indicated by the red shaded area. (b) and (c) provide a visual aid to illustrate how the signal is sensitive to different parts of the islands at different satellite peaks as indicated by the blue and yellow shaded areas respectively.

the magnetic structure within the islands.

Difference rocking curves measured at the Pd L_3 edge are shown in Figure 8.19 and are recorded at different applied fields as marked. For each difference rocking curve, the applied field is kept constant whilst the asymmetry ratio is measured as a function of q_x. As the applied field is held constant, the asymmetry ratio is obtained by reversing the helicity of the incident x-rays. The difference is shown in Figure 8.19 rather than the asymmetry ratio as the peaks are clearer. Data recorded at -11.5 mT when the magnetisation is saturated shows a change in sign in the rocking curve. As the shape of the total form factor is a combination of both the chemical and magnetic form factors, the change of sign must mean that there is a beating between the two form factors. For there to be a beating, there must be a difference between the chemical and magnetic structures, such as a magnetic dead layer. This dead layer is most likely an oxide layer that has formed on the top and sides of the islands. Note that the change in sign of the hysteresis loops shown previously in Figure 8.16(a)-(d) is caused by beating between the chemical and magnetic form factors which results in the change of sign in the A.R. at higher satellite peaks.

The data recorded at -0.004 mT is shown in Figure 8.19. At this field and

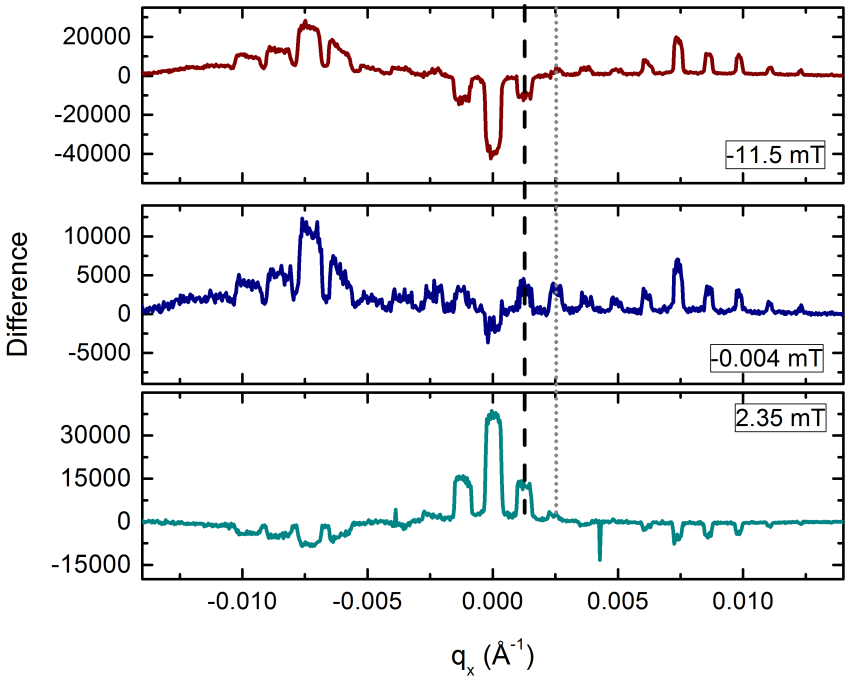

Figure 8.19: Difference spectra recorded as a function of q_x at field values as indicated. For comparison, the field values are marked on Figure 8.17.

temperature, vortex states are being formed resulting in the measured net magnetisation across the islands starting to approach zero (see Figure 8.17). The difference spectrum shows a similar change in sign to that measured at saturation but now the sign of the first peak has reversed (indicated by the black dashed line). The reversal of one peak is an indicator that across the width of the island, some of the spins have reversed before others causing a slightly different beating between the magnetic and chemical form factor.

The lower data in Figure 8.19 shows the difference rocking curve when at 2.35 mT, when the islands are in the vortex state. The peaks are now all reversed compared to the data measured at negative saturation apart from the second satellite peak (indicated by the grey dotted line) which is still positive. This indicates that although this difference rocking curve appears similar to the fully saturated state, there must still be subtle differences in the magnetic structure. Without an accurate fit of the data, we are unable to fully model the changes in magnetic structure that occur as the applied field is varied.

8.3.6 Modelling

Some very simple models were created based on the theory of scattering from patterned arrays introduced earlier in this chapter. The models were intended to help provide an insight into the mechanisms leading to the observed difference rocking curves. A lattice of delta functions was produced representing the positions of the islands in real space and was multiplied with a step function. This step function represents the sample length or coherence length, whichever is the smallest. The fast Fourier transform (FFT) of the delta functions multiplied by the coherence length was calculated. A function representing the shape of the islands was then produced and the FFT was taken of this also. According to the convolution theorem, the FFT of both the lattice and the island shape were then multiplied together to give a simulated rocking scan.

Both a chemical and magnetic island shape were produced and rocking curves were simulated with the magnetic scattering factor set to $\pm m$ to model scattering with left and right circularly polarised x-rays. The difference between these were taken and are presented in Figure 8.20 for a selection of simple island shapes and magnetic configurations.

To illustrate how the magnetic profile within the islands might effect the form factor, some examples showing possible cross-sections of the islands with different magnetic structures are shown in Figure 8.20. The difference spectrum multiplied by q_x^2 is also given as it makes the peaks more easily seen. It is shown that when

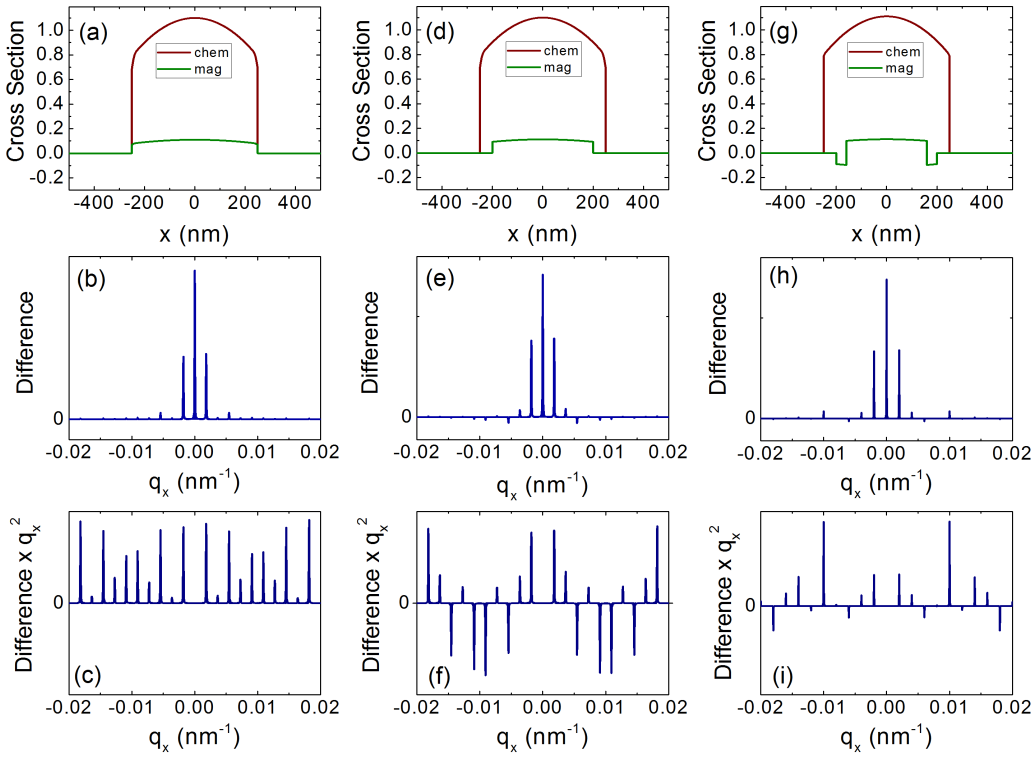

Figure 8.20: Simulated rocking curves illustrating the case where (a) the magnetisation is aligned with the field across the whole island resulting in a completely positive difference spectrum, (b). Cases are also shown for (d) a magnetic dead layer or (g) a partial reversal of the magnetisation. The resulting difference spectra are shown in (e) and (h) respectively and exhibit a change in sign for some satellite peaks. (c), (f) and (i) show the difference spectra multiplied by q_x^2 as this makes the change in sign easier to see.

a magnetic dead layer is introduced, there is a beating between the chemical and magnetic form factors which alters the shape of the difference rocking curve, such that the total envelope function changes sign in the difference spectrum, similar to that shown in the experimental data.

The difference spectrum is also calculated for a structure with both a magnetic dead layer and also an area where the magnetisation near the edge of the island has reversed but the centre is still positive, as could be the case in the islands presented here when the magnetisation starts to reverse or the vortex is induced. This again shows a change in sign in the difference spectrum similar to that observed in the experimental data. A structure of this type with a partial reversal of the magnetisation that would lead to the change in sign of the first satellite peak in Figure 8.19 (centre). To be able to ascertain how much of the structure changes at

this field and which part of the structure reverses first, the data would need to be fitted exactly which is not possible here for reasons discussed earlier in the chapter.

The magnetic structures illustrated in Figures 8.20(d) and (g) both exhibit a change in sign of the satellite peaks through beating between the chemical and magnetic form factors as shown in Figures 8.20(f) and (i). The magnetic profile in these islands could take many forms and these simulations have many limitations, but the structures in the figure were chosen to illustrate the effect that differing magnetic and chemical structures may have on the measured signal. It is apparent that more information can be gained about patterned arrays from rocking curves obtained using resonant x-ray scattering, should a suitable fitting method be developed. The principles outlined in this chapter could be used to study patterned arrays constructed from materials with a range of compositions and patterned into many different geometries. Work is ongoing to develop the fitting models to enable detailed studies of such structures.

Conclusion

This chapter first introduced some of the theory necessary for interpreting and simulating x-ray scattering data from patterned arrays. It started with the concept that the scattered signal is the Fourier transform of the aperture function which in this case is some function representing the shape and size of the islands in the array. It was shown how higher order Fourier series contain information from across different parts of the islands. The convolution theorem was introduced giving the reciprocal relationship between island periodicity and the separation of the peaks in the scattered signal; this theorem also results in an overall envelope function called the form factor which is related to the shape of the islands.

XRMS data was recorded for a continuous film of FePd showing that the layer was uniform throughout with similar chemical and magnetic profiles. Fits to XRMS data from a patterned array, however, showed SLD profiles with an extended, gradual decrease which was caused by the islands having a domed shape. The shape was confirmed with AFM images and was a result of the growth process. Additionally, the SLD profiles from the patterned array indicated that there was a magnetic dead layer between the FePd and substrate and also at the top of the islands, most likely from the formation of a non-magnetic oxide.

Element specific hysteresis loops recorded at the Pd L_3 edge were presented for both a continuous film and a patterned array of FePd. The hysteresis loops for the continuous film showed square loops which collapsed at the ordering temperature

which is typical of a ferromagnetic alloy, whereas those for the patterned sample had a change in gradient where a vortex state was created/annihilated in the islands. Hysteresis loops recorded as a function of temperature showed a loss of coercivity above the bifurcation temperature due to thermal fluctuations.

Rocking curves recorded at the Pd L_3 edge showed periodic peaks with separation consistent with the distance between the circular islands. The rocking curve had an envelope function, or form factor, the shape of which was related to the domed shape of the islands. Hysteresis loops were recorded at q_x values corresponding to the satellite peaks of the rocking curve. At higher satellite peaks the hysteresis loops collapsed and then reversed sign. This reversal of the hysteresis loops was attributed to beating between the magnetic and chemical form factors due to the magnetic dead-layers which lead to a change in sign of the A.R. at higher satellite peaks.

The sum and difference rocking curves recorded at the Pd L_3 edge were then presented for the patterned sample as a function of applied field. Rocking curves as a function of applied field showed a change in sign across the range of q_x due to beating between the chemical and magnetic form factors. As the field was increased, certain satellite peaks reversed first. As higher satellite peaks contain higher order Fourier terms, the change of some satellite peaks at different fields indicated that some parts of the islands reversed before others. Information about the magnetic structure in the islands is contained in the shape of the form factor of the difference rocking curves but without further work to accurately fit this data, it is not possible to extract the exact magnetic structure.

Simple modelling was carried out to simulate rocking curves from an array of domed islands. It was shown that the change in sign in the difference rocking curves was due to differences between the chemical and magnetic structure i.e. a dead-layer or possibly a region with opposite sign. These differences lead to a beating between the chemical and magnetic form factor resulting in the change of sign observed experimentally.

Chapter 9

Conclusions

The aim of this work was to use resonant x-ray scattering techniques to study the structural and magnetic properties of thin films, multilayers and patterned arrays.

Firstly, the effect of growth temperature on the roughness of interfaces in a Gd-Y superlattice was investigated using x-ray diffraction and x-ray resonant magnetic scattering at the Gd L_3 absorption edge. Fits to the reflectivity data revealed an overall rise in the SLD value across the superlattice as the growth temperature was decreased. The sample grown at 300°C (the middle growth temperature), however, showed the least definition between individual layers throughout the SLD in the superlattice. The overall rise in SLD value was echoed in the magnetic profile where the SLD value was higher across the superlattice and no longer reached zero for the non-magnetic Y layers due to the high roughness. XRMS studies were capable of resolving the layer-by-layer chemical and magnetic SLD profiles as a function of depth for the superlattice and were sensitive to the effect of temperature on the interface roughness. It was not, however, possible to tell whether the differences in roughness were caused by interface variations or chemical intermixing using reflectivity.

MOKE measurements were then presented giving the ordering temperatures for the three Gd-Y superlattice samples. The MOKE data showed a reduction in moment at very low temperatures, which was attributed to a canting of Gd moments and resulted in a reduction of the net in-plane component of the magnetic moment. The magnetisation as a function of temperature recorded using XRMS, however, did not show a reduction in the magnetisation at low temperature. As the XRMS data was element specific (and so only measured the magnetisation of the Gd) it was proposed that the Gd and Y have different temperature dependent behaviours due to canting or intermixing at the interfaces.

Similar superlattices containing ultrathin layers of Ho within the Y were also investigated. The expectation was that the Ho would act as a tagging layer to indirectly probe the Y moment. High roughness between layers and a low signal to noise ratio meant that these measurements did not provide the detailed information on the Y layer properties as expected. Hysteresis data at the Ho L_3 edge was recorded, which suggested that the use of Ho as a tagging layer could be a viable technique. The hysteresis measurements at the Ho L_3 edge had large amounts of noise on the data but potentially showed a different coercivity to the loop recorded at the Gd L_3 edge, supporting the hypothesis that there was canting or intermixing of Gd and Y at the interfaces. Further work is needed to conclusively determine whether Ho can be used in this way. This would require improvements in the signal to noise ratio and samples with lower roughness, in order to resolve the Ho layers.

The work presented in this thesis has shown that it is possible to use XRMS to provide a chemical and magnetic layer-by-layer profile of superlattices, although it is not possible to determine whether roughness between layers is diffusive or due to topographical variations. Although there has been very little work studying Gd-Y superlattices since the 1980s, rare-earth superlattices using other material combinations are still studied, including those constructed from rare-earth/yttrium layers. For example, there have been more recent studies of systems such as Dy-Y [239–241] and Ho-Y [242,243] which have predominantly involved neutron diffraction. It would likely be beneficial, however, to add to these studies with element specific data on the magnetic structure using resonant x-ray scattering to allow separate investigations of the Dy/Ho and Y behaviours. X-ray scattering from superlattices containing Y, however, would have similar difficulties to those presented in this work, in that the Y L_3 edge is outside the realistic operating energy range of most soft energy beamlines. There is therefore scope for using tagging layers to study the induced moment in the Y in such superlattices. Further work would be needed to look at whether adding a magnetic tagging layer intrinsically changes the magnetic properties of the superlattice, including studies of the tagging layer thickness and material. There would also be much work needed to produce good quality samples with low roughness between layers and to achieve a sufficiently good signal to noise ratio to resolve the tagging layer.

A trilayer of amorphous SmCo and CoAlZr layers was then introduced and characterised using element specific hysteresis loops recorded at the Co L_3 and Sm M_4 absorption edges at 100 K and 300 K. At both temperatures, a two-step hysteresis loop was observed in the Co data despite the presence of three separate layers containing Co. Additionally, the Sm hysteresis data had a different switching field

to that of the Co. Both observations were attributed to weaker interactions between the intra-layer Co and Sm sub-networks compared to the inter-layer Co interactions, plus regions of high Co concentration spanning the interfaces. The origin of the 'de-coupling' of the Co and Sm sub-lattices was in the random distribution of chemical species within the amorphous layers. A gradual magnetisation reversal was observed in the Sm hysteresis data which was attributed to the random distribution of Sm resulting in different switching fields for different regions in the layer.

Exchange bias was observed in minor hysteresis loops recorded at both 100 K and 300 K, indicating there was coupling between the upper and lower layers even 200 K above the ordering temperature of the middle layer. This coupling was mediated by regions of high Co concentration spanning the interface and extending through the layers. Hysteresis loops recorded using element specific XRMS resulted in studies of the separate sub-networks; this is not possible using other magnetometry techniques, such as MOKE or SQUID. As such, this work has revealed the existence of complex internal structures within amorphous layers and the consequent impact on the magnetic properties. This deviates from previous work in which exchange springs are described as being planes of rotating spins similar to a torsion spring. The findings presented in this work, however, show that there is likely to be a complex internal structure in amorphous multilayers, which could inform future work on exchange springs or other magnetic multilayered systems comprising amorphous or polycrystalline layers.

This work has shown that the use of MOKE hysteresis data alone is not sufficient to comprehensively study the internal magnetic structure of amorphous multilayers. Indeed, the MOKE data presented in this work appeared similar to that which has appeared in previous work on exchange springs, but the use of element specific minor hysteresis loops recorded at multiple resonant energies has proved to be a powerful technique here. As such, it is hoped that this thesis may influence further work studying exchange springs and other amorphous magnetic multilayers by providing evidence of the advantages of recording element specific hysteresis data at multiple resonant energies.

The effects of the random distribution of elements and the regions of high Co concentration were then modelled using a randomly distributed lattice. Percolation effects and exchange coupling were included in the models, showing that the exchange coupling between layers should be highly dependent on the Co concentration of the middle layer and the exchange constant. It would be interesting in further work to combine experimental data and modelling to investigate the effect of composition of the middle layer on the magnetic behaviour.

Changes in the scattering factors at resonant absorption edges were then described, including the large effect on the scattering length density when tuning to a resonant energy of a particular element. The scattering length would be likely to be different depending on the composition of the material containing the resonant element, because the local environment of the chemical species changes the resonant scattering factors. Fits to x-ray resonant magnetic reflectivity data for trilayers of SmCo-CoAlZr were presented at the Co L_3 and Sm M_4 resonant edges and the challenges of fitting oxides and mixing layers with complex chemical profiles were discussed. It was shown that these layers have large changes in chemical and magnetic scattering length density at the interfaces when using resonant scattering, despite their smooth, well-defined interfaces observed with TEM and laboratory x-ray reflectivity. The challenge that this poses when fitting multiple data sets recorded at different energies was discussed.

In this work, several observations have been made, for example, that different scattering factors are likely to be needed for the same element in different alloys, that a Gaussian error function may not be sufficient to describe roughness between layers and also that mixing layers or oxides may have drastically different scattering length density values at different resonant edges. These observations are likely to prove useful to other groups when simultaneously fitting x-ray reflectivity data recorded at multiple energies, or even perhaps when combining x-ray and neutron reflectivity data. Studies involving measurements at multiple energies can be challenging both experimentally and in the analysis of the data but here we have shown that this technique can reveal valuable insights into the magnetic structure of a material.

Resonant reflectivity at 100 K at the Co L_3 edge for the trilayer indicated that there was a region of enhanced magnetisation extending into the middle of the trilayer. It is conjectured that this is most likely caused by proximity to the lower SmCo layer. This theory is consistent with a model where regions of high Co concentration span the interface and the enhanced moment is propagated via these interconnected regions. Reflectivity data recorded at different applied field values showed that the top $Co_{85}AlZr_{15}$ layer reversed first, along with a portion of the middle $Co_{60}AlZr_{40}$ layer; again this is consistent with a model of interconnected Co rich regions. At 300 K (above the ordering temperature of the middle layer), a similar magnetic structure was found, but this time with a much reduced magnetisation in the middle layer (as expected). There was a small magnetisation in this middle layer (despite single layers of this material being paramagnetic at 300 K) which was attributed to an induced moment due to the proximity of the ferromagnetic layers. This small but non-negligible moment in the middle layer at 300 K explains the

observed exchange bias in the minor hysteresis loops.

Fits to reflectivity data recorded at the Sm M_4 edge indicated a single magnetic layer at both temperatures with an enhanced moment at the lower interface. The magnetisation in the lower part of the layer was shown to possibly extend into the buffer layer (as was also the case in the single layer samples). This increase in magnetisation was explained by dilute amounts of chemical intermixing which had a small effect on the chemical profile but resulted in large changes in the magnetic profile. There was not, however, sufficient sensitivity to changes in the magnetic SLD to precisely determine the shape, SLD value and thickness of a mixing layer at the Sm M_4 edge.

The extension of the magnetic moment into the middle layer observed in the Co edge SLD profiles and the injection of a domain wall when the upper layer reverses are consistent with the findings from the hysteresis data and explains why only two reversals were ever observed. It also supports the theory that the Co and Sm sub-networks are less strongly interacting than the Co-Co inter-layer interactions. The reflectivity data presented provides further evidence for a complex internal structure in amorphous multilayers, with huge potential to be manipulated and tuned for use in both basic research and technological applications. Further work could investigate the effect of changing the Co concentration in the middle layer; this could combine both experimental data with more accurate modelling (e.g. expanding to three dimensions and including the Sm interactions). The hypothesis that strong inter-layer coupling is mediated by Co rich regions could be tested by investigating whether similar effects are observed in trilayers which are composed of layers without a common element, for example with multilayers constructed of amorphous SmCo/FeAlZr.

In the final part of this thesis, element specific hysteresis loops recorded using resonant scattering at the Pd L_3 edge were used to study magnetisation reversals of patterned arrays of FePd. The hysteresis loops for a continuous film showed square loops that collapsed at the ordering temperature, as would be expected in a ferromagnetic alloy. Whereas hysteresis loops for the patterned sample exhibited a change in gradient as a vortex state was created/annihilated in the islands.

Specular reflectivity and rocking curves recorded at the Pd L_3 edge revealed that the circular islands were domed, covered in a non-magnetic oxide layer with the magnetisation evenly distributed throughout the interior. The sum and difference rocking curves recorded at the Pd L_3 edge in a saturating applied field were presented for the patterned sample. The difference rocking curve showed a change in sign across the range of q_x due to beating between the chemical and magnetic

form factors. The difference rocking curves were then measured as a function of applied field and certain satellite peaks changed sign relative to those recorded at saturation; this revealed that there was a changing magnetic structure resulting in a beating between the chemical and magnetic form factors. Simulated rocking curves confirmed that either a non-magnetic oxide layer, or a partial reversal of the magnetisation in the islands could result in certain satellite peaks changing sign.

Analysing rocking curves measured using resonant x-ray scattering would allow highly accurate studies of the magnetic structure within elements of patterned arrays, providing average measurements across larger areas of the sample than is possible with microscopy techniques. Using resonant x-ray scattering to record rocking curves provides larger scale, averaged information about the magnetic structures in a patterned array which is element specific. If the data could be fitted accurately enough, this could provide an insightful new technique for investigating the properties of patterned magnetic media in areas of research such as thermal relaxation in artificial spin ice [64, 244–246].

There is much work to be done, however, if the data is to be accurately fitted and this is beyond the scope of this work. To take this further, the simulations would need to accurately model the island shape, size and oxide layers in three dimensions, plus a better model of roughness (both for the islands and substrate). It would also need to be integrated with a fitting algorithm such as the genetic evolution algorithm used in GenX. Additionally, it would need to include experimental factors such as detector resolution and the projection length of the beam on the sample.

This thesis has shown that resonant x-ray scattering is a highly sensitive technique for the study of structural and magnetic properties in multilayers and patterned arrays as a function of depth. X-ray reflectivity techniques allow surface sensitive, non-destructive studies of thin films, making it a powerful method for studying such structures. Resonant scattering has been used here in various forms including specular reflectivity, element specific hysteresis loops and rocking curves to study various magnetic interactions. This work has demonstrated that the element specific nature of the technique can provide new insights into the complex magnetic interactions that occur in magnetic multilayers and patterned arrays.

Bibliography

[1] E. de Lacheisserie, D. Gignoux, and M. Schlenker, *Magnetism*, vol. 1 of *Collection Grenoble Sciences*. Springer, 2005.

[2] J. E. Kogel, for Mining Metallurgy, and E. (U.S.), *Industrial Minerals & Rocks: Commodities, Markets, and Uses*. Society for Mining, Metallurgy, and Exploration, 2006.

[3] S. Blundell, *Magnetism in Condensed Matter*. Oxford University Press, 2001.

[4] I. K. Schuller, S. Kim, and C. Leighton, "Magnetic superlattices and multilayers," *J. Magn. Magn. Mater.*, vol. 200, no. 1, pp. 571–582, 1999.

[5] A. Y. Cho, "How molecular beam epitaxy (MBE) began and its projection into the future," *J. Cryst. Growth*, vol. 201-202, pp. 1–7, 1999.

[6] S. S. P. Parkin, M. Hayashi, and L. Thomas, "Magnetic Domain-Wall Racetrack Memory," *Science*, vol. 320, no. 5873, pp. 190–194, 2008.

[7] R. L. Comstock, "Review Modern magnetic materials in data storage," *J. Mater. Sci. Mater. Electron.*, vol. 13, no. 9, pp. 509–523, 2002.

[8] L. Pan and D. B. Bogy, "Data storage: Heat-assisted magnetic recording," *Nat. Photonics*, vol. 3, no. 4, pp. 189–190, 2009.

[9] B. D. Terris, T. Thomson, and G. Hu, "Patterned media for future magnetic data storage," *Microsyst. Technol.*, vol. 13, no. 2, pp. 189–196, 2007.

[10] S. D. Bader and S. S. P. Parkin, "Spintronics," *Annu. Rev. Condens. Matter Phys.*, vol. 1, pp. 71–88, 2010.

[11] S. A. Wolf, D. D. Awschalom, R. A. Buhrman, J. M. Daughton, S. von Molnár, M. L. Roukes, A. Y. Chtchelkanova, and D. M. Treger, "Spintronics: A Spin-Based Electronics Vision for the Future," *Science*, vol. 294, no. 5546, pp. 1488–1495, 2001.

[12] J. Lenz and S. Edelstein, "Magnetic sensors and their applications," *IEEE Sens. J.*, vol. 6, no. 3, pp. 631–649, 2006.

[13] J. Llandro, J. J. Palfreyman, A. Ionescu, and C. H. W. Barnes, "Magnetic biosensor technologies for medical applications: a review," *Med. & Biol. Eng. & Comput.*, vol. 48, no. 10, pp. 977–998, 2010.

[14] M. Colombo, S. Carregal-Romero, M. F. Casula, L. Gutierrez, M. P. Morales, I. B. Bohm, J. T. Heverhagen, D. Prosperi, and W. J. Parak, "Biological applications of magnetic nanoparticles," *Chem. Soc. Rev.*, vol. 41, no. 11, pp. 4306–4334, 2012.

[15] D. J. Wagner and A. H. Jayatissa, "Nanoimprint lithography: Review of aspects and applications," 2005.

[16] J. Stöhr and H. Siegmann, *Magnetism, From Fundamentals to Nanoscale Dynamics*. Springer, 2006.

[17] M. Getzlaff, *Fundamentals of Magnetism*. Springer Berlin Heidelberg, 2007.

[18] K. Yosida, *Theory of Magnetism: Edition en anglais*. Solid-State Sciences Series, Springer, 1996.

[19] D. Jiles, *Introduction to Magnetism and Magnetic Materials, Third Edition*. CRC Press, 2015.

[20] E. O'Reilly, *Quantum Theory of Solids*. Master's Series in Physics and Astronomy, Taylor & Francis, 2002.

[21] M. A. Ruderman and C. Kittel, "Indirect Exchange Coupling of Nuclear Magnetic Moments by Conduction Electrons," *Phys. Rev.*, vol. 96, no. 1, pp. 99–102, 1954.

[22] T. Kasuya, "Electrical Resistance of Ferromagnetic Metals," *Prog. Theor. Phys.*, vol. 16, no. 1, pp. 58–63, 1956.

[23] K. Yosida, "Magnetic Properties of Cu-Mn Alloys," *Phys. Rev.*, vol. 106, no. 5, pp. 893–898, 1957.

[24] G. Fernando and P. Misra, *Metallic Multilayers and their Applications: Theory, Experiments, and Applications related to Thin Metallic Multilayers*. Handbook of Metal Physics, Elsevier Science, 2011.

[25] C. Kittel, *Introduction to Solid State Physics*. Wiley, 2004.

[26] M. T. Johnson, P. J. H. Bloemen, F. J. A. den Broeder, and J. J. de Vries, "Magnetic anisotropy in metallic multilayers," *Reports Prog. Phys.*, vol. 59, no. 11, p. 1409, 1996.

[27] D. M. Paige, B. Szpunar, and B. K. Tanner, "The magnetocrystalline anisotropy of cobalt," *J. Magn. Magn. Mater.*, vol. 44, no. 3, pp. 239–248, 1984.

[28] J. Crangle, *Solid State Magnetism*. Springer US, 2012.

[29] R. M. Bozorth, "Directional Ferromagnetic Properties of Metals," *J. Appl. Phys.*, vol. 8, no. 9, pp. 575–588, 1937.

[30] J. J. M. Franse and G. D. Vries, "The magnetocrystalline anisotropy energy of nickel," *Physica*, vol. 39, no. 4, pp. 477–498, 1968.

[31] C. W. Chen, *Magnetism and Metallurgy of Soft Magnetic Materials*. Dover Books on Physics, Dover Publications, 2013.

[32] H. Kronmüller and M. Fähnle, *Micromagnetism and the Microstructure of Ferromagnetic Solids*. Cambridge studies in magnetism, Cambridge University Press, 2003.

[33] O. Gutfleisch, M. A. Willard, E. Brück, C. H. Chen, S. G. Sankar, and J. P. Liu, "Magnetic Materials and Devices for the 21st Century: Stronger, Lighter, and More Energy Efficient," *Adv. Mater.*, vol. 23, no. 7, pp. 821–842, 2011.

[34] S. Tehrani, J. M. Slaughter, E. Chen, M. Durlam, J. Shi, and M. DeHerren, "Progress and outlook for MRAM technology," *IEEE Trans. Magn.*, vol. 35, no. 5, pp. 2814–2819, 1999.

[35] K. H. J. Buschow, "Intermetallic compounds of rare-earth and 3d transition metals," *Reports Prog. Phys.*, vol. 40, no. 10, p. 1179, 1977.

[36] M. Mansuripur, "Magnetization reversal, coercivity, and the process of thermomagnetic recording in thin films of amorphous rare earthtransition metal alloys," *J. Appl. Phys.*, vol. 61, no. 4, pp. 1580–1587, 1987.

[37] K. Chen, H. Hegde, S. U. Jen, and F. J. Cadieu, "Different types of anisotropy in amorphous SmCo films," *J. Appl. Phys.*, vol. 73, no. 10, pp. 5923–5925, 1993.

[38] T. D. Cheung, L. Wickramasekara, and F. J. Cadieue, "Large inplane anisotropy in amorphous SmCo and (Sm+Ti)Fe films," *J. Appl. Phys.*, vol. 57, no. 8, pp. 3598–3600, 1985.

[39] Y. Wu, J. Stöhr, B. D. Hermsmeier, M. G. Samant, and D. Weller, "Enhanced orbital magnetic moment on Co atoms in Co/Pd multilayers: A magnetic circular x-ray dichroism study," *Phys. Rev. Lett.*, vol. 69, no. 15, pp. 2307–2310, 1992.

[40] A. Taroni and B. Hjörvarsson, "Influence of the range of interactions in thin magnetic structures," *Eur. Phys. J. B*, vol. 77, no. 3, pp. 367–371, 2010.

[41] Y. Li and K. Baberschke, "Dimensional crossover in ultrathin Ni(111) films on W(110)," *Phys. Rev. Lett.*, vol. 68, no. 8, pp. 1208–1211, 1992.

[42] D. Lederman, C. A. Ramos, V. Jaccarino, and J. L. Cardy, "Finite-size scaling in FeF_2/ZnF_2 superlattices," *Phys. Rev. B*, vol. 48, no. 11, pp. 8365–8375, 1993.

[43] F. Huang, G. J. Mankey, M. T. Kief, and R. F. Willis, "Finitesize scaling behavior of ferromagnetic thin films," *J. Appl. Phys.*, vol. 73, no. 10, pp. 6760–6762, 1993.

[44] P. F. Carcia, A. D. Meinhaldt, and A. Suna, "Perpendicular magnetic anisotropy in Pd/Co thin film layered structures," *Appl. Phys. Lett.*, vol. 47, no. 2, pp. 178–180, 1985.

[45] W. B. Zeper, F. J. A. M. Greidanus, P. F. Carcia, and C. R. Fincher, "Perpendicular magnetic anisotropy and magnetooptical Kerr effect of vapor deposited Co/Pt layered structures," *J. Appl. Phys.*, vol. 65, no. 12, pp. 4971–4975, 1989.

[46] C. Lin and G. L. Gorman, "Evaporated CoPt alloy films with strong perpendicular magnetic anisotropy," *Appl. Phys. Lett.*, vol. 61, no. 13, pp. 1600–1602, 1992.

[47] V. Gehanno, A. Marty, B. Gilles, and Y. Samson, "Magnetic domains in epitaxial ordered FePd(001) thin films with perpendicular magnetic anisotropy," *Phys. Rev. B*, vol. 55, no. 18, pp. 12552–12555, 1997.

[48] J. A. C. Bland and B. Heinrich, *Ultrathin Magnetic Structures I: An Introduction to the Electronic, Magnetic and Structural Properties*. Ultrathin Magnetic Structures, Springer Berlin Heidelberg, 2006.

[49] E. F. Kneller and R. Hawig, "The exchange-spring magnet: A new material principle for permanent magnets," *IEEE Trans. Magn.*, vol. 27, pp. 3588–3600, 1991.

[50] E. E. Fullerton, J. S. Jiang, M. Grimsditch, C. H. Sowers, and S. D. Bader, "Exchange-spring behavior in epitaxial hard/soft magnetic bilayers," *Phys. Rev. B*, vol. 58, no. 18, pp. 12193–12200, 1998.

[51] E. E. Fullerton, J. S. Jiang, and S. D. Bader, "Hard/soft magnetic heterostructures: model exchange-spring magnets," *J. Magn. Magn. Mater.*, vol. 200, no. 13, pp. 392–404, 1999.

[52] H. Zabel, "Progress in spintronics," *Superlattices Microstruct.*, vol. 46, no. 4, pp. 541–553, 2009.

[53] J. Kwo, E. M. Gyorgy, D. B. McWhan, M. Hong, F. J. Disalvo, C. Vettier, and J. E. Bower, "Magnetic and Structural Properties of Single-Crystal Rare-Earth Gd-Y Superlattices," *Phys. Rev. Lett.*, vol. 55, no. 13, pp. 1402–1405, 1985.

[54] M. Salamon, S. Sinha, J. Rhyne, J. Cunningham, R. Erwin, J. Borchers, and C. Flynn, "Long-range incommensurate magnetic order in a Dy-Y multilayer," *Phys. Rev. Lett.*, vol. 56, pp. 259–262, 1986.

[55] L. Cheng, Z. Altounian, D. H. Ryan, J. O. Ström-Olsen, M. Sutton, and Z. Tun, "Pd polarization and interfacial moments in Pd-Fe multilayers," *Phys. Rev. B*, vol. 69, no. 14, p. 144403, 2004.

[56] V. S. Stepanyuk, W. Hergert, K. Wildberger, R. Zeller, and P. H. Dederichs, "Magnetism of 3d, 4d, and 5d transition-metal impurities on Pd(001) and Pt(001) surfaces," *Phys. Rev. B*, vol. 53, no. 4, pp. 2121–2125, 1996.

[57] P. Mohn, *Magnetism in the Solid State: An Introduction.* Springer Series in Solid-State Sciences, Springer Berlin Heidelberg, 2006.

[58] F. Nolting, A. Scholl, J. Stohr, J. W. Seo, J. Fompeyrine, H. Siegwart, J.-P. Locquet, S. Anders, J. Luning, E. E. Fullerton, M. F. Toney, M. R. Scheinfein, and H. A. Padmore, "Direct observation of the alignment of ferromagnetic spins by antiferromagnetic spins," *Nature*, vol. 405, no. 6788, pp. 767–769, 2000.

[59] A. Scholl, F. Nolting, J. W. Seo, H. Ohldag, J. Stöhr, S. Raoux, J.-P. Locquet, and J. Fompeyrine, "Domain-size-dependent exchange bias in CoLaFeO3," *Appl. Phys. Lett.*, vol. 85, no. 18, pp. 4085–4087, 2004.

[60] R. P. Cowburn, D. K. Koltsov, A. O. Adeyeye, M. E. Welland, and D. M. Tricker, "Single-Domain Circular Nanomagnets," *Phys. Rev. Lett.*, vol. 83, no. 5, pp. 1042–1045, 1999.

[61] J. P. Morgan, A. Stein, S. Langridge, and C. H. Marrows, "Thermal ground-state ordering and elementary excitations in artificial magnetic square ice," *Nat. Phys.*, vol. 7, no. 1, pp. 75–79, 2011.

[62] S. Ladak, D. E. Read, G. K. Perkins, L. F. Cohen, and W. R. Branford, "Direct observation of magnetic monopole defects in an artificial spin-ice system," *Nat. Phys.*, vol. 6, no. 5, pp. 359–363, 2010.

[63] S. T. Bramwell and M. J. P. Gingras, "Spin Ice State in Frustrated Magnetic Pyrochlore Materials," *Science*, vol. 294, no. 5546, pp. 1495–1501, 2001.

[64] V. Kapaklis, U. B. Arnalds, A. Farhan, R. V. Chopdekar, A. Balan, A. Scholl, L. J. Heyderman, and B. Hjörvarsson, "Thermal fluctuations in artificial spin ice.," *Nat. Nanotechnol.*, vol. 9, no. 7, pp. 514–9, 2014.

[65] S. R. Giblin, S. T. Bramwell, P. C. W. Holdsworth, D. Prabhakaran, and I. Terry, "Creation and measurement of long-lived magnetic monopole currents in spin ice," *Nat. Phys.*, vol. 7, no. 3, pp. 252–258, 2011.

[66] M. Tanaka, E. Saitoh, H. Miyajima, T. Yamaoka, and Y. Iye, "Magnetic interactions in a ferromagnetic honeycomb nanoscale network," *Phys. Rev. B*, vol. 73, no. 5, p. 52411, 2006.

[67] U. B. Arnalds, E. T. Papaioannou, T. P. A. Hase, H. Raanaei, G. Andersson, T. R. Charlton, S. Langridge, and B. Hjörvarsson, "Magnetic structure and diffracted magneto-optics of patterned amorphous multilayers," *Phys. Rev. B*, vol. 82, no. 14, p. 144434, 2010.

[68] P. J. Goodhew, J. Humphreys, and R. Beanland, *Electron Microscopy and Analysis, Third Edition*. Taylor & Francis, 2000.

[69] R. Reifenberger, *Fundamentals of Atomic Force Microscopy: Part I: Foundations*. Lessons from Nanoscience: A Lecture Notes Series, World Scientific Publishing Company, 2015.

[70] D. B. Williams and C. B. Carter, *Transmission Electron Microscopy: A Textbook for Materials Science*, vol. 2 of *Cambridge library collection*. Springer, 2009.

[71] E. Meyer, H. J. Hug, and R. Bennewitz, *Scanning Probe Microscopy: The Lab on a Tip*. Advanced Texts in Physics, Springer Berlin Heidelberg, 2013.

[72] A. K. Petford-Long and J. N. Chapman, *Lorentz Microscopy*, pp. 67–86. Berlin, Heidelberg: Springer Berlin Heidelberg, 2005.

[73] W. Zhang and K. M. Krishnan, "Epitaxial patterning of thin-films: conventional lithographies and beyond," *J. Micromechanics Microengineering*, vol. 24, no. 9, p. 93001, 2014.

[74] A. Furrer, J. Ã. Mesot, and T. StrÃssle, *Neutron Scattering in Condensed Matter Physics*. Series on Neutron Techniques and Applications, 2009.

[75] A. Furrer, *Complementarity Between Neutron and Synchrotron X-Ray Scattering*. 1998.

[76] J. Daillant and A. Gibaud, *X-ray and Neutron Reflectivity: Principles and Applications*. Lecture Notes in Physics, Springer Berlin Heidelberg, 2008.

[77] T. Chatterji, *Neutron Scattering from Magnetic Materials*. Elsevier Science, 2005.

[78] M. Blume and D. Gibbs, "Polarization dependence of magnetic x-ray scattering," *Phys. Rev. B*, vol. 37, no. 4, pp. 1779–1789, 1988.

[79] J. Als-Nielsen and D. McMorrow, *Elements of Modern X-ray Physics*. Wiley, second ed., 2011.

[80] D. H. Goldstein, *Polarized Light, Third Edition*. CRC Press, 2016.

[81] D. S. Sivia, *Elementary Scattering Theory For X-ray and Neutron Users*. Oxford University Press, 2011.

[82] J. P. Hill and D. F. McMorrow, "Resonant Exchange Scattering: Polarization Dependence and Correlation Function," *Acta Crystallogr. Sect. A*, vol. 52, no. 2, p. 236, 1996.

[83] D. W. Johnson, "A Fourier series method for numerical Kramers-Kronig analysis," *J. Phys. A. Math. Gen.*, vol. 8, no. 4, p. 490, 1975.

[84] B. Lengeler, "X-Ray Absorption and Reflection in the Hard X-Ray Range," in *Photoemiss. Absorpt. Solids Interfaces with Synchrotron Radiat.* (M. Campagna and R. Rosei, eds.), (Amsterdam, North Holland), pp. 157–202, 1990.

[85] K. K. Sharma, *Optics: Principles and Applications.* Elsevier Science, 2006.

[86] L. Parratt, "Surface Studies of Solids by Total Refiection of X-Rays," *Phys. Rev.*, vol. 95, no. 2, pp. 359–369, 1954.

[87] M. Björck and G. Andersson, "*GenX*: an extensible X-ray reflectivity refinement program utilizing differential evolution," *J. Appl. Crystallogr.*, vol. 40, no. 6, pp. 1174–1178, 2007.

[88] S. A. Stepanov, E. A. Kondrashkina, R. Köhler, D. V. Novikov, G. Materlik, and S. M. Durbin, "Dynamical x-ray diffraction of multilayers and superlattices: Recursion matrix extension to grazing angles," *Phys. Rev. B*, vol. 57, no. 8, pp. 4829–4841, 1998.

[89] L. Nevot and P. Croce, "Caractérisation des surfaces par réflexion rasante de rayons X. Application à l'étude du polissage de quelques verres silicates," *Rev. Phys. appliquée*, vol. 15, no. 3, pp. 761–779, 1980.

[90] F. de Bergevin and M. Brunel, "Diffraction of X-rays by magnetic materials. I. General formulae and measurements on ferro- and ferrimagnetic compounds," *Acta Crystallogr. Sect. A*, vol. 37, no. 3, pp. 314–324, 1981.

[91] M. Blume, "Magnetic scattering of x rays (invited)," *J. Appl. Phys.*, vol. 57, no. 8, pp. 3615–3618, 1985.

[92] C. Vettier, "Magnetic X-Ray Scattering," *Acta Phys. Pol. A Gen. Phys.*, vol. 86, no. 4, pp. 521–536, 1994.

[93] D. Gibbs, D. E. Moncton, K. L. D'Amico, J. Bohr, and B. H. Grier, "Magnetic x-ray scattering studies of holmium using synchro- tron radiation," *Phys. Rev. Lett.*, vol. 55, no. 2, pp. 234–237, 1985.

[94] E. Beaurepaire, *Magnetism: A Synchrotron Radiation Approach.* Lecture Notes in Physics, Springer, 2006.

[95] D. Gibbs, D. R. Harshman, E. D. Isaacs, D. B. McWhan, D. Mills, and C. Vettier, "Polarization and Resonance Properties of Magnetic X-Ray Scattering in Holmium," *Phys. Rev. Lett.*, vol. 61, no. 10, pp. 1241–1244, 1988.

[96] P. Willmott, *An Introduction to Synchrotron Radiation, Techniques and Applications*. Wiley, 2011.

[97] J. Stöhr, "X-ray magnetic circular dichroism spectroscopy of transition metal thin films," *J. Electron Spectros. Relat. Phenomena*, vol. 75, pp. 253–272, 1995.

[98] B. T. Thole, G. van der Laan, and G. A. Sawatzky, "Strong Magnetic Dichroism Predicted in the $M_{4,5}$ X-Ray Absorption Spectra of Magnetic Rare-Earth Materials," *Phys. Rev. Lett.*, vol. 55, no. 19, pp. 2086–2088, 1985.

[99] J. P. Hannon, G. T. Trammell, M. Blume, and D. Gibbs, "X-ray Resonance Exchange Scattering," *Phys. Rev. Lett.*, vol. 61, no. 10, pp. 1245–1248, 1988.

[100] C. T. Chantler, K. Olsen, R. A. Dragoset, J. Chang, A. R. Kishore, S. A. Kotochigova, and D. S. Zucker, "X-Ray Form Factor, Attenuation and Scattering Tables (version 2.1). `http://physics.nist.gov/ffast` [Online]," 2005. (date accessed: 05-10-2016).

[101] B. T. Thole, P. Carra, F. Sette, and G. van der Laan, "X-ray circular dichroism as a probe of orbital magnetization," *Phys. Rev. Lett.*, vol. 68, no. 12, pp. 1943–1946, 1992.

[102] P. Carra, B. T. Thole, M. Altarelli, and X. Wang, "X-ray circular dichroism and local magnetic fields," *Phys. Rev. Lett.*, vol. 70, no. 5, pp. 694–697, 1993.

[103] J. Stöhr and H. König, "Determination of Spin- and Orbital-Moment Anisotropies in Transition Metals by Angle-Dependent X-Ray Magnetic Circular Dichroism," *Phys. Rev. Lett.*, vol. 75, no. 20, pp. 3748–3751, 1995.

[104] M. Björck, M. S. Brewer, U. B. Arnalds, E. Östman, M. Ahlberg, V. Kapaklis, E. T. Papaioannou, G. Andersson, B. Hjörvarsson, and T. P. A. Hase, "Reflectivity Studies of Magnetic Heterostructures," *J. Surfaces Interfaces Mater.*, vol. 2, no. 1, pp. 24–32, 2014.

[105] D. Mannix, D. F. McMorrow, R. A. Ewings, A. T. Boothroyd, D. Prabhakaran, Y. Joly, B. Janousova, C. Mazzoli, L. Paolasini, and S. B. Wilkins, "X-ray scattering study of the order parameters in multiferroic $TbMnO_3$," *Phys. Rev. B*, vol. 76, no. 18, p. 184420, 2007.

[106] U. Staub, V. Scagnoli, Y. Bodenthin, M. García-Fernández, R. Wetter, A. M. Mulders, H. Grimmer, and M. Horisberger, "Polarization analysis in soft X-ray

diffraction to study magnetic and orbital ordering," *J. Synchrotron Radiat.*, vol. 15, no. 5, pp. 469–476, 2008.

[107] F. Magnus, R. Moubah, A. H. Roos, A. Kruk, V. Kapaklis, T. Hase, B. Hjörvarsson, and G. Andersson, "Tunable giant magnetic anisotropy in amorphous SmCo thin films," *Appl. Phys. Lett.*, vol. 102, no. 16, p. 162402, 2013.

[108] D. D. Djayaprawira, K. Tsunekawa, M. Nagai, H. Maehara, S. Yamagata, N. Watanabe, S. Yuasa, Y. Suzuki, and K. Ando, "230% room-temperature magnetoresistance in CoFeB/MgO/CoFeB magnetic tunnel junctions," *Appl. Phys. Lett.*, vol. 86, no. 9, pp. 92502–92503, 2005.

[109] C. M. Choi, J. O. Song, and S. R. Lee, "Thermal stability of magnetic tunnel junctions with new amorphous ZrAl-alloy films as the under and capping layers," in *IEEE Trans. Magn.*, vol. 41, pp. 2667–2669, 2005.

[110] T. Hase, H. Raanaei, H. Lidbaum, C. Sánchez-Hanke, S. Wilkins, K. Leifer, and B. Hjörvarsson, "Spin and orbital moment in amorphous $Co_{68}Fe_{24}Zr_8$ layers," *Phys. Rev. B*, vol. 80, no. 13, p. 134402, 2009.

[111] G. Suran, F. Machizaud, and M. Naili, "Induced anisotropy in amorphous Co-Zr- M (M =Zr,Nb,Ti) and Co-Zr-Pt thin films: A magnetic and a structural study," *Phys. Rev. B*, vol. 47, no. 22, pp. 15007–15018, 1993.

[112] T. Numata, H. Kiriyama, S. Inokuchi, and Y. Sakurai, "Magnetic anisotropy in SmCo amorphous films," *J. Appl. Phys.*, vol. 64, no. 10, 1988.

[113] P. Kelly and R. Arnell, "Magnetron sputtering: a review of recent developments and applications," *Vacuum*, vol. 56, no. 3, pp. 159–172, 2000.

[114] V. Shchukin, N. N. Ledentsov, and D. Bimberg, *Epitaxy of Nanostructures*. Springer-Verlag, 2004.

[115] "`https://www2.warwick.ac.uk/fac/sci/physics/current/postgraduate/regs/mpags/ex5/growth/pvd/`." (date accessed: 04-04-2016).

[116] M. A. Herman and H. Sitter, *Molecular Beam Epitaxy Fundamentals and Current Status*. Springer-Verlag, 1989.

[117] M. Mansuripur, *Classical Optics and Its Applications*. Cambridge University Press, 2002.

[118] N. Spaldin, *Magnetic Materials, Fundamentals and Device Applications*. Cambridge University Press, 2003.

[119] Z. Q. Qiu and S. D. Bader, "Kerr effect and surface magnetism," in *Non-linear Opt. Met.*, Oxford: Clarendon Press, 1998.

[120] C. B. Duke and E. W. Plummer, *Frontiers in Surface and Interface Science*. Elsevier, 2002.

[121] J. G. Webster and H. Eren, *Measurement, Instrumentation, and Sensors Handbook, Second Edition*. CRC Press, 2014.

[122] U. Pietsch, V. Holy, and T. Baumbach, *High-Resolution X-Ray Scattering: From Thin Films to Lateral Nanostructures*. New York: Springer, second ed., 2004.

[123] R. Van Grieken and A. Markowicz, *Handbook of X-ray spectrometry. Second edition*, vol. 29. 2002.

[124] J. C. Lang and G. Srajer, "Bragg transmission phase plates for the production of circularly polarized x rays," *Rev. Sci. Instrum.*, vol. 66, no. 2, 1995.

[125] L. Bouchenoire, R. J. H. Morris, and T. P. A. Hase, "A silicon 111 phase retarder for producing circularly polarized x-rays in the 2.1-3 keV energy range," *Appl. Phys. Lett.*, vol. 101, no. 6, 2012.

[126] "`http://www2.warwick.ac.uk/fac/cross_fac/xmas/xmasbeamline`." (date accessed: 27-01-2016).

[127] "`http://www.esrf.eu/UsersAndScience/Experiments/CRG/BM28`." (date accessed: 27-01-2017).

[128] "`https://www1.aps.anl.gov/sector-4/4-id-d`." (date accessed: 16-12-2016).

[129] J. W. Freeland, J. C. Lang, G. Srajer, R. Winarski, D. Shu, and D. M. Mills, "A unique polarized x-ray facility at the Advanced Photon Source," in *Rev. Sci. Instrum.*, vol. 73, p. 1408, 2002.

[130] C. Sánchez-Hanke, C. C. Kao, and S. L. Hulbert, "Fast-switching elliptically polarized soft X-ray beamline X13A at NSLS," *Nucl. Instruments Methods Phys. Res. A*, vol. 608, no. 2, pp. 351–359, 2009.

[131] T. P. A. Hase, *X-ray scattering from magnetic metallic multilayers.* PhD thesis, Durham University, 1998.

[132] T. P. A. Hase and I. G. Hughes, *Measurements and their uncertainties: A practical guide to modern error analysis.* Oxford: Oxford University Press, 2010.

[133] M. Björck, "Fitting with differential evolution: an introduction and evaluation," *J. Appl. Crystallogr.*, vol. 44, pp. 1198–1204, 2011.

[134] F. C. Campbell, *Elements of Metallurgy and Engineering Alloys.* ASM International, 2008.

[135] W. D. Callister and D. G. Rethwisch, *Fundamentals of Materials Science and Engineering: An Integrated Approach.* Wiley, 2012.

[136] A. L. Barabási and H. E. Stanley, *Fractal Concepts in Surface Growth.* Cambridge University Press, 1995.

[137] J. Jensen and A. Mackintosh, *Rare earth magnetism: structures and excitations.* Oxford: Clarendon Press, 1991.

[138] C. F. Majkrzak, J. W. Cable, J. Kwo, M. Hong, D. B. McWhan, Y. Yafet, J. V. Waszczak, and C. Vettier, "Observation of a magnetic antiphase domain structure with long-range order in a synthetic Gd-Y superlattice," *Phys. Rev. Lett.*, vol. 56, no. 25, pp. 2700–2703, 1986.

[139] Y. Yafet, J. Kwo, M. Hong, C. F. Majkrzak, and T. O'Brien, "Interlayer exchange in magnetic superlattices (invited)," *J. Appl. Phys.*, vol. 63, no. 8, pp. 3453–3457, 1988.

[140] C. Majkrzak, J. Kwo, M. Hong, Y. Yafet, D. Gibbs, C. Chien, and J. Bohr, "Magnetic rare earth superlattices," *Adv. Phys.*, vol. 40, no. January 2015, pp. 99–189, 1991.

[141] R. W. Erwin, J. J. Rhyne, M. B. Salamon, J. Borchers, S. Sinha, R. Du, J. E. Cunningham, and C. P. Flynn, "Magnetic structure of Dy-Y superlattices," *Phys. Rev. B*, vol. 35, no. 13, pp. 6808–6825, 1987.

[142] M. Hong, R. M. Fleming, J. Kwo, L. F. Schneemeyer, J. V. Waszczak, J. P. Mannaerts, C. F. Majkrzak, D. Gibbs, and J. Bohr, "Synthetic magnetic rareearth DyY superlattices," *J. Appl. Phys.*, vol. 61, no. 8, 1987.

[143] D. Haskel, G. Srajer, J. C. Lang, J. Pollmann, C. S. Nelson, J. S. Jiang, and S. D. Bader, "Enhanced Interfacial Magnetic Coupling of Gd /Fe Multilayers," *Phys. Rev. Lett.*, vol. 87, no. 20, p. 207201, 2001.

[144] A. Cebollada, J. L. Martnez, J. M. Gallego, J. J. de Miguel, R. Miranda, S. Ferrer, F. Batallán, G. Fillion, and J. P. Rebouillat, "Antiferromagnetic ordering in Co-Cu single-crystal superlattices," *Phys. Rev. B*, vol. 39, no. 13, pp. 9726–9729, 1989.

[145] J. A. Borchers, M. B. Salamon, R. W. Erwin, J. J. Rhyne, R. R. Du, and C. P. Flynn, "Structural and magnetic properties of Er thin films and Er/Y superlattices: Magnetoelastic effects," *Phys. Rev. B*, vol. 43, no. 4, pp. 3123–3136, 1991.

[146] K. Dumesnil, C. Dufour, A. Stunault, and P. Mangin, "Magnetic ordering in a (001) Sm layer and a Sm/Y superlattice studied by resonant x-ray magnetic scattering," *J. Phys. Condens. Matter*, vol. 12, no. 13, p. 3091, 2000.

[147] B. Everitt, J. Borchers, M. Salamon, J. Rhyne, R. Erwin, B. Park, and C. Flynn, "Magnetic ordering of Nd in Nd/Y superlattices," *J. Magn. Magn. Mater.*, vol. 140, pp. 769–770, 1995.

[148] Y. Wang, P. M. Levy, and J. L. Fry, "Interlayer magnetic coupling in Fe/Cr multilayered structures," *Phys. Rev. Lett.*, vol. 65, no. 21, pp. 2732–2735, 1990.

[149] D. A. Jehan, D. F. McMorrow, R. A. Cowley, R. C. C. Ward, M. R. Wells, N. Hagmann, and K. N. Clausen, "Magnetic structure of holmium-yttrium superlattices," *Phys. Rev. B*, vol. 48, no. 8, pp. 5594–5606, 1993.

[150] P. F. Fewster, "X-ray analysis of thin films and multilayers," *Reports Prog. Phys.*, vol. 59, no. 11, p. 1339, 1996.

[151] J. W. Cable, W. C. Koehler, and E. O. Wollan, "Magnetic Order in Rare-Earth Intermetallic Compounds," *Phys. Rev.*, vol. 136, no. 1A, pp. A240—-A242, 1964.

[152] C. F. Majkrzak, D. Gibbs, P. Böni, A. I. Goldman, J. Kwo, M. Hong, T. C. Hsieh, R. M. Fleming, D. B. McWhan, Y. Yafet, J. W. Cable, J. Bohr, H. Grimm, and C. L. Chien, "Magnetic rare–earth superlattices (invited)," *J. Appl. Phys.*, vol. 63, no. 8, pp. 3447–3452, 1988.

[153] Y. Yafet, "RKKY interactions across yttrium layers in Gd-Y superlattices," *J. Appl. Phys.*, vol. 61, no. 8, pp. 4058–4060, 1987.

[154] A. R. Wildes, J. Mayer, and K. Theis-Bröhl, "The growth and structure of epitaxial niobium on sapphire," *Thin Solid Films*, vol. 401, no. 12, pp. 7–34, 2001.

[155] G. Gutekunst, J. Mayer, V. Vitek, and M. Rühle, "Atomic structure of epitaxial Nb-Al_2O_3 interfaces II. Misfit dislocations," *Philos. Mag. A*, vol. 75, no. 5, pp. 1357–1382, 1997.

[156] B. Wölfing, K. Theis-Bröhl, C. Sutter, and H. Zabel, "AFM and x-ray studies on the growth and quality of Nb(110) on α-$Al_2O_3(11\bar{2}0)$," *J. Phys. Condens. Matter*, vol. 11, no. 13, p. 2669, 1999.

[157] C. P. Flynn, "Constraints on the growth of metallic superlattices," *J. Phys. F Met. Phys.*, vol. 18, no. 9, p. L195, 1988.

[158] "Tables of Physical and Chemical Constants (16th edition 1995). 3.1.2 Properties of the elements. Kaye and Laby Online. Version 1.0 (2005)." (date accessed: 24-02-2017).

[159] G. Gutekunst, J. Mayer, and M. Rühle, "The niobium/sapphire interface: Structural studies by HREM," *Scr. Metall. Mater.*, vol. 31, no. 8, pp. 1097–1102, 1994.

[160] S. K. Sinha, "X-ray diffuse scattering as a probe for thin film and interface structure," *J. Phys. III*, vol. 4, no. 9, pp. 1543–1557, 1994.

[161] S. K. Sinha, E. B. Sirota, S. Garoff, and H. B. Stanley, "X-ray and neutron scattering from rough surfaces," *Phys. Rev. B*, vol. 38, no. 4, pp. 2297–2311, 1988.

[162] M. Benfatto and R. Felici, "Resonant atomic scattering factor theory: A multiple scattering approach," *Phys. Rev. B*, vol. 64, no. 11, p. 115410, 2001.

[163] C. Vettier, D. B. McWhan, E. M. Gyorgy, J. Kwo, B. M. Buntschuh, and B. W. Batterman, "Magnetic x-ray scattering study of interfacial magnetism in a Gd-Y superlattice," *Phys. Rev. Lett.*, vol. 56, no. 7, pp. 757–760, 1986.

[164] H. R. Child and J. W. Cable, "Magnetic Structure Properties of GdY and GdSc Alloys," *J. Appl. Phys.*, vol. 40, no. 3, 1969.

[165] T. Ito, S. Legvold, and B. J. Beaudry, "New look at magnetism in single-crystal Gd-Y alloys," *Phys. Rev. B*, vol. 23, no. 7, pp. 3409–3413, 1981.

[166] B. D. Schrag, A. Anguelouch, S. Ingvarsson, G. Xiao, Y. Lu, P. L. Trouilloud, A. Gupta, R. A. Wanner, W. J. Gallagher, P. M. Rice, and S. S. P. Parkin, "Néel orange-peel coupling in magnetic tunneling junction devices," *Appl. Phys. Lett.*, vol. 77, no. 15, pp. 2373–2375, 2000.

[167] J. Moritz, F. Garcia, J. C. Toussaint, B. Dieny, and J. P. Nozières, "Orange peel coupling in multilayers with perpendicular magnetic anisotropy: Application to (Co/Pt)-based exchange-biased spin-valves," *EPL (Europhysics Lett.*, vol. 65, no. 1, p. 123, 2004.

[168] S. Bates, S. B. Palmer, J. B. Sousa, G. J. McIntyre, D. Fort, S. Legvold, B. J. Beaudry, and W. C. Koehler, "Magnetic structure of Gd-Y single-crystal alloys from neutron diffraction and magnetization measurements," *Phys. Rev. Lett.*, vol. 55, no. 27, pp. 2968–2971, 1985.

[169] R. J. Melville, R. S. Eccleston, G. J. McIntyre, and S. B. Palmer, "The helical-ferromagnetic phase transition in Gd-Y alloys," *J. Phys. Condens. Matter*, vol. 4, no. 49, p. 10045, 1992.

[170] S. Wang, J. I. Guzman, and M. H. Kryder, "High moment soft amorphous CoFeZrRe thinfilm materials," *J. Appl. Phys.*, vol. 67, no. 9, pp. 5114–5116, 1990.

[171] D. Givord, J. Betz, K. Mackay, J. C. Toussaint, J. Voiron, and S. Wüchner, "Properties of rare-earth–transition-metal sandwich films," *J. Magn. Magn. Mater.*, vol. 159, no. 1, pp. 71–79, 1996.

[172] *Amorphous Metallic Alloys.* Butterworths monographs in materials, Elsevier Science, 2013.

[173] S. Wüchner, J. C. Toussaint, and J. Voiron, "Magnetic properties of exchange-coupled trilayers of amorphous rare-earth-cobalt alloys," *Phys. Rev. B*, vol. 55, no. 17, pp. 11576–11585, 1997.

[174] K. M. Unruh and C. L. Chien, "Magnetic properties and hyperfine interactions in amorphous Fe-Zr alloys," *Phys. Rev. B*, vol. 30, no. 9, pp. 4968–4974, 1984.

[175] H. Lidbaum, H. Raanaei, E. T. Papaioannou, K. Leifer, and B. Hjörvarsson, "Structural and magnetic properties of multilayers," *J. Cryst. Growth*, vol. 312, no. 4, pp. 580–586, 2010.

[176] Y. Fu, I. Barsukov, H. Raanaei, M. Spasova, J. Lindner, R. Meckenstock, M. Farle, and B. Hjörvarsson, "Tailored magnetic anisotropy in an amorphous trilayer," *J. Appl. Phys.*, vol. 109, no. 11, 2011.

[177] J. Sayama, K. Mizutani, T. Asahi, and T. Osaka, "Thin films of SmCo5 with very high perpendicular magnetic anisotropy," *Appl. Phys. Lett.*, vol. 85, no. 23, 2004.

[178] E. E. Fullerton, J. S. Jiang, C. Rehm, C. H. Sowers, S. D. Bader, J. B. Patel, and X. Z. Wu, "High coercivity, epitaxial SmCo films with uniaxial in-plane anisotropy," *Appl. Phys. Lett.*, vol. 71, no. 11, 1997.

[179] H. Raanaei, H. Nguyen, G. Andersson, H. Lidbaum, P. Korelis, K. Leifer, and B. Hjörvarsson, "Imprinting layer specific magnetic anisotropies in amorphous multilayers," *J. Appl. Phys.*, vol. 106, no. 2, p. 23918, 2009.

[180] F. Magnus, M. E. Brooks-Bartlett, R. Moubah, R. A. Procter, G. Andersson, T. P. A. Hase, S. T. Banks, and B. Hjörvarsson, "Long-range magnetic interactions and proximity effects in an amorphous exchange-spring magnet," *Nat. Commun.*, vol. 7, 2016.

[181] F. Magnus, R. Moubah, U. B. Arnalds, V. Kapaklis, A. Brunner, R. Schäfer, G. Andersson, and B. Hjörvarsson, "Giant magnetic domains in amorphous SmCo thin films," *Phys. Rev. B*, vol. 89, no. 22, p. 224420, 2014.

[182] A. Liebig, P. T. Korelis, H. Lidbaum, G. Andersson, K. Leifer, and B. Hjörvarsson, "Morphology of amorphous $Fe_{91}Zr_9Al_2O_3$ multilayers: Dewetting and crystallization," *Phys. Rev. B*, vol. 75, no. 21, p. 214202, 2007.

[183] P. T. Korelis, A. Liebig, M. Björck, B. Hjörvarsson, H. Lidbaum, K. Leifer, and A. R. Wildes, "Highly amorphous $Fe_{90}Zr_{10}$ thin films, and the influence of crystallites on the magnetism," *Thin Solid Films*, vol. 519, no. 1, pp. 404–409, 2010.

[184] M. Ahlberg, G. Andersson, and B. Hjörvarsson, "Two-dimensional XY-like amorphous $Co_{68}Fe_{24}Zr_8/Al_{70}Zr_{30}$ multilayers," *Phys. Rev. B*, vol. 83, no. 22, p. 224404, 2011.

[185] J. Kortright, S.-K. Kim, E. Fullerton, J. Jiang, and S. Bader, "X-ray magneto-optic Kerr effect studies of spring magnet heterostructures," *Nucl. Instruments Methods Phys. Res. A*, vol. 467-468. P, pp. 1396–1403, 2001.

[186] U. B. Arnalds, T. P. a. Hase, E. T. Papaioannou, H. Raanaei, R. Abrudan, T. R. Charlton, S. Langridge, and B. Hjörvarsson, "X-ray resonant magnetic scattering from patterned multilayers," *Phys. Rev. B*, vol. 86, no. 6, pp. 1–9, 2012.

[187] E. E. Fullerton, J. S. Jiang, C. H. Sowers, J. E. Pearson, and S. D. Bader, "Structure and magnetic properties of exchange-spring SmCo/Co superlattices," *Appl. Phys. Lett.*, vol. 72, no. 3, 1998.

[188] A. Scholl, M. Liberati, E. Arenholz, H. Ohldag, and J. Stöhr, "Creation of an Antiferromagnetic Exchange Spring," *Phys. Rev. Lett.*, vol. 92, no. 24, p. 247201, 2004.

[189] O. C. Ibe, *Elements of Random Walk and Diffusion Processes*. Wiley, 2013.

[190] R. M. Ziff, "Spanning probability in 2D percolation," *Phys. Rev. Lett.*, vol. 69, no. 18, pp. 2670–2673, 1992.

[191] K. Malarz and S. Galam, "Square-lattice site percolation at increasing ranges of neighbor bonds," *Phys. Rev. E*, vol. 71, no. 1, p. 16125, 2005.

[192] R. Skomski, *Simple Models of Magnetism*. Oxford University Press, 2008.

[193] P. Sotta and D. Long, "The crossover from 2D to 3D percolation: Theory and numerical simulations," *Eur. Phys. J. E*, vol. 11, no. 4, pp. 375–388, 2003.

[194] D. Stauffer and J. G. Zabolitzky, "Re-examination of 3D percolation threshold estimates," *J. Phys. A. Math. Gen.*, vol. 19, no. 17, p. 3705, 1986.

[195] M. G. Dowsett, A. Adriaens, G. K. C. Jones, N. Poolton, S. Fiddy, and S. Nikitenko, "Optically Detected X-ray Absorption Spectroscopy Measurements as a Means of Monitoring Corrosion Layers on Copper," *Anal. Chem.*, vol. 80, no. 22, pp. 8717–8724, 2008.

[196] K. O. Kvashnina, S. M. Butorin, A. Modin, L. Werme, J. Nordgren, J.-H. Guo, and R. Berger, "Electronic structure of complex copper systems probed by resonant inelastic X-ray scattering at Cu edge," *Phys. B Condens. Matter*, vol. 404, no. 20, pp. 3559–3566, 2009.

[197] L. A. Grunes, "Study of the K edges of $3d$ transition metals in pure and oxide form by x-ray-absorption spectroscopy," *Phys. Rev. B*, vol. 27, no. 4, pp. 2111–2131, 1983.

[198] J. Wong, F. W. Lytle, R. P. Messmer, and D. H. Maylotte, "K–edge absorption spectra of selected vanadium compounds," *Phys. Rev. B*, vol. 30, no. 10, pp. 5596–5610, 1984.

[199] R. D. Leapman, L. A. Grunes, and P. L. Fejes, "Study of the L_{23} edges in the $3d$ transition metals and their oxides by electron-energy-loss spectroscopy with comparisons to theory," *Phys. Rev. B*, vol. 26, no. 2, pp. 614–635, 1982.

[200] T. J. Regan, H. Ohldag, C. Stamm, F. Nolting, J. Lüning, J. Stöhr, and R. L. White, "Chemical effects at metal/oxide interfaces studied by x-ray-absorption spectroscopy," *Phys. Rev. B*, vol. 64, no. 21, p. 214422, 2001.

[201] J.-H. Park, S.-W. Cheong, and C. T. Chen, "Double-exchange ferromagnetism in $La(Mn_{1-x}Co_x)O_3$," *Phys. Rev. B*, vol. 55, no. 17, pp. 11072–11075, 1997.

[202] W.-S. Yoon, K.-B. Kim, M.-G. Kim, M.-K. Lee, H.-J. Shin, J.-M. Lee, J.-S. Lee, and C.-H. Yo, "Oxygen Contribution on Li-Ion IntercalationDeintercalation in $LiCoO_2$ Investigated by O K-Edge and Co L-Edge X-ray Absorption Spectroscopy," *J. Phys. Chem. B*, vol. 106, no. 10, pp. 2526–2532, 2002.

[203] X.-C. Liu, E.-W. Shi, Z.-Z. Chen, B.-Y. Chen, T. Zhang, L.-X. Song, K.-J. Zhou, M.-Q. Cui, W.-S. Yan, Z. Xie, B. He, and S.-Q. Wei, "Effect of oxygen partial pressure on the local structure and magnetic properties of Co-doped ZnO films," *J. Phys. Condens. Matter*, vol. 20, no. 2, p. 25208, 2008.

[204] J. Vegelius, I. L. Soroka, P. T. Korelis, B. Hjörvarsson, and S. M. Butorin, "Atomic and electronic structure of amorphous AlZr alloy films," *J. Phys. Condens. Matter*, vol. 23, no. 26, p. 265503, 2011.

[205] I. L. Soroka, J. Vegelius, P. T. Korelis, A. Fallberg, S. M. Butorin, and B. Hjörvarsson, "Structural stability and oxidation resistance of amorphous ZrAl alloys," *J. Nucl. Mater.*, vol. 401, no. 13, pp. 38–45, 2010.

[206] H. Tang, Y. Liu, and D. J. Sellmyer, "Nanocrystalline $Sm_{12.5}(Co,Zr)_{87.5}$ magnets: synthesis and magnetic properties," *J. Magn. Magn. Mater.*, vol. 241, no. 23, pp. 345–356, 2002.

[207] M. Q. Huang, W. E. Wallace, M. McHenry, Q. Chen, and B. M. Ma, "Structure and magnetic properties of $SmCo_{7-x}Zr_x$ alloys (x=0–0.8)," *J. Appl. Phys.*, vol. 83, no. 11, pp. 6718–6720, 1998.

[208] S. Y. Chou, "Patterned magnetic nanostructures and quantized magnetic disks," *Proc. IEEE*, vol. 85, no. 4, pp. 652–671, 1997.

[209] S. Parkin, X. Jiang, C. Kaiser, A. Panchula, K. Roche, and M. Samant, "Magnetically engineered spintronic sensors and memory," *Proc. IEEE*, vol. 91, no. 5, pp. 661–680, 2003.

[210] P. Tartaj, M. del Puerto Morales, S. Veintemillas-Verdaguer, T. González-Carreño, and C. J. Serna, "The preparation of magnetic nanoparticles for applications in biomedicine," *J. Phys. D. Appl. Phys.*, vol. 36, no. 13, p. R182, 2003.

[211] A. Aharoni, *Introduction to the Theory of Ferromagnetism.* Oxford: Oxford University Press, second ed., 2000.

[212] W. F. Brown, *Micromagnetics.* New York: Wiley, 1963.

[213] D. Wei, *Micromagnetics and Recording Materials.* Springer, 2012.

[214] B. Hillebrands, C. Mathieu, C. Hartmann, M. Bauer, O. Büttner, S. Riedling, B. Roos, S. O. Demokritov, B. Bartenlian, C. Chappert, D. Decanini, F. Rousseaux, E. Cambril, A. Müller, B. Hoffmann, and U. Hartmann, "Static and dynamic properties of patterned magnetic permalloy films," *J. Magn. Magn. Mater.*, vol. 175, no. 12, pp. 10–15, 1997.

[215] C. Mathieu, C. Hartmann, M. Bauer, O. Buettner, S. Riedling, B. Roos, S. O. Demokritov, B. Hillebrands, B. Bartenlian, C. Chappert, D. Decanini, F. Rousseaux, E. Cambril, A. Müller, B. Hoffmann, and U. Hartmann, "Anisotropic magnetic coupling of permalloy micron dots forming a square lattice," *Appl. Phys. Lett.*, vol. 70, no. 21, pp. 2912–2914, 1997.

[216] M. Schneider, H. Hoffmann, and J. Zweck, "Magnetic switching of single vortex permalloy elements," *Appl. Phys. Lett.*, vol. 79, no. 19, pp. 3113–3115, 2001.

[217] M. Pärnaste, M. Marcellini, E. Holmström, N. Bock, J. Fransson, O. Eriksson, and B. Hjörvarsson, "Dimensionality crossover in the induced magnetization of Pd layers," *J. Phys. Condens. Matter*, vol. 19, no. 24, p. 246213, 2007.

[218] K. L. Metlov and Y. Lee, "Map of metastable states for thin circular magnetic nanocylinders," *Appl. Phys. Lett.*, vol. 92, no. 11, 2008.

[219] S.-H. Chung, R. D. McMichael, D. T. Pierce, and J. Unguris, "Phase diagram of magnetic nanodisks measured by scanning electron microscopy with polarization analysis," *Phys. Rev. B*, vol. 81, no. 2, p. 24410, 2010.

[220] V. Novosad, K. Y. Guslienko, H. Shima, Y. Otani, S. G. Kim, K. Fukamichi, N. Kikuchi, O. Kitakami, and Y. Shimada, "Effect of interdot magnetostatic interaction on magnetization reversal in circular dot arrays," *Phys. Rev. B*, vol. 65, no. 6, p. 60402, 2002.

[221] R. F. Wang, C. Nisoli, R. S. Freitas, J. Li, W. McConville, B. J. Cooley, M. S. Lund, N. Samarth, C. Leighton, V. H. Crespi, and P. Schiffer, "Artificial 'spin ice' in a geometrically frustrated lattice of nanoscale ferromagnetic islands.," *Nature*, vol. 439, no. 7074, pp. 303–306, 2006.

[222] E. Mengotti, L. J. Heyderman, A. F. Rodriguez, F. Nolting, R. V. Hugli, and H.-B. Braun, "Real-space observation of emergent magnetic monopoles and associated Dirac strings in artificial kagome spin ice," *Nat. Phys.*, vol. 7, no. 1, pp. 68–74, 2011.

[223] C. Nisoli, R. Moessner, and P. Schiffer, "Colloquium," *Rev. Mod. Phys.*, vol. 85, no. 4, pp. 1473–1490, 2013.

[224] X. M. Cheng and D. J. Keavney, "Studies of nanomagnetism using synchrotron-based x-ray photoemission electron microscopy (X-PEEM)," *Reports Prog. Phys.*, vol. 75, no. 2, p. 26501, 2012.

[225] D. S. Eastwood, T. P. A. Hase, M. van Kampen, R. Bručas, B. Hjörvarsson, D. Atkinson, and B. K. Tanner, "X-ray scattering from two-dimensionally patterned magnetic thin film nanoscale arrays," *Superlattices Microstruct.*, vol. 41, no. 23, pp. 163–167, 2007.

[226] J. P. Morgan, C. J. Kinane, T. R. Charlton, A. Stein, C. Sánchez-Hanke, D. A. Arena, S. Langridge, and C. H. Marrows, "Magnetic hysteresis of an artificial square ice studied by in-plane Bragg x-ray resonant magnetic scattering," *AIP Adv.*, vol. 2, no. 2, 2012.

[227] E. O. Brigham, *The Fast Fourier Transform and Its Applications*. 1988.

[228] S. K. Sinha, M. Tolan, and A. Gibaud, "Effects of partial coherence on the scattering of x rays by matter," *Phys. Rev. B*, vol. 57, no. 5, pp. 2740–2758, 1998.

[229] M. Tolan, *X-Ray Scattering from Soft-Matter Thin Films: Materials Science and Basic Research*. Springer Tracts in Modern Physics, Springer Berlin Heidelberg, 1998.

[230] J. Crangle, "Ferromagnetism in Pd-rich palladium-iron alloys," *Philos. Mag.*, vol. 5, no. 52, pp. 335–342, 1960.

[231] T. Herrmannsdörfer, S. Rehmann, W. Wendler, and F. Pobell, "Magnetic properties of highly dilutedPdFex andPtFex-alloys. Part I. Magnetization at kelvin temperatures," *J. Low Temp. Phys.*, vol. 104, no. 1, pp. 49–65, 1996.

[232] P. P. Craig, D. E. Nagle, W. A. Steyert, and R. D. Taylor, "Paramagnetism of Fe Impurities in Transition Metals," *Phys. Rev. Lett.*, vol. 9, no. 1, pp. 12–14, 1962.

[233] G. G. Low and T. M. Holden, "Distribution of the ferromagnetic polarization induced by iron and cobalt atoms in palladium," *Proc. Phys. Soc.*, vol. 89, no. 1, p. 119, 1966.

[234] E. T. Papaioannou, V. Kapaklis, A. Taroni, M. Marcellini, and B. Hjrvarsson, "Dimensionality and confinement effects in -doped pd(fe) layers," *Journal of Physics: Condensed Matter*, vol. 22, no. 23, p. 236004, 2010.

[235] A. Pierret, M. Hocevar, S. L. Diedenhofen, R. E. Algra, E. Vlieg, E. C. Timmering, M. A. Verschuuren, G. W. G. Immink, M. A. Verheijen, and E. P. A. M. Bakkers, "Generic nano-imprint process for fabrication of nanowire arrays," *Nanotechnology*, vol. 21, no. 6, p. 65305, 2010.

[236] E. Östman, U. B. Arnalds, E. Melander, V. Kapaklis, G. K. Pálsson, A. Y. Saw, M. A. Verschuuren, F. Kronast, E. T. Papaioannou, C. S. Fadley, and B. Hjörvarsson, "Hysteresis-free switching between vortex and collinear magnetic states," *New J. Phys.*, vol. 16, 2014.

[237] G. Mihajlović, M. S. Patrick, J. E. Pearson, V. Novosad, S. D. Bader, M. Field, G. J. Sullivan, and A. Hoffmann, "Temperature dependent nucleation and annihilation of individual magnetic vortices," *Appl. Phys. Lett.*, vol. 96, no. 11, 2010.

[238] T. S. Machado, T. G. Rappoport, and L. C. Sampaio, "Vortex core magnetization dynamics induced by thermal excitation," *Appl. Phys. Lett.*, vol. 100, no. 11, 2012.

[239] A. T. D. Grünwald, A. R. Wildes, W. Schmidt, E. V. Tartakovskaya, J. Kwo, C. Majkrzak, R. C. C. Ward, and A. Schreyer, "Magnetic excitations in dy/y superlattices as seen via inelastic neutron scattering," *Phys. Rev. B*, vol. 82, p. 014426, 2010.

[240] S. V. Grigoriev, Y. O. Chetverikov, D. Lott, and A. Schreyer, "Field induced chirality in the helix structure of Dy/Y multilayer films and experimental evidence for dzyaloshinskii-moriya interaction on the interfaces," *Phys. Rev. Lett.*, vol. 100, p. 197203, 2008.

[241] J. T. Haraldsen and R. S. Fishman, "Spin-wave dynamics of magnetic heterostructures: application to dy/y multilayers," *Journal of Physics: Condensed Matter*, vol. 22, no. 18, p. 186002, 2010.

[242] V. Tarnavich, E. Tartakovskaya, Y. Chetverikov, V. Golub, D. Lott, Y. Chernenkov, A. Devishvili, V. Ukleev, V. Kapaklis, A. Oleshkevych, V. Fedorov, V. Bairamukov, A. Vorobiev, and S. Grigoriev, "Magnetic field induced chirality in ho/y multilayers with gradually decreasing anisotropy," *Phys. Rev. B*, vol. 96, p. 014415, 2017.

[243] V. V. Tarnavich, D. Lott, S. Mattauch, A. Oleshkevych, V. Kapaklis, and S. V. Grigoriev, "Field-induced chirality in the helix structure of ho/y multilayers," *Phys. Rev. B*, vol. 89, p. 054406, 2014.

[244] A. Farhan, P. M. Derlet, A. Kleibert, A. Balan, R. V. Chopdekar, M. Wyss, J. Perron, A. Scholl, F. Nolting, and L. J. Heyderman, "Direct observation of thermal relaxation in artificial spin ice," *Phys. Rev. Lett.*, vol. 111, p. 057204, 2013.

[245] S. Zhang, I. Gilbert, C. Nisoli, G. Chern, M. J. Erickson, L. OBrien, C. Leighton, P. E. Lammert, V. H. Crespi, and P. Schiffer, "Crystallites of magnetic charges in artificial spin ice," *Nature*, vol. 500, pp. 553–557, 2013.

[246] J. Drisko, S. Daunheimer, and J. Cumings, "fepd$_3$," *Phys. Rev. B*, vol. 91, p. 224406, 2015.